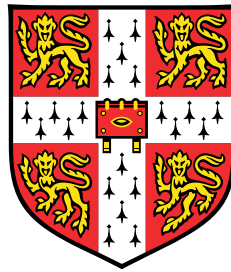


Physical and Stochastic Aspects

of

Microorganism Behaviour



Julius Bier Kirkegaard

Department of Applied Mathematics and Theoretical Physics
University of Cambridge

This dissertation is submitted for the degree of
Doctor of Philosophy

St John's College

June 2018

Declaration

I hereby declare that this dissertation is the result of my own work and includes nothing which is the outcome of work done in collaboration except as declared in the Preface and specified in the text.

It is not substantially the same as any that I have submitted, or, is being concurrently submitted for a degree or diploma or other qualification at the University of Cambridge or any other University or similar institution. I further state that no substantial part of my dissertation has already been submitted, or, is being concurrently submitted for any such degree, diploma or other qualification at the University of Cambridge or any other University or similar institution.

The subjects, ideas and approaches of this dissertation are the result of many discussions with my supervisor Raymond E. Goldstein.

The experimental parts of Chapter 2 have been done in collaboration with Alan O. Marron and François J. Peaudecerf. Alan O. Marron did preliminary studies of the swimming trajectories of *S. rosetta* cells and helped with the manual tracking of colonies in some of the final experiments. He furthermore provided the strains used as well as expertise on their biology. The experiments using *digital inline holography* were done in collaboration with François J. Peaudecerf, with whom I built the microscopic setup.

The subject of Chapter 3 is aerotaxis in choanoflagellates. This project was co-supervised by Kyriacos C. Leptos, who helped with the safety of handling gas cylinders and provided many helpful discussions. Preliminary designs for the experimental protocol on aerotaxis were developed in collaboration with Ambre Bouillant. Tests of the design on *B. subtilis* were also done in collaboration with Ambre Bouillant. Alan O. Marron provided biological insight for the choanoflagellate biology.

The experimental data of Chapter 6 were provided by Kirsty Y. Wan.

Except for my supervisor, the remaining chapters are not collaborative. Despite this, I will exercise nosism throughout.

Julius Bier Kirkegaard

June 2018

Acknowledgements

First and foremost, I would like to thank my supervisor Ray Goldstein. I am extremely grateful to have been accepted into his amazing research group. My PhD has benefited tremendously from Ray's deep scientific knowledge and exceptional overview over the scientific literature. I feel extremely fortunate to have had a supervisor who shows complete trust in one's work and allows almost complete scientific freedom. Lastly, beyond scientific insights, while patiently going through manuscripts, Ray has taught me how to present a scientific story and a lot about how to use the English language properly.

Having never done any biological experiments before, I had to be taught everything from pipetting to how to keep cultures alive. I am very grateful to Alan Marron for showing me the basics of this. Kyriacos Leptos acted as a co-supervisor on the aerotaxis project, and I am very grateful for his biological insights, his advice on safety management, and in general for his constant encouragement. With Kyriacos, I also started a project on *Dictyostelium discoideum*. It was very fun to learn how to work on a completely different species, even if the project was not successful (yet). I am also grateful to a summer student, Ambre Bouillant, who visited the lab in the summer of 2015. With Ambre, I spent a great number of hours in the lab trying to optimise the design of various devices to probe aerotactic behaviours.

I would also like to thank current and previous members of both Ray Goldstein's and Eric Lauga's group including Anne Herrmann, Aurelia Honerkamp-Smith, Debasish Das, Emily Riley, Francesco Boselli, François Peaudecerf, Gabriele de Canio, Hélène de Maleprade, Hugo Wioland, Justas Dauparas, Kirsty Wan, Kyriacos Leptos, Maciej Lisicki, Nuno Oliveira, Pierre Haas, and Stephanie Höhn. They have not only provided an amazing scientific environment, but also an amazing social one.

Special thanks goes to my office mates François Peaudecerf and Pierre Haas, with whom I have had countless (un)scientific discussions. It has been absolutely wonderful to share an office with them. Combined they can answer any experimental and theoretical question.

While not contributing directly to the present work, I feel very lucky to have been able to interact with the group of Tuomas Knowles during my time in Cambridge. This collaboration has provided me with insight into areas of biophysics very different from the subject of my

thesis, from protein aggregation dynamics (Meisl et al., 2016; Michaels et al., 2016; Varilly et al., 2017), to *C. elegans* biology and drug discovery techniques (Perni et al., 2017). It has been an absolute joy to collaborate with this group, in particular with Georg Meisl, Thomas Michaels, Alex Dear, and Michele Perni.

Finally, I would like to thank friends and family, both in Cambridge and Denmark. I feel enormously lucky to have been able to live in a house in Cambridge that I could call home with Hannah Sheahan, Jonathan Shanahan, and Rebekah Larsen. I have to thank my mom, sister and stepdad, who have been very supportive throughout my PhD and who have not pushed too hard for me to visit Denmark all the time. I can thank my dad less in this latter regard, but I am still very grateful for him fully supporting his “*fly researcher son*”. Lastly, I am extremely grateful for the love and support of my girlfriend Julie. I am absolutely thrilled that we managed a long-distance relationship on top of a PhD life and that we are still happily together.

The work in this thesis was supported by a grant from the Engineering and Physical Sciences Research Council and a Benefactors’ Scholarship from St John’s College.

Abstract

This thesis studies physical and stochastic aspects of microorganisms. From the point of view of *physics*, the studies in this thesis are motivated by the goal of gaining biological insight using the machinery of physics and mathematics. From the point of view of *biology*, the studies in this thesis focus primarily on choanoflagellates, eukaryotes that are the closest living unicellular relatives of animals. This choice of model organism was motivated by the important biological question of the origin of multicellularity. Why was it that single-celled organisms evolved to become multicellular? In particular, we study closely the species *Salpingoeca rosetta*, which has the ability to form colonies that resemble true multicellular organisms.

A large part of this thesis deals with the random walks of microorganisms. We study these active random walks both for single cells and those composed of individual organisms adhered together. The latter colonial random walkers are typified by choanoflagellates. We develop quantitative theories and use these to extract physical parameters.

The increasing ocean oxygen levels in the Precambrian era are thought to be an important factor in the emergence of complex multicellular, animal life. As a first step, we address this situation by studying the response of *S. rosetta* to oxygen gradients. We find that *S. rosetta* displays positive aerotaxis. Analysis of the spatial population distributions provides evidence for logarithmic sensing of oxygen, which enhances sensing in low oxygen neighbourhoods. Analysis of search strategy models on the experimental colony trajectories finds that choanoflagellate aerotaxis is consistent with stochastic navigation, the statistics of which are captured using an effective continuous version of classical run-and-tumble chemotaxis.

We compare this continuous run-to-tumble with the run-and-tumble seen in bacteria by formulating a general model for persistent run-and-tumble. We find that although an optimal persistence does exist for a given tumble frequency, in the full parameter space there is a continuum of optimal solutions. We develop this model further by introducing finite tumble times.

Efficient uptake of prey and nutrients from the environment is an important component in the fitness of all microorganisms, and its dependence on size may reveal clues to the

origins of evolutionary transitions to multicellularity. We examine these issues in depth for choanoflagellates, finding that in the absence of other requirements and in a homogeneously nutritious environment, the optimal strategy to maximise filter feeding is to swim fast which favours swimming unicells. In contrast, in large external flows, a sessile form becomes advantageous. Effects of prey diffusion are discussed and are also found to be advantageous for the swimming unicell.

Finally, we consider the switching between synchronous and anti-synchronous beating of flagella in the green alga *Chlamydomonas*, a phenomenon that results in run-and-tumble behaviour in eukaryotes. We develop a theoretical model to describe this beating and use it to argue that the synchrony itself is obtained intracellularly, whereas the flagella shapes are most likely strongly influenced by hydrodynamic interactions.

Contents

1	Introduction	1
1.1	Life at Low Reynolds Number	2
1.2	Stochasticity	8
1.3	Active Matter & Cell Behaviour	14
1.4	Choanoflagellates & Multicellularity	16
1.5	Outline	18
2	Random Walks of Colonies	21
2.1	Introduction	21
2.2	Flagella Dynamics	22
2.3	The Random Walk of Colonies	24
2.3.1	Experimental Results	24
2.3.2	Theory of Active Random Walkers	26
2.3.3	Species Variability	34
2.4	Fitting Short Tracks	36
2.5	Three-Dimensional Tracking	44
2.6	Conclusions	48
	Appendix 2.A Tracking Flagella	48
	2.A.1 Active Contour Model	49
	2.A.2 Morphological Skeletonisation	50
	Appendix 2.B Stochastic Swimming Speeds	52
	2.B.1 On-Off Swimming	52
	2.B.2 Ornstein-Uhlenbeck Swimming	53
	Appendix 2.C Digital Inline Holography	54
	Appendix 2.D Stochastic Simulations	57
3	Choanoflagellate Aerotaxis	59
3.1	Introduction	59

Contents

3.2	Experimental Set-up	60
3.3	Aerotaxis in Choanoflagellates	61
3.4	Navigation Strategy	63
3.5	Aerotaxis Model	65
3.6	Discussion	71
	Appendix 3.A Data Processing	74
	Appendix 3.B Effective Stochastic Models	75
	Appendix 3.C Implicit Time-Stepping for PDEs	76
4	Chemotactic Efficiency	79
4.1	Introduction	79
4.2	Model	81
4.3	Measurement Time-scale	82
4.4	Tumbling Frequency & Persistence	84
4.5	Chemotactic Strength	88
4.6	Conclusions	91
	Appendix 4.A Linearised with Mean Tumble Angle	93
	Appendix 4.B Linearised with Mean Tumble Angle — Biased Direction	94
	Appendix 4.C Persistence in 3D	95
	Appendix 4.D Simplified Effective Model	96
	Appendix 4.E Run-and-tumble in Discrete 1D	96
	4.E.1 Optimal Kernel	97
	4.E.2 Chemotaxis in a Constant Gradient	97
	4.E.3 Effective Rotational Diffusion	98
	4.E.4 Chemotaxis in a Spatially Varying Gradient	98
	Appendix 4.F Direct Gradient Sensing	100
5	Colonial Filter-Feeding	109
5.1	Introduction	109
5.2	Model	110
5.3	Flow around Dimers	112
5.4	Diffusion Effects	114
5.5	Larger Colonies	117
5.6	Thecate cells	119
5.7	Conclusions	120
	Appendix 5.A Boundary Element Method	122
	Appendix 5.B Finite Element Method	128

5.B.1	Laplace Equation	128
5.B.2	Advection-Diffusion Equation	132
5.B.3	Assessing Flux	132
5.B.4	Ensuring Incompressibility	133
6	Synchronisation of Flagella	135
6.1	Introduction	135
6.2	Flagellum Model	136
6.2.1	Feedback Control	141
6.3	Data Processing	141
6.4	Eigenvalue Problem	143
6.5	Flagella Waveforms	145
6.6	Synchronisation	148
6.7	Discussion	150
Appendix 6.A	Finite Difference Coefficients	152
7	Conclusions	155
	Bibliography	159
Appendix	Materials and Methods	175
A.1	Culturing Cells	175
A.2	Microfluidic Devices	175
A.3	Tracking	176

Chapter 1

Introduction

Microbes inhabit almost every aspect of the world that surrounds us, yet for the majority of human history we lived unaware of their existence. It was not before 1674 that Antonie van Leeuwenhoek saw the microbial world for the first time. So he writes, in a letter to the Royal Society, “*Examining this water next day, I found floating therein divers earthy particles, and some green streaks, spirally wound serpent-wise... I judge that some of these little creatures were above a thousand times smaller than the smallest ones I have ever yet seen, upon the rind of cheese, in wheaten flour, mould, and the like.*” And thus started the field of *microbiology*.

Since van Leeuwenhoek’s discovery, microscopes have improved massively, and today we can even peak inside these *little creatures* to discover tiny organelles, strands of DNA, and the folding of proteins. This has been possible due to modern techniques such as X-ray crystallography and electron microscopy. Today, a new approach to furthering the understanding of biology is gaining momentum, namely that which can be obtained through physics and mathematical modelling.

Despite the same physical laws governing the human and the microbial world, the differences are enormous. One major reason for this is the fact that the same physical law can have very different consequences at different scales. Thus, for instance, gravity is a huge factor for humans, but is barely felt at the microbial scale, where instead viscous drag dominates. Likewise, diffusion effects are significant at the microbial scale, but play little to no role at the scale of humans.

Traditionally, physics is the science of fundamental laws of nature, and mathematical descriptions hereof have had a huge impact on fields ranging from chemistry to astronomy. Biology, on the other hand, differs from the more fundamental sciences in being much too complex for a full mathematical description. Instead, the field of *biophysics* attempts to tackle biological problems at a certain level of granularity. As put forth by von Neumann,

“*Truth [...] is much too complicated to allow anything but approximations*”. This holds particularly true in the field of biophysics. The questions biophysics try to answer often become of the form of *emergence*: given a set of rules for a system, what behaviour emerges?

A biological cell is an extremely complex system, the internal processes ranging from DNA transcription in cell nuclei to ATP production in the mitochondria. This thesis deals with problems at the scale of overall cell behaviour, which is an overly complex problem if a full description of the cell is required. The problems identified and studied in this thesis, however, only depend on a few rules necessary for a valid description. The correct set of rules is guided by experimental observations. Microorganism swimming, for instance, can be modelled while neglecting the underlying complex network of connections from which this motion emerges. Simple experimental measurements inform us of the propulsion mechanism, and this alone allows modelling of swimming efficiency, feedings flows, etc.

A key theme in this thesis will be *optimality*. Evolution is nature’s stochastic algorithm for optimisation. Given the span of time since the origin of microorganisms, we expect microorganisms that have survived these countless generations of natural selection to operate close to some (local) optimum. The big question, however, is what factors are being directly optimised for. Nature is highly multivariate and trade-offs exist everywhere. In some of the studies in this thesis, we will try to optimise some *utility function*. While this might not be the precise function that is actually optimised against in nature, the approach can still reveal much insight.

The problems considered in this thesis are, at least to some extent, motivated by the question of the origin of multicellularity: why was it that single-celled organisms evolved to become multicellular? While we do not (even intend to) answer this extremely important question even slightly, the problems we consider will be peripherally associated with this question. In particular, the choice of model organisms studied in this thesis, have been guided by this overall theme of research.

1.1 Life at Low Reynolds Number

Aquatic life is subject to the laws of fluid mechanics, in particular to the fundamental governing law of fluid motion, the Navier-Stokes equations,

$$\rho \left(\frac{\partial u}{\partial t} + (u \cdot \nabla)u \right) = -\nabla p + \mu \nabla^2 u, \quad (1.1a)$$

$$\nabla \cdot u = 0, \quad (1.1b)$$

describing the fluid velocity $u(x,t)$ and pressure $p(x,t)$ for an incompressible fluid with density ρ and dynamic viscosity μ . Non-dimensionalising with the length-scale L and velocity-scale U of the problem at hand (e. g. the size of a cell and its swimming speed), such that $x^* = x/L$, $u^* = u/U$, $t^* = t/(L/U)$, and $p^* = p/(\mu U/L)$ are non-dimensional variables (another choice of pressure non-dimensionalisation is $p^* = p/(\rho U^2)$, which is appropriate for high velocity flows), the Navier-Stokes equations can be written

$$\text{Re} \left(\frac{\partial u^*}{\partial t^*} + (u^* \cdot \nabla) u^* \right) = -\nabla p^* + \nabla^2 u^*, \quad (1.2a)$$

$$\nabla \cdot u^* = 0, \quad (1.2b)$$

where the Reynolds number

$$\text{Re} = \frac{\rho L U}{\mu} \quad (1.3)$$

is a number characterising the ratio of inertial forces to viscous forces. For microorganisms, $L \sim 1 - 20 \mu\text{m}$ and $U \sim 1 - 50 \mu\text{m/s}$, and for water $\mu \sim 1 \text{ mPa}\cdot\text{s}$ and $\rho \sim 1 \text{ g/cm}^3$, such that

$$\text{Re} \sim 10^{-6} - 10^{-3}, \quad (1.4)$$

revealing that fluid inertial forces are negligible at microorganism scales. Taking the full limit $\text{Re} \rightarrow 0$ in Eq. (1.2) leads to the Stokes equations

$$\mu \nabla^2 u = \nabla p, \quad (1.5a)$$

$$\nabla \cdot u = 0, \quad (1.5b)$$

where dimensional variables have been reintroduced.

Equation (1.5) is the governing equation of fluid mechanics at the level of microorganisms. Since the equation is linear, the translational and rotational velocities of a rigid body, U and Ω , are linearly related to the drag forces and torques, F and L , acting on them,

$$\begin{pmatrix} F \\ L \end{pmatrix} = \text{D} \begin{pmatrix} U \\ \Omega \end{pmatrix}, \quad (1.6)$$

where D is the drag matrix [D^{-1} is called the mobility matrix]. For a sphere of radius a , for instance (Kim and Karrila, 2005),

$$D = \pi\mu \begin{pmatrix} 6a & 0 & 0 & 0 & 0 & 0 \\ 0 & 6a & 0 & 0 & 0 & 0 \\ 0 & 0 & 6a & 0 & 0 & 0 \\ 0 & 0 & 0 & 8a^3 & 0 & 0 \\ 0 & 0 & 0 & 0 & 8a^3 & 0 \\ 0 & 0 & 0 & 0 & 0 & 8a^3 \end{pmatrix}. \quad (1.7)$$

For instance, F could be the force due to gravity, and we immediately have that a sphere in Stokes flow falls with velocity $U = F/6\pi\mu a$ (the magnitude of F is given by Archimedes' principle). For more complex geometries, D will have off-diagonal terms. Approximating microorganisms as spheres yields the range of relevant drag forces

$$F \sim 10^{-14} - 10^{-11} \text{ N} = 10^{-2} - 10 \text{ pN}, \quad (1.8)$$

showing that the relevant force scale is piconewtons.

Another striking feature of Eq. (1.5) is that time does not explicitly appear. This means that the present boundary conditions instantaneously define the fluid velocity everywhere. It furthermore implies that any reciprocal motion cannot result in net motion, since any effect from flow resulting from a boundary deformation will be reversed when the boundary deformation is reversed. This is the celebrated Scallop theorem (Purcell, 1977), named after the reciprocal motion of a scallop opening and closing. Such a loop, opening and closing, cannot, even if opening is done much slower than closing, result in any net motion at zero Reynolds number. The scallop theorem has immediate consequences for motile microorganisms: their motion cannot be driven by reciprocal motion, as it is possible for fish wiggling their tails. Non-reciprocal motion can be generated in various ways. Fig. 1.1 shows two types of naturally occurring flagella, the microorganism appendages that propel them forwards.

In motile prokaryotes such as bacteria, Fig. 1.1(a,c), the flagellum is a passive rigid helix, typically left-handed, that when spun counter-clockwise (looking in direction of travel) propels the bacterium forwards (Berg and Anderson, 1973; Silverman and Simon, 1974). The flagellum is attached to a small flexible hook, Fig. 1.2a, that in turn is rotated by a stepper motor (Berg, 2003). The continuous spinning of the helix geometry of the flagellum overcomes the requirement of non-reciprocal motion. Solving the Stokes equations for a

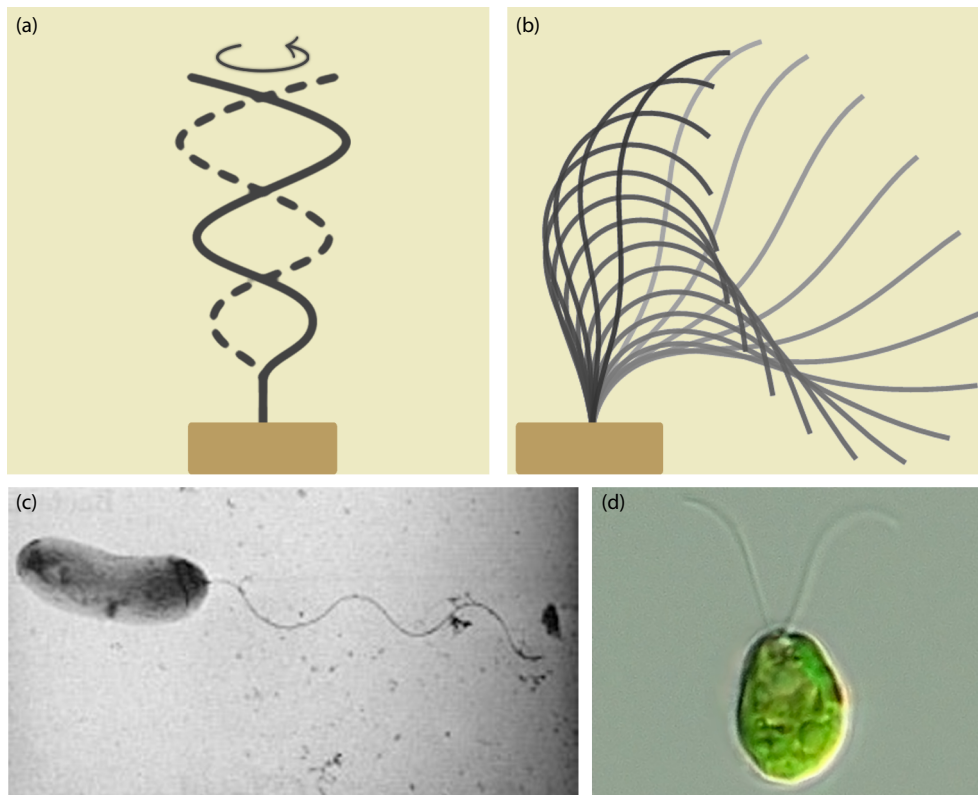


Figure 1.1 Flagella found in nature. (a) Prokaryotic flagellum. A rigid rotating helix. (b) Eukaryotes flagellum. An elastic filament deforming in a non-reciprocal manner. (c) Electron micrograph of *Vibrio cholerae* by Leodotia Pope, Department of Microbiology, University of Texas at Austin. Obtained from MicrobeWiki. (d) Bright field image on *Chlamydomonas reinhardtii*. Obtained from Alchetron under Creative Commons BY-SA License.

bacterium with a rigid helix, would result in D in Eq. (1.6) with off-diagonal terms coupling the rotation of the helix to translation velocity (Lauga and Powers, 2008).

In contrast to prokaryotes, the flagellar beat of flagellated eukaryotes resembles more a whip-like beat, Fig. 1.1(b,d). This is an elastic method for overcoming the requirement of non-reciprocal motion. In the *power-stroke* part of the beat, the flagellum is extended, while it is contracted during the *recovery* part of the stroke (Ringo, 1967), as illustrated in Fig. 1.1b. Eukaryotic flagella are often called cilia when occurring many together, such as in *Paramecium* or in human lungs. In eukaryotic flagella, the flagella beat is driven by motors distributed along the flagellum. Its typical microstructure consists of two central and nine peripheral doublets of microtubules, Fig. 1.2b. These filaments are cross-linked by dynein motors that slide the filaments relative to one another, powered by hydrolysis of ATP (Mitchell, 2000; Smith, 2002). The structure of the eukaryotic flagellum is one of the most conserved structures in biology (Pazour et al., 2005).

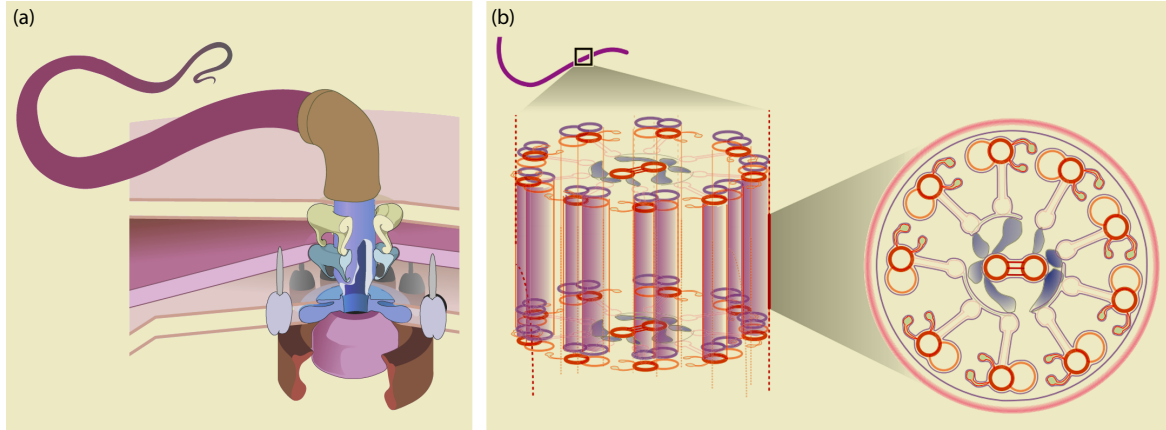


Figure 1.2 Flagella microstructure. (a) Prokaryotic flagellum. (b) Eukaryotic flagellum. Adapted from [Wan et al. \(2013\)](#), under Creative Commons BY-SA License.

Another direct consequence of inertial forces being negligible is that viscous forces will directly balance any external forces. Most microorganisms are approximately neutrally buoyant, and thus zero external forces results in microorganisms being overall force- and torque-free. This, in turn, affects the flow-signature surrounding the microorganisms. Since the Stokes equation is linear, it has a Green's function, i. e. the solution for the flow around a point force $F \delta(x)$ in unbounded flows,

$$-\nabla p + \mu \nabla^2 u = -F \delta(x - x_0), \quad (1.9a)$$

$$\nabla \cdot u = 0, \quad (1.9b)$$

subject to $|u(x)| \rightarrow 0$ as $|x| \rightarrow \infty$. The solution is the so-called Stokeslet ([Kim and Karrila, 2005](#); [Lisicki, 2013](#))

$$u(x) = G(x - x_0) \cdot F = \frac{1}{8\pi\mu |x - x_0|} \left(I + \frac{(x - x_0)(x - x_0)}{|x - x_0|^2} \right) \cdot F, \quad (1.10)$$

where G is called the Oseen tensor and I is the identity matrix. This will be the far-field signature of any object with total external force F , e. g. a microorganism that is not neutrally buoyant. The flow field is illustrated in Fig. 1.3a. The decay is quite slow, $|x|^{-1}$, and thus effects manifest far away. For instance, the forces on nearby walls will influence the swimming of microorganisms ([Berke et al., 2008](#); [Shum and Gaffney, 2015](#)). The Stokeslet is a singularity solution and diverges at $x = x_0$. By itself, it is thus only a valid description of the far-field flow.

Neutrally buoyant microorganism do not have the far-field flow signature of the Stokeslet, since they have no net force acting on them. They do have force dipoles, however. The

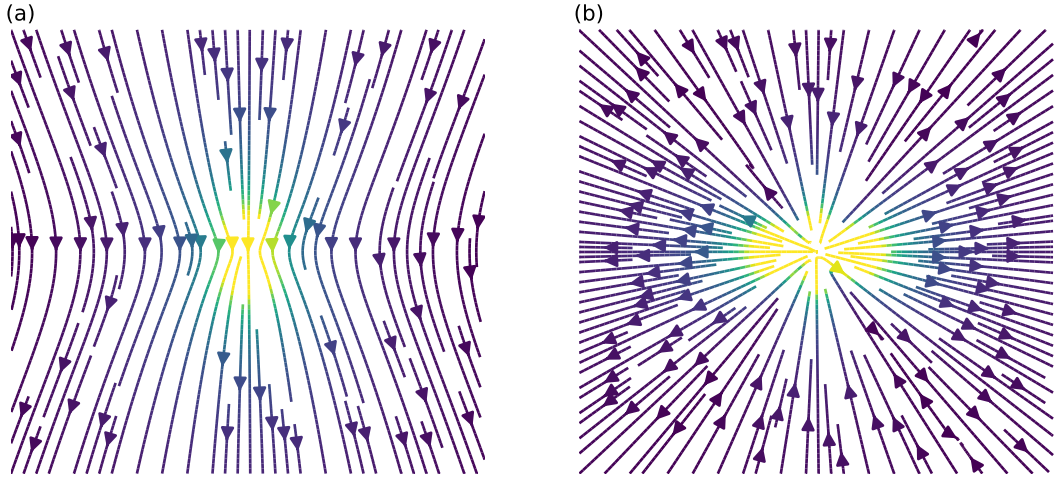


Figure 1.3 Far-field flow fields (a) Stokeslet of a downwards-pointing force at the origin. A cell falling under gravity would show this flow signature. (b) Stresslet. A bacterium (pusher) swimming left or right would show this flow signature, as would an algae (puller) swimming upwards or downwards.

flagellum in one end is acting with a propulsive force on the fluid, and the body experiences a balancing drag force. The solution for a point dipole can be obtained by taking derivatives of the Stokeslet. If the derivative (with respect to x_0) is taken along the axis of F , the solution is the stresslet,

$$u = -\frac{3(x-x_0) \cdot S \cdot (x-x_0)}{8\pi\mu |x-x_0|^5} (x-x_0), \quad (1.11)$$

where S is the stresslet strength given by a symmetric and trace-free matrix. For instance, in the case of finitely many forces $\{F_i\}$ at locations $\{x_i\}$, this can be obtained as

$$S = -\sum_i \left(\frac{1}{2}(F_i x_i^T + x_i F_i^T) - \frac{1}{3}(x_i \cdot F_i) I \right). \quad (1.12)$$

This solution to the Stokes equations is shown in Fig. 1.3b.

If the derivative is taken perpendicular to F , the solution is the rotlet, which is the forcing due to a point torque. But since neutrally buoyant microorganisms are also torque-free, their signature will typically be of a stresslet. This solution, and thus the flow fields generated by microorganisms, decays like $|x|^{-2}$.

The stresslet flow categorises swimmers into two types: *pushers* and *pullers* (Marchetti et al., 2013). Swimmers such as bacteria that have their propulsion mechanism to the back of the swimming direction [Fig. 1.1c] are called pushers (for obvious reasons), and they will have the flow signature of Fig. 1.3b if they are swimming left or right: the liquid, being pulled in from the sides, is being pushed away behind them by their flagella and away in front

of them by their swimming cell body. In contrast, swimmers such as biflagellated algae that have their propulsion mechanism in the front of swimming direction [Fig. 1.1d] are called pullers and will have the flow signature of Fig. 1.3b in the up/down direction. They pull in liquid from the front, and it is pulled along the swimmer at the back. The flow signature of swimming has consequences for how swimmers interact with both other swimmers and obstacles such as walls (Saintillan and Shelley, 2007).

1.2 Stochasticity

Brownian motion due to thermal noise affects both passive and active particles. Brownian particles can be described through the evolution of the density $\rho(x, t)$ of a collection of particles. For simple Brownian particles, the density $\rho(x, t)$ will evolve according to the diffusion equation

$$\frac{\partial \rho}{\partial t} = \nabla \cdot [D \nabla \rho], \quad (1.13)$$

where D is the (potentially varying) diffusion coefficient. The behaviour of a single particle, located at $x = 0$ at $t = 0$, can be found by solving for the Green's function of the diffusion equation, i. e. Eq. (1.13) with the initial condition $\rho(x, 0) = \delta(x)$. The solution for constant D in d dimensions is the Gaussian

$$\rho(x, t) = \frac{1}{\sqrt{(4\pi Dt)^d}} \exp\left(-\frac{x \cdot x}{4Dt}\right). \quad (1.14)$$

Instructively, we calculate the first two moments of this solution. The mean displacement,

$$\langle x \rangle = \int x \rho(x, t) dx = 0, \quad (1.15)$$

is naturally zero, since a random motion has no preferred direction. The squared displacement is

$$\langle |x|^2 \rangle = \int x \cdot x \rho(x, t) dx = 2dDt, \quad (1.16)$$

where d is the dimensionality of the space of x . This is the most elementary result for random walks, namely that the squared displacement scales linearly with time t . This is in sharp contrast to ballistic motion for which $|x|^2 \sim t^2$.

A different approach to modelling Brownian motion is through the Langevin equation. Writing Newton's second law for a particle experiencing a drag $-\lambda \partial_t x$ and an external force $\eta(t)$, we have

$$m \frac{d^2 x}{dt^2} = -\lambda \frac{dx}{dt} + \eta(t). \quad (1.17)$$

Here, $\eta(t)$ is a random noise resulting from the thermal fluctuations of the environment. Naturally, $\langle \eta(t) \rangle = 0$. The variations of $\eta(t)$ are so fast that on relevant time scales it can be considered delta-correlated:

$$\langle \eta_i(t) \eta_j(t') \rangle = B \delta_{ij} \delta(t - t'), \quad (1.18)$$

where B is a measure of noise strength. In the overdamped limit of Eq. (1.17) we have the Langevin equation

$$\lambda \frac{dx}{dt} = \eta(t). \quad (1.19)$$

The explicit solution,

$$x(t) = \frac{1}{\lambda} \int_0^t \eta(t') dt', \quad (1.20)$$

allows us again to calculate the moments of x :

$$\langle x \rangle = \frac{1}{\lambda} \int_0^t \langle \eta(t') \rangle dt' = 0, \quad (1.21a)$$

$$\begin{aligned} \langle |x|^2 \rangle &= \frac{1}{\lambda^2} \left\langle \left(\int_0^t \eta(t') dt' \right)^2 \right\rangle \\ &= \frac{1}{\lambda^2} \int_0^t \int_0^t \langle \eta(t') \cdot \eta(t'') \rangle dt' dt'' \\ &= \frac{dB}{\lambda^2} \int_0^t \int_0^t \delta(t' - t'') dt' dt'' = \frac{dB}{\lambda^2} t. \end{aligned} \quad (1.21b)$$

Thus we see that if this description should match that of the diffusion equation, we must have $B = 2D\lambda^2$. In fact, with this choice, all moments match.

Before continuing we need to formalise our notation to that of the theory of stochastic differential equations (SDEs). Currently the notation of Eq. (1.19) implies that x is differentiable while the right-hand side is noisy, leading to lack of clarity. A better notation is to introduce the fundamental Wiener process $W(t)$, which simply represents the standard random walk with $\langle W(t) \rangle = 0$ and $\langle W(t)^2 \rangle = t$. Increments dW are Gaussian distributed and $\langle dW(t) dW(t') \rangle = \delta(t - t') dt dt'$. With this notation a general one-dimensional stochastic differential equation can be written

$$dX(t) = \mu(X, t) dt + \sigma(X, t) dW, \quad (1.22)$$

where $\mu(X, t)$ and $\sigma^2(X, t)$ are general functions called the instantaneous drift and instantaneous variance, respectively. Formally, this notation is short-hand for

$$X(t) - X(0) = \int_0^t \mu(X, t) dt + \int_0^t \sigma(X, t) dW. \quad (1.23)$$

The notation avoids the awkward $\frac{dW}{dt}$, the derivative of noise. We will employ this notation throughout. If σ is not independent of X , the equation involves multiplicative noise, since both X and W are stochastic processes. With multiplicative noise, care has to be taken in order to give the product σdW a proper interpretation. In particular, we will only be considering the two standard interpretations. The first is the Itô interpretation, where we define an integral to mean

$$\int_0^T X(t) dW = \sum_{k=0}^{N-1} X(k\Delta t) [W((k+1)\Delta t) - W(k\Delta t)] \quad (1.24)$$

in the limit that Δt tends to zero ($N\Delta t = T$). The other interpretation, the Stratonovich interpretation, defines the integral as

$$\int_0^T X(t) \circ dW = \sum_{k=0}^{N-1} \frac{X((k+1)\Delta t) + X(k\Delta t)}{2} [W((k+1)\Delta t) - W(k\Delta t)], \quad (1.25)$$

where instead we take the midpoint value of X . The symbol \circ signifies a Stratonovich product. Naively, the definitions look similar in the limit $\Delta t \rightarrow 0$. But this is not case, because in contrast to the classical integral, where we would have $|W(t + (k+1)\Delta t) - W(t + k\Delta t)| = \Delta t$, now $|W(t + (k+1)\Delta t) - W(t + k\Delta t)| \sim \sqrt{\Delta t}$.

Which interpretation to use depends on the problem. Physical laws tend to be most naturally formulated in terms of Stratonovich products, since in some sense these laws are “instantaneous”. In contrast, in e. g. financial modelling, the Itô formulation is the most natural choice, since the equations evolve according to the current state only, whereas the Stratonovich product in some sense “peaks” into the future. An Itô system, such as Eq. (1.22), can always be converted to an equivalent Stratonovich by the substitution

$$\sigma(X) dW = \sigma(X) \circ dW - \frac{1}{2} \sigma'(X) \sigma(X) dt, \quad (1.26)$$

where the last term is called the “noise-induced drift”.

As an example, we briefly consider a growth model for a population X (of e. g. micro-organisms) that proliferates with a rate α , but which also has some noise which is, naturally,

proportional to the population size. The Itô model of this is

$$dX = \alpha X dt + \beta X dW, \quad (1.27)$$

where β the noise strength. This equation is also the underlying stock model in the Black-Scholes equation used in financial modelling. Taking the average, we find

$$d\langle X \rangle = \alpha \langle X \rangle dt + \beta \langle X dW \rangle = \alpha \langle X \rangle dt, \quad (1.28)$$

since in an Itô formulation $X(t)$ is completely independent of $dW(t)$ [Eq. (1.24)]. Thus we find $\langle X \rangle \propto e^{\alpha t}$ for this model. Now consider the Stratonovich version of this model

$$dX = \alpha X dt + \beta X \circ dW. \quad (1.29)$$

Now $X(t)$ and $dW(t)$ are no longer independent [Eq. (1.25)], but using Eq. (1.26), we can rewrite the above equation to

$$dX = \left(\alpha + \frac{1}{2}\beta^2 \right) X dt + \beta X dW. \quad (1.30)$$

Thus in this case we find $\langle X \rangle \propto e^{(\alpha + \beta^2/2)t}$. So in this system, if we want to interpret α as the average growth rate, we should take an Itô formulation. This also makes intuitive sense: a population grows according to the *present* population size. This example furthermore shows that even low-order moments, such as the mean value of the process, can be affected by the choice of noise interpretation.

For a given stochastic differential equation (1.22, here interpreted as Itô), the probability distribution $p(x, t)$ for X obeys a corresponding Fokker-Planck equation

$$\frac{\partial p(x, t)}{\partial t} = -\frac{\partial}{\partial x} [\mu(x, t)p(x, t)] + \frac{1}{2} \frac{\partial^2}{\partial x^2} [\sigma(x, t)^2 p(x, t)]. \quad (1.31)$$

We will often need the multi-dimensional version of this equation, which is obtained simply by replacing μ with a sum over the vectorial components of μ and σ^2 with a sum over the components of the matrix $\sigma\sigma^T$. The case $\mu = 0$ and $\sigma = \sqrt{B}/\lambda = \sqrt{2D}$ immediately gives the connection between the Langevin equation for a Brownian particle and the diffusion equation, although slight differences appear if D is dependent on x , since where exactly $D(x)$ appears in the equation depends on the microscopic details (Schnitzer, 1993); for instance, a Stratonovich interpretation gives a slightly different result.

One could also imagine including a potential $V(x)$ that is felt by the Brownian particles, such that

$$\lambda \frac{dx}{dt} = -\nabla V(x) + \eta(t). \quad (1.32)$$

A one-dimensional example of this in SDE notation is

$$\lambda dx = -\partial_x V(x) dt + \sqrt{B} dW. \quad (1.33)$$

The corresponding Fokker-Planck equation is

$$\frac{\partial p(x,t)}{\partial t} = \frac{1}{\lambda} \frac{\partial}{\partial x} [V'(x) p(x,t)] + \frac{B}{2\lambda^2} \frac{\partial^2}{\partial x^2} p(x,t), \quad (1.34)$$

and the steady state distribution thus obeys

$$V'(x) p(x,t) + \frac{B}{2\lambda} \frac{\partial}{\partial x} p(x,t) = \text{constant} \quad (1.35)$$

leading to

$$p(x) \propto \exp\left(-\frac{V(x)}{B/(2\lambda)}\right). \quad (1.36)$$

But we also know from statistical physics that if the system is in thermal equilibrium we must have

$$p(x) \propto \exp\left(-\frac{V(x)}{k_B T}\right), \quad (1.37)$$

and thus we have a fluctuation-dissipation relation $B = 2\lambda k_B T$ and using our previous result for B we obtain the Einstein relation

$$D\lambda = k_B T. \quad (1.38)$$

This equation relates the fluctuations of diffusion to the thermal temperature of the bath. The proportionality factor is the drag coefficient, i. e. the dissipation. Using the Stokes relation from earlier, Eq. (1.7), for a passive sphere suspended in a fluid at temperature T , we have

$$D_{\text{thermal}} = \frac{k_B T}{6\pi\mu a}. \quad (1.39)$$

This equation is called the Stokes-Einstein relation and from it we can estimate the diffusion coefficient of an immotile microorganism. Using $T \sim 20^\circ\text{C}$ and $a \sim 0.5 - 10\mu\text{m}$, we have

$$D_{\text{thermal}} \sim 0.02 - 0.25 \mu\text{m}^2/\text{s}. \quad (1.40)$$

This means that the time to diffuse, say, $10\mu\text{m}$ is in the range of $100 - 2500$ seconds. Therefore, thermal diffusion only has an important effect on the smallest of microorganisms. The larger ones need to supplement their motion with actual motility.

Naively, one might expect motile microorganisms to swim approximately straight, and thus move ballistically rather than diffusively. This is not the case. In fact microorganisms fail to swim straight for a number of reasons. First, thermal noise do not only translate objects but also rotate them. Using Eq. (1.7) and (1.38) we immediately have the thermal rotational diffusion coefficient for a sphere of radius a

$$D_{r,\text{thermal}} = \frac{k_B T}{8\pi\mu a^3} \sim 10^{-5} - 0.2\text{s}^{-1} \quad (1.41)$$

Thus microorganisms will be reoriented by thermal noise and unable to swim straight over long times. This effect is only significant for small microorganism, as is clear from the order-of-magnitude estimates. Secondly, chemical noise internal to the cell might prevent accurate beating of the flagella, which will also prevent straight swimming. And third, it might be in the interest of the cells to not swim straight. One navigational strategy employed by certain bacteria is to reorient themselves actively after having swum a certain distance. The navigational aspects of this strategy, which is called *run-and-tumble*, will be postponed until later chapters, but here we can use the behaviour to illustrate a simple calculation of a diffusion constant due to active swimming.

Consider a cell swimming with constant speed v in a direction e_1 . After a time T , or equally a distance $\ell = vT$, it reorients to a completely new direction e_2 , which is independent of the previous direction. After N such events its vectorial position is given by $x = \sum_{i=1}^N \ell e_i$. Naturally, the mean of this quantity is zero, but the squared average is

$$\langle |x|^2 \rangle = \left\langle \left(\sum_{i=1}^N \ell e_i \right)^2 \right\rangle = \ell^2 \sum_{i=1}^N \langle |e_i|^2 \rangle + 2\ell^2 \sum_{i=1}^N \sum_{j=i+1}^N \langle e_i \cdot e_j \rangle = \ell^2 N, \quad (1.42)$$

since $\langle e_i \cdot e_j \rangle = 0$. This is the same result as the end-to-end distance for chain-like polymers (Flory, 1969; Lovely and Dahlquist, 1974). Using $N \sim t/T$ and $\ell = vT$ we have $\langle |x|^2 \rangle \sim v^2 T t$ at long times, leading to

$$D_{\text{run-tumble}} = \lim_{t \rightarrow \infty} \frac{\langle |x|^2 \rangle}{2dt} = \frac{v^2 T}{2d}. \quad (1.43)$$

This results neglects many factors. For instance, the direction e_i, e_{i+1} are in reality somewhat correlated, and the swimming is not completely along straight lines. All of this will be remedied in later chapters. For now, this simple result allows us to estimate the active diffusion constant of a swimming microorganism. Using the range of microorganism swimming

speeds and taking $T \sim 1$ s (Berg and Brown, 1972) we obtain

$$D_{\text{run-tumble}} \sim 0.2 - 400 \mu\text{m}^2/\text{s}, \quad (1.44)$$

showing that for most swimming microorganisms, the primary source of “diffusion” is due to noisy swimming. It is sometimes customary to use Eq. (1.39) to calculate an effective temperature T_{eff} of an active swimmer, but, in our humble opinion, this tends to cause more confusion than benefit. Finally, we note that passive diffusion constants are defined to be independent of dimensionality. This has the effect that active diffusion constants do depend on dimensionality, as can be seen in the example of Eq. (1.43). This is nothing but bookkeeping, but is necessary to enable comparison between passive and active diffusion constants.

1.3 Active Matter & Cell Behaviour

Many aspects of passive materials; gases, liquids, and solids; are extremely well-understood through their *equilibrium behaviour* as defined in statistical physics. Microorganisms, on the other hand, are living matter and far from thermal equilibrium. Hence, their behaviour cannot be directly understood using the machinery of equilibrium physics.

Parts of this thesis will be dealing with ideas from what has been termed the field of *active matter*, which deals with systems whose constituents inject energy into the system at the local scale. Traditional fluids such as water can only be driven by its boundary conditions. In contrast, a fluid suspension of motile microorganisms will have energy being injected from the microorganisms’ propulsion mechanisms throughout the system. One can also consider the collection of organisms themselves a “living fluid” (Koch and Subramanian, 2011). A lot of effort is being put into understanding the fundamental physics of these active systems and how they differ from passive, equilibrium systems (Fodor et al., 2016; Solon et al., 2015; Takatori and Brady, 2015; Tiribocchi et al., 2015; Wittkowski et al., 2014).

Naturally, living matter is the most prominent example of active matter (Couzin, 2003; Couzin et al., 2011; Erra et al., 2009) and systems such as schools of fish and flocks of birds (Chaté et al., 2008; Huth and Wissel, 1992, 1994; Inada and Kawachi, 2002; Parrish et al., 2002; Reynolds, 1987; Tunstrøm et al., 2013), or even human behaviour (Helbing et al., 2002, 2006) have been studied extensively. However, also inanimate active systems exist. Liquid-free examples include vibrated granular rods (Aranson and Tsimring, 2003; Blair et al., 2003; Kudrolli et al., 2008) and collection of robots (Turgut et al., 2008). An intensively studied system in liquids is that of Janus particles. These self-propelled particles,

appropriately named after the two-faced Roman god, are coated with two different materials, often gold and platinum, which catalyses inhomogeneous surface chemical reactions that lead to mobility (Walther and Muller, 2013).

The focus of this thesis will be on microorganisms, and examples of microorganism active matter are numerous, including bacterial suspensions (Dunkel et al., 2013; Lushi et al., 2014; Wensink et al., 2012; Wioland et al., 2013), algal dynamics (Goldstein, 2015) and their flagella carpets (Brumley et al., 2012), cytoplasmic streaming in plants (Woodhouse and Goldstein, 2013, 2012), migrating cell layers such as epithelium (Kim et al., 2013; Tambe et al., 2011; Trepap and Fredberg, 2011; Trepap et al., 2009) and endothelium (Szabó et al., 2010; Vitorino et al., 2011; Vitorino and Meyer, 2008), and so on.

Our focus will be on single-cell behaviour: swimming, feeding, navigation, etc. We have already introduced active random walks. These will be at the core of our studies. In particular, active random walks can also be biased, for instance to enable migration towards preferred or away from undesired conditions. This behaviour is termed *taxis* and it is a feature shared by virtually all motile organisms. It comes in many forms, and in common is an underlying field of attractant (or repellent) and an ability to react and navigate along gradients of this field. Bacteria do *chemotaxis* towards nutrients (Adler, 1969; Berg, 1993) and away from toxins (Tso and Adler, 1974). Algae do *phototaxis* towards light (Drescher et al., 2010; Yoshimura and Kamiya, 2001) and *gyrotaxis* along gravitational potentials (Kessler, 1985). Chemotaxis provides a mechanism for the recognition and attraction of gametes (Vogel et al., 1982) and for complex behavioural patterns such as in the slime mould *Dictyostelium discoideum*, where cAMP-driven chemotaxis is a critical part of the formation of the multicellular stage of the life cycle (Bonner and Savage, 1947).

Theoretically, taxis is typically described by the Keller-Segel model (Keller and Segel, 1971),

$$\frac{\partial \rho}{\partial t} = D \nabla^2 \rho - \nabla \cdot (\mathcal{V}[c] \rho), \quad (1.45)$$

which is simply the diffusion equation (1.13) for the density of microorganisms $\rho(x)$ with an additional advective term. The functional \mathcal{V} is the average drift velocity in response to a chemoattractant field $c(x)$. The full Keller-Segel model also include an equation for c that models e. g. the diffusion of chemoattractants and their consumption by the organisms. Eq. (1.45) is the Fokker-Planck equation corresponding to the stochastic differential equation

$$dx = \mathcal{V}[c](x) dt + \sqrt{2D} dW \quad (1.46)$$

This model can, for instance, describe the gathering of microorganisms around a food source. As an example, consider a spherical source of food of radius a positioned at

$x = 0$. Assuming the food molecules diffuse fast, the food distribution will be $c(x) = a/r$, the steady state solution for the diffusion equation, where $r = \sqrt{x^2 + y^2 + z^2}$ is the radial coordinate. The simplest choice for the chemotaxis response is $\mathcal{V}[c](x) = \beta \nabla c(x, t) = -a\beta \hat{r}/r^2$, where β is termed the *taxis coefficient* and \hat{r} is the radial unit vector. This choice means that the microorganisms bias their swimming linearly in response to the gradient of the chemoattractant. In steady state, we thus have

$$D \frac{\partial}{\partial r} \left(r^2 \frac{\partial \rho(r)}{\partial r} \right) = -a\beta \frac{\partial \rho(r)}{\partial r}, \quad (1.47)$$

so that

$$\rho(r) \propto \exp\left(\frac{a\beta}{Dr}\right). \quad (1.48)$$

This will be the distribution of microorganisms around food sources if their navigation mechanism results in a linear bias (given the simplicity of this solution, it is strange that we have not been able to find a reference for it). This will not be the case in general, but can often be a good approximation.

In closing it should be mentioned that we will always be discussing the behaviour of the microorganisms themselves. The behaviour of passive tracers in an active suspension of microorganisms is another interesting field of study (Jepson et al., 2013; Leptos et al., 2009), but one that we will not pursue.

1.4 Choanoflagellates & Multicellularity

Biophysical studies of microorganisms have particularly focused on model organisms such as the green algae *Chlamydomonas reinhardtii* and *Volvox carteri*, the bacteria *Escherichia coli* and *Bacillus subtilis*, and spermatozoa.

One of the main motivators for the studies in this thesis is the question of the evolution of multicellularity. Why was it that single-celled organisms suddenly evolved to become multicellular? While we do not intend to study this question directly; many of the studies will hint at this broader line of research. In the literature, the volvocaceae are in particular

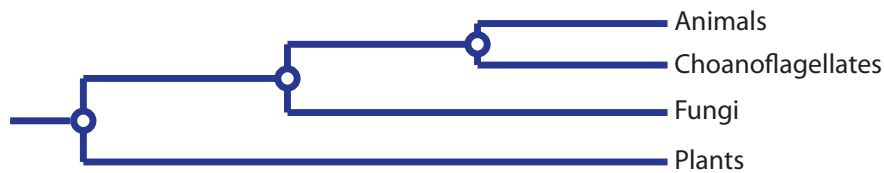


Figure 1.4 Position of choanoflagellates in the tree of life.

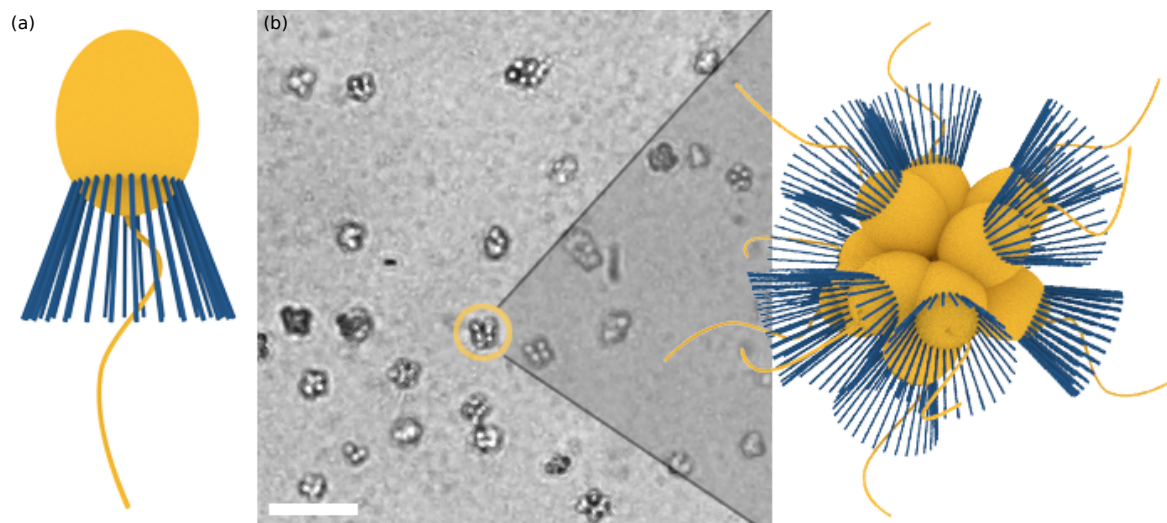


Figure 1.5 Choanoflagellates. (a) Schematic of single cell. (b) Micrograph of *S. rosetta* colonies (left) with schematic illustration (right, collars in blue). Scale bar: 50 μm . Cell body diameters are $\sim 5\mu\text{m}$.

studied in this context. The evolutionary transition from unicellularity to multicellularity, however, has happened many times in the different clades of the tree of life (Niklas, 2014) and the transition in the volvocaceae represents one in the plant kingdom. Recently it was discovered that a class of microorganisms, choanoflagellates, are the closest unicellular relatives of the animals (Lang et al., 2002), making studies of choanoflagellates increasingly relevant regarding the question of the origin of multicellularity in animals, since, in other words, choanoflagellates live right at the border between unicellularity and multicellularity. The sister relationship between choanoflagellates and animals [Fig. 1.4] was first proposed by James-Clark (1866) on the basis of the resemblance between choanoflagellates and the choanocytes of sponges (Grosberg and Strathmann, 2007), and was further confirmed in the genomic era by molecular evidence (King et al., 2008).

All choanoflagellates share the same basic unicell structure: a prolate cell body with a single beating flagellum that is surrounded by a collar of microvilli as shown in Fig. 1.5a. The beating of the flagellum creates a current in the surrounding fluid that guides suspended prey such as bacteria through the collar (Pettitt and Orme, 2002) where they can be caught and ultimately “eaten” (phagocytosed). This is called *filter-feeding*. The flagellar current also confers motility. Some choanoflagellates have an extra structure called a lorica (“armor”) surrounding their body (Leadbeater et al., 2009), but we will not present studies on this type of choanoflagellate in this thesis.

Whereas most forms of choanoflagellates are unicellular, in the presence of certain bacteria (Dayel et al., 2011; Levin et al., 2014), the species *Salpingoeca rosetta* can form

colonies with either a chain-like or a rosette-like morphology kept together by extracellular matrix, filopodia, and intercellular bridges (Dayel et al., 2011). The eponymous rosette-like shape is shown in Fig. 1.5b. Colonies form by cell division (incomplete cytokinesis), not aggregation (Fairclough et al., 2010). The evolutionary advantage of the colonial form is not fully understood.

Given their position in the tree of life, choanoflagellates are the ideal candidate to understand the transition from unicellularity to multicellularity in animals. The fact that the species *S. rosetta* can even form colonies, allow studies on systems that could be very similar to the earliest forms of multicellularity in the animal kingdom. Thus, most of the studies in this thesis focus on the choanoflagellate *Salpingoeca rosetta*. However, we will also consider some aspects of bacteria and the green algae *Chlamydomonas reinhardtii*.

1.5 Outline

The subject of Chapter 2 is the random walk of colonies. In this chapter we will discuss the general theory for active random walks. Experiments on the random walks of colonial choanoflagellates are presented, and these reveal that the colonies swim along noisy helices. Random walk statistics for these are generated and compared to a theoretical model. We furthermore discuss how to generally extract physical parameters from noisy experiments. The chapter ends with a proof-of-concept demonstration of cleaning three-dimensional tracking data. Parts of the material presented in this chapter have been published in the reference Kirkegaard et al. (2016b).

In Chapter 3 we present experimental evidence for aerotaxis (navigation towards oxygen) in colonial choanoflagellates. We study this as a *biased* random walk and compare the experimental protocol to theoretical models. Parts of the material presented in this chapter have been published in the reference Kirkegaard et al. (2016a).

In Chapter 4 we present a theoretical model for persistent run-and-tumble, i. e. a model for run-and-tumble where each reorientation event has persistence with the previous swimming direction, similar to what is observed in Chapter 3 on aerotaxis. By studying this model, we show that tumble persistence has no single optimal value if variations in tumble frequency are also allowed for. Parts of the material presented in this chapter have been published in the reference Kirkegaard and Goldstein (2017).

Chapter 5 presents a theoretical study of feeding in various morphological variations of *S. rosetta*. Using the flux across the collar of the choanoflagellates as an indicator for feeding efficiency, unicells are compared to different configurations of colonies. We also discuss the issue of prey diffusion and the effects thereof on feeding efficiency. Parts of the material

presented in this chapter have been published in the reference [Kirkegaard and Goldstein \(2016\)](#)

The subject of Chapter 6 is a theoretical study on synchronisation of flagella. Flagella switching between synchronous and asynchronous beating can be one method for reorientation in run-and-tumble-like behaviour. We compare theoretical flagella wave models to the beating behaviour in *C. reinhardtii*.

Each chapter is followed by appendices that are relevant for that chapter. Materials and Methods are found as an appendix at the end of the thesis.

Chapter 2

Random Walks of Colonies

2.1 Introduction

Active microparticles, self-propelled by stored energy or that available from the environment, typically exhibit directed motility combined with rotational diffusion, leading to random walks that at large times are statistically similar to their equilibrium counterparts, as briefly described in Sec. 1.2. For artificial swimmers such as Janus particles (Walther and Muller, 2013), powered by inhomogeneous surface chemical reactions, the source of randomness is the same thermal fluctuations that translate Brownian particles, but here rotate them (Howse et al., 2007). In biology, several paradigms for stochastic locomotion exist. For single-celled organisms, stochastic beating leads to noisy swimming paths (Ma et al., 2014), and active processes such as flagellar bundling/unbundling by bacteria (Berg, 1993) and synchronisation/desynchronisation in algae (Polin et al., 2009) enhances this stochasticity through run-and-tumble-like behaviour. Obligate eukaryotic polyflagellates such as the ciliate *Paramecium* (Michelin and Lauga, 2010) and the alga *Volvox carteri* (Brumley et al., 2012), exhibit large-scale flagellar coordination, and increased regularity of motion.

In this chapter we study the motility of the choanoflagellate *Salpingoeca rosetta*. In particular, we shall be interested in the motility of colonies of these organisms and their overall random walk behaviour.

We begin this chapter by considering the flagella dynamics of cells within colonies, Fig. 2.1. From these experimental studies we conclude that the individual flagella of the constituent cells beat very stochastically and furthermore that flagella on a given colony display negligible cross-correlation, i. e. the cells beat independently. We then move on to study the trajectories of the swimming colonies and the random walks they represent. To explain the structure of these random walks, we develop the theory appropriate for colonial random walkers, i. e. those built by stitching together individual random walkers (Schwarz-

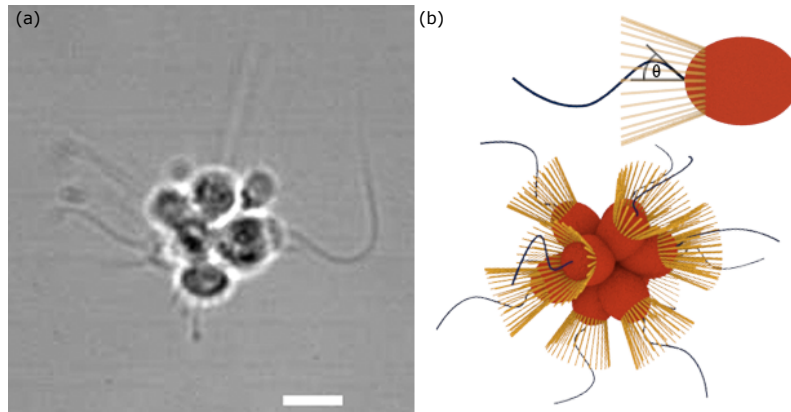


Figure 2.1 The choanoflagellate *S. rosetta*. (a) Bright field image ($5 \mu\text{m}$ scale) and (b) schematics of ‘slow-swimmer’ single cell, base angle θ , and rosette colony.

[Linek et al., 2012](#)). We use these result to discuss the random walk variability that we observe between colonies. We then move on to discuss how to extract physical parameters from short tracks, and finally end this chapter with demonstrating how three-dimensional tracks can be obtained. The culturing method for choanoflagellates is described in Appendix A.1.

2.2 Flagella Dynamics

In choanoflagellates, flagella are the generators of motility. Before studying the motility itself it thus helps to study the motion of the flagella apparatus, and in the case of colonies, potential interactions thereof in particular. In algae, flagella dynamics can be studied by holding the algal cells on micropipettes ([Brumley et al., 2014](#); [Leptos et al., 2013](#); [Wan and Goldstein, 2016](#)), thus preventing their swimming. This is possible because plant cells have cell walls, but choanoflagellates lack this. As a poor man’s substitute, we employ poly-L-lysine, a positively charged amino acid polymer that enhances electrostatic interaction between the microscope glass slide and the negatively charged ions of the cell membrane, thus promoting the attachment of cells. With poly-L-lysine, the *S. rosetta* colonies get stuck to the microscope slides, preventing swimming. However, some luck is involved in obtaining colonies that are attached in a good orientation in which multiple flagella can be observed simultaneously and which all beat without interacting with the glass slide. Furthermore, this technique is not perfect and slight motion of colonies is possible as well as wiggling of the colonies both in and out-of plane. Our tracking algorithms must therefore be quite robust. We describe the used algorithms in Appendix 2.A.

Figs. 2.2(a–b) show the base angles, as defined in Fig. 2.1b, from two flagella on the same colony, and it is clear that they have distinct frequencies. We have obtained

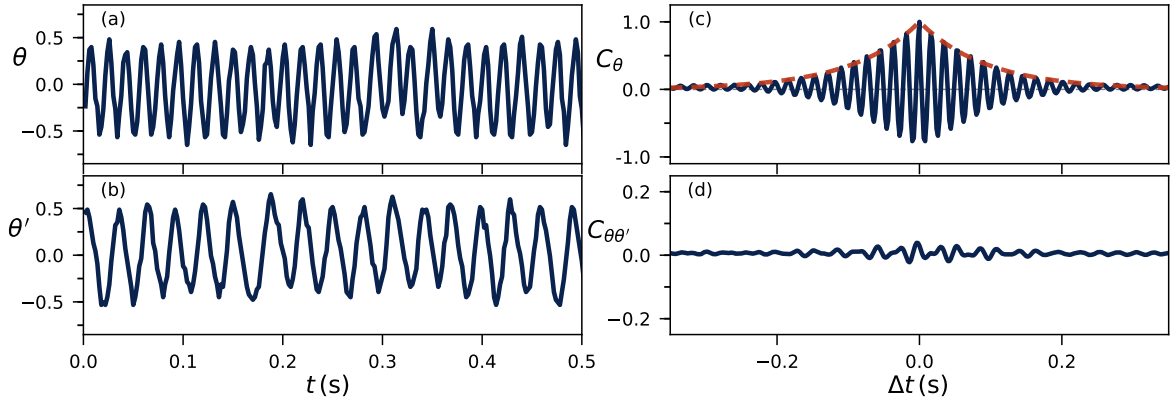


Figure 2.2 Flagellar beating dynamics. (a,b) Time series of the base angle $\theta(t)$ on two flagella within a single colony. (c) Autocorrelation function of θ for one flagellum, with fit of the envelope to an exponential decay (dashed red). (d) Cross correlation of θ between two flagella on the same colony.

such signals for a total of $n = 23$ flagella. In general, the mode beating frequencies f , found by Fourier transforming $\theta(t)$, show a surprisingly high variability [Fig. 2.3a]. The normalised autocorrelation $C_\theta(\Delta t) = \langle \theta(t)\theta(t + \Delta t) \rangle_t / \langle \theta(t)^2 \rangle_t$ for a single flagellum is plotted in Fig. 2.2c. Similar to the function discussed in Ma et al. (2014) and Wan and Goldstein (2014) in the context of flagellar beating in *Chlamydomonas*, the data are consistent with $C_\theta = \exp(-|t|/\tau) \cos(2\pi f t)$, the envelope of which is shown in the figure. The decay time τ also shows a very high degree of variability [Fig. 2.3b], but all are < 1 s suggesting high stochasticity. Within colonies, the cross correlation between flagella $C_{\theta,\theta'}(\Delta t) = \langle \theta(t)\theta'(t + \Delta t) \rangle_t / \sqrt{\langle \theta(t)^2 \rangle_t \langle \theta'(t)^2 \rangle_t}$ can reveal synchronisation. Figure 2.2d shows that virtually no correlation is present (only a very slight signal can be made out, which can be attributed to the overall wiggling of the colony). All cross-correlation signals were found to be less than 0.05 [Fig. 2.3c]. The conclusion is that there is no flagella synchronisation in *S. rosetta* colonies. This leads to an interesting idea: it is well-established that swimming microorganisms perform enhanced diffusion random walks, as briefly mentioned in the introduction. This applies for single-celled choanoflagellates as well, as shown in Fig. 2.4 (to be discussed in the next section). The constituents of the colonies beat independently and thus the colonies can be considered as biological examples of independent active random walkers stitched together. Here we will denote such entities as *aggregate random walkers*.

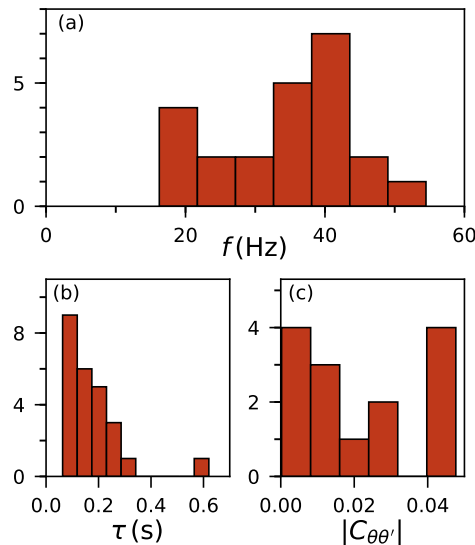


Figure 2.3 Flagellar beating statistics. (a) Peak frequencies of $n = 23$ tracked flagella found as the maximum of the third order Savitzky-Golay filtered Fourier transform. (b) Decay time of autocorrelation in single flagella. (c) Magnitude of cross correlations between flagella in same colonies.

2.3 The Random Walk of Colonies

2.3.1 Experimental Results

In this section, we present tracks of individual colonies and attempt to extract information from them. Microscopy techniques exist that can more directly find population statistics (Wilson et al., 2011), but these work under the assumptions of ergodicity, which is violated here.

Standard methods were used to track the motion of slow-swimmer *S. rosetta* unicells, similar in morphology to the individual cells that comprise a colony. The mean squared displacement, calculated as $\langle \Delta r_{xy}^2 \rangle = \langle [x_{xy}(s+t) - x_{xy}(s)]^2 \rangle_s$, is shown in Fig. 2.4, averaged over 32 *S. rosetta* slow-swimmers each filmed for ~ 1 minute. The behaviour is well-described by the equation for conventional active random walkers, to be introduced later.

In studying the swimming trajectories of colonies of *S. rosetta*, ensemble averages taken over many colonies will eliminate features related to colony-specific configurations such as cell location and flagella orientation. To overcome this lack of ‘ergodicity’, long tracks are needed. We describe in Appendix A.3 the method for obtaining such long tracks. Of course this problem is not actual lack of *ergodicity*, but simply the fact that the colonies have different swimming parameters. A collection of many of the exact same colony would have equal ensemble and time averages.

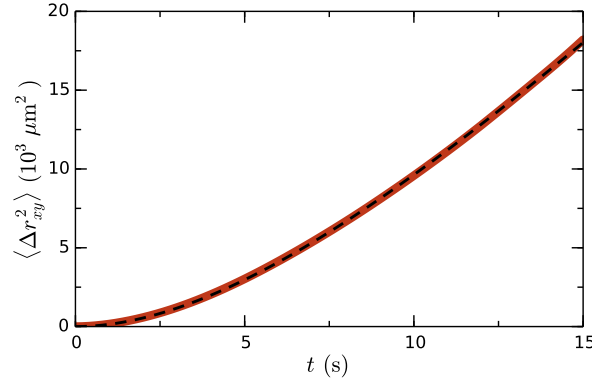


Figure 2.4 Squared distance moved averaged over 32 *S. rosetta* single cells. Overlaid fit in dashed is to Eq. (2.7) with $D = 0$. Parameters: $v = 12.3 \mu\text{m/s}$, $D_r = 0.15 \text{ s}^{-1}$.

Fig. 2.5 shows three examples of tracks, all > 20 min. On close inspection (inset of Fig. 2.5) we observe that the trajectories are noisy helices. The mean squared displacement $\langle \Delta r_{xy}^2 \rangle$, Fig. 2.6a, shows an early time ballistic $\sim t^2$ behaviour (for $t < 1$ s) and late time diffusive $\sim t$ form (inset of Fig. 2.6a) similar to that of unicells. However, a different intermediate time behaviour is observed. The bumps in the curves of Fig. 2.6a appear precisely because the organisms are colonial, and thus some of the constituent cells may beat off centre and induce internal (effective) torques producing stochastic helical trajectories. To highlight the underlying regularity of this helical swimming, we calculate the velocity autocorrelation $C_v(t) = \langle \mathbf{v}_{xy}(s+t) \cdot \mathbf{v}_{xy}(s) \rangle_s$, Fig. 2.6b, which oscillates at the frequency of the induced rotation and decays on a timescale of several oscillation periods.

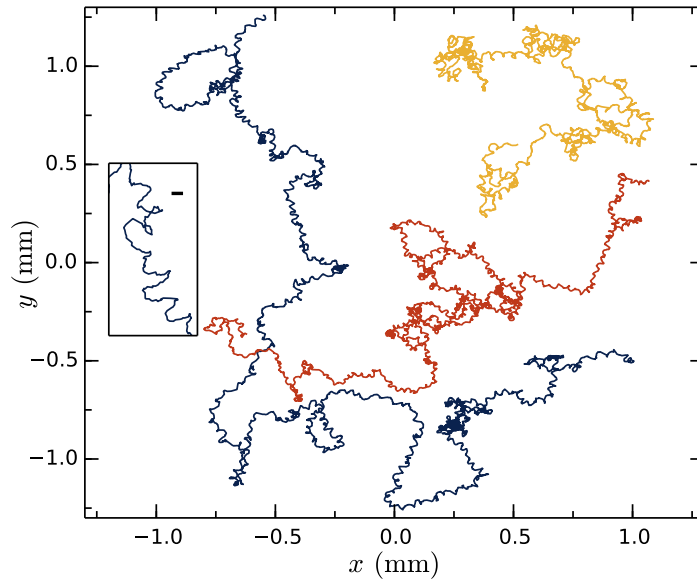


Figure 2.5 Random walks. Long tracks of swimming *S. rosetta*. Inset scale bar is $10 \mu\text{m}$.

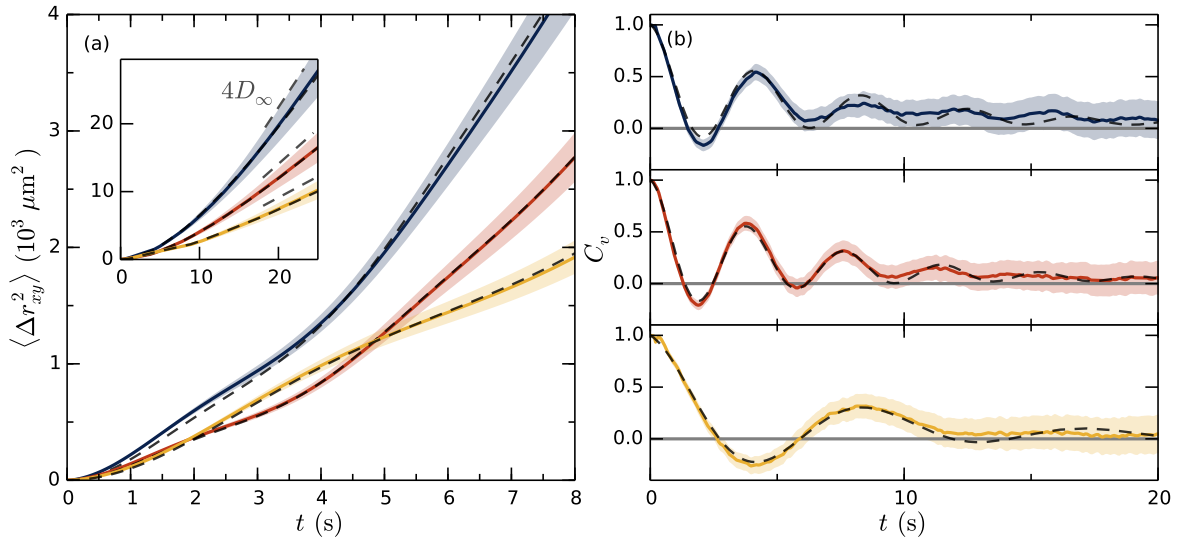


Figure 2.6 Random walk statistics. (a) Projected mean squared displacement for individual walks (solid, error shaded) and fits of model (dashed). Inset shows a zoom-out with late-time linear behaviour $\sim 4D_\infty t$ (dashed, grey). (b) Velocity autocorrelation (solid, error shaded) and model (dashed) with parameters as in (a). Fitted parameters (red curve): $\omega_0 = 1.63 \text{ s}^{-1}$, $v_p = 8.94 \mu\text{m/s}$, $v_\omega = 11.2 \mu\text{m/s}$, $D_r = 0.11 \text{ s}^{-1}$.

The study of active random walks has been the attention of much research (Lauga, 2011; Lovely and Dahlquist, 1974), but only recently have active stochastic particles been studied that include such rotational torques. *External* torques appear on e.g. magnetotactic bacteria in the presence of magnetic fields (Blakemore et al., 1980) and gyrotactic organisms such as certain algae in gravitational fields (Pedley and Kessler, 1990) and can be treated analytically (Sandoval, 2013). However, the present *internal* torques can be treated analytically only in 2D (van Teeffelen and Löwen, 2008) and numerical (Wittkowski and Löwen, 2012) or approximative (Friedrich and Jülicher, 2009) methods are needed in 3D. Below we develop an approximate 3D theory with the goal of simple analytical functions that can be used to extract physical quantities and interpret the data.

2.3.2 Theory of Active Random Walkers

The continuous swimming and diffusion of a random walker can be described in terms of the Langevin equation

$$dx(t) = v(t) dt + \sqrt{2D} dW(t), \quad (2.1)$$

where D is the translational diffusion constant and $W(t)$ a standard vector Wiener process for which $\langle dW_i(t) dW_j(t') \rangle = \delta_{ij} \delta(t - t') dt dt'$. The case $v(t) = 0$ corresponds to a passive

particle, yielding the classical result (here assuming $x(0) = 0$)

$$\langle x(t) \rangle = \sqrt{2D} \int_0^t \langle dW(t') \rangle = 0 \quad (2.2a)$$

$$\begin{aligned} \langle x(t) \cdot x(t) \rangle &= 2D \left\langle \int_0^t dW(t') \cdot \int_0^t dW(t') \right\rangle \\ &= 2D \int_0^t \int_0^t \langle dW(t') \cdot dW(t'') \rangle = 2dDt, \end{aligned} \quad (2.2b)$$

where d is the dimension of the space in which the random walk is taking place. Active particles also have a stochastic velocity term. If this velocity was constant, the particle would behave ballistically and the squared displacement would be square in time.

In reality, the majority of particles will experience some form of rotational diffusion, be it active or passive, and a constant velocity cannot be maintained. The rotational diffusion constant D_r represents diffusion in angle in the same way as D represents diffusion in position. Thus for an active particle in two dimensions with constant speed under the influence of rotational diffusion, we may write $v(t) = v(\cos \phi(t), \sin \phi(t))$ and $d\phi = \sqrt{2D_r} dW_r(t)$. The latter stochastic differential equation should be solved on the domain $[0, 2\pi)$, but given that ϕ is periodic and we are only interested in the cosine and sine of ϕ , we can simply solve on $(-\infty, \infty)$. The true solution can be found by folding this tentative solution. In the Wiener process, dW has a Gaussian distribution. Thus we see that ϕ will be a superposition of Gaussians with equal mean and standard deviation. It is a standard result that in this case ϕ will also be Gaussian (indeed by the central limit theorem, any distribution with finite variance would in the large number limit lead to a Gaussian). Hence, we need only the mean and variance of ϕ to fully specify its distribution. In precisely the same manner as Eqs. (2.2a) and (2.2b) we find $\phi \sim N(\phi_0, 2D_r t)$ ($x \sim P$ meaning x has probability distribution P). Throughout this thesis we will use $N(\mu, \sigma^2)$ to denote the normal distribution with mean μ and variance σ^2). Focusing on the x -component we have now $x(t) - x_0 = v \int_0^t \cos \phi(t') dt' + \sqrt{2D} \int_0^t dW_t(t')$ and thus

$$\langle (x(t) - x_0)^2 \rangle = v^2 \int_0^t \int_0^t \langle \cos \phi(t') \cos \phi(t'') \rangle dt' dt'' + 2D_t t. \quad (2.3)$$

To calculate $\langle \cos \phi(t) \cos \phi(t') \rangle$, we use the fact that ϕ is a Markov process to write

$$P(\phi(t) | \phi(t')) \sim N(\phi(t'), 2D_r(t - t')) \quad (2.4)$$

for $t' < t$, since starting at $\phi(t')$ leads to the same dynamics as starting from ϕ_0 . Thus, since $P(\phi(t), \phi(t')) = P(\phi(t)|\phi(t'))P(\phi(t'))$, we find

$$\begin{aligned} \langle \cos \phi(t) \cos \phi(t') \rangle &= \int_{-\infty}^{\infty} dx \int_{-\infty}^{\infty} dy \cos(x) \cos(y) \\ &\quad \times N_x(\phi_0, 2D_r \min(t, t')) N_y(x, 2D_r |t - t'|) \\ &= \frac{1}{2} e^{-D_r |t - t'|} (1 + \cos(2\phi_0) e^{-4D_r \min(t, t')}). \end{aligned} \quad (2.5)$$

By symmetry, we get the corresponding result for $\langle (y(t) - y_0)^2 \rangle$ by substituting $\phi_0 \rightarrow \phi_0 - \pi/2$, such that

$$\langle \cos \phi(t) \cos \phi(t') \rangle + \langle \sin \phi(t) \sin \phi(t') \rangle = e^{-D_r |t - t'|}. \quad (2.6)$$

Finally, we obtain

$$\langle \Delta r_{xy}^2 \rangle = \langle (x(t) - x_0)^2 \rangle + \langle (y(t) - y_0)^2 \rangle = \frac{2v^2}{D_r^2} (D_r t + e^{-D_r t} - 1) + 4Dt, \quad (2.7)$$

the averaged square displacement of an active random walker in two dimensions. Naturally, as shown by a Taylor expansion, $\langle \Delta r^2 \rangle \sim v^2 t^2 + 4Dt$, the behaviour is diffusive at *very* short time scales (thermal noise time scales), but is ballistic with speed v at early times on relevant, biological time scales. However, at later times the average motion transitions into diffusive behaviour with an effective diffusion constant

$$D_\infty = \lim_{t \rightarrow \infty} \frac{\langle \Delta r^2 \rangle}{4t} = \frac{v^2}{2D_r} + D. \quad (2.8)$$

The diffusive behaviour is confirmed by the existence of the (non-zero) limit. Typically, $D \ll v^2/D_r$ and passive diffusion can be ignored. Eq. (2.7) has been used to fit the motion of Janus particles to high accuracy (Howse et al., 2007), and also fits the behaviour of *S. rosetta* unicells well as shown in Fig. 2.4. The above calculations can also be done for higher order moments (Kurzthaler et al., 2016), and can be extended to deterministic time-dependent speed terms $v(t)$ (Babel et al., 2014). We show in Appendix 2.B how they can also be extended to noisy swimming speeds $v(t)$.

As mentioned, at the scale of choanoflagellates, the Reynolds number is so low that inertia is negligible and the fluid dynamics becomes governed by the linear Stokes equation. Accordingly, self-propelled choanoflagellates are both force- and torque-free. Assuming *S. rosetta* sphere-like, couplings between translations and rotations can be ignored. Heuristically then, the velocity of a colony $v(t)$ is approximately a linear sum of the velocities that the constituents would have had swimming independently, $v(t) \approx \eta \sum v_i(t)$, the factor η

accounting for the change in drag with the radius a of the colony, as $\eta \sim a^{-1}$. If some of the walkers comprising the colony, placed at positions $\{r_i\}$, beat off centre, an angular velocity $\omega(t) \approx \eta_r \sum r_i \times v_i$ will also be induced, where $\eta_r \sim a^{-3}$. Since $\{v_i\}$ and $\{r_i\}$ are given in the local coordinate system of the particle, they must be rotated along with the particle. For a two dimensional aggregate random walker (ARW), the resulting motion is described by $v(t) = v(t) (\cos \theta(t), \sin \theta(t))$, where $v(t) = |v(t)|$, $d\theta = \omega(t) dt + \sqrt{2D_r} dW(t)$, $\omega(t) = \pm |\omega(t)|$, and D_r is an effective rotational diffusion constant which can be calculated if the individual stochastic processes are prescribed. With $v(t)$ constant, constant $\omega(t)$ yields circles in the absence of noise. In three dimensions, such motion leads to helices, making (2D-projected) three dimensional ARWs behave very differently from 2D ones and necessitating a full 3D theory.

In 3D, we let the velocity evolve according to $dv(t) = d\Omega(t) \otimes v(t)$, where $d\Omega(t) = \omega(t) dt + \sqrt{2D_r} dW_r(t)$, and \otimes is the Stratonovich cross product. Likewise, we have $d\omega(t) = \sqrt{2D_r} dW_r(t) \otimes \omega(t)$. The Stratonovich interpretation is essential for maintaining the correct magnitude of $v(t)$ and $\omega(t)$. This can be seen by e. g. dotting the above equation for $\omega(t)$ with ω . In the Stratonovich interpretation the ordinary chain rule holds such that the left-hand side becomes $\frac{1}{2}d(\omega(t)^2)$, while the right-hand side becomes equal to zero. In Itô calculus, on the other hand, Itô's formula must be used yielding a different result and thus not a conserved magnitude of $\omega(t)$. The same holds for $v(t)$. To obtain the equivalent Itô interpretation, one may write e. g.

$$d\omega(t) = \sqrt{2D_r} \begin{pmatrix} 0 & \omega_3(t) & -\omega_2(t) \\ -\omega_3(t) & 0 & \omega_1(t) \\ \omega_2(t) & -\omega_1(t) & 0 \end{pmatrix} \circ \begin{pmatrix} dW_1(t) \\ dW_2(t) \\ dW_3(t) \end{pmatrix} \equiv \sigma(t) \circ \begin{pmatrix} dW_1(t) \\ dW_2(t) \\ dW_3(t) \end{pmatrix}, \quad (2.9)$$

leading to the Itô interpretation

$$d\omega(t) = \sigma(t) \cdot \begin{pmatrix} dW_1(t) \\ dW_2(t) \\ dW_3(t) \end{pmatrix} + \frac{1}{2} ((\sigma(t) \cdot \nabla_\omega)^T \sigma(t))^T dt \quad (2.10)$$

where T denotes transpose. The last term is the noise-induced drift, evaluating to

$$\frac{1}{2} [(\sigma(t) \cdot \nabla_\omega)^T \sigma(t)]_i = \frac{1}{2} \sum_{k=1}^3 \sum_{j=1}^3 \sigma_{kj} \frac{\partial \sigma_{ij}}{\partial \omega_k} = -2D_r \omega_i, \quad (2.11)$$

Thus $d\omega(t) = d\Omega(t) \times \omega(t) - 2D_r \omega(t) dt$. The calculation of $v(t)$ follows the same procedure, and yields $-2D_r v_i$. With the goal of a minimal model, we take the magnitude of the transla-

tional and rotational velocities constant in the approximation to follow. The simultaneous update of the translation and rotational velocity and the non-linearity of the equations make the system analytically quite intractable and thus we shall seek an approximate solution. As motivation, consider the case $D_r = 0$ with specified initial conditions $v(0) = v_0$, $\omega(0) = \omega_0$. This system can be solved exactly to yield

$$x(t) = x_0 + [\omega_0(\omega_0 \cdot v_0)\omega_0 t + \omega_0 \times (v_0 \times \omega_0) \sin(\omega_0 t) + \omega_0(\omega_0 \times v_0)(1 - \cos(\omega_0 t))]/\omega_0^3, \quad (2.12)$$

which can also be represented as

$$x(t) = \int_0^t v(t') dt', \quad (2.13a)$$

$$v(t) = R \cdot \begin{pmatrix} v_\omega \cos \omega_0 t \\ v_\omega \sin \omega_0 t \\ v_p \end{pmatrix}, \quad (2.13b)$$

where $v_\omega = |\omega_0 \times v_0|/\omega_0$, $v_p = \omega_0 \cdot v_0/\omega_0$, $\omega_0 = |\omega_0|$, and R is some orthogonal matrix. Eq. (2.13) describes a helix of radius v_ω/ω_0 and mean speed v_p (averaged over $2\pi/\omega_0$). The form of (2.13) inspires an approximative solution in the presence of noise in which the deterministic helix parameters define a continuous-time random walk with helix-like steps, the matrix r becoming a stochastic matrix process. As an effective description we assume $R(t) = R_x(\alpha) \cdot R_y(\beta) \cdot R_z(\gamma)$, where the matrix factors are rotations around the x, y, z axes and α, β, γ are taken independent and identically distributed with $d\alpha = \sqrt{2D_r} dW_\alpha(t)$, which strictly speaking is only valid at $t = 0$. While the approach breaks $x - y$ symmetry, the approximation makes the system much more manageable, and simulations show it to be an overall good approximation for the statistics of interest at early times.

For the rotation angles α , β , and γ , we again have e. g.

$$\begin{aligned} \langle \cos \alpha(t) \cos \alpha(t') \rangle &= \int_{-\infty}^{\infty} dx \int_{-\infty}^{\infty} dy \cos(x) \cos(y) \\ &\quad \times N_x(\alpha_0, 2D_r \min(t, t') |) N_y(x, 2D_r |t - t'|) \\ &= \frac{1}{2} e^{-D_r |t - t'|} (1 + \cos(2\alpha_0) e^{-4D_r \min(t, t')}), \end{aligned} \quad (2.14)$$

which in the stationary limit can be used to find the velocity autocorrelations, e. g.

$$\begin{aligned}
 \langle v_x(t)v_x(s) \rangle &= \left\langle \left(v_\omega \cos(\beta(t)) \cos(\gamma(t)) \cos(\omega_0 t) + v_p \sin(\beta(t)) \right. \right. \\
 &\quad \left. \left. - v_\omega \cos(\beta(t)) \sin(\gamma(t)) \sin(\omega_0 t) \right) \times \left(v_p \sin(\beta(s)) \right. \right. \\
 &\quad \left. \left. + v_\omega \cos(\beta(s)) \cos(\gamma(s)) \cos(\omega_0 s) - v_\omega \cos(\beta(s)) \sin(\gamma(s)) \sin(\omega_0 s) \right) \right\rangle \\
 &= \frac{1}{2} v_p^2 e^{-D_r|t-s|} + \frac{1}{4} v_\omega^2 e^{-2D_r|t-s|} \cos(\omega_0(t-s)).
 \end{aligned} \tag{2.15}$$

The function only depends on the time difference $t - s$, which is the case for stationary autocorrelations (this is the very definition of a *weakly* stationary process). From

$$\begin{aligned}
 v_y(t) &= -v_p \sin(\alpha(t)) \cos(\beta(t)) + v_w \left(\left[\sin(\alpha(t)) \sin(\beta(t)) \cos(\gamma(t)) \right. \right. \\
 &\quad \left. \left. + \cos(\alpha(t)) \sin(\gamma(t)) \right] \cos(\omega_0 t) + \left[\cos(\alpha(t)) \cos(\gamma(t)) \right. \right. \\
 &\quad \left. \left. - \sin(\alpha(t)) \sin(\beta(t)) \sin(\gamma(t)) \right] \sin(\omega_0 t) \right)
 \end{aligned} \tag{2.16}$$

we find in a similar manner

$$\langle v_y(t)v_y(s) \rangle = \frac{1}{4} v_p^2 e^{-2D_r|t-s|} + \frac{1}{8} v_\omega^2 \left(e^{-3D_r|t-s|} + 2e^{-2D_r|t-s|} \right) \cos(\omega_0(t-s)), \tag{2.17}$$

and the same for $\langle v_z(t)v_z(s) \rangle$. We project on to a random 2D plane by summing the x, y, z results followed by multiplication of $2/3$ (this gives a different result than simply summing the x and y components due to the asymmetry induced by the approximation). We thus find

$$\langle v(\Delta t) \cdot v(0) \rangle = \frac{e^{-2D_r|\Delta t|}}{6} \left[2v_p^2 \left(1 + e^{D_r|\Delta t|} \right) + v_\omega^2 \left(3 + e^{-D_r|\Delta t|} \right) \cos(\omega_0 \Delta t) \right]. \tag{2.18}$$

The mean squared displacement is obtained by integrating the autocorrelation twice

$$\begin{aligned}
 \langle \Delta r^2(t) \rangle &= \int_0^t \int_0^t \langle v(t') \cdot v(t'') \rangle dt' dt'' \\
 &= \frac{v_p^2 e^{-2D_r t}}{6D_r^2} \left(1 + 4e^{D_r t} \right) + 4D_\infty t - a_0 \\
 &\quad + v_\omega^2 e^{-2D_r t} \left(\frac{4D_r^2 - \omega_0^2}{(4D_r^2 + \omega_0^2)^2} + \frac{9D_r^2 - \omega_0^2}{3(9D_r^2 + \omega_0^2)^2} e^{-D_r t} \right) \cos \omega_0 t \\
 &\quad - v_\omega^2 e^{-2D_r t} \left(\frac{4\omega_0 D_r}{(4D_r^2 + \omega_0^2)^2} + \frac{2\omega_0 D_r}{(9D_r^2 + \omega_0^2)^2} e^{-D_r t} \right) \sin \omega_0 t,
 \end{aligned} \tag{2.19}$$

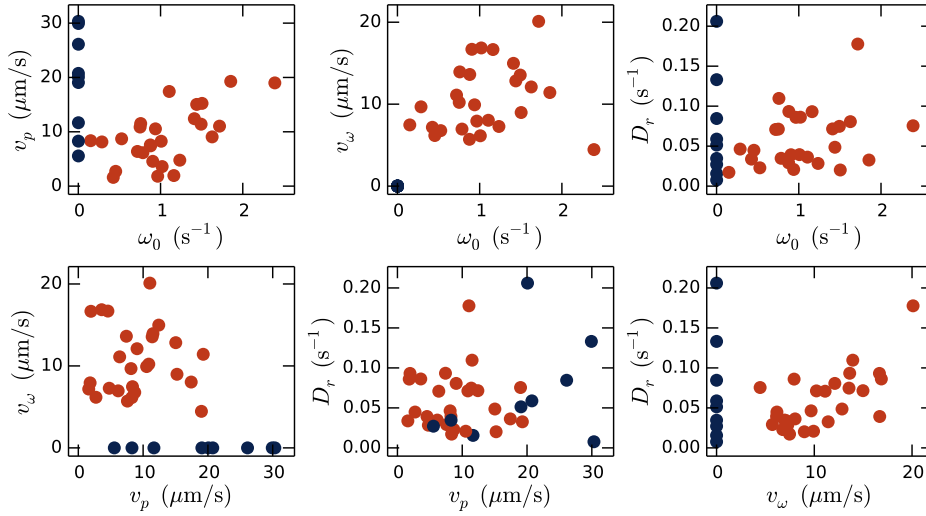


Figure 2.7 Comparison of fit parameters of 36 tracks. Tracks where ω_0, v_ω could be determined in red and tracks where ω_0, v_ω are forced to zero in blue.

where

$$a_0 = \frac{5v_p^2}{6D_r^2} + v_\omega^2 \left(\frac{4D_r^2 - \omega_0^2}{(4D_r^2 + \omega_0^2)^2} + \frac{9D_r^2 - \omega_0^2}{3(9D_r^2 + \omega_0^2)^2} \right). \quad (2.20)$$

As $t \rightarrow \infty$, $\langle \Delta r^2 \rangle \sim 4D_\infty t$, where

$$D_\infty = \lim_{t \rightarrow \infty} \frac{\langle \Delta r^2 \rangle}{4t} = \frac{v_p^2}{4D_r} + \frac{v_\omega^2 D_r}{4} \left(\frac{1}{9D_r^2 + \omega_0^2} + \frac{2}{4D_r^2 + \omega_0^2} \right). \quad (2.21)$$

These results have been verified by simulations using the Euler–Maruyama method. It has previously been shown that reciprocal swimming leads to enhanced diffusion (Lauga, 2011), and the last terms of Eq. (2.21), which are major contributions to the diffusion constant, embody this phenomenon.

Equations (2.18) and (2.19) describe the approximate functions corresponding to the curves of Fig. 2.6b and 2.6a, respectively. The long-time diffusion constant D_∞ can be extracted from the data by fitting a straight line through the late-time behaviour of $\langle \Delta r^2 \rangle$ (inset of Fig. 2.6a). This can be used in Eq. (2.21) to fix one of the parameters of the model in terms of the others, guaranteeing the correct long-time behaviour. The remaining three parameters are fitted simultaneously to the curves of Fig. 2.6a and 2.6b. Crucially, the model is able to describe well both curves, as shown by the dashed lines in the figures. The relative magnitudes of the extracted velocities, v_p and v_ω , reveal how much energy the organisms spent on effective (v_p) and circular (v_ω) swimming. For example, the blue curve in Fig. 2.5 has $v_p = 10.9 \mu\text{m/s}$ and $v_\omega = 14.3 \mu\text{m/s}$. While not producing the precise morphologies of

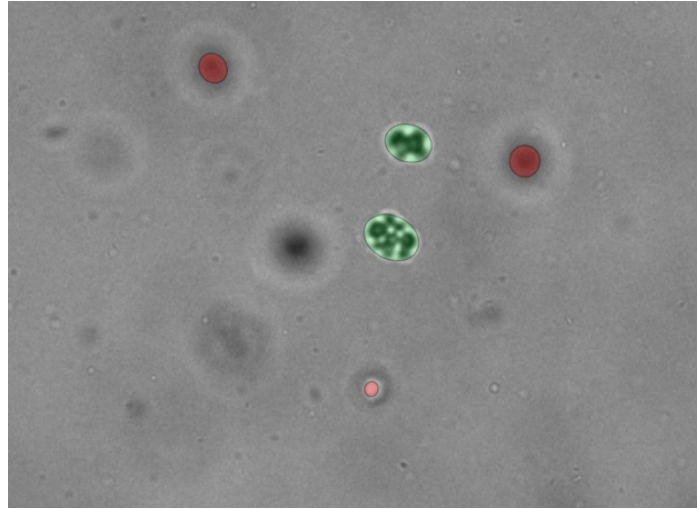


Figure 2.8 Colony size estimation. Green in focus, red out of focus.

the colonies, the fitted velocities combined with the extracted frequency ω_0 , do constrain the possible configurations. Using the fitted velocities, the Stokes drag on a sphere, $6\pi\mu a$, and a colony radius $a \sim 5 \mu\text{m}$, we find an effective translational force of $\sim 1 \text{ pN}$, and using ω_0 , a torque $\sim 4 \text{ pN}\cdot\mu\text{m}$: the small residual forces that propel and rotate a colony are on the order of that of a single cell. The *active* rotational diffusion constants for both single cells and colonies are on the order of 0.1 s^{-1} . With a beat frequency $f \sim 40 \text{ Hz}$, this corresponds to a distribution of angular deviations per beat with standard deviation $\sim \sqrt{D_r/f} = 3^\circ$. The thermal rotational diffusion constant $D_r^{\text{thermal}} = k_B T / 8\pi\mu a^3$ ranges from 0.012 to 0.0014 s^{-1} for radii 2.5 to $5.0 \mu\text{m}$, at least an order magnitude below the active one.

A fundamental operation in the theory of stochastic processes is their summation to yield a single effective process. The corresponding operation for random walkers, ‘stitching’ them together, are precisely aggregate random walkers. As discussed here, there is a crucial complexity for random walkers: the underlying flagellar beating produces physical forces that can also yield torques, so the ‘summation rules’ differ. For simple random walkers the ARWs can be described approximately through the four numbers: v_ω , v_p , ω_0 , and D_r . The question of the correct ‘summation rules’ for general random walkers (e.g. anisotropic, hydrodynamically translation-rotation coupled, or non-identical constituents) remains open. The present exemplar, *S. rosetta*, is a very good approximation to what one might call an ideal biological ARW: independent constituents and a roughly spherical shape.

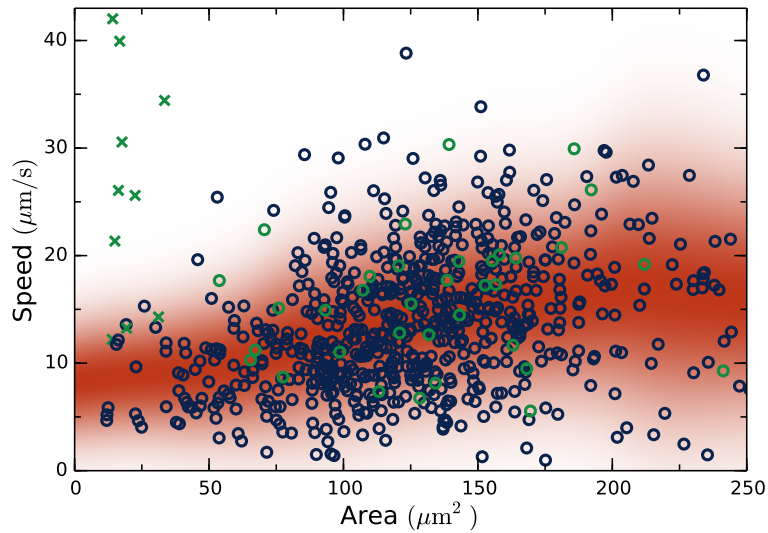


Figure 2.9 Colony size estimated by median xy -projected area. Velocity versus size for ~ 750 colonies. Green crosses are single-celled fast swimmers. Coloured background indicates running mean and standard deviation.

2.3.3 Species Variability

Fig. 2.7 shows scatter plots of fit parameters of the model to the 36 *S. rosetta* colonies, indicating the high variances of all parameters. Note, however, that the determination of some parameters are difficult in certain regions. For instance, ω_0 and v_ω are hard to determine when either one becomes small, and accordingly they have been forced to zero in these cases and plotted in blue. Naturally, these cases will have a higher v_p as is clear in the two plots in the left part of Fig. 2.7.

Just as flagella beating in *S. rosetta* varies between cells, morphology varies between colonies as a result of the cell division process (Fairclough et al., 2010). This stochasticity enables two colonies of similar size to swim very differently. To quantify this a lot more data than 36 tracks are needed. We developed code that tracked colonies and fitted an ellipse to its outline to serve as an estimator of size. When colonies are out of focus, however, they appear smaller or larger and thus the size of the ellipse is only a good estimator when the colonies are in focus. Luckily, the point spread function of our experimental setup transitions from darker to brighter precisely when going through focus. This was utilised to determine when a colony was in focus. Fig. 2.8 shows an example of two fitted ellipses in focus (green) and three out of focus (red). The resulting tracks, however, are quite short and not long enough to estimate all model parameters. On the other hand, the speed of colonies can be estimated. Fig. 2.9 shows the result of this analysis on 750 colonies. The speed from the model fits $\sqrt{v_p^2 + v_\omega^2}$ of the 36 long tracks are shown as green circles. There is a slow increase in speed

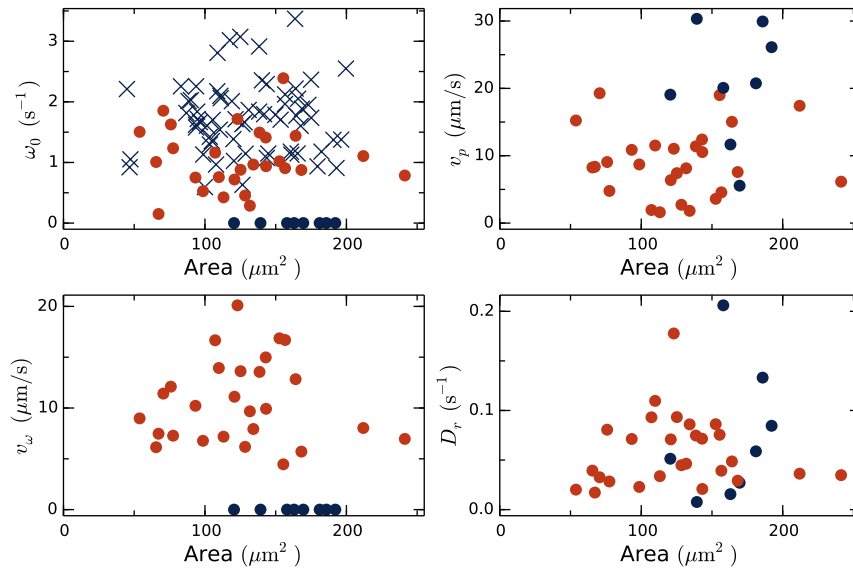


Figure 2.10 Comparison of fit parameters of 36 tracks to size of colony. Tracks where ω_0, v_ω could be determined in red and tracks where ω_0, v_ω are forced to zero in blue. ω_0 plot additionally includes estimates from the short track data in blue crosses.

with colony size. This trend can be explained by simple ad-hoc models such as random orientation of cells in a sphere-like structure: drag scales linearly with radius a but maximum propulsive force (the case where all propulsive forces point in one direction) scales like a^2 . However, there is an intriguing lack of very slow swimmers which would be predicted by such a model. Indeed giving cells an orientation more parallel with its location would only yield slower swimming speeds. More importantly, Fig. 2.9 shows just how different colonies of similar size are: the stochastic processes underlying colony formation have high variances.

Applying the same area estimator to the 36 long tracks, the model parameters can also be plotted as a function of size. Just as with swimming speed, Fig. 2.10 shows that the model parameters have very high variances and no clear dependency on size. This is contrary to e.g. bacterial clumps where rotation rate clearly decreases with size (Schwarz-Linek et al., 2012). For a subset of the short tracks we was also able to fit the model well enough to estimate ω_0 and these are shown as blue crosses. However, the short track colonies for which good estimated could be obtained are biased towards high ω_0 (and v_ω). Nonetheless, there is no clear tendency for larger colonies to rotate slower.

Contrary to the phototactic response of *Chlamydomonas* and *Volvox* in which the time-scale of rotation is matched to inner chemistry (Drescher et al., 2010; Yoshimura and Kamiya, 2001), or the chemotactic response of sperm cells in which curvature and torsion of swimming paths are directly manipulated by the single beating flagellum (Friedrich and Jülicher, 2009), due to this stochastic morphology of *S. rosetta*, knowledge of the overall colony morphology

and motion (e.g. ω_0) is arguably not available at the single-cell level, rendering ‘deterministic’ chemotactic strategies difficult. Thus one of the most important issues is the possibility of chemotaxis in aggregate random walks through suitable modulation of the independent constituents. This will be discussed in the next chapter.

2.4 Fitting Short Tracks

Fitting $\langle \Delta r^2 \rangle$ enables us to extract the physical parameters of our model directly from data. However, this approach depends crucially on whether good averages can be made from the data, which, in turn, depends on how much data is available. Long tracks are hard to obtain, and typically only short tracks are available.

In this section, we attempt to develop methods that can estimate the stochastic model parameters even when data is scarce. To gain intuition we start by considering the standard random walk

$$dx = \sqrt{2D}dW. \quad (2.22)$$

Given data points $\{x(t_i)\}$, can we estimate D ? Of course this contrived example has a very simple solution. Since $x(t_i) - x(t_{i-1}) \sim N(0, 2D(t_i - t_{i-1}))$, one can easily guess a simple and optimal estimator. In the case $t_i - t_{i-1} = \Delta t$, this estimator is

$$\hat{D}_{\text{std}} = \frac{\langle [x(t) - x(t - \Delta t)]^2 \rangle_t}{2\Delta t}. \quad (2.23)$$

However, this approach only works for such simple SDEs, and does not generalise to active random walks, for which such formulae do not exist. We could attempt the approach used for long tracks: fitting $\langle x^2(t) \rangle$ with, in this case, $f(t) = 2Dt$. On a data set of N measurements, we calculate

$$\langle x^2(t = k\Delta t) \rangle_{\text{data}} = \frac{1}{N-k} \sum_{i=0}^{N-k-1} [x(t_i + k\Delta t) - x(t_i)]^2. \quad (2.24)$$

In this sense, the experimental value of $\langle x^2(t = k\Delta t) \rangle$ is an average over $N - k$ values. Early values are thus much better determined than later ones. Fig. 2.11a shows $\langle x^2(t = k\Delta t) \rangle_{\text{data}}$ on a data set of $N = 200$ steps, and the shaded background indicates the standard error $\sigma(t)$.

It is clear that only the early part of the graph is linear. This will (almost) always be the case. We are thus left with a subjective choice: over what range of t should $f(t)$ be fit? Fig. 2.11 shows how various choices lead to very different estimates of D . Assuming the estimated errors $\sigma(t)$ on the averages of Eq. (2.24) Gaussian, we can also calculate the

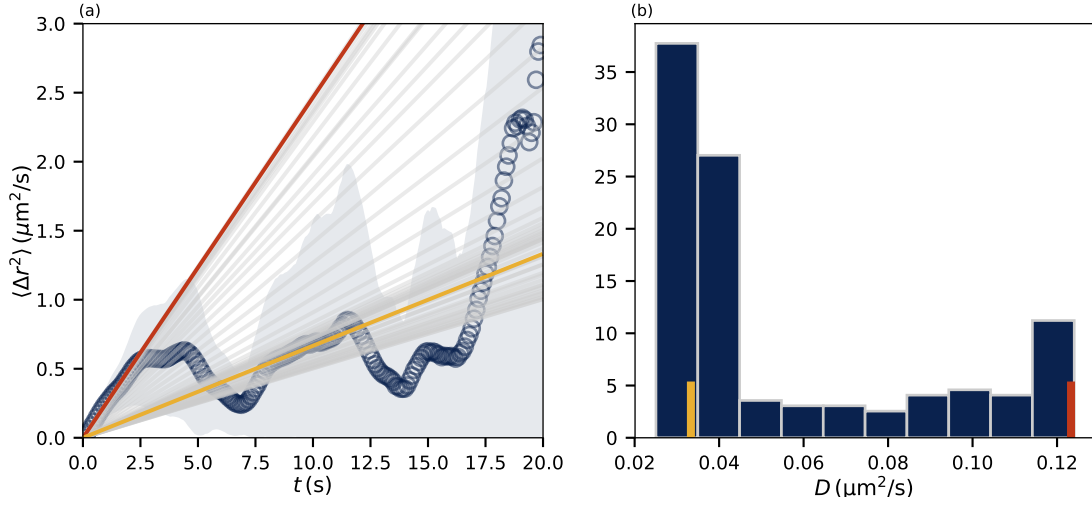


Figure 2.11 Fits of $f(t) = 2Dt$ to $\langle \Delta x^2 \rangle(t)$ estimated for a random walk with $N = 200$ steps using $\Delta t = 0.1$. True value is $D = 0.1 \mu\text{m}^2/\text{s}$ and standard deviation estimate is $\hat{D}_{\text{std}} = 0.102 \mu\text{m}^2/\text{s}$. (a) Data in blue circles and standard error in shaded. Fits are done using data in the section $[0, T]$, grey lines corresponding to different choices of T . Red line is for $T = 1$ s. Yellow line is the maximum likelihood fit. (b) Histogram of fitted values of D , with red and yellow fit indicated separately.

maximum likelihood estimate,

$$\hat{D}_{\text{ML}} = \frac{1}{2} \sum_i \frac{t_i \langle x^2(t_i) \rangle}{\sigma(t_i)^2} / \sum_i \frac{t_i^2}{\sigma(t_i)^2} = 0.033 \mu\text{m}^2/\text{s}, \quad (2.25)$$

which is shown in yellow in Fig. 2.11 and vastly underestimates the true value $D = 0.1 \mu\text{m}^2/\text{s}$. Part of the reason we obtain such a poor estimate using maximum likelihood is that the $\langle x^2(t = k\Delta t) \rangle_{\text{data}}$ values are highly correlated. However, we could instead try to formulate a maximum likelihood estimate based directly on the data. Thus we write (here for $N + 1$ measurements of $x(t_i)$)

$$\begin{aligned} \log \mathcal{L}(D) &= \log P(\{x_i\} | D) \\ &= \log \prod_{i=1}^N N(x_i - x_{i-1}, 2D\Delta t) \\ &\propto -\frac{N}{2} \log(4\pi D\Delta t) - \sum_{i=1}^N \frac{(x_i - x_{i-1})^2}{4D\Delta t}. \end{aligned} \quad (2.26)$$

By maximising the likelihood, we are implicitly assuming an improper prior on D that is uniform on $[0, \infty]$. Solving $\partial_D \log \mathcal{L}(D) = 0$ leads to

$$\hat{D} = \frac{1}{2N\Delta t} \sum_{i=1}^N (x_i - x_{i-1})^2, \quad (2.27)$$

which is exactly the same as the estimator we intuitively wrote down in Eq. (2.23). This is of course to be expected, and the only reason we show this approach here is to motivate its use for active random walks. However, the approach requires some modification to work on active random walks, which we will now discuss.

To exemplify active random walks, we consider again the 2D process

$$dx = v \cos \theta dt + \sqrt{2D} dW, \quad (2.28a)$$

$$dy = v \sin \theta dt + \sqrt{2D} dW, \quad (2.28b)$$

$$d\theta = \sqrt{2D_r} dW. \quad (2.28c)$$

Experimentally, we observe $x(t)$ and $y(t)$, but not $\theta(t)$, although an estimate of $\theta(t)$ can be obtained as $\arctan2(y_s(t), x_s(t))$, where x_s, y_s are some smoothed versions of x and y . From simulation data, we can again estimate $\langle \Delta r^2 \rangle(t)$ and try to fit this with Eq. (2.7). Again we have the issue of subjectively choosing an interval $[0, T]$ over which we perform the fit. Fig. 2.12 shows the resulting fits for different choices. Compared to Fig. 2.11, the resulting curves now all fit the data well. However, the fits now have to constrain three parameters: v , D_r , and D , and these, as shown in Fig. 2.13(a–c), vary significantly between the fits, despite each fit visually matching the data well. Furthermore, for the simple random walk in Fig. 2.11, the $\langle \Delta r^2 \rangle$ maximum likelihood estimate did poorly because it used too much of late-time data, whereas for the data in Fig. 2.12 and 2.13 it does poorly because it uses too little of the late-time data. There is thus no consistency in that sense. Again this is partly due to correlations in the data points of $\langle \Delta r^2 \rangle$.

The overarching problem is that there is a data reduction from the initial data set of $x(t), y(t)$ to $\langle \Delta r^2 \rangle$. A lot of information is simply not being used. The approach works if the datasets are so large that averages can be confidently calculated, but when the data sets are small we cannot afford to waste any information. To exploit all the available data, we can again write down a likelihood directly based on the observed data. If our observation rate is

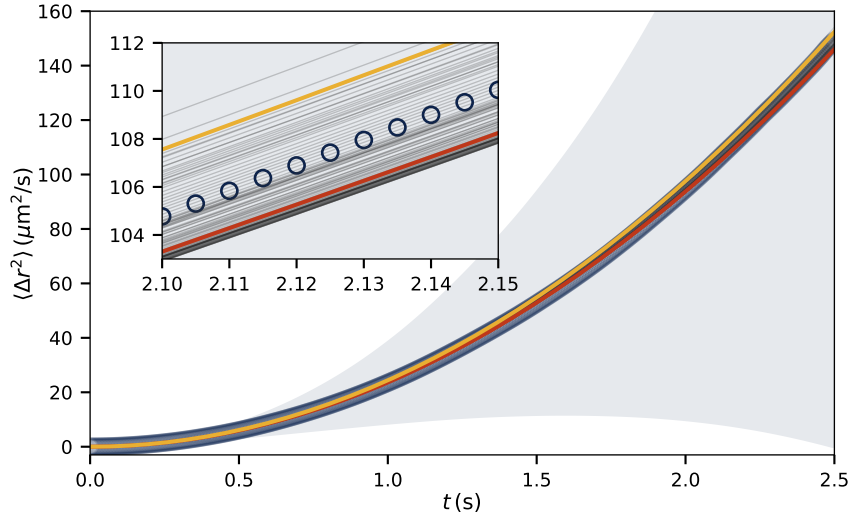


Figure 2.12 Fits of Eq. (2.7) to $\langle \Delta r^2 \rangle(t)$ estimated for an active random walk with $N = 500$ steps using $\Delta t = 0.005$. Data in blue circles and standard error in shaded. Fits are done using data in the section $[0, T]$, grey lines corresponding to different choices of T . Red line is for $T = 1$ s. Yellow line is the maximum likelihood fit. Simulation parameters: $v = 5 \mu\text{m/s}$, $D_r = 0.1 \text{ s}^{-1}$, $D = 0.01 \mu\text{m}^2/\text{s}$. Inset is a zoom-in to clearly show the various fits.

fast, i. e. $\Delta t \ll 1/D_r$, then this can be written

$$\begin{aligned} \mathcal{L}(v, D_r, D, \{\theta_i\}) &= \prod_{i=1}^{N-1} N(\theta_i - \theta_{i-1}, 2D_r \Delta t) \prod_{i=1}^N N(x_i - x_{i-1} - v \Delta t \cos \theta_{i-1}, 2D \Delta t) \\ &\times \prod_{i=1}^N N(y_i - y_{i-1} - v \Delta t \sin \theta_{i-1}, 2D \Delta t). \end{aligned} \quad (2.29)$$

However, this time we cannot simply maximise the likelihood to obtain the best estimate of our parameters because $\theta(t)$ is unknown. If we maximise $\log \mathcal{L}(v, D_r, D, \{\theta_i\})$, we will also obtain the maximum likelihood value of $\{\theta_i\}$, but (as counter-intuitive as it sounds) the maximum likelihood value of a random process is extremely unlikely. For example, the maximum likelihood estimate for a simple Wiener process is $W(t) = 0$ at all times, since for each step the most likely outcome is no motion, i. e. $dW = 0$.

A random process is a high (infinite) dimensional object. As one moves away from the maximum likelihood estimate in probability space, the volume increases as $dV \sim \text{distance}^{\text{dim}}$. And thus, even though the probability distribution P decreases its value away from the maximum, a typical realisation of the process will be found where $P dV$ is large, not where P is large. Concisely, samples from probability distributions are most likely to come from the *typical set* of the distribution not from the maximum likelihood neighbourhood (Betancourt, 2017). In low dimensions the typical set and the maximum likelihood neighbourhood are

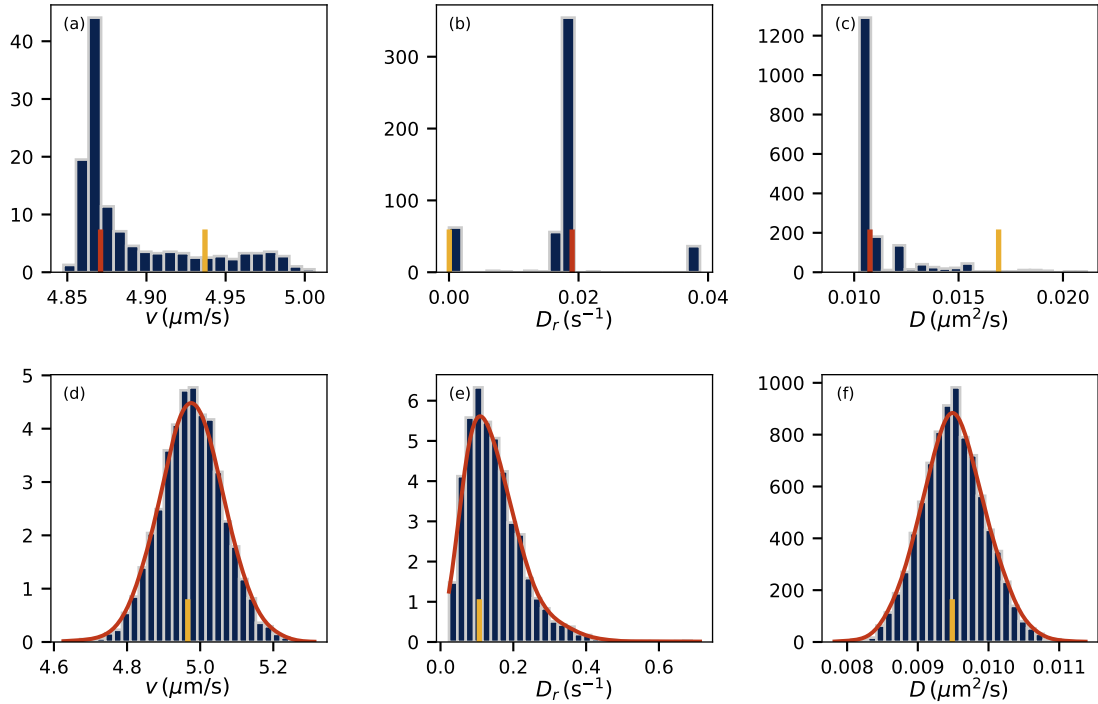


Figure 2.13 Histograms of estimated parameters. True parameters are $v = 5 \mu\text{m/s}$, $D_r = 0.1 \text{ s}^{-1}$, and $D = 0.01 \mu\text{m}^2/\text{s}$. (a–c) Results of fitting $\langle \Delta r^2 \rangle(t)$ as shown in Fig. 2.12. Red and yellow indications correspond to the same colours as in Fig. 2.12. (d–f) Histogram of Hamiltonian Monte Carlo samples with kernel density estimate shown in red. Yellow indications are the simultaneous maximum of all parameters found by kernel density estimation. The maximum likelihood estimate is $v = 4.97 \mu\text{m/s}$, $D_r = 0.107 \text{ s}^{-1}$, and $D = 0.00949 \mu\text{m}^2/\text{s}$.

in the same vicinity, which is why we have this wrong intuition that does not work with high-dimensional objects. Instead, what we really want is the maximum likelihood estimate of v , D_r and D from the distribution where $\theta(t)$ has been marginalised out, i. e. from

$$\mathcal{L}(v, D_r, D) = \int \mathcal{L}(v, D_r, D, \{\theta_i\}) \prod d\theta_i. \quad (2.30)$$

We note that of the variables v , D_r , D and $\{\theta_i\}$ only v is Gaussian distributed, and thus we have no chance of carrying out the integral above. In fact, we cannot even hope to do this using conventional numerical schemes, since it is an integral over many dimensions (number of data points) and we need its value for all values of v , D_r , and D .

What we can do, however, it is to consider the probability distribution defined by normalising Eq. (2.29) and sample values $\{v, D_r, D, \{\theta_i\}\}$ directly from it. Ignoring the $\{\theta_i\}$ parts of the samples, the remaining samples correspond precisely to sampling from the probability distribution defined by Eq. (2.30). With enough samples of Eq. (2.29) we can then estimate

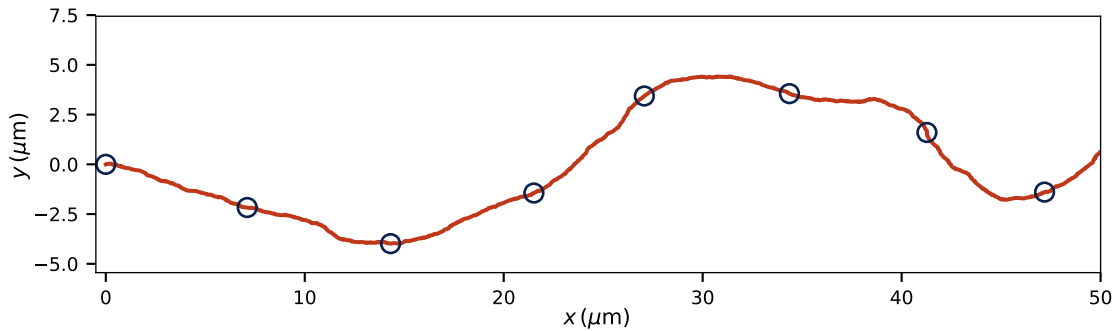


Figure 2.14 Simulation of active random walker with $v = 5 \mu\text{m/s}$, $D_r = 0.1 \text{ s}^{-1}$, and $D = 0.01 \mu\text{m}^2/\text{s}$. Simulation performed with $\Delta t = 0.005 \text{ s}$, but subsampled to $\Delta t = 1.5 \text{ s}$ as indicated by the blue circles.

the full distribution of Eq. (2.30) using kernel density estimation methods and from there obtain the maximum likelihood estimate.

To obtain samples from Eq. (2.29) we turn to Monte Carlo methods. Markov Chain Monte Carlo is the de-facto standard for sampling from probability distributions that cannot be analytically inverted. The most used widely algorithm, Metropolis-Hastings (Hastings, 1970; Metropolis et al., 1953), does not scale well to high dimensions, however, and so it is not applicable here. Instead, we will employ Hamiltonian Monte Carlo (Neal, 2012), which is to Metropolis-Hastings what ballistic motion is to diffusive motion in terms of sampling efficiency. This analogy is actually very accurate in terms of how the algorithms work: Metropolis-Hastings moves around probability space as a random walk, while Hamiltonian Monte Carlo exploits gradient information in order to define a momentum that helps in exploring probability space with ballistic speed. In that sense, the algorithms are basically like a passive and active random walker, respectively. We will not go into the details of these algorithms here, but simply exploit them. Mathematical details can be found in Neal (2012) and Betancourt (2017). We will use the implementation called STAN (Carpenter et al., 2017).

Fig. 2.13(d-f) shows the results of 4,000 Hamiltonian Markov Chain samples from Eq. (2.29). Using three-dimensional kernel density estimation we find the maximum likelihood estimate of Eq. (2.30) (the method of kernel density estimation is described in Appendix 3.A). The estimate is much better than what we obtained from the $\langle \Delta r^2 \rangle$ fits. But almost as important, this estimation method does not require us to make any subjective choices. For free, we furthermore obtain not only errors on our parameter estimates, but their full distributions. This method is very general and can be applied to many types of SDEs. However, the method is, naturally, quite dependent on the correct model having been chosen. For instance, if the speed of the microorganisms also vary, this needs to be modelled. In contrast, the method of fitting averages such as $\langle \Delta r^2 \rangle$ is less sensitive to such issues and will

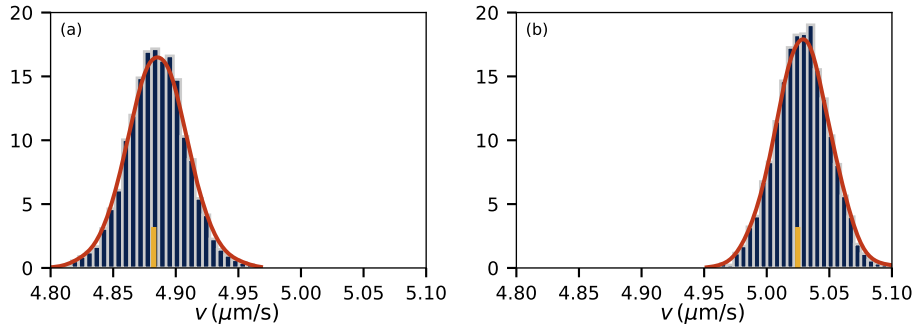


Figure 2.15 Hamiltonian Monte Carlo results without (a) and with (b) subsampling on the data of Fig. 2.14 which has $N = 65$ data points. Yellow bar indicate maximum likelihood estimate from the full parameter space kernel density estimation, and red curves show the 1D kernel density estimate on the histograms. Correct value is $v = 5.0 \mu\text{m/s}$.

obtain good “effective” parameters even if the underlying model does not perfectly describe the data.

In the above we have assumed that our data is sampled fast i. e. that $\Delta t \ll 1/D_r$. Typically $1/D_r \sim 10\text{s}$, so we do not need that small a Δt for this to be true. For the sake of generality, however, we now consider how to deal with the situation of slow sampling. Fig. 2.14 shows an active random walker realisation sub-sampled to $\Delta t = 1.5\text{s}$. Notice that, in the absence of any significant translational diffusion, the distance between sub-sampled points $|x_i - x_{i-1}|$ will always be smaller than $v\Delta t$ due to rotational diffusion. This means that applying directly the sampling of Eq. (2.29) can only lead to an underestimation of v , just as estimating the microorganisms’ swimming speed as $\langle |x_i - x_{i-1}| \rangle / \Delta t$ would do. Fig. 2.15a shows the result of Monte Carlo sampling using Eq. (2.29). It is clear that v is biased to smaller values. In fact the true value is given zero probability. This is just one example of a bias that can be introduced by having Δt large.

The underlying problem, of course, is that where in equation Eq. (2.29) we write $N(x_i - x_{i-1} - v\Delta t \cos \theta_{i-1}, 2D\Delta t)$, it really should be $P(x_i | x_{i-1}, \theta_{i-1})$: the probability of transitioning to x_i in time Δt given that right now the process is at (x_{i-1}, θ_{i-1}) . However, this probability is not known analytically. To remedy this problem, we introduce unobserved values of x and sample these just like we sample for θ . Thus we choose an integer k such that $\hat{\Delta t} = \Delta t/k$ is small, and consider the values

$$x_1, \hat{x}_1^1, \hat{x}_1^2, \dots, \hat{x}_1^k, x_2, \hat{x}_2^1, \hat{x}_2^2, \dots, \hat{x}_2^k, x_3, \hat{x}_3^1, \dots, \hat{x}_{N-1}^k, x_N, \quad (2.31)$$

where the hatted variables are unobserved.

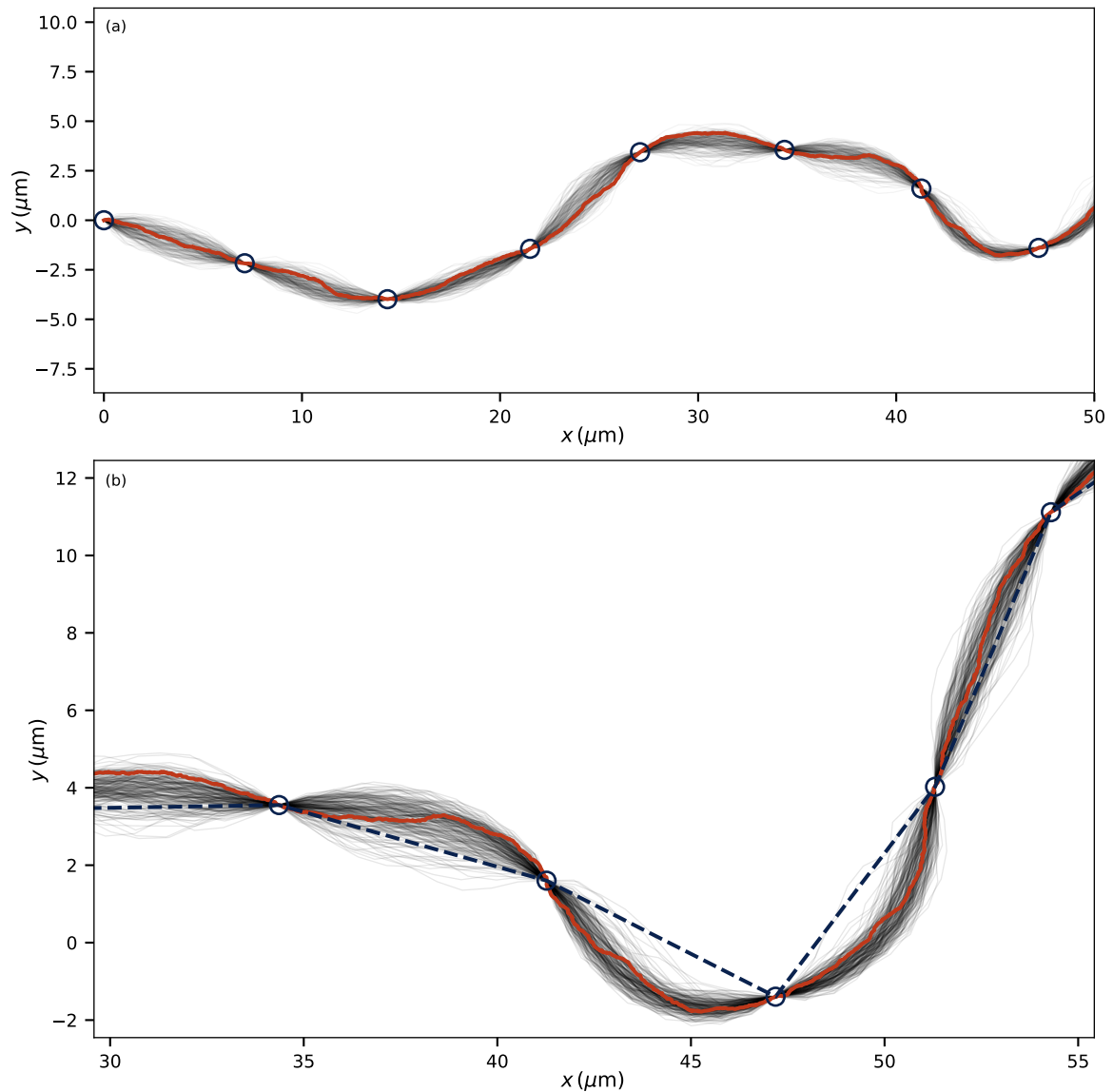


Figure 2.16 Hamiltonian Monte Carlo reconstruction of the active random walks of Fig. 2.14. 200 sample trajectories are shown. Reconstruction is based only on the datapoints marked as blue circles. (a) Same as Fig. 2.14 with reconstruction overlaid. (b) Zoom-in showing that reconstruction naturally finds the most likely curvature, which matches original data (red curve).

Thus, we now wish to sample from the likelihood

$$\begin{aligned}
 \mathcal{L}(v, D_r, D, \{\theta_i\}, \{\hat{\theta}_i^j\}, \{\hat{x}_i^j\}, \{\hat{y}_i^j\}) &= \prod_{i=2}^{N-1} N(\theta_i - \hat{\theta}_{i-1}^k, 2D_r \hat{\Delta}t) \prod_{i=1}^{N-1} N(\hat{\theta}_i^1 - \theta_i, 2D_r \hat{\Delta}t) \\
 &\times \prod_{i=1}^{N-1} \prod_{j=2}^k N(\hat{\theta}_i^j - \hat{\theta}_i^{j-1}, 2D_r \hat{\Delta}t) \prod_{i=2}^N N(x_i - \hat{x}_{i-1}^k - v \hat{\Delta}t \cos \hat{\theta}_{i-1}^k, 2D \hat{\Delta}t) \\
 &\times \prod_{i=1}^{N-1} N(\hat{x}_i^1 - x_i - v \hat{\Delta}t \cos \theta_i, 2D \hat{\Delta}t) \prod_{i=1}^{N-1} \prod_{j=2}^k N(\hat{x}_i^j - \hat{x}_i^{j-1} - v \hat{\Delta}t \cos \hat{\theta}_i^{j-1}, 2D \hat{\Delta}t) \\
 &\times \prod_{i=2}^N N(x_i - \hat{x}_{i-1}^k - v \hat{\Delta}t \sin \hat{\theta}_{i-1}^k, 2D \hat{\Delta}t) \prod_{i=1}^{N-1} N(\hat{x}_i^1 - x_i - v \hat{\Delta}t \sin \theta_i, 2D \hat{\Delta}t) \\
 &\times \prod_{i=1}^{N-1} \prod_{j=2}^k N(\hat{x}_i^j - \hat{x}_i^{j-1} - v \hat{\Delta}t \sin \hat{\theta}_i^{j-1}, 2D \hat{\Delta}t).
 \end{aligned} \tag{2.32}$$

Although horrible to write down, once it is written it is easy to sample from. Fig. 2.15b shows the result on this data set. Now the true value of v has finite probability, and in general with this method the resulting parameter estimates will be unbiased. The Hamiltonian Markov Chain will furthermore sample values of \hat{x} and \hat{y} allowing us to reconstruct the trajectory. Fig. 2.16a shows such example samples. Note that each of these curves will have different parameters and some will be more likely than others. In general, this reconstruction works remarkably well. Fig. 2.16b shows how even kinks in the trajectories match the original data well despite the Hamiltonian Markov Chain sampler only knowing about the subsampled datapoints (marked as blue circles). This is possible because curvature in both directions might seem equally likely when considering only two subsequent datapoints, but the curvature is further constrained by next-neighbouring points.

2.5 Three-Dimensional Tracking

The helical structure of the random walks presented in the previous chapter was inferred indirectly. Here, we employ a microscope technique known as *digital inline holography* to observe this structure more directly. The experimental technique is described in Appendix 2.C.

Digital inline holography is a technique that is developed for 3D tracking of small particles that can be approximated as spherical scatterers. Choanoflagellate unicells obey this requirement, however, colonies do not, since they are a cluster of small cells. The technique is therefore not perfect for tracking colonies. It can, nonetheless, be applied, but the resulting

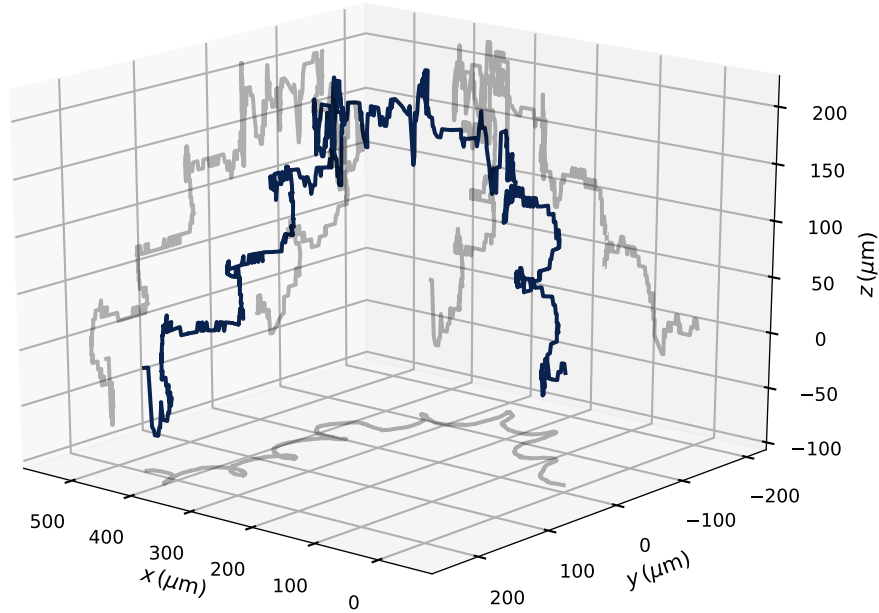


Figure 2.17 Holographic tracking of a choanoflagellate colony in 3D. Shadows show projections of the data. The x , y data has much lower noise than the z data.

tracks have quite noisy data in the z -direction. An example track is shown in Fig. 2.17. In particular, the noise, unfortunately, is very large in the most interesting region: where the colony is reorienting the fastest. The data in the x - and y -directions have almost no noise.

Although the z -part of the data is very noisy, it is clear that the trajectory is the result of helical swimming in three dimensions. One question is then if we can use the fact that we understand that the mode of swimming is helical to transfer information of the well-constrained data in the x – y -direction to improve the measurements in the z -direction. To do this, we will again exploit Markov Chain Monte Carlo to sample for the underlying ‘true’ trajectory.

We cannot assume the assumptions used in Section 2.3.2 on aggregate random walkers hold perfectly along the tracks, and thus we wish to formulate quite a general theoretical model for helical swimming. For instance, the values $|v|$, $|\omega|$, $v \cdot \omega$, and $|v \times \omega|$ can in reality vary slowly along the tracks and independently of one another. Allowing this behaviour while maintaining the helical nature, we consider a model of the form

$$dx = v dt + \sqrt{2D} dW_1, \quad (2.33a)$$

$$d\omega = \sqrt{2D_r} |\omega| dW_2, \quad (2.33b)$$

$$dv = \omega \times v dt + \sqrt{2D_r} |v| dW_3, \quad (2.33c)$$

where this time we allow the noise on $\omega(t)$ to be different to the one used on $v(t)$. A more complicated, but also more realistic model is to have v and ω behave similar to Ornstein-Uhlenbeck processes. Presently, however, we do not need such complicated models, since the data will constrain the possible trajectories, allowing us to take this very general model.

The true trajectory is represented by $x(t) = [x(t), y(t), z(t)]$. Our measurements x_{data} have noise on them as well. A Gaussian noise model is quite restrictive because of its short tails. To allow for outliers we instead take a Cauchy noise model, such that

$$x_{\text{data}}(t) \sim C(x_0 = x(t), \gamma_{xy}), \quad (2.34a)$$

$$y_{\text{data}}(t) \sim C(x_0 = y(t), \gamma_{xy}), \quad (2.34b)$$

$$z_{\text{data}}(t) \sim C(x_0 = z(t), \gamma_z), \quad (2.34c)$$

where x_0 is the location parameter, and γ the scale parameter in the Cauchy distribution

$$C(x; x_0, \gamma) = \frac{1}{\pi\gamma} \left(\frac{\gamma^2}{(x - x_0)^2 + \gamma^2} \right). \quad (2.35)$$

The parameter γ is a measure of the noise levels, and we allow this to be higher in the z direction. Noise models like these are easy to incorporate in the Hamiltonian Monte Carlo method, and so we directly write down the likelihood of the data

$$\begin{aligned} \mathcal{L} = & \prod N(x_i - x_{i-1} - v_x \Delta t, 2D\Delta t) \prod N(\omega_{x,i} - \omega_{x,i-1}, 2D_r |\omega_{i-1}|^2 \Delta t) \quad (2.36) \\ & \times \prod N(v_{x,i} - v_{x,i-1} - [\omega_{y,i-1} v_{z,i-1} - \omega_{z,i-1} v_{y,i-1}] \Delta t, 2D_r |v_{i-1}|^2 \Delta t) \\ & \times \prod C(x_i - x_{\text{data},i}, \gamma_{xy}) \times (y \text{ and } z \text{ terms}). \end{aligned}$$

Although we could sample for the noise levels themselves, we fix $\gamma_{xy} = 1 \mu\text{m}$ and $\gamma_z = 5 \mu\text{m}$. The results of running this Markov Chain sampling is shown in Fig. 2.18. As can be seen from Fig. 2.18b, the data is well-matched in the x - y -directions. The data in the z direction is only used slightly, as can be seen in Fig. 2.18c. Overall, we obtain a very constrained estimate for the true underlying trajectory [Fig. 2.18a]. The Cauchy noise model is what enables the model to ignore many of the outliers in the z -direction. Where the data is most noisy, the standard deviation of our sample paths also grow [Fig. 2.18c], and thus this model also enables us to understand how certain we are of our estimates.

Future studies employing the method described in this section on large data sets could allow, for example, detailed study of the reorientation dynamics of colonial choanoflagellates.

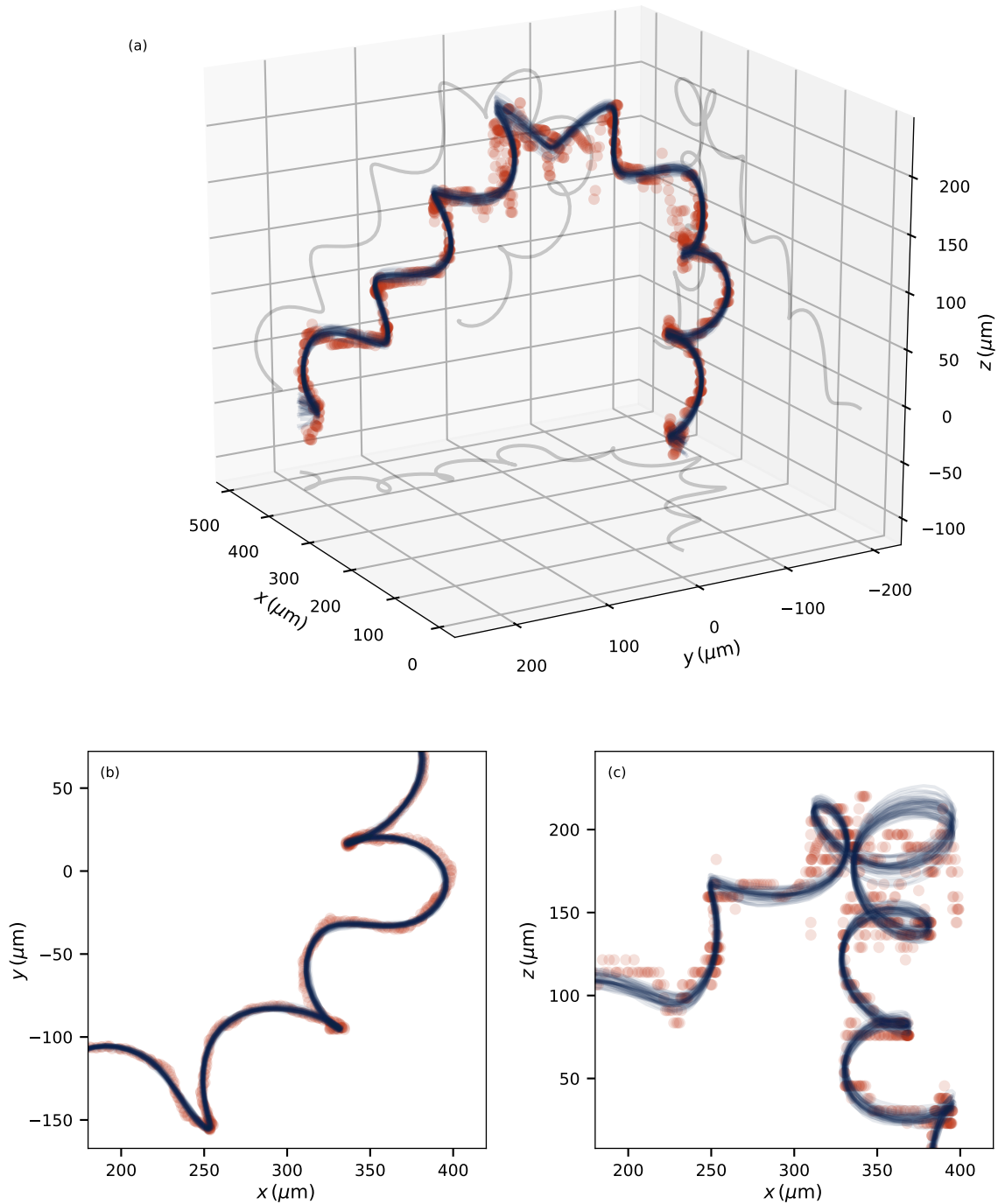


Figure 2.18 Hamiltonian Monte Carlo sampling of true underlying trajectory in holographic track. Data shown as red circles, sample trajectories as blue lines. (a) 3D plot with projections of the average sample path shown as shadows. (b) x - y projection showing the low noise in this plane. (c) x - z projection showing the large noise in the z -direction and that uncertainty in the model grows near very noisy data. Hamiltonian Monte Carlo was run with $\gamma_{xy} = 1 \mu\text{m}$ and $\gamma_z = 5 \mu\text{m}$ fixed.

2.6 Conclusions

In this chapter we have studied the flagellar beating dynamics and the (unbiased) swimming behaviour of *S. rosetta*.

We found that the flagellar beats within colonies of *S. rosetta* are uncorrelated with one another. In fact, as we have seen, they beat at distinct frequencies showing that interactions between them, intra- and extra-cellularly, must be minute. Naturally, we have only studied a finite number of colonies, and most of these consisted only of few consistent cells. It could be the case that in larger colonies extra-cellular (hydrodynamic) synchronisation, such as seen in *Volvox* (Brumley et al., 2012), could occur. Such studies of *S. rosetta*, however, would require different fixation and visualisation techniques than the ones used here.

By tracking their trajectories, we have shown that *S. rosetta* colonies swim along noisy helices. We have argued that this is the natural consequence of having a colony of cells in which each cell beats off-center, thus creating an effective internal torque. By writing down an appropriate stochastic differential equation for the system, we found that each colony could be characterised by four physical parameters: the helical frequency ω_0 , the swimming speed along the helix v_ω , the mean swimming speed v_p , and an effective rotational diffusion constant D_r , describing the stochasticity of the flagellar beats. The number of parameters makes sense: There must be two parameters to describe the average helix shape, one parameter to describe how fast the organism swims along this helix, and one to describe the noise levels. We have showed that these parameters vary widely from colony to colony, without much correlation between them. This is indicative of high variances in the stochastic processes that underlie colony formation.

Lastly, we have shown how digital inline holography can be used to obtain three-dimensional tracks of the helical colony swimming. The data quality in the z -direction, however, is not great. But using the knowledge of the mode of swimming, namely that it is helical, we have shown how Markov Chain Monte Carlo methods can be used to ‘fix’ the data in one direction by exploiting the quality of the data in the remaining two directions. This method could prove useful in obtaining high quality data from otherwise noisy and low resolution measurements, in this system and in others.

Appendix 2.A Tracking Flagella

Two techniques for flagella tracking were employed. The precise description of these methods can get quite lengthy, but we have outlined the main ideas of both below. Both techniques require some initial image processing. As background subtraction we used a

temporal median-filter (using median instead of mean is an overlooked trick that gives great results). The result is shown in Fig. 2.21b. A subsequent anisotropic diffusion filter was used to remove noise, Fig. 2.21c. Anisotropic diffusion was chosen for its edge-preserving capabilities. Lastly, we employed image template matching to adjust for the small overall motion of the colony and to mask out the cell body, Fig. 2.21d.

2.A.1 Active Contour Model

For the first approach, inspiration was found in the active contour model (Kass et al., 1988). In this method, we consider the flagellum a worm-like spline $x(s)$. For an image with intensity I , define $\mathcal{E}[x, I] = \mathcal{E}_{\text{snake}}[x] + \mathcal{E}_{\text{image}}[x, I]$, where

$$\mathcal{E}_{\text{snake}}[x] = \frac{1}{2}\alpha \int_0^L |\partial_s x(s)|^2 ds + \frac{1}{2}\beta \int_0^L |\partial_s^2 x(s)|^2 ds, \quad (2.37a)$$

$$\mathcal{E}_{\text{image}}[x, I] = -\omega \int_0^L |I(x(s))| ds. \quad (2.37b)$$

The flagellum is then found as minimiser of this energy, i. e. $f[I] = \operatorname{argmin}_x \mathcal{E}[x, I]$. The $\mathcal{E}_{\text{snake}}$ term enables one to control how much the model flagellum can stretch and bend. This energy can be adapted to the specific purpose with other terms. The minimisations of the snake energy can be done analytically through the corresponding Euler equations, but the image energy has to be minimised by explicit time stepping. For instance, for the x -component, the Euler equation becomes

$$\alpha \frac{\partial^2 x}{\partial s^2} + \beta \frac{\partial^4 x}{\partial s^4} + \frac{\partial E_{\text{image}}}{\partial x} = 0. \quad (2.38)$$



Figure 2.19 Tracking individual flagella within colonies with active contours. (a) Original. (b) Processed. (c) Tracked.

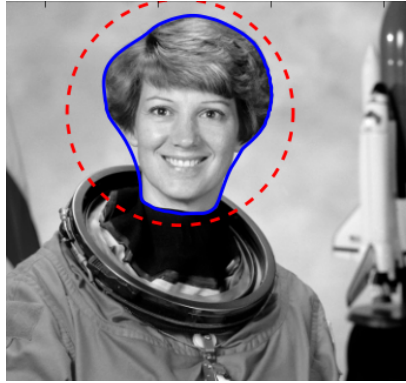


Figure 2.20 Active Contour Model. Dashed red is initial spline and blue is final shape obtained by the active contour model.

The left hand side can be approximated with finite differences resulting in a matrix A . Introducing an explicit time step parameter γ , the iterative algorithm becomes

$$Ax_{i+1} + \frac{\partial E_{\text{image}}}{\partial x_i} = -\gamma(x_{i+1} - x_i), \quad (2.39)$$

or,

$$x_{i+1} = (A + \gamma I)^{-1} \left(\gamma x_i - \frac{\partial E_{\text{image}}}{\partial x_i} \right). \quad (2.40)$$

Note that the matrix $(A + \gamma I)$ need only be inverted once. The image derivatives are taken on a second order bivariate spline approximation. An initial guess x_0 is needed. For videos the initial guess of one image can be taken from the final minimum of the previous image. An initial guess for the first image is always needed though. The method's name comes from its ability to find smooth contours. By minimising the energy on the laplacian of an image, edges are found. An example of this is shown in Fig. 2.20. The dashed red line is the initial guess of the face outline and the blue curve is after minimisation. The minimisation is done in custom-made software, the code of which we have made publicly as part of the Python image library *scikit-image* (Kirkegaard, 2015; van der Walt et al., 2014).

Fig. 2.19 shows the result of the tracking. The original data (a) is processed (b) and the minimisations yield the bases of the flagella (c).

2.A.2 Morphological Skeletonisation

One disadvantage of the previous method is its temporal correlation through the initial guesses. A completely different approach is to threshold the preprocessed video resulting in

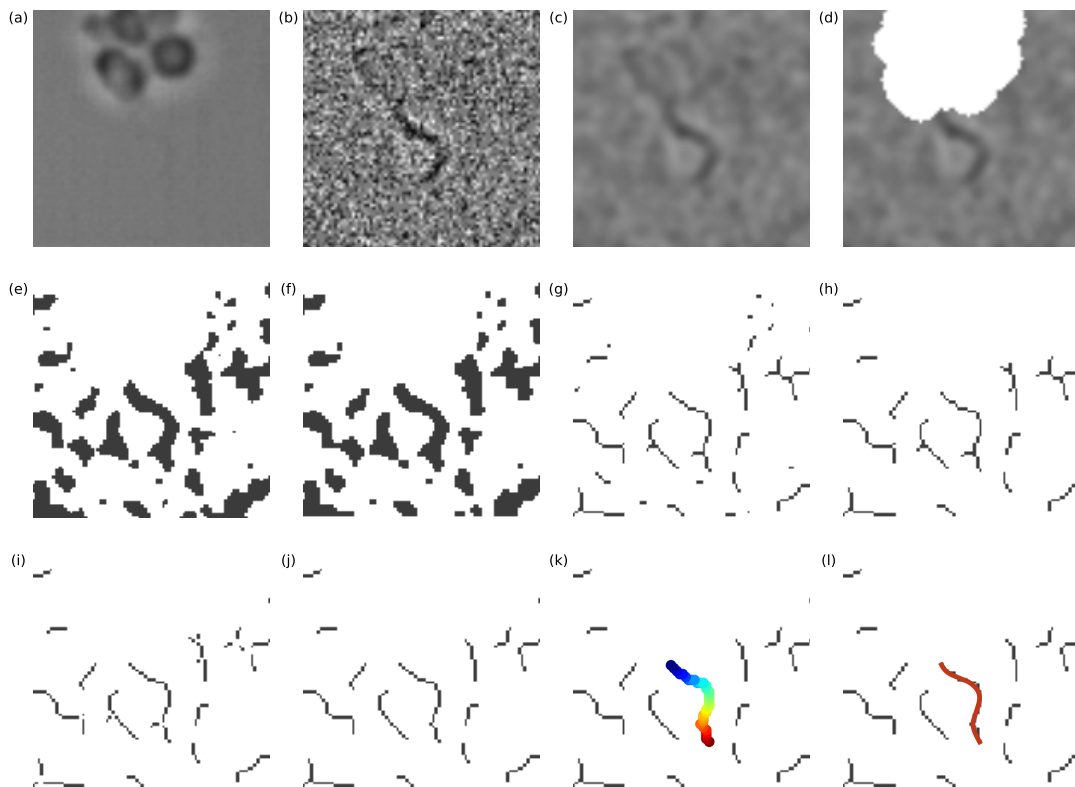


Figure 2.21 Flagellum tracking by skeletonisation. (a) Original video. (b) Background subtraction. (c) Filtered. (d) Masked. (e) Binary threshold. (f) Morphological opening and closing. (g) Morphological thinning. (h) Remove short skeletons. (i) Break at branch points. (j) Remove small and reintroduce cuts. (k) Graph sort longest skeleton. (l) Fitted spline.

binary images, an example of which is shown in Fig. 2.19e. Morphological openings and closings remove speckles and fills holes (f). A *skeletonisation* is any method of turning such binary images into 1 pixel wide lines. The standard skeletonisation method is the medial axis transform defined as the set of all points having more than one nearest point on the object boundary. This method, however, results in a lot of branches: small lines attached to the main line. We wish to minimise these as the end result should be a line with only two endpoints, the base and end point of the flagellum.

A better skeletonisation approach is a so-called morphological thinning: iteratively remove border pixels that when removed do not change the connectivity of the binary image. The resulting image has lines with far fewer branches, but still some (g). Next, small lines are removed (h). Branch points (pixels after a subsequent medial axis transform with three or more neighbours) are removed (i) and resulting small lines are removed. Special care has to be given to loops. The branch points are then reintroduced (j) and the flagellum is chosen by

proximity to the previous found flagellum. The final line has only two endpoints. The one end point that is nearest the previous base point is chosen as the new base point. The pixels are then sorted by graph distance through the Floyd-Warshall algorithm (k) and lastly the pixels are fitted by a second order spline (l) representing, finally, the flagellum.

These two algorithms can also be combined: the active contour model can be guided by the skeletonised image described here. We employed this to track inverting *Volvox* embryos as described in Haas et al. (2017).

Appendix 2.B Stochastic Swimming Speeds

In this chapter we have for the most part assumed the swimming speed v of the microorganisms constant. However, this is unrealistic as this speed itself will be noisy. Here we give two examples of how noisy swimming speeds can also be incorporated into the calculations.

2.B.1 On-Off Swimming

We start by considering a swimmer that switches between swimming with velocity v_0 and idling. The individual periods of swimming and idling are of a random and exponentially distributed duration. A similar problem with $v(t)$ being a deterministic square wave of fixed period has been considered in Babel et al. (2014). We define "rates" λ, μ , such that $1/\lambda, 1/\mu$ are the average period of on and off, respectively. We assume the swimming speed $v(t)$ independent of the direction of swimming $\phi(t)$, and thus we need to calculate

$$\langle (x(t) - x_0)^2 \rangle = \int_0^t \int_0^t \langle v(t')v(t'') \rangle \langle \cos \phi(t') \cos \phi(t'') \rangle dt' dt'' + 2Dt. \quad (2.41)$$

Thus we need to find the autocorrelation function $\langle v(t)v(t') \rangle$ for the on-off process. Let the vector $(1, 0)^T$ denote the on-state and $(0, 1)^T$ the off-state. The process can then be described by the infinitesimal generator

$$\mathcal{G} = \begin{pmatrix} -\lambda & \mu \\ \lambda & -\mu \end{pmatrix} \quad (2.42)$$

The probability distribution vector $p = (p_{\text{on}}, p_{\text{off}})^T$ evolves according to

$$p(t) = e^{\mathcal{G}t} p_0 = \frac{1}{R} \begin{pmatrix} \mu + \lambda e^{-Rt} & \mu - \mu e^{-Rt} \\ \lambda - \lambda e^{-Rt} & \lambda + \mu e^{-Rt} \end{pmatrix} p_0, \quad (2.43)$$

where $R = \lambda + \mu$. We shall assume, even though the full calculation can be done, that the system is stationary, i. e. $p(t) = \pi$ where

$$\mathcal{G} \pi = 0 \Leftrightarrow \pi = \frac{1}{R} \begin{pmatrix} \mu \\ \lambda \end{pmatrix}, \quad (2.44)$$

which can also be found by taking $t \rightarrow \infty$ in Eq. (2.43).

Now note that for $t' < t$, $\langle v(t)v(t') \rangle = v_0^2 p_{\text{on}}(t|t') \pi_{\text{on}}$, where $p_{\text{on}}(t|t')$ is probability of being in the on-state at time t given that the process was in the on-state at time t' . Hence using Eq. (2.43),

$$\langle v(t)v(t') \rangle = v_0^2 \frac{\mu^2 + \lambda \mu e^{-(\lambda+\mu)|t-t'|}}{(\lambda + \mu)^2}. \quad (2.45)$$

We can now carry out the double integral of Eq. (2.41), leaving the result

$$\begin{aligned} \langle \Delta r^2(t) \rangle = & \frac{2\mu v_0^2}{D_r^2 R^2 (D_r + R)^2} \left(D_r^2 (D_r t - 1) (\lambda + \mu) + D_r^2 \lambda e^{-(D_r + R)t} + D_r^2 \mu e^{-D_r t} \right. \\ & \left. + D_r R (D_r t (\lambda + 2\mu) - 2\mu) + \mu R^2 e^{-D_r t} + \mu R^2 (D_r t - 1) + 2D_r \mu R e^{-D_r t} \right) + 4Dt. \end{aligned} \quad (2.46)$$

Note that both $\mu \rightarrow \infty$ and $\lambda \rightarrow 0$ correctly yields the constant velocity particle case used in the main part of the chapter. Likewise, $\mu \rightarrow 0$ and $\lambda \rightarrow \infty$ yields pure translational diffusion. The long-term effective diffusion constant becomes

$$D_\infty = \lim_{t \rightarrow \infty} \frac{\langle \Delta r^2 \rangle}{4t} = \frac{\mu (D_r + \mu)}{R (D_r + R)} \frac{v_0^2}{2D_r} + D \quad (2.47)$$

Note that with λ fixed, $D_\infty \rightarrow D$ as $\mu \rightarrow 0$ corresponding to a passive particle, and $D_\infty \rightarrow v^2/2D_r + D$ as $\mu \rightarrow \infty$ corresponding to the constant velocity particle presented above. The ballistic behaviour is

$$\langle \Delta r^2 \rangle \sim \frac{\mu}{R} v_0^2 t^2 + 4Dt, \quad (2.48)$$

where indeed μ/R is the probability that the process is on at $t = 0$.

2.B.2 Ornstein-Uhlenbeck Swimming

As an example of a continuous stochastic swimming speed, we consider the Ornstein-Uhlenbeck process, defined by the SDE

$$dv(t) = \frac{v_0 - v(t)}{\tau} dt + \gamma dW(t). \quad (2.49)$$

In principle this allows for negative values of v (meaning backwards swimming), but this will only happen rarely if v_0 is a few times larger than $\sqrt{\tau}\gamma$. The above SDE has the stationary solution

$$P(v) = \frac{1}{\sqrt{\pi\tau\gamma^2}} \exp\left(-\frac{(v-v_0)^2}{\tau\gamma^2}\right). \quad (2.50)$$

For an Ornstein-Uhlenbeck process it is simple to show that $\langle v(t)v(t') \rangle = v_0^2 + \frac{1}{2}\tau\gamma^2 e^{-|t-t'|/\tau}$ in the stationary limit. Using again Eq. (2.41), we find

$$\begin{aligned} \langle \Delta r^2(t) \rangle = & \frac{1}{D_r^2(D_r\tau + 1)^2} \left[D_r^2\tau \left(\gamma^2\tau^2 e^{-t(D_r+\tau^{-1})} + \gamma^2\tau(D_r t\tau + t - \tau) + 2v_0^2(t(D_r\tau + 2) - \tau) \right) \right. \\ & \left. + 2v_0^2(e^{-D_r t}(D_r\tau + 1)^2 + D_r(t - 2\tau) - 1) \right] + 4Dt \end{aligned} \quad (2.51)$$

This has an early time ballistic behaviour of

$$\langle \Delta r^2(t) \rangle \sim (v_0^2 + \frac{1}{2}\gamma^2\tau)t^2 + 4Dt \quad (2.52)$$

and a late time diffusive behaviour of

$$D_\infty = \lim_{t \rightarrow \infty} \frac{\langle \Delta r^2 \rangle}{4t} = \frac{1}{4} \frac{\gamma^2\tau^2}{1 + D_r\tau} + \frac{v_0^2}{2D_r} + D \quad (2.53)$$

Note that even in the absence of mean driving ($v_0 = 0$) there is still some ballistic behaviour due to the finite correlation of the stochastic forcing.

Appendix 2.C Digital Inline Holography

Many variations on holographic microscopy exist. We employed the version used in [Wilson and Zhang \(2012\)](#), which we will briefly describe here. More advanced versions (see e.g. [Katz and Sheng \(2010\)](#)) lead to better results.

The key to the technique is to use a monochromatic light source. By observing the interference between the light scattered from our sample with the unscattered light, we can reconstruct the samples' 3D positions by recording 2D data only.

Without any sample in the setup, we observe a background image $a(x,y) = |E_0(x,y,0)|^2$, where $E_0(x,y,z)$ is the background electric field and $z = 0$ is the focal plane. Adding samples to the observation chamber, we also have the field due to scattered light on the samples E_s . These fields interfere and we observe

$$I(x,y) = |E_0(x,y,0)|^2 + 2\text{Re}[E_0(x,y,0) \cdot E_s(x,y,0)] + |E_s(x,y,0)|^2. \quad (2.54)$$

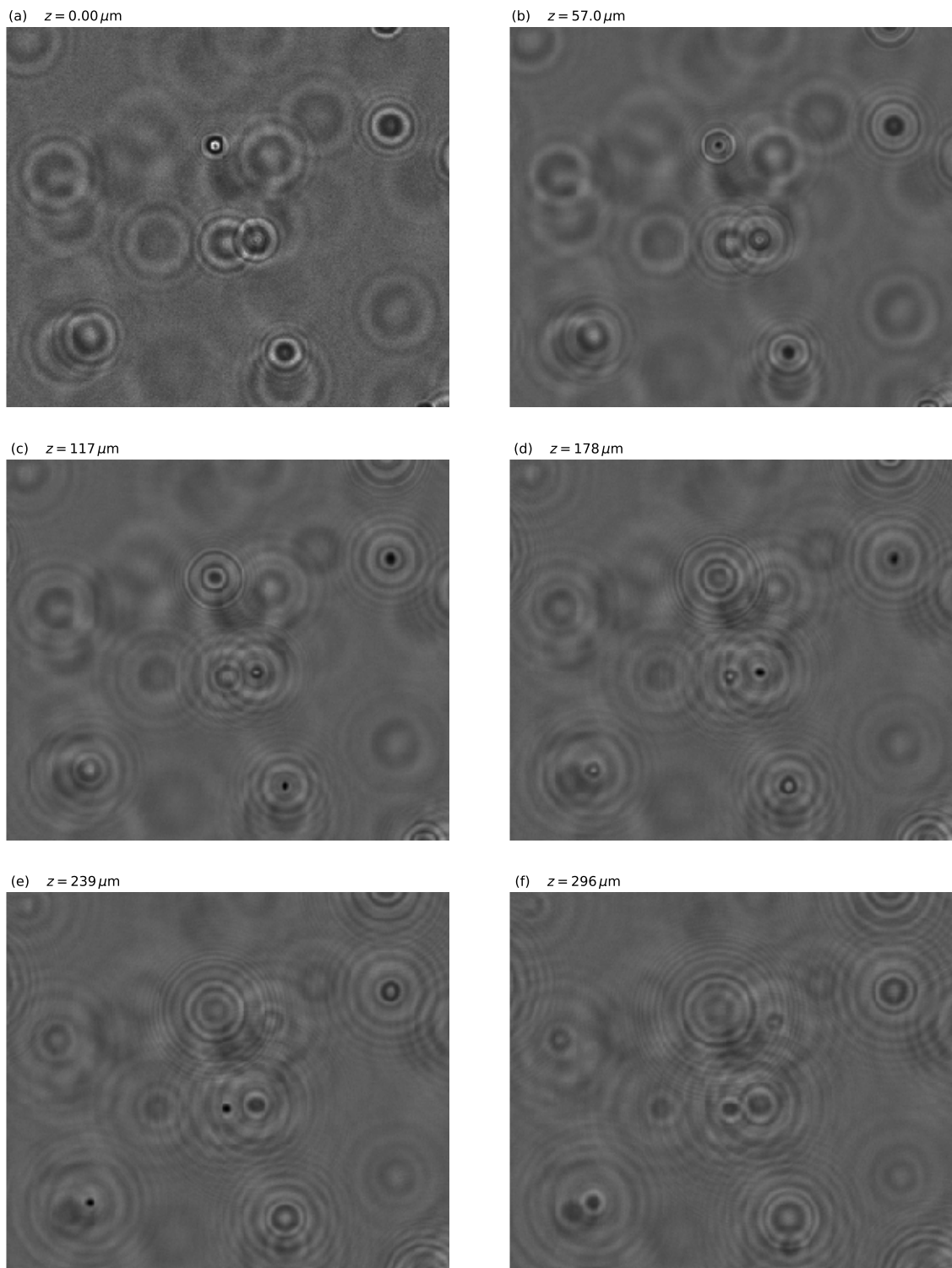


Figure 2.22 Rayleigh-Sommerfeld reconstruction at various heights. (a) Original image. (b-f) Reconstructions.

The scattered field is weak and so we can assume the last term negligible. By first observing the background image $a(x, y)$, we can calculate

$$b(x, y, 0) = \frac{I(x, y)}{a(x, y)} - 1 \approx 2 \operatorname{Re} \left[\frac{E_0(x, y, 0) \cdot E_s(x, y, 0)}{|E_0(x, y, 0)|^2} \right] \quad (2.55)$$

immediately from our data. For objects that are not close to focal plane, the scattered polarisation will be small and we can write (Cheong et al., 2010)

$$b(x, y, 0) \approx 2 \operatorname{Re} \left[\frac{E_s(x, y, 0)}{E_0(x, y, 0)} \right]. \quad (2.56)$$

The goal of the approach is to calculate field $b(x, y, z)$ at various z given the only the value $b(x, y, 0)$, i. e. calculate what we would have seen if we had measured at a general z and not at $z = 0$. The Rayleigh-Sommerfeld propagator gives us (Cheong et al., 2010; Lee and Grier, 2007)

$$E_s(x, y, z) = E_s(x, y, 0) * h_{-z}(x, y), \quad (2.57)$$

where $*$ means convolution and

$$h_{-z}(x, y) = \frac{1}{2\pi} \frac{\partial}{\partial z} \frac{e^{ikr}}{r}, \quad (2.58)$$

where $r^2 = x^2 + y^2 + z^2$ and k is the wavenumber of the monochromatic light. Under the assumption of uniform illumination, by Fourier transforming the above, one finds (Cheong et al., 2010)

$$b(x, y, z) = \frac{e^{ikz}}{4\pi^2} \int_{-\infty}^{\infty} \tilde{b}(q) \tilde{h}_{-z}(q) e^{iq \cdot r} d^2q, \quad (2.59)$$

where \tilde{b} is the Fourier transform of the data $b(x, y, 0)$ and \tilde{h}_{-z} is the Fourier transform of Eq. (2.58),

$$\tilde{h}_{-z}(q) = \exp \left(iz [k^2 - q^2]^{1/2} \right). \quad (2.60)$$

Fig. 2.22 shows an example reconstruction using this technique. Fig. 2.22a is the image at the focal plane $z = 0$, and Fig. 2.22(b–f) shows calculations for various z . The particles come into focus at their z location. For instance, the bottom-left hologram in Fig. 2.22a comes into focus at around $z = 239 \mu\text{m}$ as shown in Fig. 2.22e. We detect the focus points by convolving $b(z)$ with

$$\kappa(z) = z \exp \left(-(z/\ell)^2 \right), \quad (2.61)$$

where ℓ is some parameter to be manually chosen. The sign of $b(z) * \kappa(z)$ determines if the cell is above or below the focal plane.

The calculation are computationally quite intense. We therefore adapted existing code by D.G. Grier to use GPU acceleration via PYCUDA and ran it on an nVidia Titan X GPU. The code is available in Ref. [Kirkegaard and Peaudecerf \(2017\)](#).

Calibration of the system is not needed, but to test the setup we used a micro-manipulator (Scientifica, UK) to raise and lower, with micrometer precision, beads that had sedimented to the bottom of the glass slide. We could thus check that the vertical distances moved, as measured by the micro-manipulator, matched the one extracted using holographic reconstruction.

Appendix 2.D Stochastic Simulations

In this chapter we have, and in many of the following we will, use numerical realisations of the stochastic differential equations. Here we present the numerical methods used throughout. We consider the simple case of a 1D Itô SDE:

$$dx = \mu(x) dt + \sigma(x) dW. \quad (2.62)$$

Stratonovich can be transformed to a corresponding Itô form (with noise-induced drifts, as discussed), and so we do not need to present methods for these here.

Euler–Maruyama method

The simplest method for simulating SDEs is a small extension to the classical Euler’s Method. Discretising Eq. (2.62) with time-stepping parameter Δt we have

$$x(t + \Delta t) = x(t) + \mu(x(t)) \Delta t + \sigma(x(t)) \Delta W. \quad (2.63)$$

Since W is a Wiener process, we know that

$$\Delta W = W(t + \Delta t) - W(t) \sim N(0, \Delta t). \quad (2.64)$$

Thus the method becomes

$$x(t + \Delta t) = x(t) + \mu(x(t)) \Delta t + \sigma(x(t)) \sqrt{\Delta t} \times \text{RANDN}(), \quad (2.65)$$

where $\text{RANDN}()$ is a standard normal distributed random number. Eq. (2.65) is the Euler–Maruyama method. Similar to Euler’s method, it is not very stable unless Δt is very small. In fact, this method is even worse in the sense that the (strong) order of convergence is only $\sqrt{\Delta t}$.

Milstein Method

The reason the Euler–Maruyama method has such slow convergence is because $\Delta W \propto \sqrt{\Delta t}$. The Milstein method (Mil'shtein, 1974) includes the next term in the Itô–Taylor expansion such that we include all terms that are proportional to Δt . The method is

$$x(t + \Delta t) = x(t) + \mu(x(t)) \Delta t + \sigma(x(t)) \Delta W + \frac{1}{2} \sigma(x(t)) \sigma'(x(t)) (\Delta W^2 - \Delta t), \quad (2.66)$$

where again $\Delta W = \sqrt{\Delta t} \times \text{RANDN}()$, i. e. the two ΔW 's that appear use the same random number. The extra term is a sort of finite-difference version of noise-induced drift. Intuition for the formula can be obtained by considering the Itô integral (valid for any value of $\Delta t > 0$)

$$\int_0^{\Delta t} W \, dW = \frac{1}{2} (\Delta W^2 - \Delta t), \quad (2.67)$$

but see Higham (2001) for full details on the derivation.

This method has order of convergence Δt like Euler's method for ordinary differential equations. The Milstein method is important when there is multiplicative noise, such as in the case of our aggregate random walker system. If there is no multiplicative noise, the method coincides with the Euler–Maruyama method, since $\sigma'(x) = 0$.

Lastly, we should mention that Hamiltonian Monte Carlo, as presented in Sec. 2.4, can also be used as a simulation method. In particular, this methods can be used to simulate constrained random walks; for instance random walks with boundary conditions, such as e. g. Brownian bridges.

Chapter 3

Choanoflagellate Aerotaxis

3.1 Introduction

Aerotaxis, defined as oxygen-dependent migration, is well-characterised in bacteria (Taylor et al., 1999), but is poorly studied in more complex organisms. This is despite the essentiality of oxygen for all aerobic life, and the important role that Precambrian oxygen levels played in the emergence and evolution of multicellular animal life (Nursall, 1959). Here, we study *S. rosetta* and show that it exhibits aerotaxis, i. e. navigation along gradients of oxygen. No evidence of any form of taxis for choanoflagellates had previously been reported, and so this study was further motivated by understanding any form of taxis in choanoflagellates, and in particular in colonial forms.

As discussed in the previous chapter, the colony morphology of *S. rosetta* is variable, and the constituent flagella beat independently of one another. The random and independent flagellar motion argues against there being any coordination between cells in a colony. The geometry, flagella independence and lack of taxis observed in *S. rosetta* colonies contrast with other lineages, such as the Volvocales (Goldstein, 2015). Phototaxis is clearly observable in both unicellular (*Chlamydomonas*, Yoshimura and Kamiya (2001)) and colonial (*Volvox*, Drescher et al. (2010)) volvocalean species, in order to maintain optimum light levels for photosynthesis. Volvocalean phototaxis is *deterministic*, requiring precise tuning between the internal biochemical timescales and the rotation period of the organism as a whole. Although *S. rosetta* colonies also rotate around an internal axis, as described in the previous chapter, due to the variable colony morphology and the independent beating of the individual flagella, this rotation rate will itself be random, rendering a strategy similar to that of the Volvocales unlikely in *S. rosetta*.

An alternative strategy is *stochastic* taxis, sometimes referred to as kinesis. The classic example of stochastic taxis is the run-and-tumble chemotaxis of certain peritrichous bacteria

(Berg, 1993). By spinning their left-handed helical flagella in different directions, such bacteria can alternate between swimming in straight lines (running) and randomly reorienting themselves (tumbling). Through biasing tumbles to be less frequent when going up the gradient, the bacteria exhibit biased motion towards a chemoattractant without directly steering towards it (Berg, 1993). This method of taxis will be further studied in Chapter 4.

Beyond answering the question of whether *S. rosetta* is aerotactic in the positive, we further examine and statistically analyse the behaviour of *S. rosetta* colonies under spatio-temporal variations of oxygen at the level of total colony populations and at the level of the trajectories of individual colonies. From these experiments we establish two key features of the aerotactic response of choanoflagellates: they employ a stochastic reorientation search strategy and the sensing of oxygen concentration gradients is logarithmic. Finally, we render these results quantitative through the use of mathematical analysis of a generalised Keller-Segel model (Keller and Segel, 1971).

3.2 Experimental Set-up

The study of aerotaxis in bacteria has led to numerous methods for creating spatial oxygen gradients (Shioi et al., 1987; Taylor et al., 1999; Wong et al., 1995; Zhulin et al., 1996), one of which is the exploitation of soft lithography techniques (Adler et al., 2012; Rusconi et al., 2014). Since PDMS, the most commonly used material for microfluidic chambers, is permeable to gases, gas channels can be introduced in the devices to allow gaseous species to diffuse into the fluid. For example, an oxygen gradient can be created using a source channel flowing with normal air and a sink channel flowing with pure nitrogen.

Our device, shown schematically in Fig. 3.1, is a modified version of that used by Adler et al. (2012). Viewed from above, the sample channel (yellow) consists of a wide observation chamber with thin inlet and outlet channels. The outlet leads to a serpentine channel that hinders bulk fluid flows. On each side of the sample channel are gas channels, the inlets of which are connected to a valve system allowing for the flow of air (20% oxygen) and nitrogen. The flow of air and nitrogen can be conducted in any combination and configuration, e. g. oxygen in one channel and nitrogen in the other, and can be easily swapped over. The PDMS chamber is plasma etched to a glass slide, and an extra glass slide is etched on top of the device, preventing air from diffusing in from the surrounding environment. A detailed account of the fabrication method used for microfluidic devices is given in Appendix A.2.

Experiments were carried out immediately after plasma etching as the permeability of gases slowly decreases thereafter. Cultures of *S. rosetta*, concentrated by centrifugation, were introduced at the inlet of the device, and both the inlet and outlet were then closed to prevent

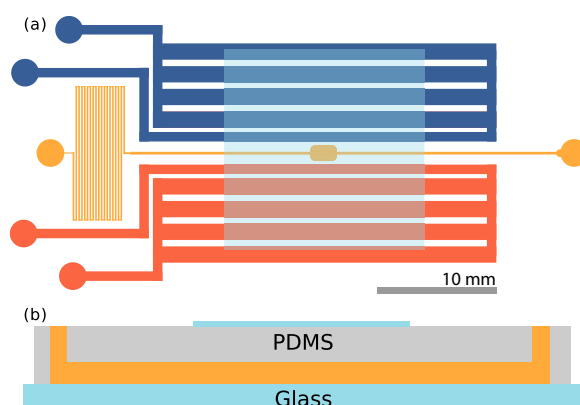


Figure 3.1 Microfluidic device. (a) Top view of the microfluidic device. The sample channel (yellow) is loaded with culture and observed in the middle chamber. The side channels (red, blue) are gas channels in which oxygen and nitrogen may be flown. Scale bar: 10 mm. (b) Side view of the device. PDMS is plasma etched to a glass slide, and a cover slip is plasma etched on top, centred on the imaging chamber, also shown in (a). Thickness of the channels are $\approx 115\ \mu\text{m}$.

evaporative flows. A gradient of oxygen was set up by having air flowing in one of the side channels and nitrogen in the other. Experiments were filmed (Imaging Source, Germany) in bright field at 10 fps on an inverted Zeiss LSM 700 Microscope.

3.3 Aerotaxis in Choanoflagellates

The main experimental result of this chapter, shown in Figs. 3.2(a–b), is the observation that *S. rosetta* colonies accumulate at the oxygen-rich side and away from the oxygen-poor side, i. e. that they are aerotactic. We also found aerotaxis in the unicellular fast swimmer form (Dayel et al., 2011) of *S. rosetta*, showing that this is not an exclusive phenomenon to colonies.

With the present microfluidic device we can explore more details of choanoflagellate aerotaxis by dynamically changing the oxygen boundary conditions, for instance by flipping the gradient direction or by removing all oxygen influx after a uniform distribution has been reached. Fig. 3.2c shows the result of such a dynamic experiment over the course of ~ 3.5 hours. The density is normalised for each frame and the noise present is partly due to colonies missing in the tracking in some frames. Many repetitions of the experiment show that the behaviour in Fig. 3.2c is highly repeatable and robust to changes in the details of the cycling protocol (another example is given in Fig. 3.3a). For consistency all other figures in this chapter are based on the data of Fig. 3.2.

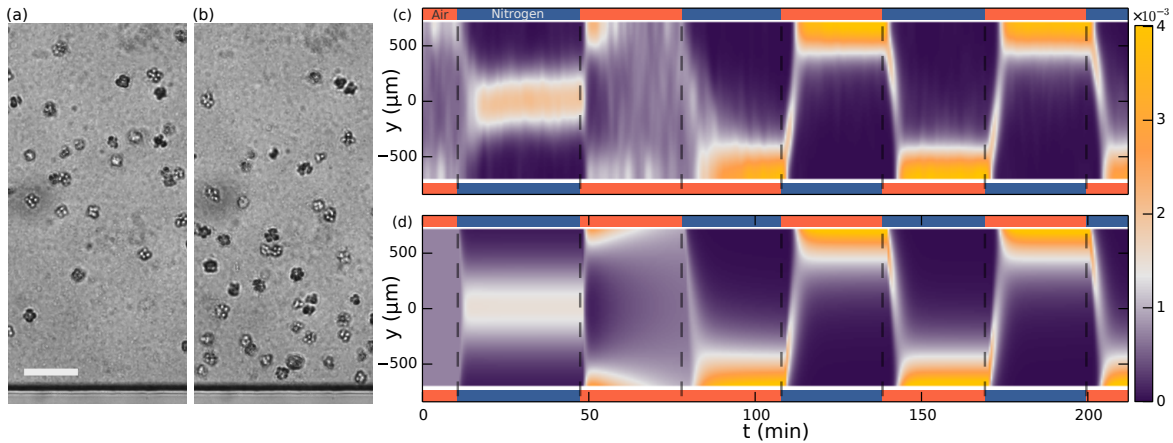


Figure 3.2 Aerotaxis of *S. rosetta* colonies. (a-b) Micrographs near an oxygen-rich wall at twice the resolution of that used in the density experiments. Scale bar: $50 \mu\text{m}$ (a) Colonies approach a wall where the oxygen-concentration is high. (b) Colonies staying near this wall. (c) Density evolution of *S. rosetta* during experiment. At each time step the distribution is normalised to a probability distribution [colourbar units in μm^{-1}]. Colours on the side indicate what gas is flowing in that side channel, red for oxygen and blue for nitrogen. $N_{\text{colonies}} \sim 150$, concentration $\sim 5 \cdot 10^6 \text{ mL}^{-1}$. (d) Keller-Segel model with log-concentration input given by Eq. (3.4), $D = 865 \mu\text{m}^2/\text{s}$, $\alpha = 1850 \mu\text{m}$, $v_{\text{drift}} = 5.2 \mu\text{m}/\text{s}$.

Whenever one gas channel contains oxygen and the other nitrogen, the colonies swim towards the oxygen-rich side. In the time after a gas channel swap, the slope of the maximum density reveals the ensemble drift velocity v_{drift} . When there is oxygen in both gas channels, we observe that the density reaches an approximately uniform distribution within the time frame of the experiment.

For periods in which nitrogen flows in both channels, this is not the case. Under these experimental conditions, the colonies accumulate in the middle of the chamber, where there is still some residual oxygen. The fact that in this nitrogen-only configuration the colonies accumulate mid-chamber shows that accumulation does not depend on the presence of a nearby surface. With only nitrogen flowing, eventually there will be no oxygen gradient. Nonetheless, we observed the colonies to stay in the middle of chamber even after 90 minutes (as evident from Fig. 3.3). At that time, the highest oxygen levels are estimated by the diffusion equation to be less than $\sim 0.2\%$.

This contrasting behaviour between the oxygen-only and nitrogen-only configurations suggests an asymmetry or non-linearity in the aerotactic response. If the response to oxygen concentration had been linear, the observation of the density band in the nitrogen-only section would imply similar density bands at the chamber edges in the oxygen-only section, which is not observed. Instead one might hypothesise that the colonies navigate along *relative*

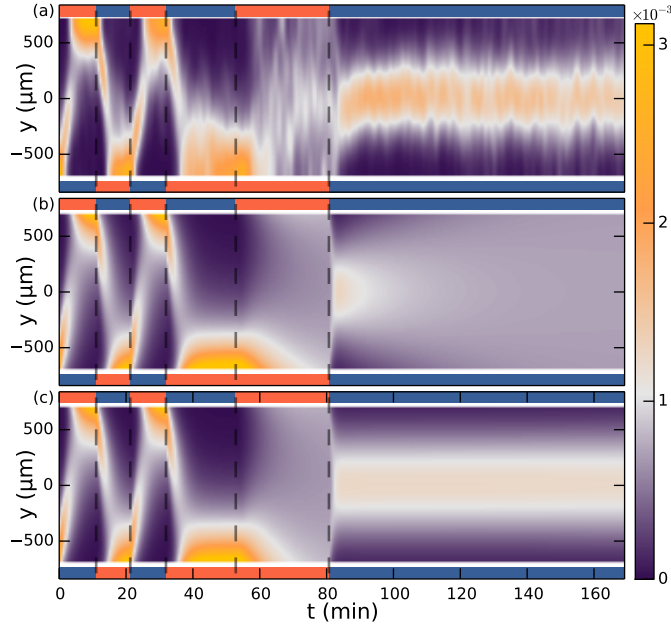


Figure 3.3 Separate aerotaxis experiment. (a) Density evolution of *S. rosetta* during experiment [colourbar units in μm^{-1}]. $N_{\text{colonies}} \sim 60$, concentration $\sim 2 \cdot 10^6 \text{ mL}^{-1}$. (b) Keller-Segel model with linear concentration input $\mathcal{V}[c] = v_{\text{drift}} \tanh(\alpha c_y)$, with $\alpha = 8.2$, and otherwise same parameters as in Fig. 3.2. (c) Keller-Segel model with log concentration input, same parameters as in Fig. 3.2. Experiment and simulation was started in steady-state configuration of oxygen down and nitrogen up.

$(\nabla c/c)$ instead of *absolute* (∇c) gradients, i. e. reacting to gradients that are comparable in magnitude to the background concentration. This is also known as logarithmic sensing, and we will confirm in the modelling section that this hypothesis can quantitatively explain the experiments.

3.4 Navigation Strategy

Strategies of taxis can be categorised into two main classes: *deterministic* and *stochastic*. In both strategies the swimming organism measures the attractant gradient. A deterministic strategy, then, is one in which the organism directly steers towards the attractant, such as seen in sperm cells that modulate their flagellar beat to adjust directly the curvature and torsion of its swimming path in the gradient direction (Friedrich and Jülicher, 2007; Jikeli et al., 2015). Contrasting is a stochastic strategy such as bacterial run-and-tumble locomotion (Berg, 1993), where modulation of the frequency of random reorientations biases the motion in the gradient direction without directly steering towards it.

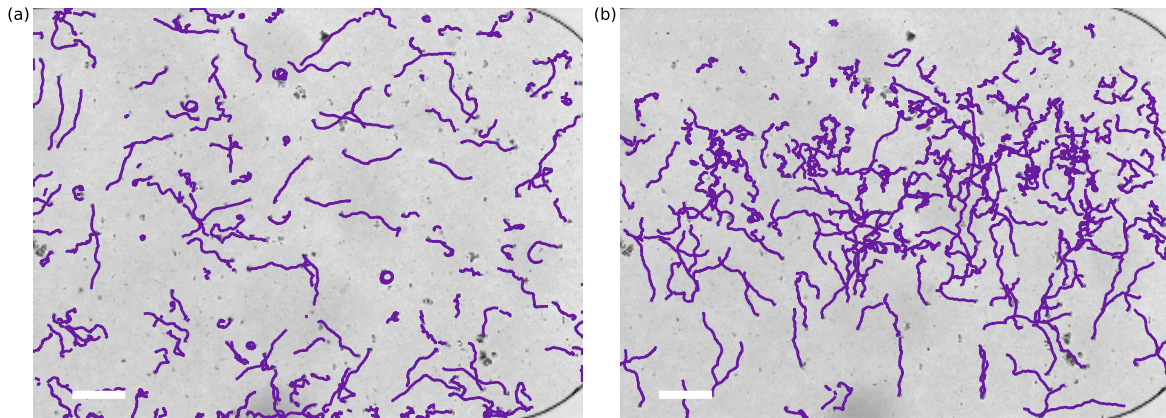


Figure 3.4 Example tracks. Trajectories are from the experiment of the main text. (a) $t = 70$ min. Trajectories at uniform oxygen concentration. (b) $t = 142$ min. Migration downwards after a swap to oxygen in the lower channel. Tracks were obtained by the algorithm described in Appendix A.3. Scale bars: $150\ \mu\text{m}$.

One simple method of taxis results from an organism swimming faster when it is moving up the gradient, creating an overall bias towards the attractant. Fig. 3.4 shows examples of tracks during periods of uniform swimming ($t = 70$ min) and after a gas channel swap ($t = 142$ min). From the colony-tracking data it is possible to test whether this mechanism is in operation with *S. rosetta*. Figure 3.5 shows the evolution of the mean colony swimming speed v (green) as well as the component velocities v_x (yellow) and v_y (purple), averaged over ~ 150 colonies in each frame. For most times, the component velocities average to zero, but after a gas channel swap the y -component peaks. The ensemble average swimming speed in these sections, however, does not show an increase, suggesting that a velocity modulation is not the method of taxis. To quantify this further, the inset of Fig. 3.5 shows the swimming speed in these sections plotted against the alignment to the gradient $\hat{c} v_y / v$ where $\hat{c} = \pm 1$ signifies the direction of the gradient. The plot shows a very small ($\sim 3\%$) change in swimming speed going up the gradient. Velocity-biased taxis can be described by $v(t) = v(\hat{p}) \hat{p}$, where e. g. $v(\hat{p}) = v(1 + \gamma \hat{p} \cdot \nabla c / |\nabla c|)$, γ being the velocity-modulation taxis parameter. \hat{p} , the direction of swimming, is unbiased by the attractant field c and evolves by rotational diffusion. To obtain a drift velocity $\sim 1/3$ of the swimming velocity, as we find for *S. rosetta* in the following section, the velocity modulation would have to be $\gamma = 2/3$ for a two-dimensional swimmer and $\gamma = 1$ in three dimensions, much larger than the $\sim 3\%$ observed. We conclude that the primary mechanism of aerotaxis in *S. rosetta* is therefore not a modulation of swimming speed.

As shown in the previous chapter, *S. rosetta* colonies swim along noisy helical paths, and each colony displays distinct helix parameters. To perform any kind of statistical angle

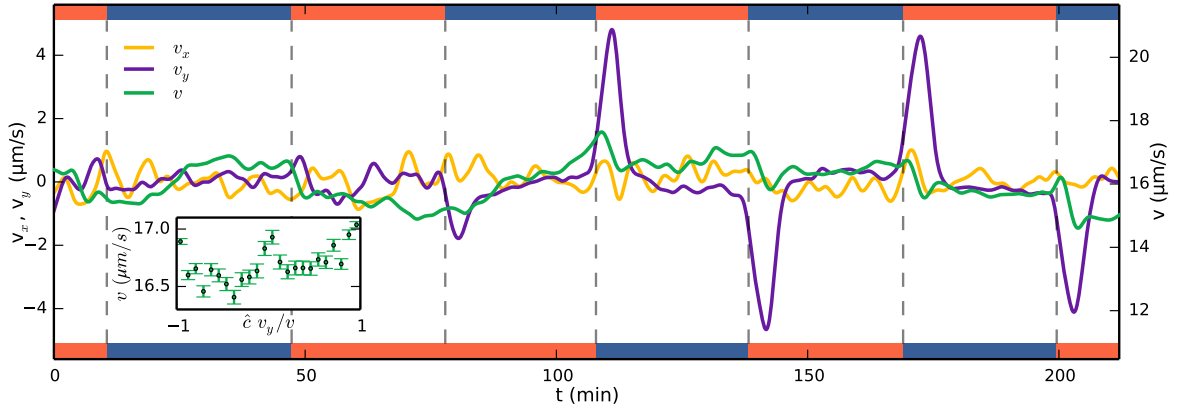


Figure 3.5 Running mean velocity statistics, showing that the primary mechanism of aerotaxis is not by modulation of swimming speed. Evolution of mean speed (green, right axis) and velocity in the x -direction (yellow, left axis) and y -direction (purple, left axis), y being along the gradient of oxygen. Left and right axes have equal ranges. Side bars indicate gas flowing, oxygen (red) or nitrogen (blue). The peaks of v_y do not quite reach the true drift velocity due to smoothing of the curves. Inset shows the speed as function of alignment with the gas gradient $\hat{c} v_y/v$ at times after a swap. $\hat{c} = 1$ if the gradient is up and $= -1$ if down.

analysis, we consider ensemble average quantities: the speed v and rotational diffusion d_r , and average helix rotations out. Figure 3.6a shows the angular distribution data during the swaps, where, for the purposes of displaying all the data in a single graph, we have let $\theta \rightarrow -\theta$ for times when the oxygen gradient were pointing down. This distribution favours the up-direction $\theta = \pi/2$. More interesting is the distribution of reorientations. For this we define the angle turned by a colony in a time Δt as $\Delta\phi = |\theta(t + \Delta t) - \pi/2| - |\theta(t) - \pi/2|$ such that it is positive if the turn is in the direction of the gradient and negative otherwise, and choose Δt low enough that $-\pi < \Delta\phi < \pi$. Fig. 3.6b shows this distribution. The distribution is centred on zero, revealing that the colonies do as many turns in the wrong direction as in the correct direction. This indicates that the colonies navigate by a *stochastic* strategy.

3.5 Aerotaxis Model

We study the spatio-temporal evolution of the choanoflagellate colony population within the observation chamber with the Keller-Segel model (Keller and Segel, 1971), which has broad applicability for taxis (Tindall et al., 2008a). In describing the phenomenon of aerotaxis the two quantities of interest are the colony population density $\rho(x, t)$, and the oxygen concentration $c(x, t)$. The former obeys the Keller-Segel equation, defined in Sec. 1.3 as

$$\frac{\partial \rho}{\partial t} = D \nabla^2 \rho - \nabla \cdot (\mathcal{V}[c] \rho) \quad (3.1)$$

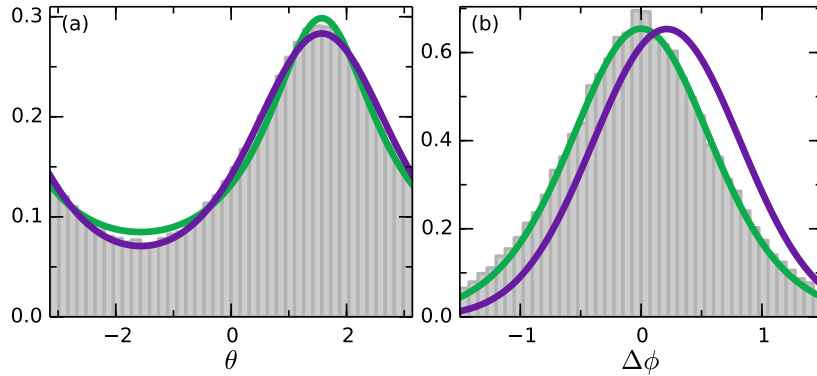


Figure 3.6 Angle statistics for swimming colonies. Experimental data in grey bars. Deterministic model in purple and stochastic in green. (a) Distribution of θ . $\theta = \pi/2$ is along the gradient. (b) Change in angle $\Delta\phi$ for $\Delta t = 0.65$ s. Positive change corresponds to a turn towards the gradient. Deterministic parameters: $\varepsilon_d = 0.28 \text{ s}^{-1}$, $d_r = 0.52 \text{ s}^{-1}$. Stochastic parameters: $\varepsilon_s = 0.55$, $d_r = 0.33 \text{ s}^{-1}$.

and the latter follows the diffusion equation,

$$\frac{\partial c}{\partial t} = \nabla \cdot (D_c \nabla c). \quad (3.2)$$

The functional \mathcal{V} specifies the population drift velocity's dependency on the local oxygen concentration, i. e. the drift of cells due to taxis. For a fixed response, the functional would equal a constant $\mathcal{V} = v_{\text{drift}}$. D and $D_c(x)$ are the colony and oxygen diffusion constants, the latter of which varies with position inside the microfluidic device, with values $D_{c,\text{PDMS}} = 3.55 \times 10^{-3} \text{ mm}^2/\text{s}$ in PDMS (Cox, 1986) and $D_{c,\text{water}} = 2.10 \times 10^{-3} \text{ mm}^2/\text{s}$ in water (Cussler, 2009).

Using the method described in Appendix 3.C, we solve Eq. (3.2) on a cross-section of the microfluidic device with time dependent boundary conditions corresponding to the experimental protocols. Gas channels with oxygen flowing have the condition $c = 20\%$ (for theory the unit of oxygen is not important and we find percentage to be the most intuitive measure). For channels with nitrogen flowing $c = 0$. Glass interfaces have no-flux conditions $\hat{n} \cdot \nabla c = 0$, where \hat{n} is the surface normal.

A snapshot from the numerical studies is shown in Fig. 3.7a at a time following a swap of nitrogen and oxygen channels, thus showing residual oxygen above the channels now filled with nitrogen and vice versa. The simulation can now be evaluated at the position of the observation chamber. Note that the no-flux conditions at the glass interface render the concentration gradients in the z -direction very small, so the precise height of evaluation is not significant. The simulation with boundary conditions corresponding to those in

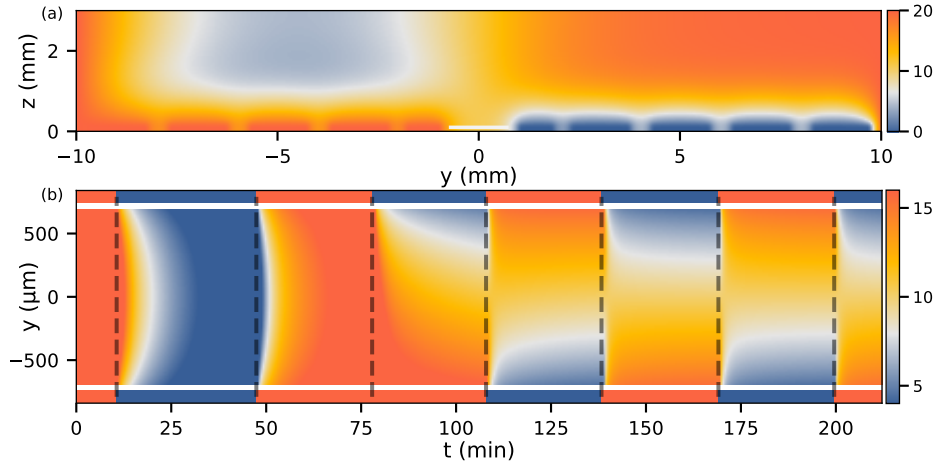


Figure 3.7 Simulation of oxygen concentration in microfluidic device. (a) Simulation of 2D cross-section of the device. Oxygen concentration boundary conditions are imposed at the gas channel positions. Snapshot shows $t = 110$ min, ~ 1.5 min after the swap. White line (at $y = 0$, $z = 100\mu\text{m}$) indicates evaluation location at the observation chamber used in (b) and Fig 3.8. (b) Evolution of oxygen concentration at $z = 100\mu\text{m}$. The colour scales indicate oxygen concentration in percentages, 20 % corresponding to atmospheric air.

the experiment of Fig. 3.2c is shown in Fig. 3.7b. To a very good approximation the concentration field is constant along the x -direction. Fig. 3.8 shows the oxygen field evaluated at $y = -250\mu\text{m}$ (red curve). Neglecting the consumption of oxygen by the colonies, these results provide the input concentration field c for the Keller-Segel model.

The simplest and widely-used response functional in the Keller-Segel model is linear in spatial gradients, $\mathcal{V} = \beta \nabla c(x, t)$, where β is termed the *taxis coefficient*. This was discussed briefly in the introduction to this thesis. Such a response can, however, reach unrealistic drift velocities, i. e. higher than the swimming velocity, if the oxygen gradients are large. This defect can be eliminated by various functional forms (Tindall et al., 2008a), such as the choice

$$\mathcal{V}[c] = v_{\text{drift}} \tanh(\alpha |\nabla c|) \frac{\nabla c}{|\nabla c|}, \quad (3.3)$$

where v_{drift} must be smaller than the swimming velocity. This choice behaves linearly for small gradients, but tends asymptotically to a maximum value for large gradients. Most of the behaviour of Fig. 3.2c and 3.3a can be explained by this model, as shown in Fig. 3.3b, but not the section where nitrogen is flowing in both side channels. The reason is the aforementioned asymmetry between the sensing-signalling in low versus high oxygen concentrations, which we argued may be explained by relative gradient sensing, also known as logarithmic sensing since $\nabla \log c = \nabla c / c$.

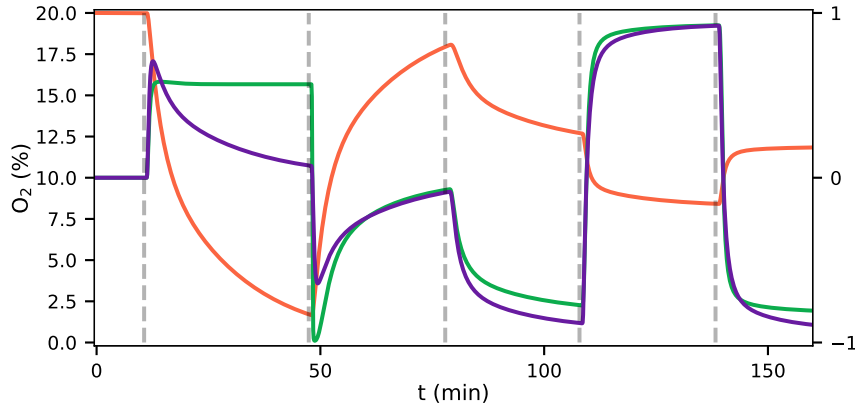


Figure 3.8 Simulation of oxygen concentration in microfluidic device. Simulation evaluated at $y = -250\ \mu\text{m}$. Oxygen percentage in red (left axis), and spatial gradient in purple normalised to fit in $[-1, 1]$ (right axis), response function $\tanh(\alpha \nabla c(x, t)/c(x, t))$ in green (right axis).

To examine quantitatively this hypothesis we consider

$$\mathcal{V}[c] = v_{\text{drift}} \tanh\left(\alpha \left| \frac{\nabla c}{c} \right| \right) \frac{\nabla c}{|\nabla c|}. \quad (3.4)$$

For unidirectional gradients (say, in the y -direction) this expression reduces to $\mathcal{V}[c] = v_{\text{drift}} \tanh(\alpha c_y/c) \hat{y}$, where $c_y = \partial c/\partial y$. Since the logarithmic sensing cannot be maintained at infinitely small concentrations, there must naturally be some lower cutoff to this expression in absolute concentration levels. Nonetheless, from a modelling perspective we can ignore this for the present experiments with nitrogen-only sections lasting less than 1.5 hours as discussed. Fig. 3.8 shows that the spatial oxygen gradient c_y (purple curve) compares to $\hat{y} \cdot \mathcal{V}[c]$ of Eq. (3.4) (green curve) at all times except in the nitrogen-only section, where the log-response function does not decay towards zero. A positive value of the response function means a positive (y) drift velocity.

The Keller-Segel equation with log-sensing is able to explain all sections of the experiment, as demonstrated in Figure 3.2d and 3.3c. The parameters obtained from a numerical fit include the drift velocity $v_{\text{drift}} = 5.2\ \mu\text{m/s}$ (which should be compared to the ensemble average swimming speed $v = 16.5\ \mu\text{m/s}$, the speed averaged over all colonies) and the diffusion constant $D = 865\ \mu\text{m}^2/\text{s}$. Using the ensemble-averaged speed, the diffusion constant can be related to an effective rotational diffusion constant $D_r = v^2/2D = 0.16\ \text{s}^{-1}$.

The parameter v_{drift} represents the coupling between the oxygen-gradient response and the resulting population drift, but it is a purely phenomenological quantity in which the underlying microscopic mechanism of aerotaxis is hidden. To explain the origin of v_{drift} we must consider the navigation strategy.

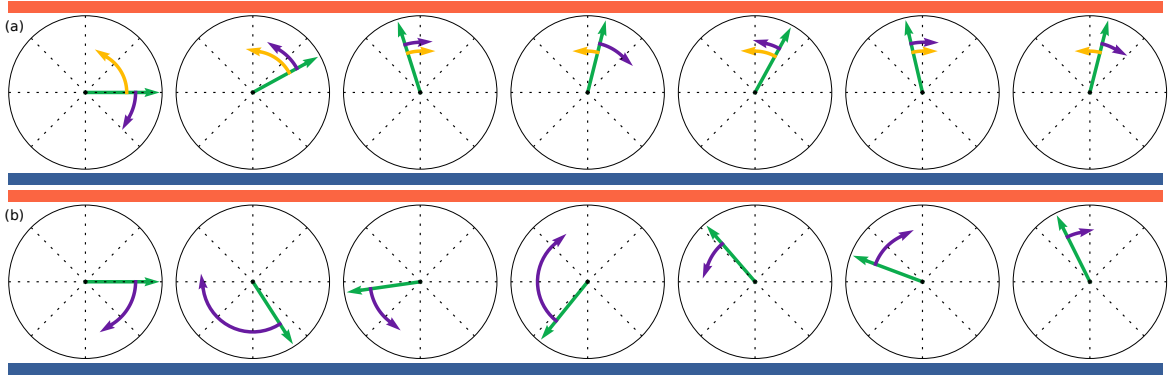


Figure 3.9 Illustration of deterministic and stochastic strategies based on discretised simulations with exaggerated steps. Time evolves from left to right. Orientations, shown by green arrows, are trying to align to up-motion, $\theta = \pi/2$, indicated by red (oxygen) at the top and blue (nitrogen) at the bottom. (a): Deterministic strategy, described by Eq. (3.6). Deterministic part in yellow and stochastic part in purple. The deterministic part is always in the correct direction. (b): Stochastic strategies, described by Eq. (3.7). All steps are stochastic, but largest when furthest away from $\theta = \pi/2$.

To distinguish deterministic and stochastic strategies we introduce two effective models and in the following consider them in the context of a constant oxygen gradient along the y -axis, but the generalisation is immediate. We furthermore ignore translational diffusion due to thermal noise, since this contribution is orders of magnitude smaller than that of active diffusion. Thus in a quasi-2D system, an organism's path is described by

$$dx = \begin{pmatrix} \cos \theta(t) \\ \sin \theta(t) \end{pmatrix} v dt, \quad (3.5)$$

where θ is the instantaneous swimming direction, and we choose motion along the positive y -axis ($\theta = \pi/2$) to be toward the attractant.

In the deterministic model, the organisms actively steer towards the gradient. We model this with the Langevin equation

$$d\theta = \varepsilon_d \cos \theta dt + \sqrt{2d_r} dW(t), \quad (3.6)$$

where $W(t)$ is a Wiener process for which $\langle dW(t) dW(t') \rangle = \delta(t - t')$. This process is illustrated in Fig. 3.9a, yellow arrows showing $\varepsilon_d \cos \theta \Delta t$ and purple arrows $\sqrt{2d_r} \Delta W$. For the stochastic model we take a 'continuous' version of run-and-tumble, in which the rotational diffusion is modulated,

$$d\theta = \sqrt{2d_r(1 - \varepsilon_s \sin \theta)} dW(t), \quad (3.7)$$

where $-1 \leq \varepsilon_s \leq 1$ and the multiplicative noise is interpreted in the Itô sense. This process is illustrated in Fig. 3.9b. In both models, ε is an effective ensemble average response. To compare to the experiments, ε should be replaced by a function coupled to the gas concentration field through $\mathcal{V}[c]$, thus coupling to Eq. (3.5). The steady state gradient in the experiment is approximately linear, and thus as a first approximation Eqs. (3.6, 3.7) should describe the angle statistics in the time between the swap of gas channels and reaching the opposite side.

In our experiments, after a flip in the oxygen gradient direction, the colonies reach the opposite wall in a time comparable to that for oxygen to diffuse across the chamber. Thus, a true steady state is not reached, but during the intermediate times a steady state approximation is fair. Solving the Fokker-Planck equations corresponding to the systems Eq. (3.6) and (3.7) in steady-state, we obtain theoretical angle distributions (see Appendix 3.B). Both models are able to describe the data in Fig. 3.6a well, with the deterministic model (purple) fitting the down-gradient swimming best, and the stochastic model (green) fitting the up-gradient swimming best. Both fits involve a single parameter, $k_d = \varepsilon_d / \sqrt{2d_r}$ in the deterministic model and ε_s in the stochastic one.

We now move beyond steady-state distributions to examine the detailed statistics of the trajectories themselves. We recall our definition of the angle turned by a colony in a time Δt as $\Delta\phi = |\theta(t + \Delta t) - \pi/2| - |\theta(t) - \pi/2|$ such that it is positive if the turn is in the direction of the gradient and negative otherwise. The equations (3.6) and (3.7) imply distributions of $\Delta\phi$ (see Appendix 3.B). Figure 3.6b shows the best fit of both models to the data. For the stochastic model (green) ε_s is known and the fit is in d_r and matches well. The deterministic (purple) is constrained by $k_d = \varepsilon_d / \sqrt{2d_r}$, and the fit can be done in d_r as well. We see clearly that the deterministic model does not provide a satisfactory fit to the data. In detail, the value of ε_d needed to fit the data in Fig. 3.6a shifts the mean of $p_d(\Delta\phi)$ in the positive direction. This result persists with any amount of smoothing applied to the data, averaging out active rotations. We thus conclude that the colonies navigate by a stochastic strategy, and that the ensemble angle statistics can be captured by this simple model. We will develop a more detailed version of this model in Chapter 4, and evaluate how effective a navigation strategy it is.

The navigation strategy model must be consistent with the Keller-Segel population dynamics model. Having shown that the data favour a stochastic model, we may now couple Eq. (3.7) to Eq. (3.5) and let the Fokker-Planck equation (Appendix 3.B) replace the Keller-Segel model. Such an approach leads to similar results as Fig. 3.2d. Furthermore, we now recognise that the Keller-Segel model is a quasi-stationary approximation and we can

calculate the stationary-approximation drift velocity

$$v_{\text{drift}} = v \langle \sin \theta \rangle = v \left[1/\varepsilon_s - \sqrt{1/\varepsilon_s^2 - 1} \right]. \quad (3.8)$$

In other words $\varepsilon_s = (2 v v_{\text{drift}})/(v^2 + v_{\text{drift}}^2)$ is the ratio of the squared geometric mean to the quadratic mean of the average and drift velocities. For the fitted $\varepsilon_s = 0.55$, $v_{\text{drift}} \approx 0.3 v \approx 5 \mu\text{m/s}$, consistent with the fitted value in the Keller-Segel model.

3.6 Discussion

We have shown that colonies of *S. rosetta* can navigate along gradients of oxygen, thus exhibiting positive aerotaxis. The cells navigate along relative oxygen gradients and the navigation strategy is stochastic in nature, achieved by modulating not speed but direction of swimming.

The experimental observation that choanoflagellates are aerotactic raises a number of questions. One concerns the actual sensing mechanism, and how this compares to those of animals, given the close evolutionary relationship between choanoflagellates and metazoans. In animals, oxygen concentrations can be sensed by the highly-conserved hypoxia-inducible factor (HIF) transcription factor pathway (Kaelin and Ratcliffe, 2008; Loenarz et al., 2011; Rytkönen et al., 2011). At normal oxygen levels, the activity of specific prolyl-hydroxylase (PHD) enzymes labels the HIF protein complexes for degradation. At low oxygen levels, however, PHD activity is inhibited, leading to elevated HIF levels. The transcription factor activity of HIF up-regulates expression of genes involved in hypoxia response (e.g. glycolysis enzymes) for survival in low-oxygen conditions (Greer et al., 2012). The genes involved in HIF signalling are widespread in metazoans, with evidence suggesting that some components of this pathway are descended from prokaryotic ancestors (Scotti et al., 2014).

Preliminary experiments involving exposing *S. rosetta* cultures to DMOG (an inhibitor of the prolyl-hydroxylase step in the HIF pathway (Fong and Takeda, 2008)) had no observable effect on aerotaxis within our experimental system. This was the case for both short- and long-term exposure. In hindsight, this is perhaps unsurprising, given that choanoflagellates lack some important components of the HIF pathway (Rytkönen et al., 2011). Additionally, the aerotactic response observed here is acute, within a timeframe on the order of seconds to minutes, rather than the being a longer-term response to lowered oxygen levels by modulation of gene expression. In certain aerotactic bacteria, it is known that oxygen concentrations are measured indirectly via energy-sensing, which can then influence the rotation of the bacterial flagella between running and tumbling (Taylor et al., 1999). An analogous mechanism may

be at play in choanoflagellates, possibly via reactive oxygen species (Cash et al., 2007) and oxygen-sensitive ion channels (Lahiri et al., 2006; Ward, 2008) modulating the beating shape or rate of the flagella of each *S. rosetta* cell. Thus the question of the molecular and cellular mechanisms underpinning aerotaxis in choanoflagellates is a promising avenue for further research.

Oxygen is implicated as having an important influence on animal evolution (Lenton et al., 2014; Nursall, 1959), with some hypotheses that the emergence of complex animal ecosystems (Sperling et al., 2013) were only triggered when oxygen levels rose above certain thresholds. Sponges, believed to be the most basal animal group, were recently shown to have very low oxygen requirements, disputing the importance of oxygen in early animal evolution (Mills et al., 2014). Our results raise the possibility that the common ancestor from which choanoflagellates and animals evolved was aerotactic, and that oxygen sensing and responding has thus been under strong selection throughout the holozoans. If the ancestors of animals and choanoflagellates were strongly aerotactic, this would be indicative of the importance of oxygen as a resource during the Precambrian (Lyons et al., 2014). Equally, it could be the case that choanoflagellates themselves have evolved aerotaxis after the split from the animal stem lineage. To answer this question, the oxygen requirements and aerotactic capabilities of other opisthokont groups, e.g. ichthyosporeans, filasterians (Ruiz-Trillo et al., 2008; Sebé-Pedrós et al., 2013), as well as basal animals such as sponges, ctenophores and placozoans (Dunn et al., 2008; Pisani et al., 2015; Ryan et al., 2013; Whelan et al., 2015), requires investigation. Such an analysis can be further complimented by determining the oxygen sensing and signalling mechanisms across the opisthokont phylogeny.

If aerotaxis was key to the ancestral unicellular holozoan, it is crucial that the evolution to multicellularity did not hinder this ability. The experimental results of this chapter show that both the unicellular and colonial morphotypes of *S. rosetta* can perform efficient aerotaxis and navigation in general, despite lacking coordination between the constituent cells of the colony. Therefore, an evolutionary transition to a multicellularity resembling the unicellular-to-colonial transition in *S. rosetta* (Dayel et al., 2011) would not require additional cell-cell communication mechanisms to coordinate navigation. Not only would this allow aerotaxis towards oxygen, but also taxis in response to other stimulants, such as bacterial signals (Woznica et al., 2016). This is a particular feature of the stochastic navigation strategy, which works equally well for both single cells and colonies formed from multiple units of the same cells.

Other systems of multicellular chemotaxis exist. For instance, cell-cell communication can enhance chemotactic ability (Ellison et al., 2016; Varennes et al., 2016), since cells can “calculate” the gradient over larger distances via communication which can reduce the error

(see e. g. calculation in Appendix 4.F on the role of shape). Multicellular chemotaxis can also be emergent (Varenes et al., 2017). Consider for instance, a type of cell that modulates its swimming speed based on the local concentration $c(x)$, i. e. not based on the gradient. Alone this type of cell will not chemotax. However, if one ties such cells together in a clump, even though individually they are only reacting to local concentration, overall the clump will have a speed that is proportional to the gradient. Such methods can be quite efficient (Varenes et al., 2017).

Here, we have described the stochastic strategy of *S. rosetta* in terms of an effective model. The effective bias parameter ε_s is the result of flagella modulation. As demonstrated in the previous chapter, flagella can be imaged on colonies stuck to the microscope slide, but measuring directly the flagella modulation proved challenging, since the oxygen changes that can be induced in a microfluidic device are on a time scale of minutes, whereas the flagella beating is on a time scale of tens of milliseconds. In such experiments, we did not observe modulations that surpassed the noise and did not pursue this further. The swimming trajectories suggest that the modulation is a mixture of many types, ranging from slow to vigorous, as also seen in other organisms (Jikeli et al., 2015), but direct imaging is needed to make more quantitative statements.

We have shown that in spatio-temporal varying environments, considerations of population dynamics can distinguish between linear- and logarithmic-sensing mechanisms, and concluded that choanoflagellates do logarithmic sensing. The fact that conclusions of logarithmic sensing can be made from analysis of the population dynamics alone shows that individual tracks are not needed and thus allows for such analysis in dense experiments. Logarithmic sensing is a key attribute for survival: it allows sensing of and reacting to gradients in very low concentration environments, while still being able to effectively navigate along large gradients. Logarithmic sensing has also been experimentally observed for other species, e. g. bacteria (Kalinin et al., 2009; Mesibov et al., 1973).

With logarithmic sensing, cells only navigate along oxygen gradients that are significant compared to the absolute concentration. This is a well-known phenomenon also from human behaviour, where, for instance, dim lights are seen only when it is dark and weak sounds heard only when it is quiet. It is known as Weber's law (Weber, 1834), which states that the magnitude of just-noticeable differences of a stimuli is proportional to the stimuli magnitude itself. This is closely related to Weber-Fechner law, stating that stimuli magnitude grows logarithmically with the actual signal, which we have found to be in agreement with the experimental observation of *S. rosetta* aerotaxis.

For microorganisms, a Weber lower limit can be understood, at least partly, as a physical limitation. Because of thermal fluctuations, the error on any concentration gradient measure-

ment increases with the local absolute concentration (Berg and Purcell, 1977; Endres and Wingreen, 2008), and thus it immediately follows that the limit of just-noticeable gradients must decrease with absolute concentration. Quantitatively, the noise scales as $\sim c^{1/2}$ in the absolute concentration (Endres and Wingreen, 2008). Such a scaling is not observed for bacteria's just-noticeable limits, where instead Weber's law hold (Mesibov et al., 1973). Sensor adaptation enables the bacteria to have the linear scaling $\sim c$ (Sourjik and Wingreen, 2012) leading to logarithmic sensing and high dynamic range, but it is nonetheless the case that for purely physical reasons a lower limit scaling with concentration must be present. The fitting of the Keller-Segel model to the population data were optimal precisely for relative gradient sensing. Sensing functionals such as $\nabla c/\sqrt{c}$ or $\nabla c/c^2$ only decreased the fit quality. This implies that Weber's law and logarithmic sensing, at least to a good approximation, is occurring in choanoflagellates. This scaling could be further studied by measuring the aerotactic response to an order-of-magnitude range of concentration gradients under a range of absolute concentrations. Precision control of gas mixtures would allow the extraction of any biological deviations from Weber's law and potentially reveal a transition to the physical limit of \sqrt{c} scaling for very low concentrations, i. e. at the limit of sensing.

Appendix 3.A Data Processing

Tracks were obtained using the method described in Appendix A.3. This method yields an $x(t)$ and $y(t)$ for each colony. Density distributions were then estimated by kernel density estimation, while taking care of boundaries. We first calculate

$$\eta(y) = \frac{\sum_i \exp(-(y_i - y)^2/2\sigma^2)}{\int_{y_0}^{y_1} \exp(-(y' - y)^2/2\sigma^2) dy'}, \quad (3.9)$$

where y_i are the tracked positions, σ a standard deviation of separation, and the denominator adjusts for boundary effects. Hereafter $\rho(y) = \eta(y)/\int_{y_0}^{y_1} \eta(y') dy'$ is the normalised density. This method (without boundary adjustments) was also used in Sec. 2.4, as well as its immediate generalisation to higher dimensions (using k -d trees).

For velocity and angle statistics, the tracked positions were linked solely by proximity. If the image analysis algorithm failed to identify a given colony over fewer than three successive frames the integrity of the track was preserved by keeping a running memory. After the trajectories were obtained, spurious trajectories less than three frames in length were removed. Examples of trajectories are shown in Fig. 3.4. The final tracks contain ~ 150 trajectories in each frame, varying slightly over the course of the experiment due to loss of colonies in the tracking and swimming in and out of observation chamber.

Appendix 3.B Effective Stochastic Models

Given the stochastic dynamics (3.6) for individual particles following a deterministic strategy, the probability distribution function $p_d(\theta, t)$ for the population obeys the Fokker-Planck equation

$$\frac{\partial p_d}{\partial t} = d_r \frac{\partial^2 p_d}{\partial \theta^2} - \varepsilon_d \frac{\partial}{\partial \theta} (\cos(\theta) p_d). \quad (3.10)$$

The steady state distribution is found to be a von-Mises distribution

$$p_d(\theta) = \frac{1}{2\pi I_0(\varepsilon_d/\sqrt{2d_r})} \exp\left(\frac{\varepsilon_d \sin \theta}{\sqrt{2d_r}}\right), \quad (3.11)$$

where I_0 is the modified Bessel function of order zero. On the other hand, for the Fokker-Planck equation for the stochastic model,

$$\frac{\partial p_s}{\partial t} = \frac{\partial^2}{\partial \theta^2} (d_r(1 - \varepsilon_s \sin \theta) p_s), \quad (3.12)$$

we find the steady-state distribution

$$p_s(\theta) = \frac{1}{2\pi} \frac{\sqrt{1 - \varepsilon_s^2}}{1 - \varepsilon_s \sin \theta}. \quad (3.13)$$

In the time right before a channel swap, we have $p(\theta) \approx 1/2\pi$, since the colonies stay near the wall. In the deterministic model, for small Δt , $\Delta\phi = |\theta(t + \Delta t) - \pi/2| - |\theta(t) - \pi/2|$ is composed of deterministic $\delta = \varepsilon_d \cos(\theta)\Delta t$ and stochastic $\xi = \sqrt{2d_r}\Delta W$, where $\Delta W \sim \sqrt{\Delta t}$. Since we are assuming $p(\theta) = 1/2\pi$, we have $p(\delta) = 1/\pi\sqrt{(\varepsilon_d\Delta t)^2 - \delta^2}$ for $\delta \in [-\varepsilon_d\Delta t; \varepsilon_d\Delta t]$. The distribution of $\Delta\phi = |\delta| + \xi$ is then found as the convolution

$$p_d(\Delta\phi) = \int_0^{\varepsilon_d\Delta t} \frac{\exp(-(\Delta\phi - \delta)^2/4d_r\Delta t)}{\sqrt{\pi^3 d_r\Delta t [(\varepsilon_d\Delta t)^2 - \delta^2]}} d\delta, \quad (3.14)$$

which can be evaluated numerically by Gaussian quadrature. In the stochastic model there is only $\xi = \sqrt{2d_r(1 - \varepsilon_s \sin \theta)}\Delta W$, but this is conditional on θ . We marginalise for the final distribution

$$p_s(\Delta\phi) = \int_{-\pi}^{\pi} \frac{\exp(-\Delta\phi^2/4d_r(1 - \varepsilon_s \sin \theta)\Delta t)}{\sqrt{16\pi^3 d_r(1 - \varepsilon_s \sin \theta)\Delta t}} d\theta. \quad (3.15)$$

Appendix 3.C Implicit Time-Stepping for PDEs

Consider the linear PDE

$$\frac{\partial p(t,x)}{\partial t} = \mathcal{A}(x)p(t,x) \quad (3.16)$$

where \mathcal{A} is some differential operator. Using some discretisation, the operator \mathcal{A} becomes an $n \times n$ matrix A and p a vector p . For solving the diffusion equation and Keller-Segel model in this Chapter, we used finite difference. With implicit time stepping,

$$\frac{p(t + \Delta t) - p(t)}{\Delta t} = A \cdot p(t + \Delta t). \quad (3.17)$$

Boundary conditions, be they Dirichlet or Neumann (we have both in the diffusion equation system) can be written as

$$B \cdot p = b, \quad (3.18)$$

where B is an $b \times n$ matrix, b being the number of boundary conditions and n the number of points. For each boundary condition, a corresponding point is chosen. The vector p is then reordered such that these are the last b entries, and A and B are permuted similarly. We now need to solve for the remaining $r = n - b$ points. Eq. (3.17) becomes

$$\left[\frac{1}{\Delta t} - \begin{pmatrix} A_{rr} & A_{rb} \\ A_{br} & A_{bb} \end{pmatrix} \right] \cdot \begin{pmatrix} p_r(t + \Delta t) \\ p_b(t + \Delta t) \end{pmatrix} = \frac{1}{\Delta t} \cdot \begin{pmatrix} p_r(t) \\ p_b(t) \end{pmatrix} \quad (3.19)$$

The first r equations for $p_r(t + \Delta t)$ are

$$\left[\frac{1}{\Delta t} - A_{rr} \right] \cdot p_r(t + \Delta t) - A_{rb} \cdot p_b(t + \Delta t) = \frac{p_r(t)}{\Delta t}, \quad (3.20)$$

but from Eq. (3.18) we have $p_b = B_b^{-1}(b - B_r p_r)$, finally giving

$$\left(\frac{1}{\Delta t} - A_{rr} + A_{rb} B_b^{-1} B_r \right) \cdot p_r(t + \Delta t) = \frac{p_r(t)}{\Delta t} + A_{rb} B_b^{-1} b \quad (3.21)$$

which is precisely r equations for r unknowns.

This can be done similarly for the Crank-Nicolson scheme,

$$\frac{p(t + \Delta t, x) - p(t, x)}{\Delta t} = \frac{1}{2} [\mathcal{A}(x)p(t + \Delta t, x) + \mathcal{A}(x)p(t, x)], \quad (3.22)$$

i. e. on

$$\left(\frac{1}{\Delta t} - \frac{A}{2}\right) p(t + \Delta t) = \left(\frac{1}{\Delta t} + \frac{A}{2}\right) p(t). \quad (3.23)$$

Chapter 4

Chemotactic Efficiency

4.1 Introduction

Run-and-tumble motion is comprised of approximately straight lines (runs) interrupted by reorientation events (tumbles), as described in Sec. 1.2 and as shown in Fig. 4.1. For example, in peritrichous bacteria, the helical flagella rotate counter-clockwise and form a coherent bundle during swimming. A tumble is induced when (some of) the flagella reverse their rotational direction and the bundle is disrupted [Fig. 4.1a]. This creates a large, transient, reorientation. Navigation along a gradient of chemoattractant becomes possible if the frequency of tumbling is biased in response to the chemoattractant distribution. This is a type of *stochastic* navigation in the sense that the organisms that perform it do not swim directly in the desired direction, but rather in a random direction and later decide whether such a turn was correct.

The tumbling frequency is modulated through measurements of the variation in concentration of chemoattractants, illustrated by the background of Fig. 4.2. In an idealised scenario, the reorienting tumbles result in unbiased new directions, uniformly chosen from the unit sphere, but this is not typically the case. Instead, a persistence with the previous direction is present (Berg and Brown, 1972). As discussed in Chapter 3, in choanoflagellates the individual reorientations are so small that they are hardly observable. These reorientation events may simply arise from slight modulation of the beating of a single flagellum [Fig. 4.1b]. These smaller tumbles, or directionally persistent tumbles, add up to a smoother swimming while still allowing navigation. Fig. 4.2 shows two realisations of run-and-tumble swimming. In blue is the case of full-reorientation tumbles and in red is very persistent tumbles occurring with higher frequency. Over long time-scales both of these swimmers perform random walks biased in the direction of the chemoattractant signal.

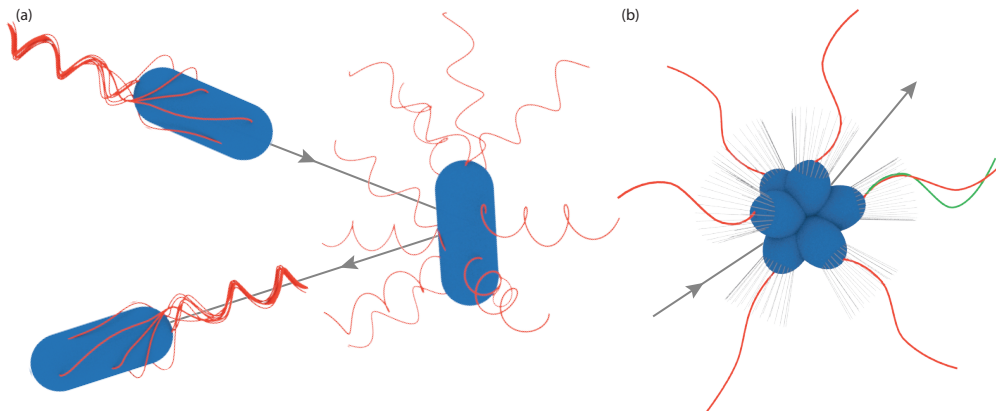


Figure 4.1 Run-and-tumble. (a) Swimming and tumbling of a peritrichous bacterium. During swimming the flagella rotate counter-clockwise and form a bundle resulting in a run. Clockwise rotation one or more of the flagella breaks the bundle and results in a tumble that reorients the cell. (b) Choanoflagellate colony reorientation event. Each cell's flagellum beats independently of the others. A change in the beating dynamics of one cell (green flagellum) can cause a small reorientation of the colony as a whole.

A strong theoretical understanding of chemotaxis exists (Tindall et al., 2012, 2008a,b), including the filtering of chemoattractant signals to which the cells react (Celani and Vergassola, 2010; Segall et al., 1986), the fundamental limits of measurement accuracy of such signals (Mora and Wingreen, 2010) and the limits they impose on navigation (Hein et al., 2016). Theories of chemotaxis are typically developed in the weak-chemotaxis limit (Celani and Vergassola, 2010; Locsei, 2007; Locsei and Pedley, 2009; Mortimer et al., 2011; Reneaux and Gopalakrishnan, 2010), the linear theory of which provides accurate explanations of many experimental observations. Theory (Locsei, 2007) and simulation (Nicolau et al., 2009) of chemotactic bacteria have also showed that for otherwise equal chemotactic parameters, directional persistence of tumbles, as observed in experiments, can lead to enhanced chemotaxis.

This raises a more general question: could the effect of changing one parameter, such as directional persistence, be compensated by simultaneously changing another? In this chapter, we address this question of global optimality, and examine effects that lead to the existence of optima. For example, in linearised theories, the drift velocities for large chemotactic strength and for steep gradients can become unbounded, and thus the evaluation of one effect is done at fixed chemotactic response. But microorganisms do not have the restrictions that come with choosing theories that are analytically tractable. In real systems, the drift velocity will be limited (trivially) due to the finite swimming speed of the organisms and (more importantly) by uncertainties of measurements in noisy environments combined with

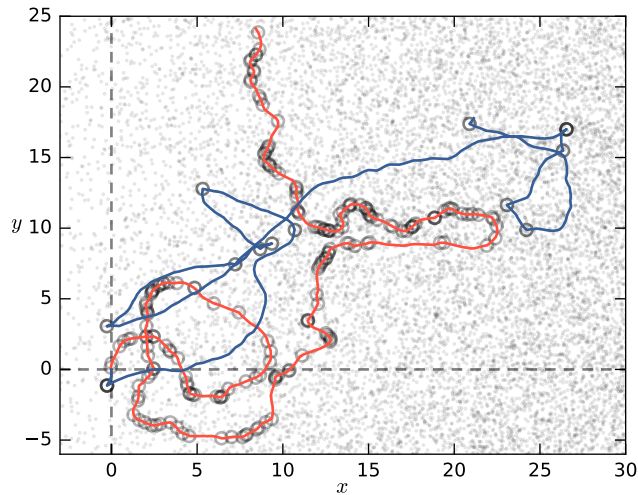


Figure 4.2 Run-and-tumble trajectories. Both simulated trajectories drift to the right, starting from the origin. Full tumbles are shown in blue ($k = 0$, $\lambda_0 = 0.1$) and persistent but frequent tumbles in red ($k = 10$, $\lambda_0 = 2.0$). Circles indicate tumbles. Shared parameters: $D_r = 0.1$, $\beta = 1/2$, $\gamma = 1$.

diffusion. Throughout this chapter we optimise for the performance of a single organism, neglecting population effects (Peaudecerf and Goldstein, 2015).

4.2 Model

The model of chemotaxis used here assumes that organisms determine concentration gradients by comparing their concentration measurements at different times as they move through the medium, rather than detecting gradients over their own body, as is possible for organisms considerably larger than bacteria (Berg and Purcell, 1977). We show in Appendix 4.F how sensing over the body length induces an error, similar to that presented in Berg and Purcell (1977), but in two dimensions as pursued here.

To be precise, we assume that as a cell swims it measures only the local chemoattractant concentration $c(x, t)$ at its present position x . Moreover, in this section the concentration is taken to be linear in position, $c(x) = c_0 + \alpha x$, allowing the notation $c(t) = c(x(t))$ for a given trajectory $x(t)$. Cells are thought to store the history of these measurements, and use this to bias their tumbling frequency λ . In the present model, this is embodied by the relationship $\lambda = \lambda_0 [1 + q]$, where $[\cdot] = \max(0, \cdot)$. Here, q is the biaser, determined by a linear convolution of c ,

$$q(t) = \int_0^\infty c(t - t') \kappa(t') dt'. \quad (4.1)$$

We take the kernel to be one studied previously and which corresponds well to experimental measurements (Celani and Vergassola, 2010; Segall et al., 1986),

$$\kappa(t) = \frac{\beta\gamma^2}{\alpha v} e^{-\gamma t} \left[\frac{(\gamma t)^2}{2} - \gamma t \right], \quad (4.2)$$

where v is the swimming speed and γ^{-1} is the memory time scale of past measurements. The normalisation is chosen such that $\max |q| = \beta$ in the absence of noise, and hence β solely specifies the chemotactic strength. The kernel satisfies $\int k(t) dt = 0$ which gives perfect adaptation to any background chemoattractant concentration. This criteria arises naturally from maximising the minimum chemotactic efficiency over all chemoattractant profiles (Celani and Vergassola, 2010). In particular, this is an important feature that will not arise from maximising drift velocity alone and which we thus impose *a priori* here.

We consider cells swimming in two dimensions in an instantaneous direction $\theta(t)$ with velocity v , and discuss the three-dimensional case in Appendix 4.C. This direction is modulated by both rotational diffusion as $d\theta = \sqrt{2D_r} dW$, where W again is a standard Wiener process, and by tumbles, the size of which are chosen from a von-Mises distribution with parameter k ,

$$p(\Delta\theta) = \frac{1}{2\pi I_0(k)} \exp(k \cos(\Delta\theta)), \quad (4.3)$$

where I_n are the modified Bessel functions of the first kind. Thus k specifies the persistence of the tumbles, $k = 0$ corresponding to full tumbles.

4.3 Measurement Time-scale

If the time $1/\lambda_0$ between tumbles is too long compared to the rotational diffusion time $1/D_r$, the trajectories will be reoriented by rotational diffusion and the organism will have lost the ability to bias its motion in any useful way. Thus, the biasing of tumbles must outcompete rotational diffusion and we expect $\lambda_0 \gtrsim D_r$. In the absence of measurement noise, and if the organism can make instantaneous measurements ($\gamma \rightarrow \infty$), increasing the chemotactic strength will monotonically increase the chemotactic drift, and in the limit $\beta \rightarrow \infty$ chemotaxis becomes perfect, despite the hindering effects of rotational diffusion. But, we emphasise that this is only possible in the absence of measurement noise. Here, in contrast, we are interested in the noise-limited situation, and with noise comes another time scale, that over which accurate measurements can be made (see Appendix 4.E for a simple lattice calculation illustrating this point).

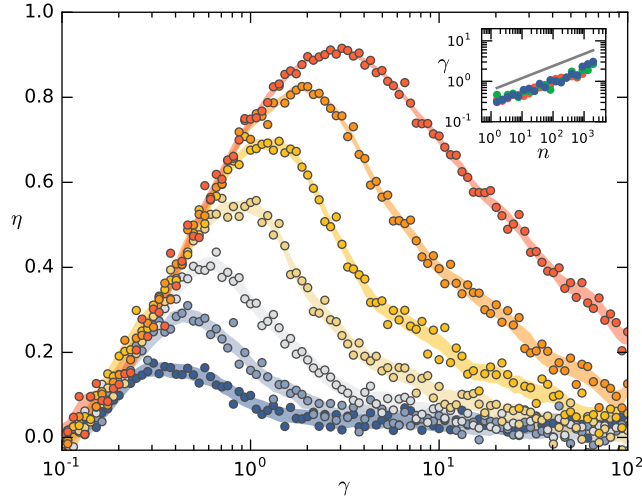


Figure 4.3 Chemotactic efficiency as a function of γ . Each curve corresponds to different concentration levels; at the lowest concentration (blue data) each cell senses on average $n \sim 1.5$ molecules, while at the highest (red), $n \sim 2000$ are sensed. Shaded background indicates standard error of the simulations. Inset shows optimal γ as a function of n for $\lambda_0 \in \{0.1, 1.0, 5.0\}$. $D_r = 0.1$, $\gamma = 1$.

To illuminate this situation we perform simulations in which cells are placed in a constant gradient (linear increase) of discrete chemoattractants. In a periodic $2L \times 2L$ box, N molecules are placed, decreasing linearly in concentration from $x = 0$. This is achieved by choosing each molecule's position as $x = L\sqrt{|U_1|} \text{sign}(U_1)$, $y = LU_2$, where U_i is uniformly distributed on $[-1, 1]$. $c(t)$ is then defined to be the number of molecules within a cell's area. This can be evaluated efficiently by storing the molecules in a k -D tree, allowing for fast simulations with billions of molecules.

For the purposes of the present discussion, we define the chemotactic efficiency proportional to the average value of the concentration experienced by the organism in steady state

$$\eta \propto \langle c \rangle = \int c(x)P(x) dx, \quad (4.4)$$

where $P(x)$ is the steady-state probability distribution. The normalisation is chosen such that $\eta = 1$ corresponds to perfect chemotaxis.

Fig. 4.3 shows η as function of the measurement rate γ for various molecular concentrations. The curves clearly reveal the existence of an optimal γ for each choice of the (average) number of molecules sensed. Choosing γ too low means slow reaction, but with γ too high the organism does not have time to make an accurate measurement before previous information is forgotten. Varying the chemoattractant concentration (but not the gradient) shifts the optimal γ . At higher concentrations, the measurement noise is lower (Mora and Wingreen, 2010),

and thus less time is needed to make an accurate measurement. The inset of Fig. 4.3 shows how the optimal γ varies with the concentration, and further shows that, within the resolution of our simulations, this optimum is independent of the base tumbling frequency λ_0 . This independence means that we can fix γ to its optimal value without specifying the value of λ_0 .

In this noise-dominated regime, γ is thus set by the chemoattractant concentration. If cells are kept in a chemostat with fixed concentration and gradient, as is the case considered here, the optimal γ is thus indicative of the underlying noise levels. In the following sections we fix γ , thus implicitly defining the noise levels. The goal then becomes to find the optimal choice of the remaining parameters for a given γ . Our approach ignores spatial variations in noise, but conclusions made are confirmed by checking them against the full simulation setup used in this section.

4.4 Tumbling Frequency & Persistence

In earlier theoretical work, persistence of tumbles has been shown to enhance the chemotactic drift velocity (Locsei, 2007; Nicolau et al., 2009). Possible rationalisations for this effect include the idea of information relevance; for persistent tumbles, the gradient information (stored in q , Eq. 4.1) remains more relevant than for full tumbles, where a completely random direction is chosen. It has also been shown that an optimum base tumbling frequency λ_0 exists (Celani and Vergassola, 2010). Intuitively, in the low-noise limit, this optimum should be set by the rotational diffusion constant D_r , in order to dominate rotational diffusion but not hinder drift. Intuitively, one expects that introducing persistence, which results in smaller angular deflections from tumbles, would shift the optimal tumble frequency to higher values. So while it is clear that persistence can increase the chemotactic drift for a given base tumble frequency, it is not clear what the effect is if variations in λ_0 are also allowed.

To study this, we simulated cells performing chemotaxis in a constant gradient for various persistence parameters k , while varying λ_0 . The results shown in Fig. 4.4 confirm the intuition outlined above; for large base tumbling frequency λ_0 , increasing the persistence k leads to increased chemotactic drift, as previously found. However, for low values of λ_0 the opposite effect is found. There is thus a trade-off between frequency and persistence of tumbles.

To gain further insight we study the relevant Fokker-Planck equation. As shown previously (Celani and Vergassola, 2010), the dynamics of the biaser q can be made Markovian by introducing three internal variables (moments of c)

$$m_j = \int_{-\infty}^t e^{-\gamma(t-t')} (t-t')^j c(t') dt', \quad (4.5)$$

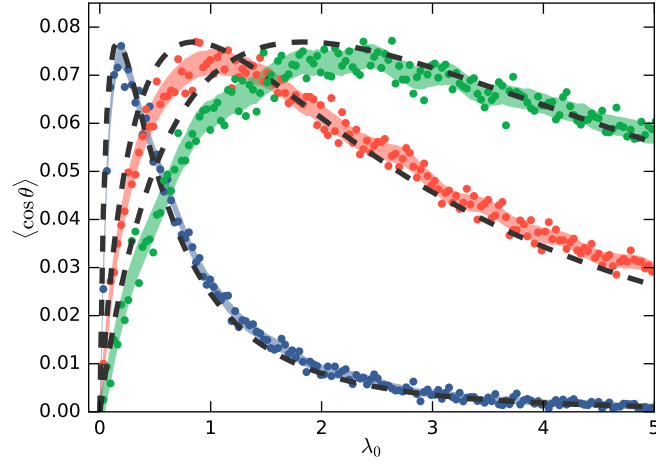


Figure 4.4 Drift efficiency as a function of tumble frequency. Data from direct simulation of full model are shown for $k = 0$ (blue), $k = 3$ (red), and $k = 6$ (green). Each data point is the result of 10,000 simulations and shaded background indicates standard error, with $D_r = 0.1$, $\beta = 1/2$, $\gamma = 1$. Linearised theory is indicated by dashed lines.

which obey a coupled system of differential equations $\partial_t m_j = c(t)\delta_{j0} - \gamma m_j + j m_{j-1}$. It follows that our system can be fully described by a Fokker-Planck equation for a distribution function $P(x, \theta, \{m_j\}, t)$

$$\begin{aligned} \frac{\partial P}{\partial t} + v \cos \theta \frac{\partial P}{\partial x} = & D_r \frac{\partial^2 P}{\partial \theta^2} + \lambda_0 [1 + q(t)] \left[\int \frac{e^{k \cos(\theta - \theta')}}{2\pi I_0(k)} P(\theta') d\theta' - P \right] \\ & - \sum_j \partial_{m_j} [\delta_{j,0} c(x) + j m_{j-1} - \gamma m_j] P, \end{aligned} \quad (4.6)$$

where

$$q(t) = \frac{\beta \gamma^2}{\alpha v} \left(\frac{1}{2} \gamma^2 m_2 - \gamma m_1 \right). \quad (4.7)$$

We begin by solving this system for small β . Later we will argue that our conclusions remain qualitatively correct also for large β . To find the drift $\langle \cos \theta \rangle$ linearised in β , we multiply Eq. (4.6) by $\cos \theta$, whereafter integration yields

$$\partial_t \langle \cos \theta \rangle = -D_r \langle \cos \theta \rangle - \lambda_0 \left(1 - \frac{I_1(k)}{I_0(k)} \right) (\langle \cos \theta \rangle + \langle q \cos \theta \rangle), \quad (4.8)$$

using

$$\int e^{k \cos(\theta - \theta')} \cos \theta d\theta = 2\pi I_1(k) \cos \theta'. \quad (4.9)$$

Since $q(t) = \frac{\beta\gamma^2}{\alpha v}(\gamma^2 m_2/2 - \gamma m_1)$ we continue, neglecting quadratic terms

$$\partial_t \langle m_0 \cos \theta \rangle = -(D_r + \lambda_k + \gamma) \langle m_0 \cos \theta \rangle + \alpha \langle x \cos \theta \rangle, \quad (4.10a)$$

$$\partial_t \langle m_1 \cos \theta \rangle = -(D_r + \lambda_k + \gamma) \langle m_1 \cos \theta \rangle + \langle m_0 \cos \theta \rangle, \quad (4.10b)$$

$$\partial_t \langle m_2 \cos \theta \rangle = -(D_r + \lambda_k + \gamma) \langle m_2 \cos \theta \rangle + 2 \langle m_1 \cos \theta \rangle, \quad (4.10c)$$

$$\partial_t \langle x \cos \theta \rangle = \frac{v}{2} - (D_r + \lambda_k) \langle x \cos \theta \rangle. \quad (4.10d)$$

Solving these equations for the steady state, we find

$$\langle \cos \theta \rangle = \frac{\beta \gamma^3 \lambda_k}{2(D_r + \lambda_k)(D_r + \gamma + \lambda_k)^3} + \mathcal{O}(\beta^2), \quad (4.11)$$

where $\lambda_k = \lambda_0 [1 - I_1(k)/I_0(k)]$. Note that the only place λ_0 enters is through the quantity λ_k , which has the optimal value

$$\lambda_k^* = \frac{1}{3} \left(\sqrt{4D_r^2 + 3\gamma D_r} - D_r \right). \quad (4.12)$$

From this fact, we conclude that the trade-off between tumbling frequency and tumble persistence is perfectly balanced; changes in k can be precisely compensated by changes in λ_0 .

Fig. 4.4 shows how this small- β result accurately matches the full numerical results even for $\beta = 1/2$. So while persistence can lead to enhanced chemotaxis, we find that this has nothing inherently to do with the persistence of the tumbles themselves, as the same increase can be achieved simply by lowering the base tumbling frequency.

With constant λ_0 , letting $k \rightarrow \infty$ results in negligible drift. For large k , $[1 - I_1(k)/I_0(k)]^{-1} \sim 2k$. Thus we see that a continuous version of run-and-tumble (as presented in Chapter 3) emerges in the limit $k \rightarrow \infty$ if λ_0 is scaled linearly with k , and we conclude that such a strategy is equally optimal to any other persistence of tumbles with the correct choice of tumble frequency. These results arise because we allow λ_0 to be chosen independently of γ . Without persistence, chemotaxis is optimised for λ_0 and γ of similar order. For cells with large persistence, however, optimisation leads to λ_0 much larger than γ .

The expansion $P(\theta, \dots) = a_0(\dots) + a_1(\dots) \cos \theta$ captures the steady state distribution well, and the form of λ_k can only change if higher order Fourier modes become important. This is not case even in the high β regime, and so these conclusions are also valid there. Second order effects such as small dependencies of the optimal γ on λ_0 and k could also perturb the result of perfect trade-off between tumble frequency and persistence. Furthermore, although we only considered the steady state here, the conclusions apply to the transient

behaviour of the system. Our conclusions also hold in three dimensions as demonstrated in Appendix 4.C.

Real bacteria are observed to have an angular distribution of tumbles with a non-zero mode (Berg and Brown, 1972). To model this, we consider the reorientation distribution $g(\theta, \theta') = \sum_{\pm} e^{k \cos(\pm\mu + \theta - \theta')} / 4\pi I_0(k)$. This results in the substitution $I_1(k)/I_0(k) \rightarrow I_1(k)/I_0(k) \cos \mu$ in Eq. (4.11) (see Appendix 4.A), leaving unchanged our conclusions. If the turns are biased in one direction (e. g. turning more clockwise than counter-clockwise), such that $g(\theta, \theta') = e^{k \cos(\mu + \theta - \theta')} / 2\pi I_0(k)$, the efficiency can surpass that of unbiased cells. In this case the optimum strategy involves cells that continuously rotate, modulating their rotation speed as they swim (Appendix 4.B). While this is interesting behaviour, such a bias is a 2D phenomenon, although a related optimality may exist in 3D.

The fact that no single persistence value is globally preferable fits well with the experimental variations seen between biological species. The question still remains, however, if there are other effects that could induce a preferred tumble persistence. So far we have assumed the tumbles to be instantaneous. Including a finite tumble time can change the conclusions. In particular, since the optimal tumbling frequency for persistent tumbles is large, adding a constant time for each tumble results in large amounts of time in which no chemotactic progress is made, hence disfavouring persistence. On the other hand, one would expect a persistent tumble to take less time than a full tumble. The average tumble time $\langle \tau \rangle$ should depend on the average angle turned. The precise form of this dependence will change with reorientation method. If the tumbling rotation is ballistic, the mean reorientation time should be proportional to the mean angle turned. If, on the other hand, the cell relies on a diffusive method (which includes simply not swimming), the reorientation time will be proportional to the mean of the squared angle. We parametrise this with the exponent α , with $\alpha = 1$ for ballistic reorientations and $\alpha = 2$ for diffusive and a mixture for values in-between. The mean tumbling time is thus

$$\langle \tau \rangle = \frac{\tau_0}{\pi I_0(k)} \int_0^\pi \delta^\alpha e^{k \cos \delta} d\delta. \quad (4.13)$$

The insets of Fig. 4.5 show trajectories for ballistic diffusive and intermediate exponents. For small chemotactic strength it is easy to incorporate this effect. The fraction of time spent swimming will be $1/(1 + \langle \tau \rangle \lambda_0)$, so we find

$$\langle \cos \theta \rangle \rightarrow \frac{1}{1 + \langle \tau \rangle \lambda_0} \frac{\beta \gamma^3 \lambda_k}{2(D_r + \lambda_k)(D_r + \gamma + \lambda_k)^3}. \quad (4.14)$$

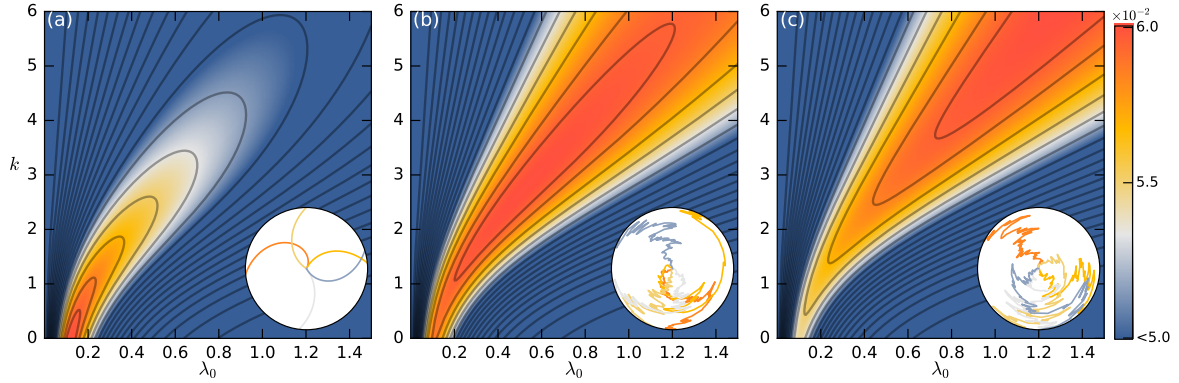


Figure 4.5 Drift efficiency $\langle \cos \theta \rangle$ with finite tumbling time. Panels correspond to different tumble time exponents: (a) $\alpha = 1.0$, (b) 1.7, and (c) 2.0. Colour scale shows the top 20% range of drift velocities. Insets show examples of reorientation trajectories for with exponent α , the angle on the circle indicating the orientation and the radial distance indicating time. Common parameters: $D_r = 0.1$, $\beta = 1/2$, $\gamma = 1$, $\tau_0 = 1$.

Crucially, λ_0 now appears alone, and we thus expect a global optimum to appear. Fig. 4.5 shows $\langle \cos \theta \rangle$ evaluated for various exponents. For ballistic ($\alpha = 1$) we find that full tumbles ($k = 0$) are optimal. For diffusive $\alpha = 2$, the continuous dynamics ($k \rightarrow \infty$) become optimal. In-between, as shown in Fig. 4.5b, a finite k optimum appears. A finite non-zero persistence also appears for diffusive scaling with an added constant, i. e. for Eq. (4.13) plus a constant.

4.5 Chemotactic Strength

We now ask whether optimality exists for the chemotactic strength parameter β . Of course, in models linearised in β no such optimality can appear, and we must seek a different approach. Averaging over many numerical realisations of the model would allow these effects to be captured, but a large number of realisations is needed to gain accurate statistics, rendering parameter space exploration hard. Hence, we begin this section by gaining intuition through a more tractable model, which gives a good qualitative understanding of the problem.

The crucial insight for this simplified model is that in a constant gradient there is nothing to distinguish one value of the position variable x from another. In our full model, the biaser $q(t)$ relaxes to $-\beta$ times the cell's estimate of $\cos \theta$ on a time scale $\sim \gamma$. Such a behaviour can be modelled by the Langevin equation

$$dq = -\frac{\gamma}{4}(q + \beta \cos \theta) dt + \beta \sqrt{2\sigma} dW, \quad (4.15)$$

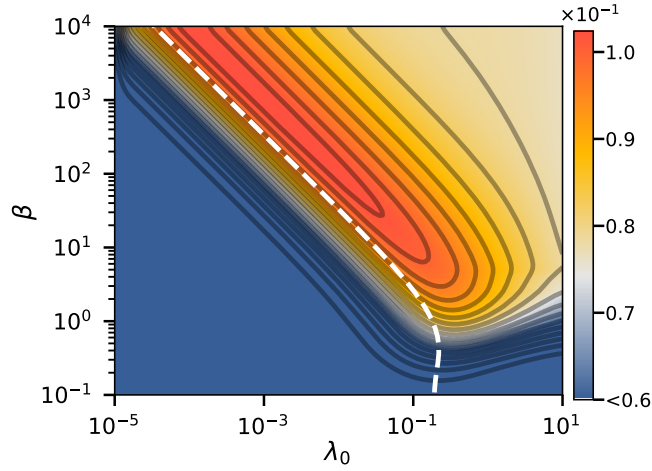


Figure 4.6 Drift efficiency as a function of chemotactic strength. Variations in β and λ_0 reveal a maximum as $\beta \rightarrow \infty$, $\lambda_0 \rightarrow 0$. Dashed curve is analytical approximation to optimum region. Parameters: $D_r = 0.1$, $\beta = 1/2$, $\gamma = 1$.

where the prefactor of $1/4$ is chosen so that the effective relaxation time matches that of the kernel κ used in the full model, and we have introduced a noise term (such a noise term plays no role in the linearised system). We can specify this system fully through a Fokker-Planck equation for $P(\theta, q, t)$

$$\begin{aligned} \frac{\partial P}{\partial t} = & \frac{\gamma}{4} \frac{\partial}{\partial q} (q + \beta \cos \theta) P + \sigma \beta^2 \frac{\partial^2 P}{\partial q^2} \\ & + D_r \frac{\partial^2 P}{\partial \theta^2} + \lambda_0 [1 + q] \left[\int \frac{e^{k \cos(\theta - \theta')}}{2\pi I_0(k)} P(\theta') d\theta' - P \right]. \end{aligned} \quad (4.16)$$

The optimal behaviour of the original system is well-captured by this reduced model (Appendix 4.D). Crucially, equation (4.16) is simple enough to be solved numerically using a hybrid spectral-finite difference method. Again we find that for all parameters the same efficiency can be obtained for any k by a simple rescaling of λ_0 . We thus set $k = 0$ in the remainder of this section without loss of generality.

Fig. 4.6 shows the resulting chemotactic drift under variation of the chemotaxis strength β and the base tumbling frequency λ_0 . For a given λ_0 , an optimal chemotactic strength does indeed exist. Choosing the chemotactic strength too high, evidently, also results in too many tumbles. Fig. 4.6 also shows, however, that under variations of both β and λ_0 , the optimum is found for $\beta \rightarrow \infty$. For large β the optimum lies on a straight line (power law) relating β to λ_0 .

To understand what sets the optimal chemotactic strength, we seek an analytical approach, but since there is no perturbative small parameter we examine instead a Fourier-Hermite

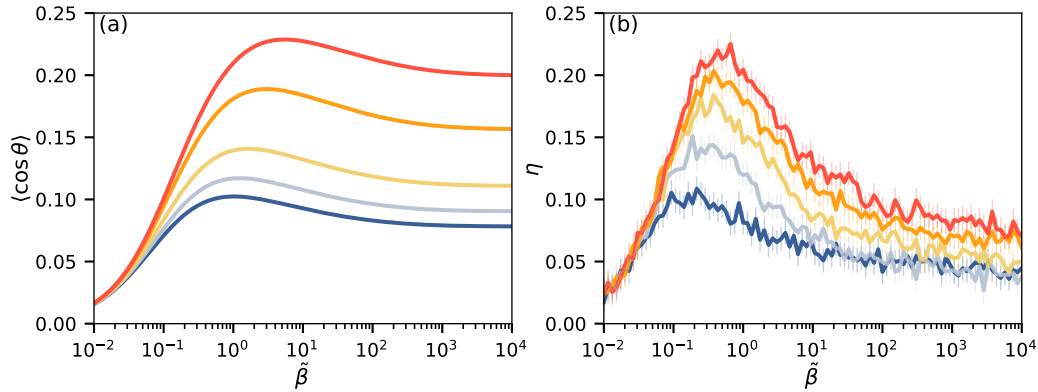


Figure 4.7 Drift efficiency as a function of chemotactic strength. (a) Chemotactic drift with modulation of the form $\beta[q]$. Curves vary from $\sigma = 0.15$ (red) to $\sigma = 1.0$ (blue). (b) Full particle simulations with average molecules sensed by cells varying from 0.5 (blue) to 3 (red). Common parameters: $D_r = 0.1$, $\beta = 1/2$, $\gamma = 1$.

expansion of the form

$$p(\theta, q) = \sum_{n=0}^N \sum_{m=0}^M a_{nm} \cos(n\theta) H_m(q/\zeta) e^{-q^2/\zeta^2}, \quad (4.17)$$

where H_m are the Hermite polynomials. The choice of this expansion arises from the fact that q resembles an Ornstein-Uhlenbeck process, the solution of which is Gaussian, with a scale ζ , which, for a true Ornstein-Uhlenbeck process would be $\sim \sqrt{4\sigma/\gamma}$. Presently, $\cos \theta$ also contributes to variations in q , and so $\zeta \sim \sqrt{1 + 4\sigma/\gamma}$. Here, we truncate at $N = M = 1$, which, while yielding numerically inaccurate results nevertheless reveals the key dynamics. In fact, this truncation makes $p(\theta, q)$ negative for some values, but still gives valid estimates of the drift efficiency. Higher-order terms can easily be calculated, but the expressions become lengthy. Exploiting orthogonality, the steady state coefficients $\{a_{nm}\} = (a_{00}, a_{10}, a_{01}, a_{11})$ are found as the null space of

$$\begin{pmatrix} 0 & 0 & 0 & 0 \\ 0 & -\frac{\gamma}{4} & -\frac{\gamma}{8\zeta} & 0 \\ 0 & 0 & \frac{\lambda_0}{2} \operatorname{erfc}\left(\frac{1}{\zeta\beta}\right) - \frac{\lambda_0\zeta\beta}{2\sqrt{\pi}} \exp\left(\frac{-1}{\zeta^2\beta^2}\right) - \lambda_0 - D_r & -\frac{1}{2}\lambda_0\zeta\beta\left(1 + \operatorname{erfc}\left(\frac{1}{\zeta\beta}\right)\right) \\ -\frac{\gamma}{4\beta} & 0 & -\frac{1}{4}\lambda_0\zeta\beta\left(1 + \operatorname{erf}\left(\frac{1}{\zeta\beta}\right)\right) & \frac{1}{2}\lambda_0 \operatorname{erfc}\left(\frac{1}{\zeta\beta}\right) - \lambda_0\left(1 + \frac{\zeta\beta}{\sqrt{\pi}} \exp\left(\frac{-1}{\zeta^2\beta^2}\right)\right) \end{pmatrix}, \quad (4.18)$$

whence $\langle \cos \theta \rangle = a_{10}/(2a_{00})$. Optimising this for λ_0 we obtain the dashed white curve in Fig. 4.6. In the limit $\beta \rightarrow \infty$ this has the form

$$\lambda_0 \sim \frac{D_r(D_r + \gamma/4)}{\sqrt{1 + 4\sigma/\gamma}} \frac{1}{\beta}. \quad (4.19)$$

Although the expansion does not quite capture the location of the optimum, the correct scaling is obtained. The global optimum is found at $\beta \rightarrow \infty$ and we learn that $\lambda_0\beta$ tends to a finite value in that limit. In detail, the optimisation tries to diminish the base tumbling contribution in the expression $\lambda_0[1+q]$ and the optimum is found in limit where $\lambda_0[1+q] \rightarrow \lambda_0[q]$. Explicitly making this substitution in Eq. (4.16) and defining $\tilde{\beta} = \lambda_0\beta$, we obtain a system that has a finite optimal value of chemotactic strength. This is shown in Fig. 4.6 for various noise strengths σ . To verify our conclusions based on this model we turn to the full simulation. Exactly as in the simplified model, we find optimum behaviour after making the substitution $\lambda_0[1+q] \rightarrow \lambda_0[q]$. This is shown in Fig. 4.7b for various levels of chemoattractant concentrations, confirming our conclusions.

It is perhaps surprising that the optimum is found in this limit, since no modulation of tumbling frequency then can occur if $q < 0$, which is the case when the cell swims just slightly in the correct direction, and thus in the limit of no noise, the angular distribution will be governed simply by rotational diffusion on $\theta \in [-\pi/2, \pi/2]$. In this optimal limit, the cells have minimised the time they spend swimming in any wrong direction, which, evidently, even though it leads to no active modulation for $q < 0$, is also the optimum for the total chemotactic drift. For stochastic taxis to work, the modulation must necessarily be a monotonically increasing function of q . Strong reaction when swimming in the wrong direction ($q > 0$) is thus typically coupled with smaller reaction when swimming in the correct direction ($q < 0$). Our results show, at least for the presently chosen form of modulation, that with this trade-off the best choice is to react very strongly when swimming in the wrong direction, even though this reduces the effectiveness of chemotaxis while swimming in the right direction.

4.6 Conclusions

In this chapter we have taken an approach to understanding run-and-tumble chemotaxis based on global parameter optimisation. For the specific system studied here, cells in constant gradients, we have focused on the base tumbling frequency λ_0 , tumbling persistence k , and chemotactic strength β as key parameters. Varying any one parameter alone, there is a

unique value that optimises the chemotactic drift, but when all parameters are free there is a higher-dimensional optimal locus.

In particular, the trade-off in optimality between the base tumbling frequency and tumble persistence is “perfect” in the sense that any increase, say, in persistence can be countered by an increase in base tumble frequency. After a persistent tumble, it would seem that the current value of q would stay more relevant than for a full tumble, indicating that persistence could lead to enhanced chemotaxis. The intuition behind this argument is based on comparing a *single* full tumble to a *single* persistent tumble, but a more appropriate comparison would be to a *series* of persistent tumbles. And as evident by our calculations, comparing in this way the argument of preservation of information leads to similar behaviour for all persistence parameters. One might also argue for the opposite: after a full tumble (or a series of persistent tumbles) there is a high risk that the new direction is wrong. Therefore, one could argue that keeping q large is a desirable strategy, since it increases the probability of correcting the tumble quickly. Our results show that both of these arguments are incorrect. Although one could imagine a model in which q is explicitly altered after each tumble, say $q \rightarrow aq$, the study of this variant would require relaxing the assumption of fixed γ in order to find global optima.

Introducing a finite tumble time moves the model away from the perfect trade-offs described above. We have shown that an optimum persistence emerges that depends on the manner in which the tumble time depends on reorientation angle. For ballistic tumbles, zero persistence is optimal, while continuous tumbling is optimal for diffusive tumbles. A finite persistence emerges for exponents in-between, i. e. for tumbles that are superdiffusive, but not ballistic. Such a tumble could simply be a mixture of ballistic and diffusive reorientations that when taken together have a super-diffusive behaviour. Diffusive tumbles are easy to generate: a cell can do so by simply not swimming, and more generally by wiggling its flagella in random directions. Ballistic tumbles require directed motion of the flagella (even though the actual direction is chosen randomly). Actual tumbles might be a combination of a fixed tumble time plus a diffusive scaling, which would favour a finite tumble persistence (non-zero and non-infinite). One could furthermore imagine minimising tumble times by maintaining a finite swimming speed during tumbles, e. g. via polymorphic transformations of the flagella (Goldstein et al., 2000).

In addition to studying the weak chemotaxis limit, we have also investigated the effects of strong chemotaxis. While this is, naturally, dependent on the precise functional form chosen for the biasing of tumbles, we have shown that optima in chemotactic strength can also emerge. Through an analytical approximation we found that the form $\lambda_0[1+q]$ has an optimal value of β for constant λ_0 . Allowing for variations in λ_0 the optimum shifts to

$\beta \rightarrow \infty$, and instead $\tilde{\beta} = \beta \lambda_0$ as $\beta \rightarrow \infty$ has an optimal value. This naturally leads to the question of the optimal form of the modulation. Preliminary results have shown that other simple choices, e. g. $\lambda_0 e^q$, do not perform better than the form studied here. In general such problems can be considered partially observable Markov decision processes, and a potential optimal functional form could be found by methods such as reinforcement learning. Results from such analysis, however, will probably be strongly dependent on the model setup, and a form that optimises for drift in constant gradients will not necessarily do well in other gradients.

Comparing to experimental systems, our result that persistence does not have a unique optimum when allowing for variations in base tumble frequency fits well with the variation that exists between species. The chemotactic strength result that the optimum is found as $\lambda_0 \rightarrow 0$ is a special outcome of maximising the drift velocity in a constant gradient. In more complex domains, the cells will need to react also to spatial variations (Appendix 4.D) and thus need a finite λ_0 and smaller β . Maximising the minimum chemotactic efficiency over many chemoattractant profiles reveals the experimental values associated with the kernel κ and base tumbling frequency (Celani and Vergassola, 2010). A linear approach cannot, however, reveal an optimal chemotactic strength. An interesting question for future research is thus: can maximising the minimum chemotactic efficiency over suitably chosen noise models reveal an optimal finite chemotactic strength? While difficult to tackle analytically, numerical methods may be able to answer such questions.

Appendix 4.A Linearised with Mean Tumble Angle

The reorientation distribution is now

$$g_k(\theta, \theta') = \frac{1}{4\pi I_0(k)} \left(e^{k \cos(\theta - \theta' - \mu)} + e^{k \cos(\theta - \theta' + \mu)} \right) \quad (4.20)$$

such that

$$\partial_t \langle \cos \theta \rangle = -D_r \langle \cos \theta \rangle - \lambda_0 \left(1 - \frac{I_1(k)}{I_0(k)} \cos \mu \right) (\langle \cos \theta \rangle + \langle q \cos \theta \rangle), \quad (4.21)$$

where we used that $\cos \mu$ is an even function and $\sin \mu$ odd. So having a finite μ corresponds to changing the persistence. At precisely $\mu = \pm\pi/2$, persistence no longer changes the behaviour.

Appendix 4.B Linearised with Mean Tumble Angle — Biased Direction

Here we take

$$g_k(\theta, \theta') = \frac{1}{2\pi I_0(k)} e^{k \cos(\theta - \theta' - \mu)}. \quad (4.22)$$

We now have

$$\begin{aligned} \partial_t \langle \cos \theta \rangle &= -D_r \langle \cos \theta \rangle - \lambda_0 \left(1 - \frac{I_1(k)}{I_0(k)} \cos \mu \right) (\langle \cos \theta \rangle + \langle q \cos \theta \rangle) \\ &\quad - \lambda_0 \frac{I_1(k)}{I_0(k)} \sin \mu (\langle \sin \theta \rangle + \langle q \sin \theta \rangle). \end{aligned} \quad (4.23)$$

And then

$$\begin{aligned} \partial_t \langle m_0 \cos \theta \rangle &= -D_r \langle m_0 \cos \theta \rangle - \lambda_0 \left(1 - \frac{I_1(k)}{I_0(k)} \cos \mu \right) \langle m_0 \cos \theta \rangle \\ &\quad - \lambda_0 \frac{I_1(k)}{I_0(k)} \sin \mu \langle m_0 \sin \theta \rangle + \alpha \langle x \cos \theta \rangle - \gamma \langle m_0 \cos \theta \rangle, \end{aligned} \quad (4.24a)$$

$$\begin{aligned} \partial_t \langle m_1 \cos \theta \rangle &= -D_r \langle m_1 \cos \theta \rangle - \lambda_0 \left(1 - \frac{I_1(k)}{I_0(k)} \cos \mu \right) \langle m_1 \cos \theta \rangle \\ &\quad - \lambda_0 \frac{I_1(k)}{I_0(k)} \sin \mu \langle m_1 \sin \theta \rangle + \langle m_0 \cos \theta \rangle - \gamma \langle m_0 \cos \theta \rangle, \end{aligned} \quad (4.24b)$$

$$\begin{aligned} \partial_t \langle m_2 \cos \theta \rangle &= -D_r \langle m_2 \cos \theta \rangle - \lambda_0 \left(1 - \frac{I_1(k)}{I_0(k)} \cos \mu \right) \langle m_2 \cos \theta \rangle \\ &\quad - \lambda_0 \frac{I_1(k)}{I_0(k)} \sin \mu \langle m_2 \sin \theta \rangle + 2 \langle m_1 \cos \theta \rangle - \gamma \langle m_2 \cos \theta \rangle, \end{aligned} \quad (4.24c)$$

$$\begin{aligned} \partial_t \langle x \cos \theta \rangle &= \frac{v}{2} - D_r \langle x \cos \theta \rangle - \lambda_0 \left(1 - \frac{I_1(k)}{I_0(k)} \cos \mu \right) \langle x \cos \theta \rangle \\ &\quad - \lambda_0 \frac{I_1(k)}{I_0(k)} \sin \mu \langle x \sin \theta \rangle \end{aligned} \quad (4.24d)$$

and similarly for the $\sin \theta$ terms, except no $v/2$ term appears in the equation for $\partial_t \langle x \sin \theta \rangle$.

This can be solved for the steady solution of $\langle \cos \theta \rangle$, but the expression is quite lengthy. Analysing it, we find that the optimum is found for $k \rightarrow \infty$. Taking this limit we find

$$\begin{aligned} \langle \cos \theta \rangle \rightarrow & \beta \gamma^3 \lambda_0 \left[\lambda_0^2 (\cos(2\mu) (3(\gamma + D_r + \lambda_0)(\gamma + 2(D_r + \lambda_0)) + \lambda_0(3\gamma \right. & (4.25) \\ & + 4(D_r + \lambda_0))) + \lambda_0 (\cos(3\mu) (-3\gamma - 4D_r - 5\lambda_0) + \lambda_0 \cos(4\mu)) \\ & - \cos \mu (\gamma + D_r + \lambda_0) (\lambda_0^2 (10\gamma + 17D_r) + \lambda_0 (\gamma + D_r) (2\gamma + 7D_r) + D_r (\gamma + D_r)^2 \\ & + 11\lambda_0^3) + (\gamma + D_r + \lambda_0)^2 ((D_r + \lambda_0)(\gamma + D_r + \lambda_0) + \lambda_0 (\gamma + 4(D_r + \lambda_0))) \left. \right] \\ & / \left[2(-2\lambda_0(D_r + \lambda_0) \cos \mu + (D_r + \lambda_0)^2 + \lambda_0^2) (-2\lambda_0 \cos \mu (\gamma + D_r + \lambda_0) \right. \\ & \left. + (\gamma + D_r + \lambda_0)^2 + \lambda_0^2)^3 \right]. \end{aligned}$$

The optimum is found at $\mu \rightarrow 0$, $\lambda_0 \rightarrow \infty$, keeping $\lambda_0 \mu$ constant. The motion is thus continuously rotating cells, where the rotation speed is modulated by the chemoattractants.

Appendix 4.C Persistence in 3D

The linearised calculation is very similar in 3D. Defining p as a unit vector in the swimming direction, we can write the Fokker-Planck equation with von-Mises tumbles as

$$\begin{aligned} \frac{\partial P(t, x, p, m)}{\partial t} + v p_x \frac{\partial P}{\partial x} = & D_r \nabla_p^2 P + \lambda_0 [1 + q(t)] \left[\int \frac{k e^{k p \cdot p'}}{4\pi \sinh k} P(p') d\Omega' - P \right] & (4.26) \\ & - \sum_j \partial_{m_j} [\delta_{j,0} c(x) + j m_{j-1} - \gamma m_j] P, \end{aligned}$$

where ∇_p^2 is the angular Laplacian.

This leads to

$$\partial_t \langle p_x \rangle = -2D_r \langle p_x \rangle - \lambda_0 \left[1 + \frac{1}{k} - \frac{1}{\tanh k} \right] (\langle p_x \rangle + \langle q p_x \rangle), \quad (4.27)$$

showing an only slightly altered persistence modification to λ_k compared to 2D, and thus leading to similar conclusions as in 2D.

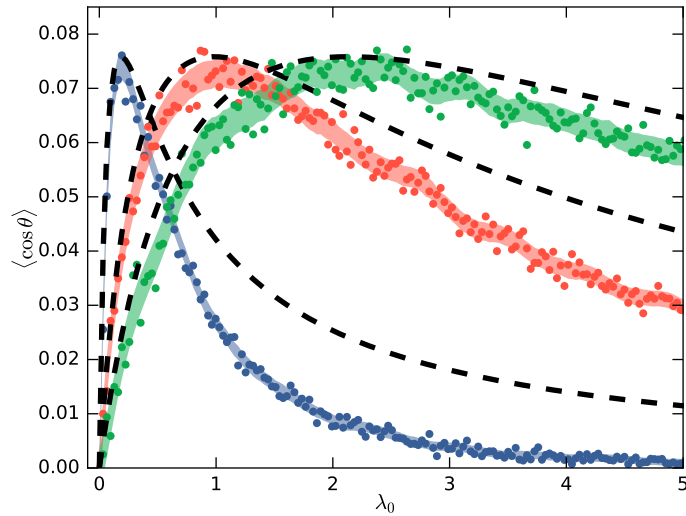


Figure 4.8 Similar to Fig. 4.4, but with theoretical curves (dashed) obtained from the analysis of Eq. (4.16).

Appendix 4.D Simplified Effective Model

Fig. 4.8 shows the performance of the simplified model of Eq. (4.16) compared to the simulations shown in Fig. 4.4.

Appendix 4.E Run-and-tumble in Discrete 1D

In this section we study run-and-tumble in one spatial dimension. Such simplifications have proven to yield much insight in the case of no noise (Rivero et al., 1989). For the present purpose we will consider the case of a very noisy signal. To simplify further we put the cells and chemoattractants on an equilateral grid. We assume that each measurement carries the same error σ . In reality, the measurement of a concentration c has an error $\propto \sqrt{c}$, but such effects are expected to be second order. Thus at each grid position i , the cell measures a concentration $c_i \sim N(c(x_i), \sigma^2)$, where $c(x_i)$ is the time-average of the signal at that position.

In particular, a cell will swim n lattice points and calculate $Q = \sum_j k_j c_{i(j)}$, where k_j is some kernel, reminiscent of the continuous kernel used in the main text of this chapter. In the simplest model, if $Q > 0$ the cell will keep going in the same direction, but turn if $Q < 0$. We begin by determining the optimal $\{k_j\}$.

4.E.1 Optimal Kernel

We determine $\{k_j\}$ in such a way that Q makes the best estimate of a constant gradient. Thus we consider $c_i \sim N(c_0 + \alpha i, \sigma^2)$. Then $Q = \sum k_j c_j$ is an unbiased estimator of α if

$$\langle Q \rangle = \sum k_j \langle c_j \rangle = \sum k_j (c_0 + \alpha j) = c_0 \sum k_j + \alpha \sum k_j j = \alpha, \quad (4.28)$$

so we must require $\sum k_j = 0$ and $\sum k_j j = 1$. The variance becomes

$$\text{Var}Q = \langle Q^2 \rangle - \langle Q \rangle^2 = \sigma^2 \sum k_j^2. \quad (4.29)$$

Writing $Q = \sum k_i c_i$, minimising the variance subject to the unbiased estimation yields

$$k_i = \frac{6(2i - n_1 - n_2)}{(n_2 - n_1 + 2)(n_2 - n_1 + 1)(n_2 - n_1)} \quad (4.30)$$

for a measurement on $[n_1, n_2]$. Thus

$$k_j = \frac{6(2j - n)}{(n + 2)(n + 1)n}, \quad (4.31)$$

where $n = n_2 - n_1$. Assuming a Gaussian distribution we thus have

$$Q \sim N\left(\alpha, \sigma^2 \sum k_j^2\right) = N\left(\alpha, \frac{12\sigma^2}{(n+2)(n+1)n}\right) \equiv N(\alpha, \sigma_n^2). \quad (4.32)$$

4.E.2 Chemotaxis in a Constant Gradient

The probability that $Q < 0$ after a swim of n lattice points follows a geometric distribution with parameter

$$q = \frac{1}{\sqrt{2\pi\sigma_n^2}} \int_{-\infty}^0 e^{-(x-\alpha)^2/2\sigma_n^2} dx = \frac{1}{2} \text{erfc}\left(\frac{\alpha}{\sqrt{2\sigma_n^2}}\right). \quad (4.33)$$

After a run left and right, the cell will have travelled on average

$$\frac{n}{q} - \frac{n}{1-q}, \quad (4.34)$$

while in that time it could have travelled on average the distance

$$\frac{n}{q} + \frac{n}{1-q}. \quad (4.35)$$

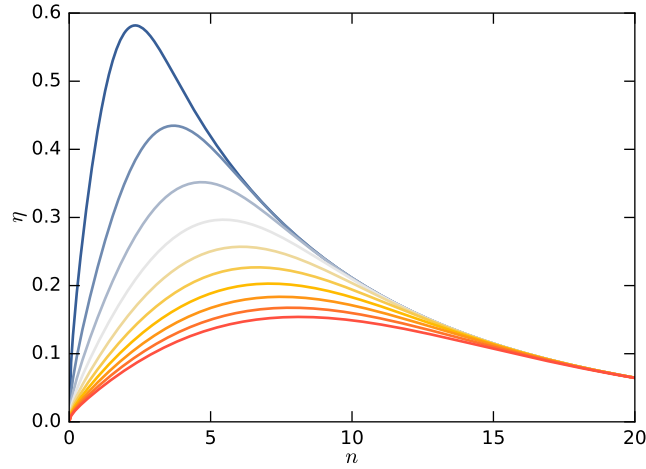


Figure 4.9 Efficiency η as a function of n as in Eq. (4.36). Noise varies from $\sigma/\alpha = 1$ (blue) to $\sigma/\alpha = 10$ (red). $D_r = 0.1$.

The efficiency is thus $\eta = 1 - 2q$, which is maximised for $q \rightarrow 0$, corresponding to $n \rightarrow \infty$. This is in the absence of spatial variations and diffusion effects.

4.E.3 Effective Rotational Diffusion

We now add the feature that after each jump the particle will flip either because $Q < 0$ or another process $R < 0$, which has parameter D_r for a single jump. The probability $R < 0$ after n jumps will thus be $r = 1 - (1 - D_r)^n$. Thus the probability of a turn after the n jumps is $\tilde{q} = q + r - qr$ when going right, and when going left $\tilde{p} = (1 - q) + r - (1 - qr)$. Calculating the efficiency we thus find

$$\eta = \frac{(1 - 2q)(1 - D_r)^n}{2 - (1 - D_r)^n}, \quad (4.36)$$

where q is defined as in Eq. (4.33). This defines an optimal n as shown in Fig. 4.9. The emergence of an optimal n corresponds to the emergence of an optimum γ in the main text.

4.E.4 Chemotaxis in a Spatially Varying Gradient

Spatial variation from linear concentration profiles can also affect the optimal choice of n . Consider cells swimming in a gradient being held to a fixed value $c_0 > 0$ at the origin. The diffusion equation allows for linear steady state solutions. We thus consider 1D swimmers in

$$c(x) = c_0 - \alpha|x|. \quad (4.37)$$

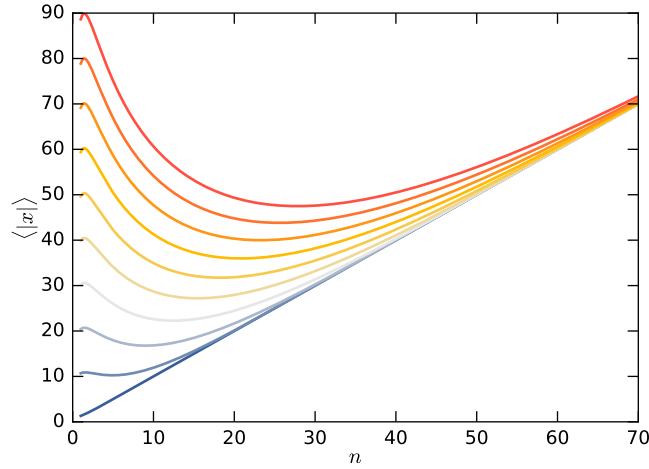


Figure 4.10 Average $|x|$ for as a function of n , the number of jumps before deciding to change direction, as described by Eq. (4.43). Chemotaxis is optimal when $\langle |x| \rangle$ is minimised, since the chemoattractant concentration decreases from $x = 0$. Parameters as in Fig. 4.9.

We again discretise space and allow the cells to choose an n , the number of lattice points to swim before making a decision on whether to change direction. This n determines σ_n and thus q . This also makes the cells only visit sites that are multiples of n and we thus reindex by that. We further note that a state moving right at position i is by symmetry the same as moving left at site $-i$. We exploit this symmetry and consider only $i \geq 0$. Our states are then called

$$(i, s) \in \mathbb{N}_0 \times \{+, -\} = \left\{ (0, +), (0, -), (1, +), (1, -), (2, +), (2, -), \dots \right\}. \quad (4.38)$$

The jumps form an infinite dimensional Markov chain with transition matrix

$$\mathbb{T} = \begin{pmatrix} 0 & 0 & 0 & p & 0 & 0 & 0 & 0 & 0 & \dots \\ 0 & 0 & 0 & q & 0 & 0 & 0 & 0 & 0 & \dots \\ p & q & 0 & 0 & 0 & p & 0 & 0 & 0 & \dots \\ q & p & 0 & 0 & 0 & q & 0 & 0 & 0 & \dots \\ 0 & 0 & p & 0 & 0 & 0 & 0 & p & 0 & \dots \\ 0 & 0 & q & 0 & 0 & 0 & 0 & q & 0 & \dots \\ 0 & 0 & 0 & 0 & p & 0 & 0 & 0 & 0 & \dots \\ 0 & 0 & 0 & 0 & q & 0 & 0 & 0 & 0 & \dots \\ 0 & 0 & 0 & 0 & 0 & 0 & p & 0 & 0 & \dots \\ 0 & 0 & 0 & 0 & 0 & 0 & q & 0 & 0 & \dots \\ \vdots & \ddots \end{pmatrix}, \quad (4.39)$$

where $p = 1 - q$. The steady state distribution is found by solving

$$p = \mathbb{T} p. \quad (4.40)$$

To solve this infinite set of equations, we truncate in an appropriate manner at m equations and then let $m \rightarrow \infty$. We assume m even and to conserve probability, for finite m set $\mathbb{T}_{m-1, m-1} = p$ and $\mathbb{T}_{m, m-1} = q$. This leads to

$$p_{i,s} = \frac{1}{A} \cdot \begin{cases} \frac{q^k}{p^{k-2}(1-2q+2q^2)} & (0, +) \\ \frac{q^{k+1}}{p^{k-1}(1-2q+2q^2)} & (0, -) \\ \frac{q^{k-i}}{p^{k-i}} & (i \geq 1, +) \\ \frac{q^k}{p^{k-2}(1-2q+2q^2)} & (1, -) \\ \frac{q^{k-i+1}}{p^{k-i+1}} & (i \geq 2, -) \end{cases} \quad (4.41)$$

where $k = m/2 - 2$ and A is a normalisation constant determined by

$$\sum_{i,s} p_{i,s} = 1. \quad (4.42)$$

After a long calculation we find (for $q > 1/2$) in the limit $m \rightarrow \infty$,

$$\langle |x| \rangle = \frac{\Delta x n}{2} \left(2 - \frac{1}{q(n)} + \frac{1}{2q(n) - 1} \right). \quad (4.43)$$

Fig. 4.10 shows a minimum appearing for large noise. Thus we see that an optimal measurement distance must also be balanced with potential spatial variations, not just with rotational diffusion.

Appendix 4.F Direct Gradient Sensing

In a seminal paper, [Berg and Purcell \(1977\)](#) presented the physical limits to the accuracy of concentration sensing. In particular they introduced a 'perfect instrument', a sphere through which chemicals are free to diffuse and which at any time knows the number of molecules inside it. By measuring for a time T , this perfect instrument can calculate and approximate the local concentration c_0 . The error on this estimate Berg and Purcell found to be $\sqrt{3/5\pi DaT} c_0$, where a is the sphere radius and D the diffusion constant of the molecules. Recently, this was extended to the case of gradient sensing ([Endres and Wingreen, 2008](#)),



Figure 4.11 Neutrophil chasing bacterium through a maze of red blood cells. The bacteria are seen as small black dimer-like objects. (a–b) chasing. (c) Bacterium caught. Stills from movie by David Rogers, Vanderbilt University.

and it was shown that the 'perfect' instrument could actually be improved upon if the sphere absorbed the molecules in addition to sensing their presence. Additional work has been done to include receptor dynamics (Bialek and Setayeshgar, 2005; Endres and Wingreen, 2009a,b).

These results were obtained for the case of 3D. Here we derive the 2D sensing limits. Integrals that converge in 3D, but not in 2D, were used in the 3D derivations of Berg and Purcell (1977), so the generalisation is not immediate. This study was originally motivated by how a neutrophil chases a bacterium, as shown in Fig. 4.11. The neutrophil is crawling and can thus be considered pseudo-2D,

This appendix is a preliminary study. It is presented here only to contrast with the run-and-tumble chemotaxis. Further studies will explore the bias-variance trade-off (to be presented) more completely.

Following Endres and Wingreen (2008), the cell can spend a time T to calculate an approximate average density of chemoattractants

$$\rho(t, x) = \frac{1}{T} \int_{-T}^0 \sum_{i=1}^{N(t)} \delta(x - X_i(t)) dt, \quad (4.44)$$

where N and $\{X_i\}$ are random processes. In addition to this we will consider a different, weighed average, the reason being two-fold: first, chasing a moving bacterium is different from making a single estimate of the gradient and temporal correlations in the gradient can be exploited. In addition to this first, we see in Fig. 4.11b that the white blood cell comes into proximity with a second bacterium, but seems to completely ignore this. This hints at persistence in either direction of motion or in gradient sensing, which thus should be included in a model. Secondly, to sense shallow gradients a long time can be needed to obtain an accurate estimate of the gradient, but during this estimation the prey can have moved and thus later measurements are more important. This is similar to a bias-variance tradeoff. For

these reasons we also consider density averaging of the type

$$\rho(t, x) = \frac{2}{\tau} \int_{-\infty}^0 e^{2t/\tau} \sum_{i=1}^{N(t)} \delta(x - X_i(t)) dt, \quad (4.45)$$

where choosing $2/\tau$ will ease comparison between the two models.

We consider the cell a circle of radius a . The cell can make a best estimate of the local concentration field, $c(x) = c_0 + c_r \cdot x$, by minimising (Endres and Wingreen, 2008)

$$\begin{aligned} \mathcal{E} &= \int_A (\rho - c_0 - c_r \cdot x)^2 dA \\ &= \int_0^{2\pi} \int_0^a (\rho - c_0 - c_x r \cos \theta - c_y r \sin \theta)^2 r d\theta dr. \end{aligned} \quad (4.46)$$

For c_x for instance, we have

$$0 = \frac{\partial \mathcal{E}}{\partial c_x} = 2 \int_0^{2\pi} \int_0^a (\rho - c_0 - c_x r \cos \theta - c_y r \sin \theta) r^2 \cos \theta d\theta dr, \quad (4.47)$$

leading to

$$c_x = \frac{4}{\pi a^4} \int_0^{2\pi} \int_0^a \rho r \cos \theta r d\theta dr. \quad (4.48)$$

We are interested in the accuracy of the estimation, or equally, in the variance of the estimation

$$\langle \delta c_x^2 \rangle = \left(\frac{4}{\pi a^4} \right)^2 (\langle n_x^2 \rangle - \langle n_x \rangle^2). \quad (4.49)$$

In the exponentially weighted case we have

$$\begin{aligned} \langle n_x^2 \rangle &= \left\langle \left(\int_0^{2\pi} \int_0^a \frac{2}{\tau} \int_{-\infty}^0 e^{2t/\tau} \rho r \cos \theta dt r d\theta dr \right)^2 \right\rangle \\ &= \left\langle \left(\frac{2}{\tau} \int_{-\infty}^0 e^{2t/\tau} m_x(t) dt \right)^2 \right\rangle = \frac{4}{\tau^2} \iint_{-\infty}^0 e^{2(t+t')/\tau} \langle m_x(t) m_x(t') \rangle dt' dt, \end{aligned} \quad (4.50)$$

where

$$m_x(t) = \int_0^{2\pi} \int_0^a \rho(t) r \cos \theta r d\theta dr = \sum_{i=1}^N x_i(t). \quad (4.51)$$

N is the number of cells inside the shape. Following the 3D calculations, we can also write this in terms of M cells inside a much larger area and use indicator functions I_i to denote whether or not a particle is inside the shape:

$$m_x(t) = \sum_{i=1}^M I_i(t) x_i(t). \quad (4.52)$$

Thus we need to calculate

$$\begin{aligned} \langle m_x(t) m_x(t') \rangle &= \sum_{i=1}^M \sum_{j=1}^M \langle I_i(t) x_i(t) I_j(t') x_j(t') \rangle \\ &= \left\langle \sum_{i=1}^M I_i(t) x_i(t) I_i(t') x_i(t') \right\rangle + \left\langle \sum_{i \neq j} I_i(t) x_i(t) I_j(t') x_j(t') \right\rangle \\ &\approx \langle N \rangle u(t-t') + \langle N \rangle^2 \langle m_x(t) \rangle^2, \end{aligned} \quad (4.53)$$

where $u(t-t') = \langle I(t) x(t) I(t') x(t') \rangle$. Thus we have

$$\langle \delta n_x^2 \rangle = \langle n_x^2 \rangle - \langle n_x \rangle^2 = \frac{4 \langle N \rangle}{\tau^2} \iint_{-\infty}^0 e^{2(t+t')/\tau} u(t-t') dt' dt. \quad (4.54)$$

To calculate $u(t-t')$ it turns out that the contribution from the gradient vanishes (this will become evident later), so we are left with

$$\begin{aligned} u(t-t') &= \mathbb{E} [I(t) I(t') r(t) r(t') \cos \theta(t) \cos \theta(t')] \\ &= \mathbb{E} [\mathbb{E} [I(t) r(t) r(t') \cos \theta(t) \cos \theta(t') | I(t') = 1, r(t'), \theta(t')]] \\ &= \frac{1}{\pi a^2} \iiint \int_A \frac{r r' \cos \theta \cos \theta'}{4\pi D |t-t'|} \exp\left(-\frac{r^2 + r'^2 - 2rr' \cos(\theta - \theta')}{4D |t-t'|}\right) r d\theta r' d\theta' dr dr'. \end{aligned} \quad (4.55)$$

Swapping the order of the integrals of Eq. (4.54) and (4.55) we find an integral of the form

$$I = \frac{4}{\tau^2} \iint_{-\infty}^0 e^{2(t+t')/\tau} \frac{\exp(-\alpha/|t-t'|)}{|t-t'|} dt dt', \quad (4.56)$$

where $\alpha = [r^2 + r'^2 - 2rr' \cos(\theta - \theta')]/4D$.

Typically, a cell will sense for a time much longer than the diffusion time scale. For $\tau \gg a^2/D > \alpha$, we find

$$I \approx -\frac{4\gamma}{\tau} - \frac{2}{\tau} \log\left(\frac{2\alpha}{\tau}\right), \quad (4.57)$$

where γ is the Euler-Mascheroni constant. The logarithmic singularity above is not present in three dimensions, but must be picked up in 2D to obtain the correct results. In the case of sensing for a time T we find

$$I = \frac{1}{T^2} \iint_{-T}^0 \frac{\exp(-\alpha/|t-t'|)}{|t-t'|} dt dt' \approx -\frac{2+2\gamma}{T} - \frac{2}{T} \log\left(\frac{\alpha}{T}\right). \quad (4.58)$$

Terms independent of α will not contribute to the spatial integration of Eq. (4.55). Hence we find that both methods of sensing will have the same variance, since the only terms with α in I are $-2/\tau \log(\alpha)$ and $-2/T \log(\alpha)$, respectively.

Thus we find for both averaging mechanisms (swap τ for T) that

$$\langle \delta n_x^2 \rangle = \frac{-\langle N \rangle}{2\pi^2 a^2 D \tau} \iiint_A r^2 r'^2 \cos \theta \cos \theta' \log(r^2 + r'^2 - 2rr' \cos(\theta - \theta')) d\theta d\theta' dr dr'. \quad (4.59)$$

Because of its singular nature, care has to be taken to find the correct value of the above integral. We substitute $\phi = \theta - \theta'$ and find

$$\begin{aligned} I &= \iiint_A r^2 r'^2 \cos(\phi + \theta') \cos \theta' \log(r^2 + r'^2 - 2rr' \cos \phi) d\phi d\theta' dr dr' \\ &= \pi \iiint_A r^2 r'^2 \cos \phi \log(r^2 + r'^2 - 2rr' \cos \phi) d\phi dr dr', \end{aligned} \quad (4.60)$$

where we used $\cos(\phi + \theta') = \cos \phi \cos \theta' - \sin \phi \sin \theta'$. We now see that the contribution from a gradient fields yields 0 in the above integral, since it would introduce an extra factor $\cos \theta'$, thus validating our previous assumption.

Now we need

$$\int_0^{2\pi} \cos \phi \log(r^2 + r'^2 - 2rr' \cos \phi) d\theta d\theta' = -2\pi \begin{cases} r/r', & r < r' \\ r'/r, & r > r' \end{cases}. \quad (4.61)$$

The integral is undefined at the singularity $r = r'$. The integrand is symmetric in r, r' , so the final value is obtained as

$$I = -4\pi^2 \int_0^a \int_0^{r'} r^3 r' dr dr' = -\frac{\pi^2 a^6}{6}. \quad (4.62)$$

Thus

$$\langle \delta n_x^2 \rangle = \frac{a^4 \langle N \rangle}{12D\tau} \quad (4.63)$$

and using $\langle N \rangle = \pi a^2 \bar{c}_0$, where \bar{c}_0 is the true average local concentration, we finally find

$$\langle \delta c_x^2 \rangle = \frac{4 \langle N \rangle}{3 a^4 \pi^2 D \tau} = \frac{4 \bar{c}_0}{3 a^2 \pi D \tau}. \quad (4.64)$$

Lastly, we should consider the limit of small τ or T . In the extreme case this corresponds to only performing one measurement, i. e.

$$\rho(x) = \sum_{i=1}^N \delta(x - X_i) \quad (4.65)$$

and we have simply

$$\langle n_x \rangle = \langle N \rangle \langle r_i \cos \theta_i \rangle \quad (4.66a)$$

$$\langle n_x^2 \rangle \approx \langle N \rangle \langle r_i^2 \cos^2 \theta_i \rangle + \langle n_x \rangle^2, \quad (4.66b)$$

This calculation is much simpler, and we find

$$\langle n_x^2 \rangle - \langle n_x \rangle^2 = \frac{a^2 \langle N \rangle}{4} \quad (4.67)$$

and end up with

$$\langle \delta c_x^2 \rangle = \frac{4 \bar{c}_0}{\pi a^4}. \quad (4.68)$$

This serves as the lower cut-off to Eq. (4.64). Combined, they may be written

$$\langle \delta c_x^2 \rangle = \frac{4 \bar{c}_0}{\pi a^4 + 3 \pi a^2 D \tau}. \quad (4.69)$$

This result is compared to a simulation in Fig. 4.12, blue curve. The orange particles perform a random walk with diffusion constant D , and a linear gradient is maintained by having reflecting boundary conditions on the right and teleporting boundary conditions on the left. The theory (dashed) works very well in two limits $T \ll a^2/D$ and $T \gg a^2/D$, but is also reasonable in the intermediate range.

The role of shape

The above calculations were done for a circle, but real crawling cells extend lamellipodia, filopodia, and blebs. In other words, they are highly non-circular. To see the effects of shape

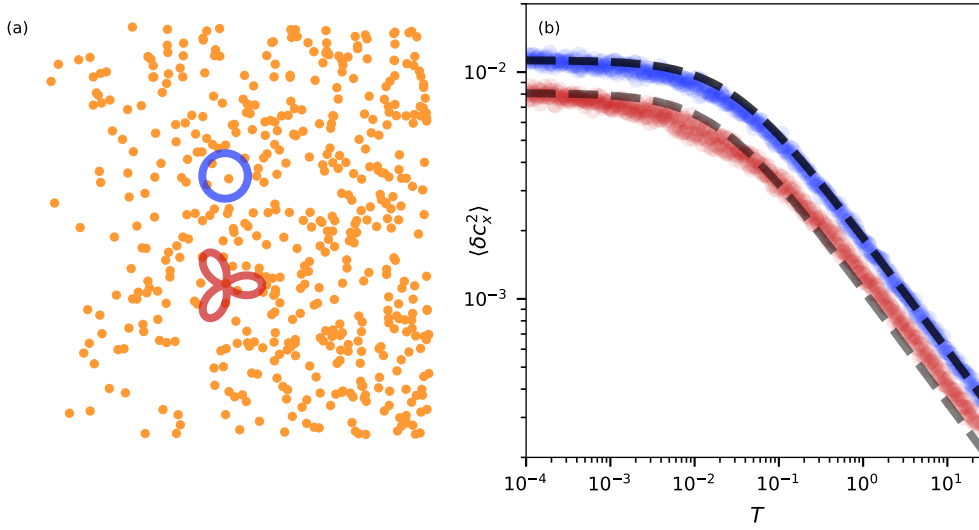


Figure 4.12 Comparison of theory to simulation. (a) Snapshot of simulation. (b) Error on gradient sensing for a circle (blue) and $m = 3$, $\epsilon = 0.95$ shape (red). Each point in plot is the result of averaging over 100 simulations.

consider a region

$$A = \left\{ (r, \theta) \mid \theta \in [0, 2\pi), 0 \leq r \leq \sqrt{\frac{2}{2+\epsilon^2}} a (1 + \epsilon \cos m\theta) \right\}. \quad (4.70)$$

Note that this has area

$$\iint_A dA = \int_0^{2\pi} d\theta \int_0^{\sqrt{\frac{2}{2+\epsilon^2}} a (1 + \epsilon \cos m\theta)} r dr = \pi a^2 \quad (4.71)$$

equivalent to the circle.

In the short time sensing, the calculation can still be done and we find

$$\langle \delta c_x^2 \rangle = \frac{8(2 + \epsilon^2)^2 \bar{c}_0}{(8 + 24\epsilon^2 + 3\epsilon^4)\pi a^4}, \quad (4.72)$$

i. e. a shape factor

$$s_f = \frac{2(2 + \epsilon^2)^2}{(8 + 24\epsilon^2 + 3\epsilon^4)}. \quad (4.73)$$

Note that the result is independent of m (for $m \geq 3$). Fig. 4.12 (red) shows a comparison of the Eq. (4.69) with this shape factor compared to a simulation. The theory matches the simulation for small T as it should, but underestimates slightly for large T , due to diffusion in and out of this shape differing from the diffusion in and out of a circle. Nonetheless, it does

give a reasonable estimate and we find that a cell taking a different, but still fairly regular, shape can decrease its sensing error by $\sim s_f = 0.5 = 50\%$ (for $\varepsilon = 1$).

Chapter 5

Colonial Filter-Feeding

5.1 Introduction

Competitive advantages over single cells must be one of the driving forces behind the existence of multicellular life forms. *S. rosetta*, and other single-celled organisms, mimic true multicellular behaviour by forming colonies. While such colonies do not have the advantages that accrue with division of labour, they do obtain potential benefits from their increased size, otherwise limited by intracellular nutrient mixing by diffusion. In Fig. 5.1 we show some of the various morphologies that *S. rosetta* can obtain (Alegado et al., 2012; Dayel et al., 2011; Leadbeater, 2015). The colonies are held together by extracellular matrix (Dayel et al., 2011).

Crucial to this chapter is that Choanoflagellates *filter feed* by beating their flagella and thereby driving fluid through a collar of microvilli onto which prey (bacteria) get trapped and ingested. As discussed in the introduction, they live at low Reynolds numbers (Purcell, 1977), are when swimming freely force- and torque-free, and the surrounding flow u obeys the Stokes equations

$$\mu \nabla^2 u = \nabla p, \quad (5.1a)$$

$$\nabla \cdot u = 0, \quad (5.1b)$$

where p is the pressure field and μ the dynamic viscosity. Being neutrally buoyant, the far-field flow around both unicells and colonies of choanoflagellates is dominated by the stresslet contribution which decays as r^{-2} , as described in Sec. 1.1. The influx of fluid through a sphere of radius r is thus independent of r as $r \rightarrow \infty$. Using this result, recent work (Roper et al., 2013) argued that certain morphologies of colonies such as chains can increase this flux per constituent cell, thus potentially creating a *hydrodynamic feeding advantage* for

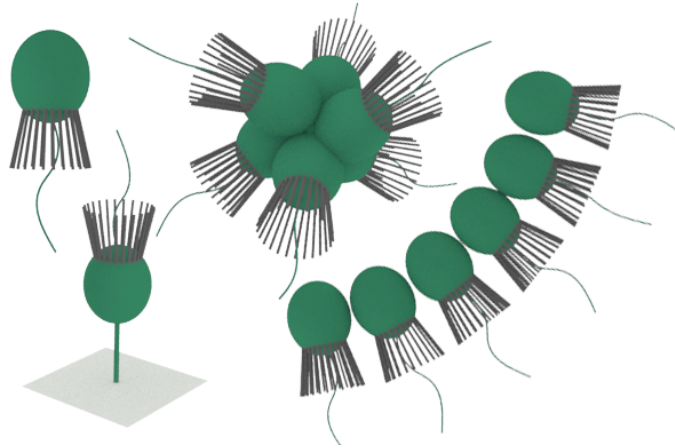


Figure 5.1 Morphologies of *S. rosetta* (as described in Dayel et al. (2011)) considered here. From left to right: swimming unicell, thecate cell, rosette colony and chain colony.

colonies, in a parallel to the situation previously examined for the green alga *Volvox* (Short et al., 2006; Solari et al., 2013). For choanoflagellates with n constituent cells, the influx \mathcal{F} was shown to grow faster than linearly with n already from $n = 2$ and even in the limit $n \rightarrow \infty$ (Roper et al., 2013).

Theoretically, filter feeding is possible even in the absence of diffusion of the target particles. In the contrasting case of absorbers, feeding occurs across a thin diffusive boundary layer, as has been studied in squirmer-type models (Magar and Pedley, 2005; Short et al., 2006) consisting of spheres with imposed tangential velocity fields. For squirmers it has been shown that optimal nutrient uptake precisely corresponds to optimal swimming, at all Péclet numbers (Michelin and Lauga, 2011). If this result carries over to the filter feeding of colonies of choanoflagellates, it would suggest that optimally swimming colonies would also be optimal feeding, in contrast to conclusions made based on long-range fluxes (Roper et al., 2013). Inspired by these studies, we examine here theoretically the near-field flows around colonial choanoflagellates and the near-field fluxes across the cell collars where feeding occurs.

5.2 Model

We approximate the choanoflagellate body by a sphere. Contrary to the prokaryotic case, eukaryotic flagella, such as those of choanoflagellates, are not rigid rotating helices but instead their shape is modulated by distributed molecular motors along the flagella to yield a whip-like beat. These eukaryotic beats will be studied further in Chapter 6. Time-averaging over this beat approximately yields a straight rod, which we will take as a proxy for the

flagella. Although there is evidence of some influence on the flow of the collar, via a pressure drop across it (Pettitt and Orme, 2002), we will ignore the collar in the modelling of the fluid flow. Including such effects would reduce the *absolute* flux of each cell, but our interest lie in the *relative* flux between colony cells and single cells, and thus such effects can be neglected here. Our system of (colonies of) choanoflagellates thus consists only of spheres and thin rods.

To calculate the flow in unbounded domains, we utilise a boundary element method. Cortez et al. (2005) found the Stokes flow due to a regularised, localised forcing

$$\mu \nabla^2 u - \nabla p = \delta^\varepsilon(r) f = \frac{15\varepsilon^4}{8\pi(r^2 + \varepsilon^2)^{7/2}} f, \quad (5.2)$$

where $r = |x - x_0|$ and δ^ε is a regularised version of the Dirac delta function. The solution,

$$\begin{aligned} u(x) &= \frac{(r^2 + 2\varepsilon^2) f + f \cdot (x - x_0)(x - x_0)}{8\pi\mu(r^2 + \varepsilon^2)^{3/2}} \\ &\equiv G^\varepsilon(x - x_0) \cdot f, \end{aligned} \quad (5.3)$$

is called the regularised Stokeslet, and indeed tends to the classic, singular Stokeslet as $\varepsilon \rightarrow 0$. The flow around a set of boundaries D in an infinite domain can then be approximated by the boundary integral equation (Cortez et al., 2005)

$$u(x) = \iint_D G^\varepsilon(x - x') \cdot f(x') dS \quad (5.4)$$

with a suitable choice of $\varepsilon(x)$.

Inspired by spectral methods, and as detailed in Appendix 5.A, we expand the force distribution on the flagellar elements in terms of Legendre polynomials and on cell bodies in terms of spherical harmonics. Boundary conditions are no-slip on the cell bodies. For the flagella boundary conditions we consider two cases. In both of these cases we take a constant velocity along the flagella: $u = u_0 \hat{d}_i$ (but other velocity distributions could easily be applied). \hat{d}_i is the orientation of the i -th cell's flagellum. Then u_0 may be regarded as known or we can let it be indirectly defined by letting the total propulsive force $f_0 \cdot \hat{d}_i$ that the flagellum exerts on the fluid be known. These two choices lead to similar behaviour for single cells, but will matter in the case of colonies. The method detailed in Appendix 5.A yields the surrounding flow u , and the translational and rotational swimming velocities, U and Ω .

5.3 Flow around Dimers

We begin by considering dimers: colonies consisting of two cells. The two can be placed in various relative orientations; we focus here on the subset of configurations in which the flagella lie in a plane and where both flagella make the same angle φ with the y -axis, since these are optimal configurations under variation of the remaining angles. Figures 5.2(a–b) shows the resulting flow fields for $\varphi = 0$ and $\varphi = \pi/2$, respectively. For $\varphi = 0$ the colony is swimming and the streamlines of passive tracers pass from the front of the colony to the back, while for $\varphi = \pi/2$ the forces of the two beating flagella exactly cancel and the colony does not swim. Passive tracers are dragged in from the sides. For all φ , $\Omega = 0$. From these calculations we can reproduce qualitatively the results of [Roper et al. \(2013\)](#). The long-range flux produced by colonies is given by

$$\mathcal{F} = \lim_{R \rightarrow \infty} \iint_{S_R, u \cdot \hat{n} > 0} u(x) \cdot \hat{n}(x) dS, \quad (5.5)$$

where S_R is the surface of a sphere with radius R and \hat{n} is the inward normal to this surface. The flux per cell, normalised by the flux for the single cell system, is shown in purple in Fig. 5.3. Solid curves is the case where u_0 is prescribed and dashed is the case $f_0 \cdot \hat{d}$ prescribed. Both cases have $\varphi = 0$ and $\varphi = \pi/2$ as local optima, the latter being globally optimal. This long-range flux per cell is larger than that of a single cell in the pole-pole configuration as previously found ([Roper et al., 2013](#)), although we find an overall lower magnitude of this long-range flux, due to hydrodynamic interactions between the two cells and differences in

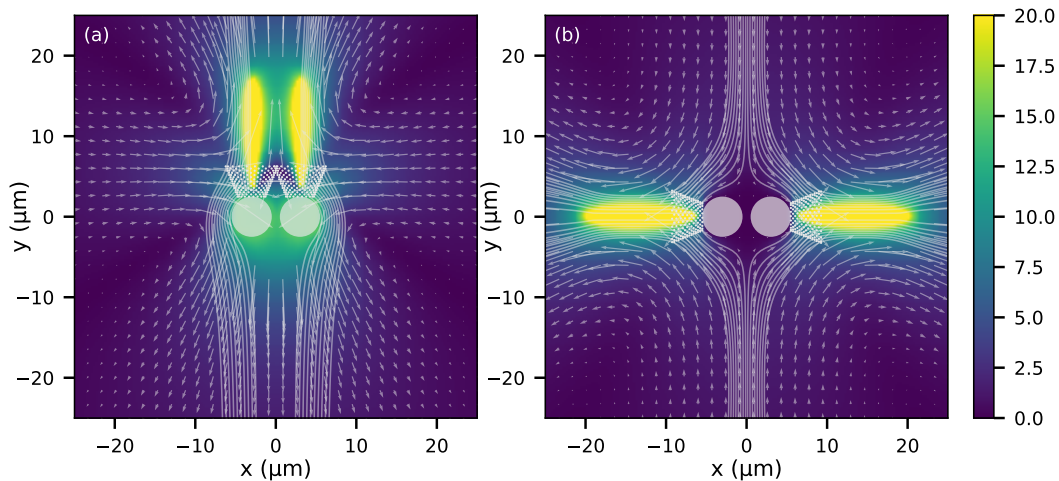


Figure 5.2 Fluid flow of dimers. (a–b) Background color and vector field quantify the velocity field in the laboratory frame, with color scale in units of $\mu\text{m/s}$. Streamlines are calculated in the swimming frame with $z = 0$. Configuration (a) has $\varphi = 0$ and (b) $\varphi = \pi/2$.

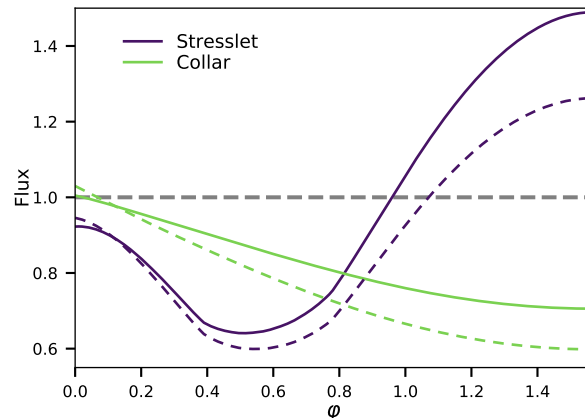


Figure 5.3 Flux of dimers. Influx through a sphere of radius $R \rightarrow \infty$ (neglecting advective flux) shown in purple and flux through the collar of cells in green. Fluxes are calculated per cell and normalised by the flux of a unicell. Solid lines are calculated with velocity described on the flagella and dashed lines with forces prescribed on the flagella.

geometry choices (e. g. distance between cells). We furthermore find an increased flux in the case of prescribed velocity over prescribed force.

The near-field flow enables us also to calculate the flux not just of an infinite sphere, but also at the actual collars where the choanoflagellates feed. We define the collars as the surface of a cone with lower radius $1.8\mu\text{m}$, upper radius $3.3\mu\text{m}$, and height $4.0\mu\text{m}$. Evaluating such fluxes allows for the inclusion of the flux due to swimming at speed U . While earlier work (Roper et al., 2013) found that this advective flux was negligible, this conclusion was based on use of the stresslet flow, which is only valid far away from the colony. Secondly, although the advective flux may be small compared to the rest of the flux in a particular system, it can still be important when evaluating the relative flux between systems, as indeed turns out to be the case here. We find that including the advective flux makes a significant change, and as shown in green in Fig. 5.3 by including this in the flux calculation across the collar, the swimming side-by-side configuration becomes globally optimal, and the advantage over single cells of colonies disappears (but does not become disadvantageous in the optimal configurations). Moreover, this behaviour is not strongly dependent on the shape of the collar or the distance between the two cells, in sharp contrast to the long-range flux, the value of which tends to infinity as this distance is increased. We also find that the prescribed force side-to-side system outperforms single cells slightly due to drag cancellation.

5.4 Diffusion Effects

The flux calculations above were done in the limit of infinite Péclet number, i. e. ignoring prey diffusion. This includes ignoring the effect of crowding: one cell eating leaves less food in the area for its neighbours. To study these effects we consider the axially symmetric pole-to-pole arrangement shown in Fig. 5.2b, the system which has the highest stresslet flux, and compare it to the single-celled swimmer (which is also axially symmetric). The prey field $c(x)$, which can be thought of as a probability field for the occurrence of prey, obeys the advection-diffusion equation

$$D\nabla^2 c - u \cdot \nabla c = -R(x) \quad (5.6)$$

with sinks $R(x)$ at the position of the collars: $R(x) = \sum_k R_k \delta(x - x_k)$. By posing the problem in a weak formulation with no-flux conditions at the sphere boundaries, we obtain

$$\begin{aligned} \int_{\Omega} \left[D\rho \frac{\partial c}{\partial \rho} \frac{\partial q}{\partial \rho} + D\rho \frac{\partial c}{\partial x} \frac{\partial q}{\partial x} + \rho u_{\rho} \frac{\partial c}{\partial \rho} q + \rho u_x \frac{\partial c}{\partial x} q \right] dx \\ = \sum_k Z_k q(x_k) \quad \forall q \in Q, \end{aligned} \quad (5.7)$$

where q is a test function from some Sobolev space Q , we have replaced y by ρ to make explicit the use of cylindrical coordinates, and $Z_k = \rho R_k$ such that $Z = \sum_k Z_k$ is representative for the prey uptake of the axially symmetric sinks. Another way to do this calculation would be to not add sinks and directly consider the flux across the collars due to the diffusive boundary layer.

Far away from the colony we require the prey field to be unaffected by the colony, and thus have the boundary condition $c(r) \rightarrow c_0$ as $r \rightarrow \infty$. Diffusion-dominated decay to c_0 will be of the form $c - c_0 \sim r^{-1}$, but for swimming colonies and large Péclet numbers, advection will dominate even far from the colony. Therefore, we have to solve the system on a massive domain. The mesh used is shown in Fig. 5.4. We produced this mesh by taking the geometry from the boundary element simulations and defined ad-hoc an area function $A(x)$ of required maximum triangle areas in order to obtain details near crucial elements such as the collar. We then subdivided each triangle recursively until the requirement was satisfied, at each iteration employing standard Delaunay triangulation.

Taking the choanoflagellates to be perfect eaters, the values of Z_k can be calculated by imposing $c(x) = 0$ on the collars. We solve Eq. (5.7) by implementing the finite element method as described in Appendix 5.B. The velocity field is taken from the boundary element

simulation and projected onto a solenoidal field to prevent finite numerical compressibility (details in Appendix 5.B).

In general, including diffusion increases the prey uptake for both the swimming unicell and the dimer colony. The quantity of interest is the prey uptake of the cells in the colony relative to that of the single swimming cell. Fig. 5.5 shows the solution $c(x)$ with $c_0 = 1$ for (a) the swimming unicell and (b) the pole-to-pole colony at two different values of diffusion constant D . The diffusion coefficient of passive prey, such as non-motile bacteria, can be calculated from the Stokes-Einstein relation $D = k_B T / 6\pi\mu a$, where a is the effective radius of the prey. For typical prey such as *Algoriphagus machopongensis* this yields $D = 0.5 \mu\text{m}^2/\text{s}$ (Roper et al., 2013), and increases for smaller prey. For motile prey the diffusion constant can be much larger, since it is enhanced by swimming. For an organism swimming with speed v and with rotational diffusion constant D_r , the effective diffusion constant scales as $D \sim v^2/D_r$, as demonstrated in Section 2.3.2. Thus for $v \sim 10 \mu\text{m}/\text{s}$ and $D_r \sim 0.1 \text{s}^{-1}$, $D \sim 10^2 - 10^3 \mu\text{m}^2/\text{s}$. Moreover, even for non-motile prey, the surrounding fluid environment may be inhomogeneous and noisy, and such noisy flow can heuristically be associated with an increased diffusion constant. Overall the prey diffusion constant can vary over several orders of magnitude.

Figure 5.6 shows how increasing the diffusion constant from zero gives a decrease in feeding of the colony compared to the swimming unicell at small diffusion constants. This arises from the fact that as diffusion increases, the fluid flux across the collar of the non-swimming colony is no longer pristine; the prey of the fluid crossing the collar in steady state have already been partly consumed. Swimming counteracts this effect, and accordingly the unicell is not affected significantly by this. As the diffusion constant becomes large, the effects of advection diminish. This regime is shown in the inset of Fig. 5.6. In the limit $D \rightarrow \infty$ (dashed line), the effects of advection can be ignored, and with it the difference due to flow produced by the unicell and the colony. However, also in this limit the unicell outperforms the colony, since there is a reduction in feeding due to the sharing of prey between cells in a colony.

The importance of advective fluxes due to swimming depends on the opening angle of the collar. The solid curve of Fig. 5.6 corresponds to the angle, 20° , shown in Fig. 5.5, the dashed curves show the result for smaller opening angles. The top (orange) curve is for straight collars, and even in this case is it quite advantageous to be swimming.

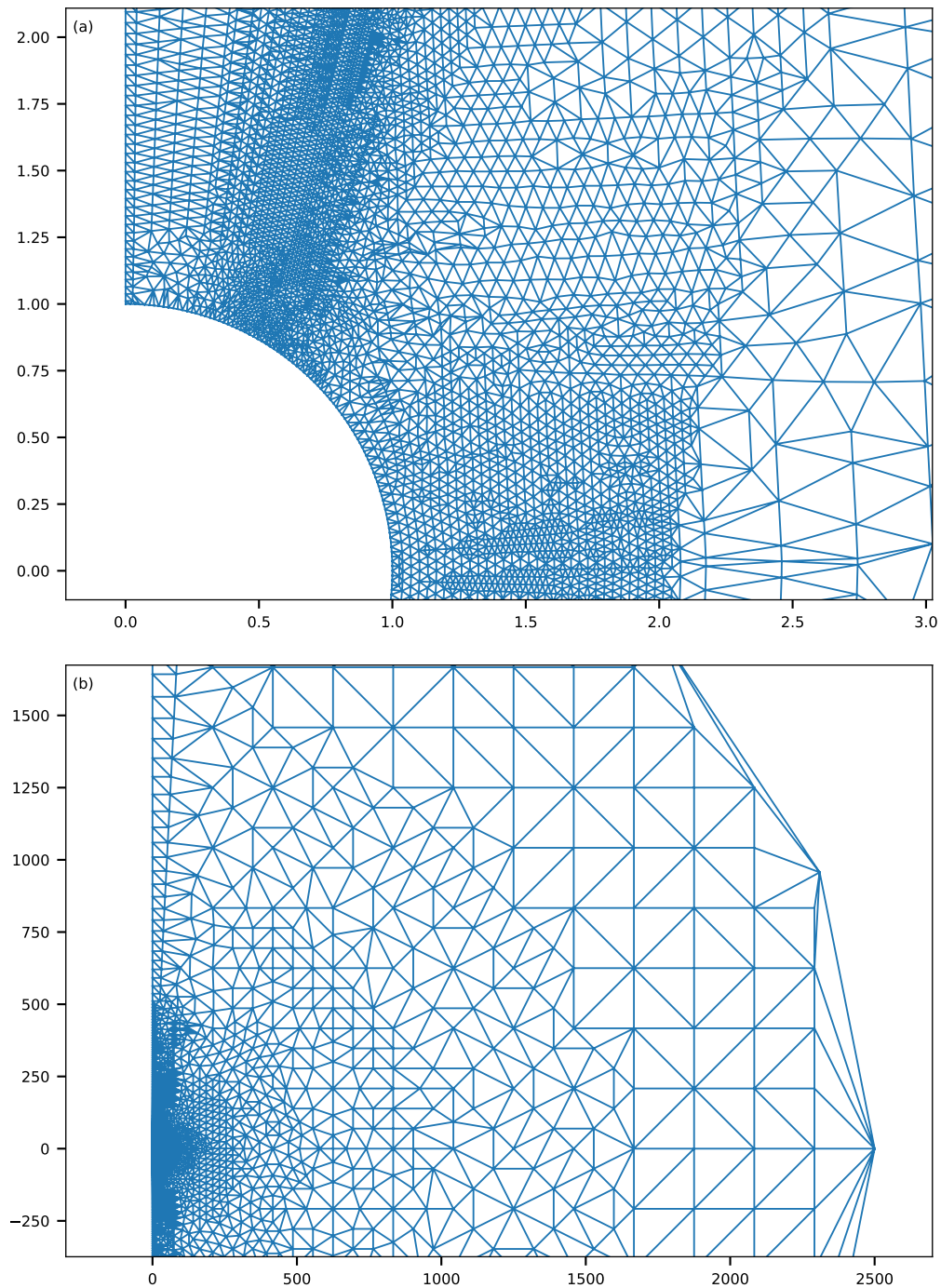


Figure 5.4 Computational mesh for solving advection-diffusion equation. Axes are in units of cell radius. (a) Close-up near cell showing the increasing detail near the cell and collar. (b) Zoom-out showing the edge where boundary condition $c = c_0$ is applied.

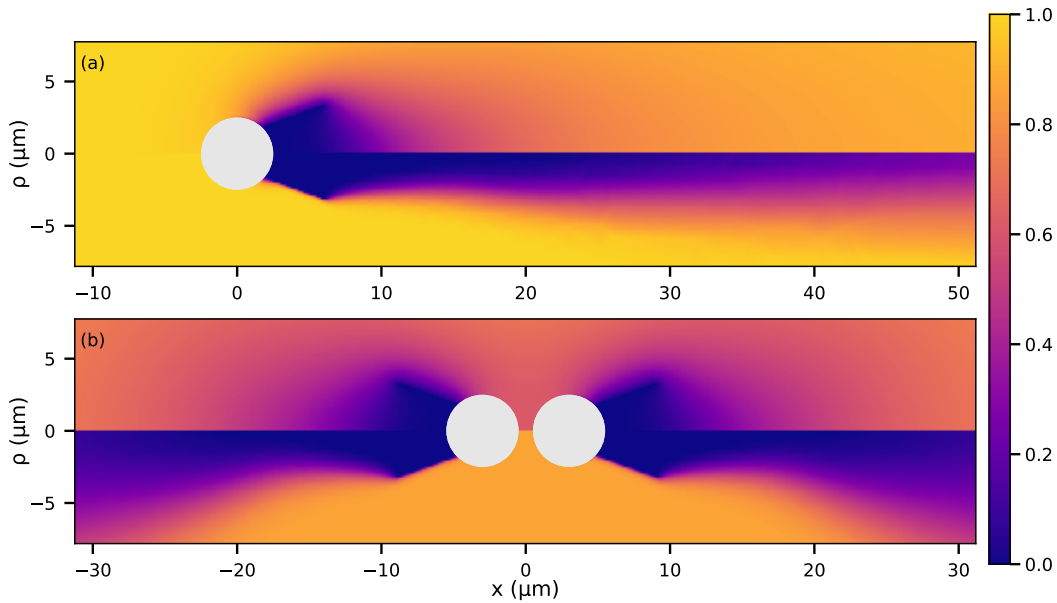


Figure 5.5 Prey field. (a) Axially symmetric field around swimming unicell at $D = 1 \mu\text{m}^2/\text{s}$ (lower part) and $D = 25 \mu\text{m}^2/\text{s}$ (upper part). Field is normalised to $c_0 = 1$ at $r \approx 10 \text{ mm}$. (b) Field around pole-to-pole dimer colony for the same values of D with velocity prescribed boundary condition on the flagella.

5.5 Larger Colonies

Colonies of *S. rosetta* exist with both chain and rosette morphologies. From the above study of dimers, we expect the collar fluid flux to be maximised for a straight chain of cells. Fig. 5.7 shows the result on chains of six cells with varying exterior cell-to-cell angle φ — from straight to regular hexagonal shapes. Fig. 5.7a shows the flow around the straight configuration ($\varphi = 0$), and Fig. 5.7b shows a semicircle ($\varphi \approx 0.63$). For the long-range flux, shown by the purple curve in Fig. 5.8, we find as in Roper et al. (2013) that the semicircle configuration is the global maximum. This rich behaviour of the long-range flux disappears completely in the collar flux as shown by the green curve in Fig. 5.8, and again we find that the globally optimal configuration is the one that swims the fastest: the straight chain.

To exemplify rosette colonies, we take a tetrahedron of cells and consider three distinct flagella configurations, the resulting flow fields of which are shown in Fig. 5.9: (a) flagella pointing outwards parallel with the line from the centre-of-mass to the cell, (b) flagella pointing approximately in the same direction, and (c) one flagellum propelling the colony and the remaining three rotating it. Configuration (a) will neither swim nor rotate. The flagella of configuration (b) point almost in the same direction, except for a small angle necessary to prevent overlap of collars. This configuration swims faster than a unicell due to

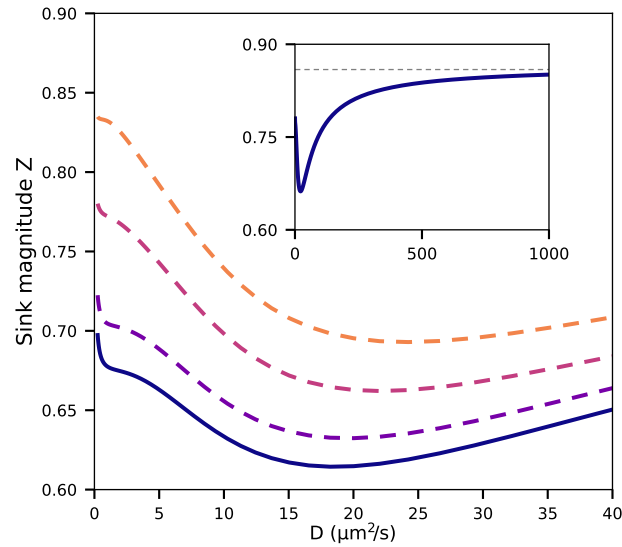


Figure 5.6 Predation efficiency. Ratio of Z for a cell in the dimer configuration to swimming unicell. $D = 0$ corresponds to infinite Péclet number and compares to the flux calculations shown in Fig. 5.2. Solid curve corresponds to configurations shown in (a,b) with collar opening angle $\sim 20^\circ$. Dashed lines for lower collar opening angles, $\sim 0^\circ, 4^\circ$ and 16° , respectively, from top to bottom. Inset shows a larger range of D and the asymptote of vanishing Péclet number (dashed).

reduced drag from the tetrahedron configuration. The collars of a rotating colony will sweep a larger volume, which is exemplified by configuration (c). In terms of the flux across the collar, we compare in Fig. 5.10 these tetrahedra to the other morphologies considered. The non-swimming tetrahedron is the worst of all considered configurations. With all considered configurations we have found the fastest swimmer also has the highest collar flux. This does not hold for configuration (b), however. Although it swims $\sim 20\%$ faster than a unicell, the proximity of neighbouring cells results in an overall lowered flux. Also individually, none of the constituent cells surpasses the flux of a single swimming cell, which is true for all configurations considered in this study. Furthermore, our flux calculations do not include the effects of prey sharing, as was considered in the section on diffusion effects. In fact in this configuration, many of the streamlines passing through the middle cell have already passed through neighbouring cells and so the feeding flux that we calculate is only an upper bound on the true value. The rotating colony (c) is also at the lower end of the collar flux. Since the flagella are already drawing the surrounding fluid through the collars, the extra volume swept by rotation makes no difference — one side of the collar will have an increased flux, but the opposing side will be approximately equally reduced, since rotating around the colony centre of mass gives the opposite effects on either side of the collar. As in the previous configuration, the effect of prey sharing is significant here as well. The propelling cell will

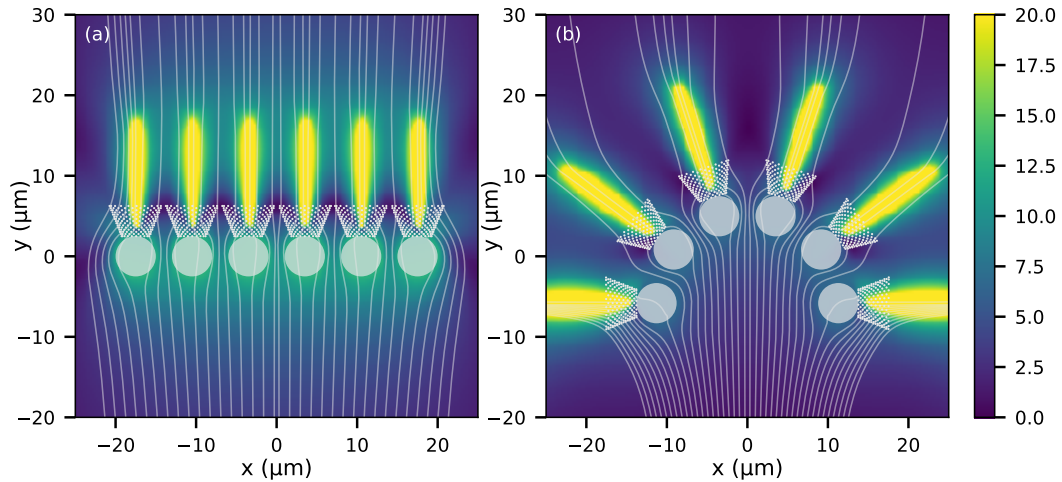


Figure 5.7 Fluid flow of chain colonies. (a-b) Background color shows the magnitude of the velocity field in the laboratory frame, with color scale in units of $\mu\text{m/s}$. Streamlines are calculated in the swimming frame from $y = -20 \mu\text{m}$, $z = 0.1 \mu\text{m}$ and projected onto the $z = 0$ plane. Configuration (a) has exterior cell-to-cell angle $\phi = 0$ and (b) $\phi = 36^\circ \approx 0.63$ rad, corresponding to a half circle and the maximum long-range flux.

have a reduced feeding efficiency because of the surrounding cells. We do not, however, observe streamlines from one of the rotating cells reaching one of the neighbours.

5.6 Thecate cells

For completeness, we must include in this study the sessile form of *S. rosetta*. These attach to a wall by building a so-called theca. Such single-celled sessile feeders have previously been studied (Higdon, 1979; Pepper et al., 2013). To account for the no-slip condition on the nearby wall, we add image singularity solutions to Eq. (5.3) at the mirror point over the wall. For a singular Stokeslet, the images that give no-slip on the wall are a Stokeslet of opposite sign, a potential dipole, and a Stokeslet doublet (Blake, 1971a; Rizzo, 1994). Similar to the unbounded version, Eq. (5.3), a regularised version is known (Ainley et al., 2008), which we exploit (with the correction of Smith (2009)) and replace G (in Appendix 5.A, Eq. (5.11)) with a tensor including these images. Fig. 5.11 shows the resulting flow. We consider straight thecate cells, which is the configuration with highest flux, although in the absence of external flow, feeding at an angle can be advantageous in order to reduce recirculating eddies (Pepper et al., 2013). In the inset of Fig. 5.11 the collar flux is plotted as a function of the height h above the wall that the cell is attached to. Overall the flux is reduced compared to the swimming unicell, but this results only holds in the absence of external flow. Being stuck to the wall, thecate cells gain an advantage from external flows that suspended cells do not. As

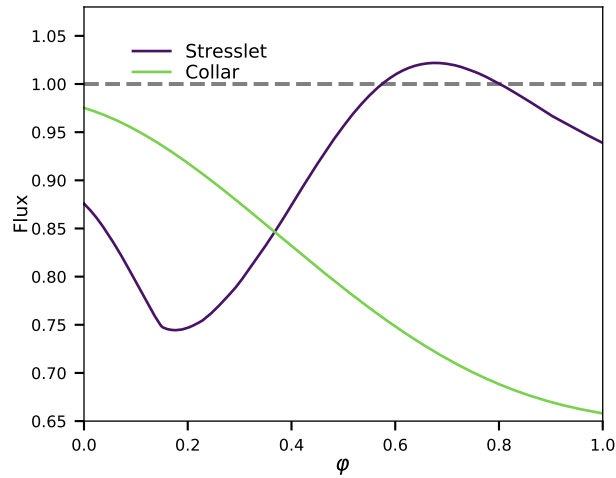


Figure 5.8 Flux of chain colonies. Influx through a sphere of radius $R \rightarrow \infty$ (neglecting advective flux) shown in purple and flux through the collar of cells in green. Boundary conditions are velocity-prescribed. The graph ends at $\phi = 60^\circ \approx 1.0$ rad corresponding to a regular hexagon.

long as the external flow is comparable to or larger than the swimming speed of a unicell, the thecate form becomes advantageous. Not surprisingly, Fig. 5.11 shows that placing the cell further away from the wall increases the flux; this is the very reason that the cells build a stalk on the theca. The difference in terms of flux between no stalk and an infinitely long stalk (dashed line in Fig. 5.11 inset) is about 10% of the flux of the swimming unicell.

5.7 Conclusions

We have found that swimming is the best strategy to maximise the prey flux across the feeding collar in choanoflagellates, in agreement with the result found for absorbing feeders modelled as squirmers (Michelin and Lauga, 2011), and that there is no hydrodynamic feeding advantage for colonies compared to single cells. With flagella orientations parallel to cell positions in rosette colonies, the swimming speeds will be significantly lowered. However, real rosette colonies tend to swim at speeds that are comparable to unicell slow-swimmers [Fig. 2.9]. One might hypothesise that the advective flux is a selection factor for flagellar orientations that allow swimming. Swimming moreover is a natural method for replenishing the surrounding fluid, and as discussed, thereby limit the hindering effects of diffusion. However, in this study we have only considered uniform and steady prey distributions. One could imagine distributions that disfavour fast swimmers, i. e. where such swimmers would quickly escape the local prey-rich areas, but where stationary rosette colonies could feed efficiently.

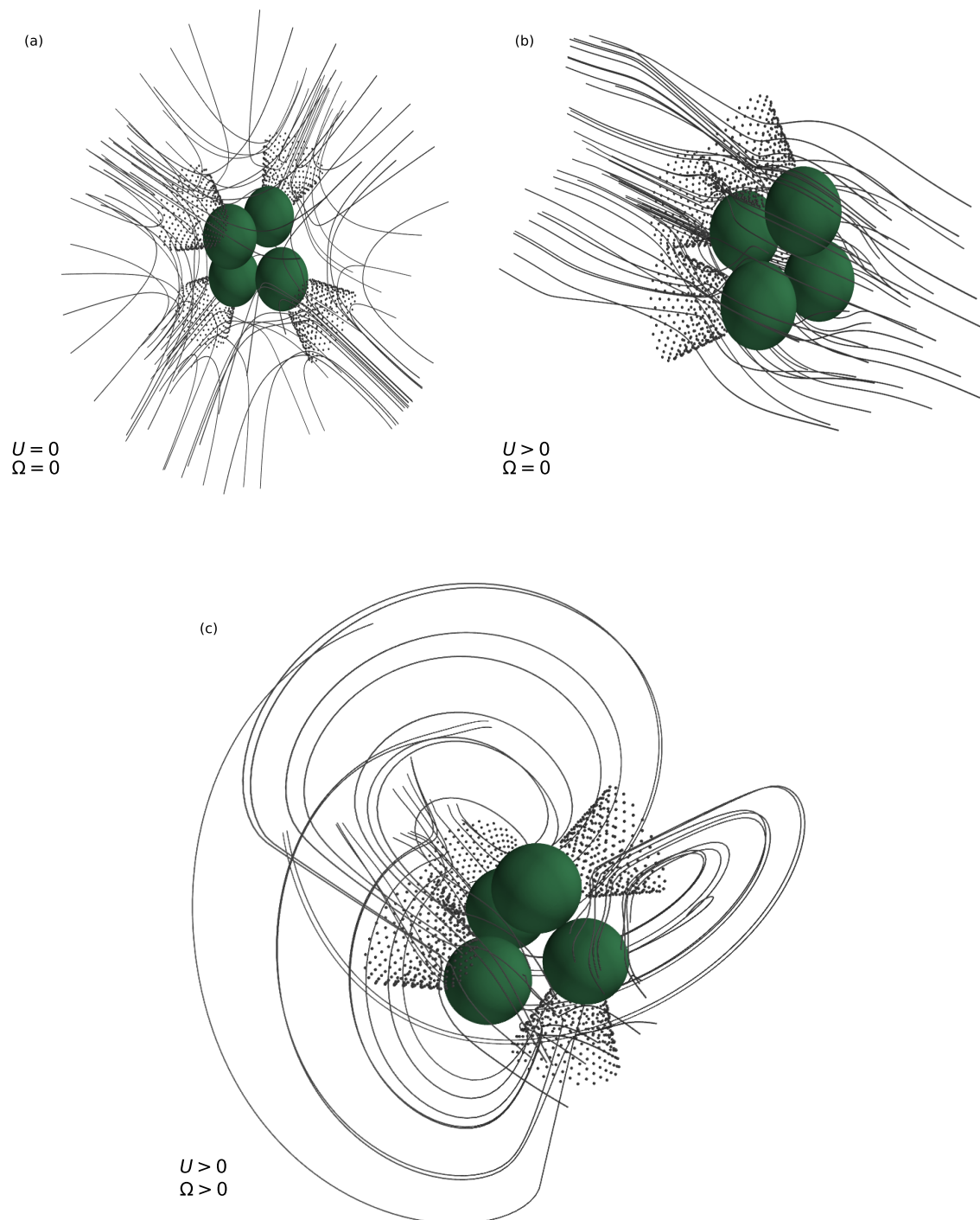


Figure 5.9 Tetrahedron rosette colonies and streamlines of the surrounding flow calculated in the swimming frame. (a) All flagella pointing outwards. (b) All flagella pointing approximately in the same direction, making the colony swim faster than a unicell. (c) One flagellum propelling the colony, the remaining rotating it.

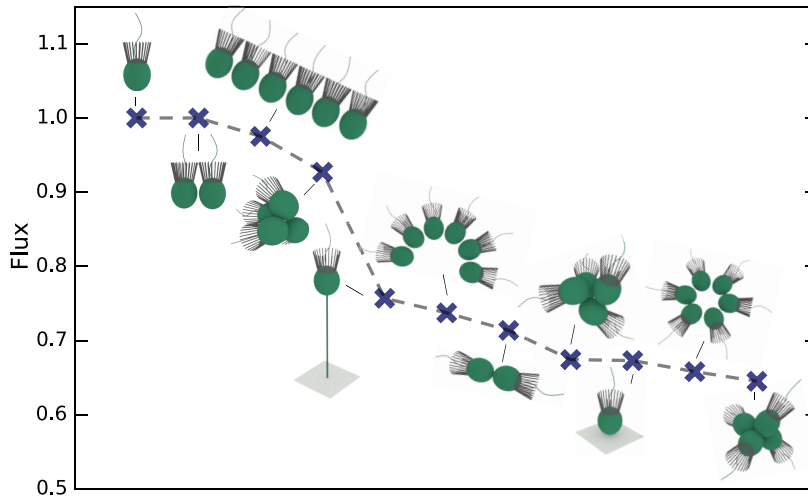


Figure 5.10 Overview of flux across collars on the various considered configurations in no external flow with velocity-prescribed boundary conditions. All normalised by the flux of the swimming unicell. From left to right: swimming unicell, side-by-side dimer, straight chain, straight rosette, long-stalk thecate cell, semi-circle chain, pole-to-pole dimer, rotating rosette, short-stalk thecate cell, hexagonal chain, parallel rosette.

Prey trajectories are more aligned with the collar for swimming cells than for stationary cells, and if the capture probability decreases with alignment (e. g. if prey bounce off the collar) this will favour stationary cells. But live imaging is needed to assess the magnitude of such an effect, and it would have to be very large in order to give to colonies the overall advantage. For *S. rosetta* the fact that colonies tend to form when a culture is kept in log phase, i. e. with plenty of prey, suggests that enhanced feeding efficiency per se is not a driving force behind colony formation, and other factors such as size as a prevention against predation could be more important. Taken together with the fact that a molecular species released by certain prey bacteria triggers the formation of the multicellular form (Alegado et al., 2012) suggests that the driving forces behind transitions to multicellularity are subtle indeed.

Appendix 5.A Boundary Element Method

The Stokes flow around thin elements such as thin rods is often described by slender body theory. Utilising the present framework they may also be described as in Eq. (5.3) by a line integral of regularised Stokeslets with ε suitably chosen to model the thickness of the line (Smith, 2009). Instead of discretising $f(x)$ over triangular elements, for example, we parametrise $f(x)$ on the spheres in terms of spherical harmonics and on the lines with

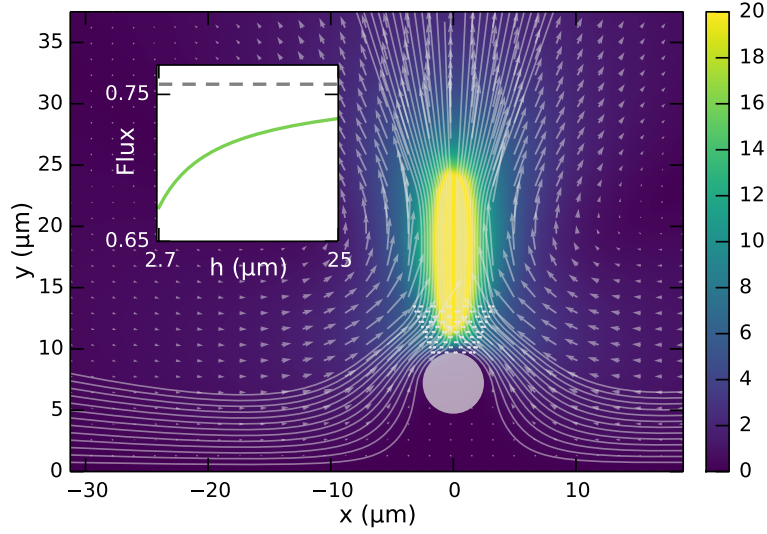


Figure 5.11 Thecate cell above wall at $y = 0$. Background color and vector field shows the velocity field, with color scale in units of $\mu\text{m/s}$. Streamlines are at $z = 0$. Inset shows collar flux normalised by that of a swimming unicell as a function of height h above the wall.

Legendre polynomials. On a sphere S_i we thus write

$$f_j^{S_i} = \sum_{l=0}^{\infty} \sum_{m=-l}^l c_{lm}^{ij} Y_{lm}(\phi, \theta), \quad (5.8)$$

where Y_{lm} are the real spherical harmonics defined in terms of the conventional spherical harmonics as

$$Y_{lm} = \begin{cases} Y_m^l & m = 0 \\ (-1)^m \sqrt{2} \text{Im}[Y_m^l] & m < 0 \\ (-1)^m \sqrt{2} \text{Re}[Y_m^l] & m > 0. \end{cases} \quad (5.9)$$

And on line ℓ_i we write

$$f_j^{\ell_i} = \sum_{n=0}^{\infty} c_n^{ij} P_n(s), \quad (5.10)$$

where P_n is the n -th Legendre polynomial. Eq. (5.4) thus becomes

$$\begin{aligned} u(x)_j = & \sum_{i=1}^{n_S} \sum_{l=0}^{\infty} \sum_{m=-l}^l c_{lm}^{ik} \int_{-\pi}^{\pi} d\phi \int_0^{\pi} \sin \theta d\theta \\ & G_{jk}(x - [r_i + ay(\phi, \theta)]) Y_{lm}(\phi, \theta) \\ & + \sum_{i=1}^{n_{\ell}} \sum_{n=0}^{\infty} c_n^{ik} \int_{-1}^1 ds G_{jk}(x - y_i(s)) P_n(s), \end{aligned} \quad (5.11)$$

where the Einstein summation is implied over k , G_{ij} is the (i, j) entry of G^e , and

$$y(\phi, \theta) = \begin{pmatrix} \sin \theta \cos \phi \\ \sin \theta \sin \phi \\ \cos \theta \end{pmatrix} \quad (5.12)$$

spans a sphere such that $r_i + ay(\phi, \theta)$ is a sphere of radius a centred on r_i . The flagella lines are spanned by

$$y_i(s) = \ell_i + \frac{s+1}{2} d_i, s \in [-1, 1], \quad (5.13)$$

where ℓ_i is the base position, \hat{d}_i its orientation, and $|d_i|$ its length. Truncating the spherical harmonic expansion at $l = n_Y$ and the Legendre expansion at $n = n_P$, we have $3n_S(1 + n_H)^2 + 3n_\ell(n_P + 1)$ unknown coefficients to determine. The integrals must be evaluated numerically. Gauss-Legendre quadrature enables exact numerical integration of polynomials, and for other functions gives good approximations to the integrals by

$$\int f(s) ds \simeq \sum_i w_i^\ell f(s_i), \quad (5.14)$$

where w_i^ℓ are weights associated with the quadrature points s_i . Likewise, Lebedev quadrature enables exact numerical integration of spherical harmonics. Thus spherical integrals can be numerically approximated as

$$\iint f(\phi, \theta) \sin \theta d\theta d\phi \simeq \sum_i w_i^S f(\phi_i, \theta_i), \quad (5.15)$$

where w_i^S are weights associated with the quadrature points (θ_i, ϕ_i) . The numerical schemes become exact if f can be expanded precisely up to some order by using an appropriate number of quadrature points.

Neutrally buoyant microorganisms, of which choanoflagellates are good approximations, are furthermore force- and torque-free. Therefore,

$$\sum_{i=1}^{n_S} \int_{S_i} f^{S_i}(x) dS + \sum_{i=1}^{n_\ell} \int_{\ell_i} f^{\ell_i}(x) d\ell = 0, \quad (5.16)$$

$$\sum_{i=1}^{n_S} \int_{S_i} x \times f^{S_i}(x) dS + \sum_{i=1}^{n_\ell} \int_{\ell_i} x \times f^{\ell_i}(x) d\ell = 0. \quad (5.17)$$

These equations set the swimming velocity U and rotational velocity Ω such that swimming drag forces and torques precisely cancel the propulsive ones. In the frame of reference of

the swimming organism we thus add to Eq. (5.11) the term $(U + x \times \Omega)_j = U_j + \varepsilon_{j pq} x_p \Omega_q$, where $\varepsilon_{j pq}$ is the Levi-Civita symbol. In terms of the coefficients $\{c\}$, Eq. (5.16) becomes

$$2\sqrt{\pi} \sum_{i=1}^{n_S} c_{00}^{ij} + 2 \sum_{i=1}^{n_\ell} c_0^{ij} = 0 \quad (5.18)$$

and Eq. (5.17)

$$\begin{aligned} & \sum_{i=1}^{n_S} \varepsilon_{j pq} \left[2\sqrt{\pi} (r_i)_p c_{00}^{iq} + 2a \sqrt{\frac{\pi}{3}} c_{1,m(q)}^{iq} \right] \\ & + \sum_{i=1}^{n_\ell} \varepsilon_{j pq} \left[[2(\ell_i)_p + (d_i)_p] c_0^{iq} + \frac{1}{3} (d_i)_p c_1^{iq} \right] = 0, \end{aligned} \quad (5.19)$$

where $m(1) = 1$, $m(2) = -1$, $m(3) = 0$.

By choosing the same of number collocation points $\{x_i\}$ for evaluating the velocities $\{u(x_i)\}$ as the total number of coefficients $\{c\}$ the linear system of equations can be solved for $\{c\}$, U and Ω .

By exploiting orthogonality, we could expand u on the spheres and lines in terms of spherical harmonics and Legendre polynomials, i. e. as

$$(u_i)_j = \sum_{l=0}^{\infty} \sum_{m=-l}^l b_{lm}^{ij} Y_{lm}(\phi, \theta), \quad (5.20)$$

on sphere i and

$$(u_i)_j = \sum_{n=0}^{\infty} b_n^{ij} P_n(s) \quad (5.21)$$

on the flagellum i . Using orthogonality,

$$\iint Y_{lm}(\phi, \theta) Y_{\bar{l}\bar{m}}(\phi, \theta) \sin \theta \, d\theta \, d\phi = \delta_{l\bar{l}} \delta_{m\bar{m}}, \quad (5.22)$$

$$\int P_n(s) P_{\bar{n}}(s) \, ds = \frac{2}{2n+1} \delta_{n\bar{n}}, \quad (5.23)$$

one finds

$$b_{lm}^{ij} = \iint [u_i(r_i + ay(\phi, \theta))]_j Y_{lm}(\phi, \theta) \sin \theta \, d\theta \, d\phi, \quad (5.24)$$

$$b_n^{ij} = \frac{2n+1}{2} \int [u_i(y_i(s))]_j P_n(s) \, ds. \quad (5.25)$$

In other words, $\{b_{lm}^{ijs}\}$, $\{b_n^{ijs}\}$ are easy to calculate from the boundary conditions directly.

We can then solve for the c coefficient in the modified equations,

$$\begin{aligned}
 b_{\tilde{l}\tilde{m}}^{\tilde{i}j} &= \sum_{i=1}^{n_S} \sum_{l=0}^{\infty} \sum_{m=-l}^l c_{lm}^{ik} \iiint\!\!\!\int G_{jk}([r_{\tilde{i}} + ay(\tilde{\phi}, \tilde{\theta})] - [r_i + ay(\phi, \theta)]) \\
 &\quad \times Y_{lm}(\phi, \theta) Y_{\tilde{l}\tilde{m}}(\tilde{\phi}, \tilde{\theta}) \sin \theta \sin \tilde{\theta} d\theta d\phi d\tilde{\theta} d\tilde{\phi} \\
 &+ \sum_{i=1}^{n_S} \sum_{n=0}^{\infty} c_n^{ik} \iiint G_{jk}([r_{\tilde{i}} + ay(\tilde{\phi}, \tilde{\theta})] - y_i(s)) P_n(s) Y_{\tilde{l}\tilde{m}}(\tilde{\phi}, \tilde{\theta}) \sin \tilde{\theta} ds d\tilde{\theta} d\tilde{\phi} \\
 &+ 2\sqrt{\pi} [U_j + \varepsilon_{j pq} (r_i)_p \Omega_q] \delta_{\tilde{l}0} \delta_{\tilde{m}0} + 2a\sqrt{\frac{\pi}{3}} \varepsilon_{j pq} \Omega_q \delta_{\tilde{m}, m(p)} \delta_{\tilde{l}1}
 \end{aligned} \tag{5.26}$$

and

$$\begin{aligned}
 b_{\tilde{n}}^{\tilde{i}j} &= \frac{2\tilde{n}+1}{2} \sum_{i=1}^{n_S} \sum_{l=0}^{\infty} \sum_{m=-l}^l c_{lm}^{ik} \iiint\!\!\!\int G_{jk}(y_{\tilde{i}}(\tilde{s}) - [r_i + ay(\phi, \theta)]) Y_{lm}(\phi, \theta) P_{\tilde{n}}(\tilde{s}) \sin \theta d\theta d\phi d\tilde{s} \\
 &+ \frac{2\tilde{n}+1}{2} \sum_{i=1}^{n_S} \sum_{n=0}^{\infty} c_n^{ik} \iint G_{jk}(y_i(\tilde{s}) - y_i(s)) P_n(s) P_{\tilde{n}}(\tilde{s}) ds d\tilde{s} \\
 &+ 2U_j \delta_{\tilde{n}0} + \sum_{n=0}^{\infty} \varepsilon_{j pq} \Omega_q \int (y_i(s))_p P_{\tilde{n}}(s) ds.
 \end{aligned} \tag{5.27}$$

However, for the systems considered here, with this method, the computational bottle neck becomes the Gaussian quadratures, the number of which is squared when this method were employed compared to the direct method. Thus it was computationally more efficient to not expand the boundary conditions in basis functions as well. It has recently come to our attention that a similar approach can actually be made very efficient in a system consisting only of spheres using non-regularised expansions (Singh et al., 2015).

Fig. 5.12 compares the boundary element solution (using $n_Y = 3$) to the analytical solution of the flow around a sphere, given in spherical coordinates by

$$u_r = U_0 \left(1 + \frac{a^3}{2r^3} - \frac{3a}{2r} \right) \cos \theta, \tag{5.28}$$

$$u_\theta = -U_0 \left(1 - \frac{a^3}{4r^3} - \frac{3a}{4r} \right) \sin \theta. \tag{5.29}$$

The numerical solution matches the analytical extremely well, the maximum relative error being 0.05 near the cell. The solution becomes perfect as one moves away from the sphere. Some error must be present, since regularised Stokeslets produce a slightly “smeared-out” sphere, whereas the analytical solution considers a perfectly rigid sphere.

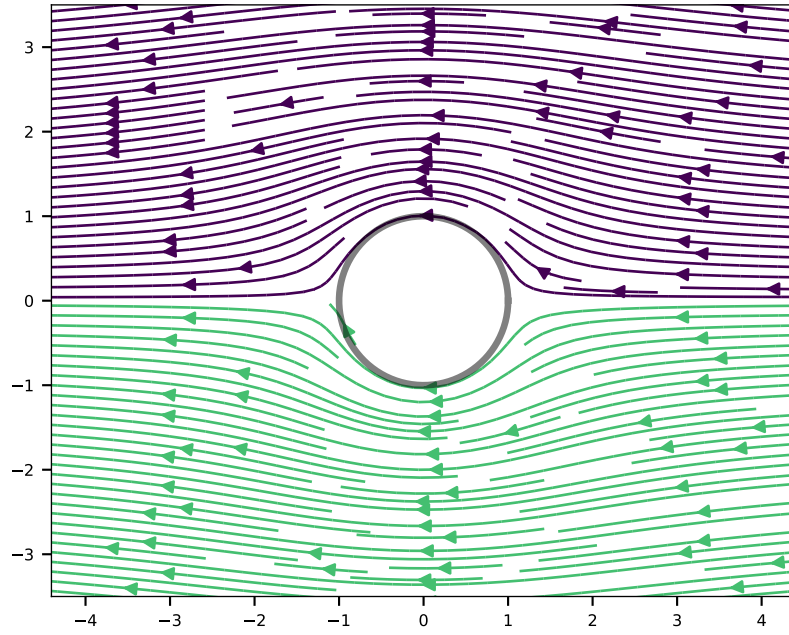


Figure 5.12 Stokes flow around a moving sphere (in the frame of reference of the sphere). Top (purple) from boundary element solution with the spherical harmonic expansion truncated at $n_Y = 3$. Bottom (green) shows analytical solution.

We can also compare to the case of a Stokeslet outside a sphere, which can be solved analytically using the method of images. Consider a sphere of radius $a = 1$ located at x_1 and a Stokeslet at x_2 . Define $R = |x_2 - x_1|$ and $d = (x_2 - x_1)/R$. The solution for a Stokeslet force that is axis-symmetric, i. e. $F = F d$ is given in part by normal Stokeslet solution and in part by images all located at a point x_2^* inside sphere defined by being on the lines between x_1 and x_2 , and obeying $|x_1 - x_2^*| |x_1 - x_2| = 1$. With these definitions the solution is (Kim and Karrila, 2005)

$$v_i(x) = F d_j G_{ij}(x - x_2) + \left(\frac{3}{2R} - \frac{1}{2R^3} \right) F d_j G_{ij}(x - x_2^*) \\ + \left(\frac{1}{R^2} - \frac{1}{R^4} \right) F d_j d_k \partial_k G_{ij}(x - x_2^*) + \frac{1}{4R} \left(1 - \frac{1}{R^2} \right)^2 F d_j \nabla^2 G_{ij}(x - x_2^*). \quad (5.30)$$

Fig. 5.13 shows this solution compared to that obtained using our boundary element method using $n_Y = 6$, where we have added a singular Stokeslet at $x = 1.5$.

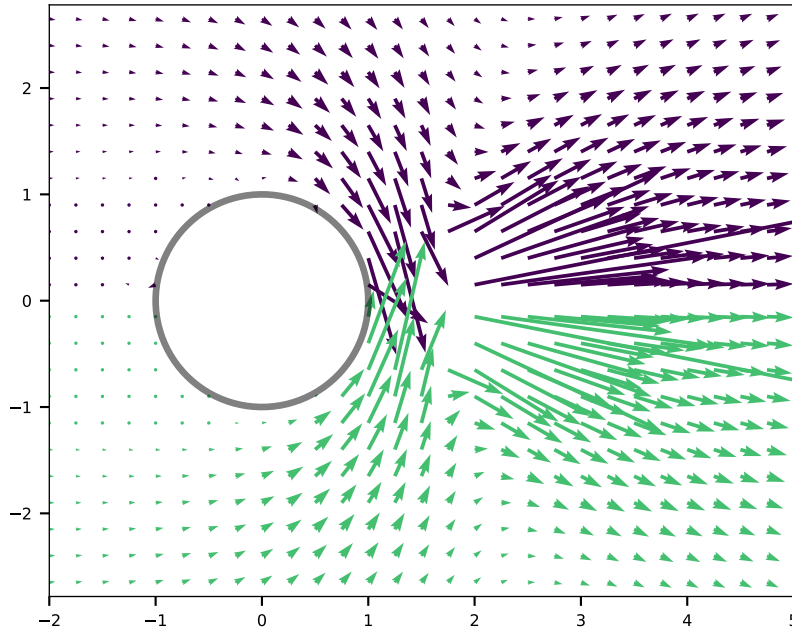


Figure 5.13 Stokeslet outside a sphere. Top (purple) from boundary element solution with the spherical harmonic expansion truncated at $n_Y = 6$. Bottom (green) shows analytical solution.

Appendix 5.B Finite Element Method

The advection-diffusion equation must be solved on the irregular grid shown in Fig. 5.4. For this we turn to the Finite Element Method, which is very natural to formulate on irregular grids. We furthermore need to impose the axial symmetry of our system and interpolate the Boundary Element solutions of the flow field onto the grid. These requirements together forces us to manually implement the method. The implementation used is described (fairly informally) here.

5.B.1 Laplace Equation

To introduce the method, consider the Laplace equation

$$\nabla^2 p(x) = 0. \quad (5.31)$$

This can equally be formulated in a weak formulation as

$$\int [\nabla^2 p(x)] q(x) dx = 0 \quad \forall q \in Q, \quad (5.32)$$

where Q is the solution space and q is called a ‘test function’.

We denote our mesh M_h , which contains nodes $\{N_i\}$ and triangles $\{T_i\}$ connecting the nodes. The true solution space Q can then be approximated by linear basis functions on each triangle. In other words; our numerical approach is to look for the best solution in the function space

$$Q_h = \{q \in Q \mid q(x) = a_i \cdot x + b_i, x \in T_i \in M_h\}. \quad (5.33)$$

A complete basis $\{\phi_i\}$ for Q_h is indirectly defined by requiring

$$\phi_i(N_j) = \begin{cases} 1 & : i = j, \\ 0 & : i \neq j. \end{cases} \quad (5.34)$$

Any basis function ϕ_i centred on $N_i = (x_1, y_1)$ will have the form

$$\phi_i(x) = \alpha_1 + \alpha_2 x + \alpha_3 y \quad (5.35)$$

inside any triangle with vertices $(x_1, y_1), (x_2, y_2), (x_3, y_3)$. The coefficients $\alpha = (\alpha_1, \alpha_2, \alpha_3)^T$ are determined by the nodal point coordinates alone,

$$\begin{pmatrix} 1 & x_1 & y_1 \\ 1 & x_2 & y_2 \\ 1 & x_3 & y_3 \end{pmatrix} \alpha = \begin{pmatrix} 1 \\ 0 \\ 0 \end{pmatrix}. \quad (5.36)$$

This matrix is invertible since (obviously) the coordinates span a triangle. Thus we find

$$\alpha = \frac{1}{2A} \begin{pmatrix} x_2 y_3 - x_3 y_2 \\ y_2 - y_3 \\ x_3 - x_2 \end{pmatrix} \quad (5.37)$$

where

$$A = \frac{1}{2} \begin{vmatrix} 1 & x_1 & y_1 \\ 1 & x_2 & y_2 \\ 1 & x_3 & y_3 \end{vmatrix} \quad (5.38)$$

is area of the triangle. We may thus describe the part of any basis function within a neighbouring triangle by

$$\phi_i(x) = \frac{1}{2A} [(x_2 y_3 - x_3 y_2) + (y_2 - y_3)x + (x_3 - x_2)y], \quad (5.39)$$

and any function $p \in Q_h$ can be written as

$$p(x) = \sum_i p_i \phi_i(x). \quad (5.40)$$

We shall denote $p = (p_1, p_2, \dots, p_N)^T$.

Some useful integrals over triangles to be used in the following are

$$\int_{T_i} dx = A, \quad (5.41)$$

$$\int_{T_i} x dx = \frac{A}{3} (x_1 + x_2 + x_3), \quad (5.42)$$

$$\int_{T_i} y dx = \frac{A}{3} (y_1 + y_2 + y_3). \quad (5.43)$$

Cartesian

Expanding the Laplace equation, Eq. (5.32), in our basis functions we find

$$\sum_i p_i \int_{\Omega} [\nabla^2 \phi_i] \phi_j dx = 0 \quad \text{for } j = 1..N, \quad (5.44)$$

which by partial integration and applying no-flux boundary conditions yields

$$\sum_i p_i \int_{\Omega} (\nabla \phi_i) \cdot (\nabla \phi_j) dx = 0 \quad \text{for } j = 1..N. \quad (5.45)$$

Within a specific triangle, we write

$$\phi_i(x) = \frac{1}{2A} [(x_2^i y_3^i - x_3^i y_2^i) + (y_2^i - y_3^i)x + (x_3^i - x_2^i)y], \quad (5.46)$$

$$\phi_j(x) = \frac{1}{2A} [(x_2^j y_3^j - x_3^j y_2^j) + (y_2^j - y_3^j)x + (x_3^j - x_2^j)y]. \quad (5.47)$$

Then within that triangle

$$(\nabla \phi_i) \cdot (\nabla \phi_j) = \frac{1}{4A^2} [(y_2^i - y_3^i)(y_2^j - y_3^j) + (x_3^i - x_2^i)(x_3^j - x_2^j)] \quad (5.48)$$

and thus

$$\int_T (\nabla \phi_i) \cdot (\nabla \phi_j) dx = \frac{1}{4A} [(y_2^i - y_3^i)(y_2^j - y_3^j) + (x_3^i - x_2^i)(x_3^j - x_2^j)]. \quad (5.49)$$

Axial symmetry

Let $x \rightarrow \rho \geq 0$ be the radial component in cylindrical coordinates. Now

$$\int_{\Omega} [\nabla^2 \phi_i] \phi_j \, dx = 0 \quad (5.50)$$

becomes (with axial symmetry applied)

$$\int_{\Omega} \left[\frac{1}{\rho} \frac{\partial}{\partial \rho} \left(\rho \frac{\partial \phi_i}{\partial \rho} \right) \right] \phi_j \, dx + \int_{\Omega} \left[\frac{\partial^2 \phi_i}{\partial y^2} \right] \phi_j \, dx = 0, \quad (5.51)$$

which by partial integration yields

$$\int_{\Omega} \rho \frac{\partial \phi_i}{\partial \rho} \frac{\partial \phi_j}{\partial \rho} \, dx + \int_{\Omega} \frac{\partial \phi_i}{\partial y} \frac{\partial \phi_j}{\partial y} \, dx = 0, \quad (5.52)$$

or

$$\int_{\Omega} \frac{\partial \phi_i}{\partial \rho} \frac{\partial \phi_j}{\partial \rho} \, dx + \int_{\Omega} \frac{\partial \phi_i}{\partial y} \frac{\partial \phi_j}{\partial y} \, dx - \int_{\Omega} \frac{\partial \phi_i}{\partial \rho} \frac{\phi_j}{\rho} \, dx = 0. \quad (5.53)$$

The first two terms are the same as the Cartesian terms, but a correction term has appeared.

In a triangle the integrand evaluates to

$$\frac{\partial \phi_i}{\partial \rho} \frac{\phi_j}{\rho} = \frac{1}{4A^2 \rho} [y_2^i - y_3^i] \left[(x_2^j y_3^j - x_3^j y_2^j) + (y_2^j - y_3^j) \rho + (x_3^j - x_2^j) y \right], \quad (5.54)$$

the integral of which involves logarithms.

Removing the axis singularity

If we want to consider problems at $\rho = 0$ the current formulation does not work. Instead we multiply the entire equation by ρ before integrating:

$$\int_{\Omega} \left[\frac{\partial}{\partial \rho} \left(\rho \frac{\partial \phi_i}{\partial \rho} \right) \right] \phi_j \, dx + \int_{\Omega} \left[\frac{\partial^2 \phi_i}{\partial y^2} \right] \rho \phi_j \, dx = 0, \quad (5.55)$$

which becomes after partial integration becomes

$$\int_{\Omega} \rho \frac{\partial \phi_i}{\partial \rho} \frac{\partial \phi_j}{\partial \rho} \, dx + \int_{\Omega} \rho \frac{\partial \phi_i}{\partial y} \frac{\partial \phi_j}{\partial y} \, dx = 0. \quad (5.56)$$

We calculate

$$\int_T \rho \frac{\partial \phi_i}{\partial \rho} \frac{\partial \phi_j}{\partial \rho} dx = \frac{1}{12A} (x_1^i + x_2^i + x_3^i)(y_2^i - y_3^i)(y_2^j - y_3^j), \quad (5.57)$$

$$\int_T \rho \frac{\partial \phi_i}{\partial y} \frac{\partial \phi_j}{\partial y} dx = \frac{1}{12A} (x_1^i + x_2^i + x_3^i)(x_3^i - x_2^i)(x_3^j - x_2^j). \quad (5.58)$$

5.B.2 Advection-Diffusion Equation

For incompressible flow,

$$D\nabla^2 p(x) - v \cdot \nabla p(x) = 0. \quad (5.59)$$

If we take v constant within triangles, in the weak formulation the new term becomes (with no sign change from partial integration)

$$v_x \int_T \frac{\partial \phi_i}{\partial x} \phi_j dx + v_y \int_T \frac{\partial \phi_i}{\partial y} \phi_j dx \quad (5.60)$$

in the Cartesian formulation. In axial symmetry with coordinate singularity removed we have

$$v_\rho \int_T \rho \frac{\partial \phi_i}{\partial \rho} \phi_j dx + v_y \int_T \rho \frac{\partial \phi_i}{\partial y} \phi_j dx \quad (5.61)$$

The new integral needed is

$$\begin{aligned} \int_T \rho \phi_j dx &= \frac{1}{6} (x_1 + x_2 + x_3)(x_2 y_3 - x_3 y_2) + \frac{1}{12} (y_2 - y_3)(x_1^2 + x_2^2 \\ &\quad + x_2 x_3 + x_3^2 + x_1(x_2 + x_3)) + \frac{1}{24} (x_3 - x_2)(x_1(2y_1 + y_2 + y_3) \\ &\quad + x_2(y_1 + 2y_2 + y_3) + x_3(y_1 + y_2 + 2y_3)) \end{aligned} \quad (5.62)$$

since $\frac{\partial \phi_i}{\partial \rho}$ and $\frac{\partial \phi_i}{\partial y}$ are constant. All variables have implied j indices.

5.B.3 Assessing Flux

We wish to calculate the flux across the collars. However, if we simply impose $c(x) = 0$ at the collars, the advective flux will be zero. To correctly calculate the flux, we add to the equation sink terms $R(x)$ as

$$D\nabla^2 p(x) - v \cdot \nabla p(x) - \sum_k R_k \delta(x - x_k) = 0. \quad (5.63)$$

For perfect eaters, the R_k can be tuned, i. e. as Lagrange multipliers, to obey the zero concentration boundary conditions. The integrals are

$$\int_{\Omega} \delta(x - x_k) \phi_j dx = \phi_j(x_k) = \delta_{jk}, \quad (5.64)$$

where the last equality holds if x_k is also a node point.

5.B.4 Ensuring Incompressibility

The velocity field v from the boundary element simulation is, naturally, incompressible, but evaluating it on a grid can introduce small numerical compressibility. We remove this by projecting v onto a solenoidal field. Any vector field can be decomposed into $v = v_{\text{sol}} + \nabla\psi$, where v_{sol} is a purely solenoidal field. Taking the divergence of this equation we have

$$\nabla^2\psi = \nabla \cdot v \quad (5.65)$$

from which we can determine ψ and then $v_{\text{sol}} = v - \nabla\psi$.

With axial symmetry this becomes

$$\frac{\partial}{\partial \rho} \left(\rho \frac{\partial \psi}{\partial \rho} \right) + \rho \frac{\partial^2 \psi}{\partial y^2} = \frac{\partial(\rho v_{\rho})}{\partial \rho} + \rho \frac{\partial v_y}{\partial y} \quad (5.66)$$

Expanding in basis functions we find

$$\sum_i p_i \left[\int_{\Omega} \rho \frac{\partial \phi_i}{\partial \rho} \frac{\partial \phi_j}{\partial \rho} dx + \int_{\Omega} \rho \frac{\partial \phi_i}{\partial y} \frac{\partial \phi_j}{\partial y} dx \right] = \int_{\Omega} \rho v_{\rho} \frac{\partial \phi_j}{\partial \rho} dx + \int_{\Omega} \rho v_y \frac{\partial \phi_j}{\partial y} dx. \quad (5.67)$$

For this we need

$$\int_T \rho \frac{\partial \phi_j}{\partial \rho} dx = \frac{1}{6} (x_1^j + x_2^j + x_3^j)(y_2^j - y_3^j), \quad (5.68)$$

$$\int_T \rho \frac{\partial \phi_j}{\partial y} dx = \frac{1}{6} (x_1^j + x_2^j + x_3^j)(x_3^j - x_2^j). \quad (5.69)$$

The correction to the x -velocity, for instance, is

$$\Delta v_x = -\frac{\partial \psi}{\partial x} = - \left[p_i \frac{\partial \phi_i}{\partial x} + p_j \frac{\partial \phi_j}{\partial x} + p_k \frac{\partial \phi_k}{\partial x} \right], \quad (5.70)$$

where $\{i, j, k\}$ are the triangle nodes.

Chapter 6

Synchronisation of Flagella

6.1 Introduction

This Chapter is a preliminary study of the synchronisation of flagella in *Chlamydomonas reinhardtii*. *Chlamydomonas* has two flagella that typically beat in synchrony and in phase. This is the classic breast-stroke beat shown in Fig. 1.1 in the introduction to this thesis. However, some mutants of *Chlamydomonas* show a stochastic switching between in-phase (IP) and anti-phase (AP) beating (Leptos et al., 2013; Wan et al., 2013). This switching leads to run-and-tumble-like trajectories (Polin et al., 2009), which could potentially be used for navigation. Similar gait-switching has been found in other green algae (Wan and Goldstein, 2017).

Fig. 6.1 shows how the flagella waveforms differ during IP and AP beating, respectively [experimental data provided by Kirsty Wan]. IP beating has a frequency around 60 Hz, whereas the AP mode beats at around 85 Hz. The difference in waveforms is not the result of inertia, since such effects, as discussed several times, are negligible in Stokes flow. During the IP mode, single *slips* can also occur, in which one flagellum makes one extra beat over the course of a few beats (Wan et al., 2013). Interestingly, the beat waveform during these slips have the same instantaneous frequency and waveform as the AP state (Leptos et al., 2013).

In this Chapter, we introduce a theoretical model for the beating flagella in order to understand these synchronous states. The ultimate goal of this study is to be able to understand both the synchrony (IP and AP) and the stochastic switching. However, this chapter is only a preliminary study and we start with the simpler goal of trying to understand only the flagella *shapes* in the two phases.

Different models have been used to model flagella. Ignoring the molecular machinery that leads to the flagella beating, kinematic models (Wiggins and Goldstein, 1997) are simple

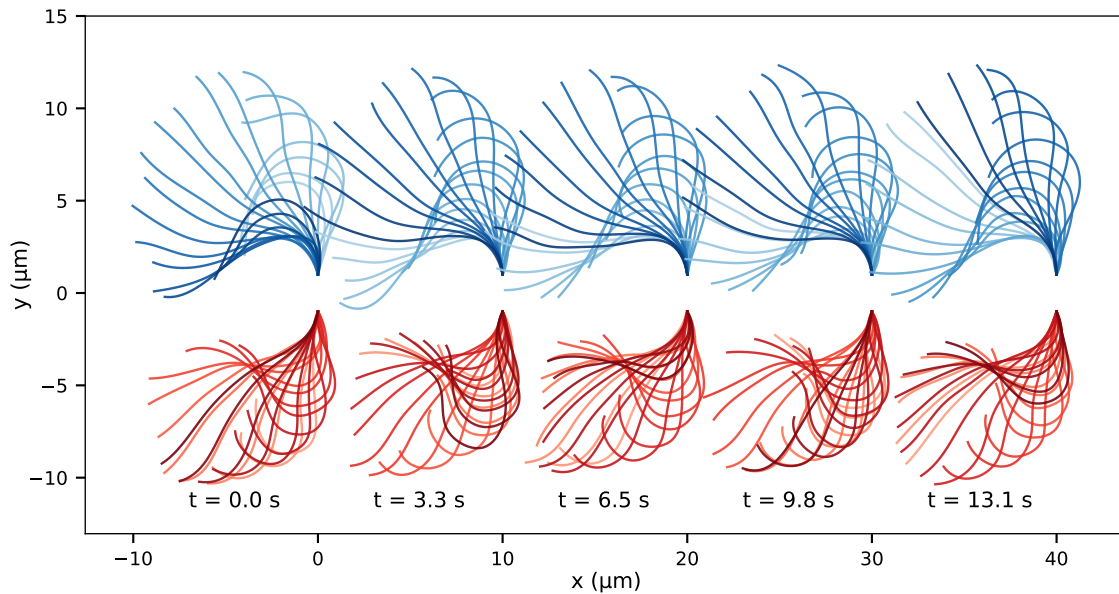


Figure 6.1 Experimental flagella beat waveforms. Top (blue) shows in-phase beating shape and bottom (red) show anti-phase waveform. The beating is stochastic which can be seen by the variation in each beat. Fig. 6.4 shows an effective mean shape.

models that can, for instance, be used to derive the most efficient flagellum waveform (Eloy and Lauga, 2012; Osterman and Vilfan, 2011). The kinematics of a collection of flagella can be modelled using envelope models (Blake, 1971b) or by particle models, which can be used to understand hydrodynamic synchronisation (Brumley et al., 2012; Kotar et al., 2010; Vilfan and Jülicher, 2006).

Here, we wish to understand what sets the flagella waveforms and we must therefore also model their actuation (Camalet and Jülicher, 2000; Hines and Blum, 1978). It has recently been shown that basal coupling, not hydrodynamic interactions, is the reason for flagellar synchrony (Quaranta et al., 2015; Wan and Goldstein, 2016). Hydrodynamic synchronisation of flagella has previously been studied in the context of actuation models (Goldstein et al., 2016). In contrast, we set out to study basal coupling within the framework of actuation models.

6.2 Flagellum Model

The key feature of the eukaryotic flagellum is the dynein motors linking opposing sides of the flagellum and thus providing local torques [Fig. 1.2b]. Here, we consider a simplified two-dimensional version of this, as shown in Fig. 6.2.

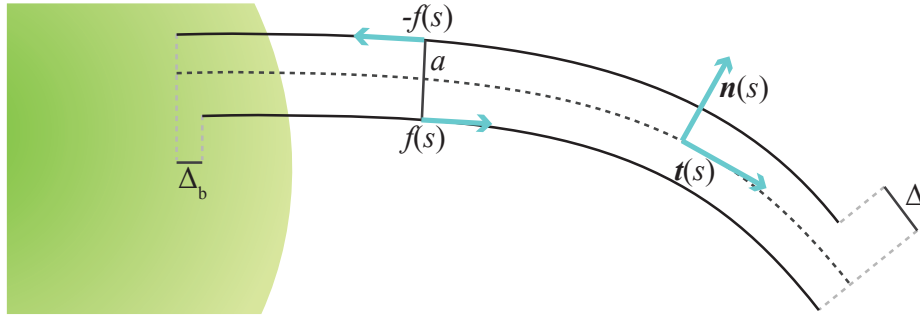


Figure 6.2 Simplified 2D flagellum model. The distance between the two flagellar filaments is a . Dynein motors apply a force (per unit length) $\pm f$ on each side of the flagellum, giving a local torque af around the midpoint. A local coordinate system along the arclength s is given by the local tangent vector t and normal vector n . In this diagram the basal sliding Δ_b and general sliding $\Delta(s)$ are negative.

The shape of a flagellum of length L may be described both by its coordinates $x(s), y(s)$ parametrised by its arclength s , or as an integral over its tangent angle $\psi(s)$,

$$r(s) = \begin{pmatrix} x(s) \\ y(s) \end{pmatrix} = r_0 + \int_0^s t(s') ds' = r_0 + \int_0^s \begin{pmatrix} \cos \psi(s') \\ \sin \psi(s') \end{pmatrix} ds', \quad (6.1)$$

where t the tangent vector as defined in Fig. 6.2.

To describe the evolution of the flagellum centreline $r(s)$ we follow [Camalet and Jülicher \(2000\)](#) to derive the appropriate equations ([Hines and Blum, 1978](#)) and boundary conditions using an enthalpy approach. We thus define the energy of the flagellum

$$G = \int_0^L \left(\frac{\kappa}{2} (C - C_0)^2 + f\Delta + \frac{\Lambda}{2} \dot{r}^2 \right) ds + \frac{k_b}{2} \Delta_b^2 + \frac{k_0}{2} \psi(0)^2, \quad (6.2)$$

where dotted variables denote spatial derivatives, $C = \dot{\psi}$ is the curvature, and the sliding

$$\Delta(s) = \Delta_b + a \int_0^s C(s') ds' = \Delta_b + a [\psi(s) - \psi(0)] \quad (6.3)$$

couples with the inter-filament forces. Further, κ is the bending stiffness and Λ the tension ensuring $|\dot{r}| = |t| = 1$ such that s measures actual arc-length. We consider the inter-filament spacing a constant value a , kept fixed by e. g. springs connecting either side of the flagellum. We have also introduced an intrinsic curvature C_0 , which will enable modelling of asymmetric beats such as those seen in *Chlamydomonas*. By contrast, [Sartori et al. \(2016\)](#) placed forces at the flagellum tip to produce this behaviour. The base is modelled through the basal sliding

stiffness k_b , and for maximum generality, we also allow some basal rotation, which is resisted by a torsional stiffness k_0 .

Upon partial integration the enthalpy becomes

$$G = \int_0^L \left(\frac{\kappa}{2}(C - C_0)^2 + f\Delta_b - aCF + \frac{\Lambda}{2}\dot{r}^2 \right) ds + \frac{k_b}{2}\Delta_b^2 + \frac{k_0}{2}\psi(0)^2, \quad (6.4)$$

where

$$F(s) = - \int_s^L f(s') ds'. \quad (6.5)$$

Doing a variation with respect to r , we obtain the force acting on the filament $\frac{\delta G}{\delta r}$,

$$\delta G = \int_0^L \left(\kappa(C - C_0) \delta C + f\delta\Delta_b - aF \delta C + \Lambda \dot{r} \delta \dot{r} \right) ds + k_b\Delta_b \delta\Delta_b + k_0 \delta\psi(0). \quad (6.6)$$

Note that we do not vary f even though we will later define this f in terms of ψ . Thus we are strictly speaking not being self-consistent. A full calculation including this variation is postponed as future work.

Using $\dot{i} = Cn$, we have $C = \dot{i} \cdot n = \ddot{r} \cdot n$, such that $\delta C = \delta(\ddot{r} \cdot n) = n \cdot \delta\ddot{r} + \ddot{r} \cdot \delta n = n \cdot \delta\ddot{r}$, since $n \cdot \delta n = 0$. Thus

$$\delta G = \int_0^L \left([\kappa(C - C_0) - aF] n \cdot \delta\ddot{r} + \Lambda \dot{r} \delta \dot{r} \right) ds + [k_b - F(0)] \delta\Delta_b. \quad (6.7)$$

Finally, doing two partial integrations we find

$$\begin{aligned} \delta G = & \int_0^L \partial_s [(\kappa\dot{C} - af)n - \tau t] \cdot \delta r ds \\ & + [((af - \kappa\dot{C})n + \tau t) \cdot \delta r]_0^L \\ & + [(\kappa(C - C_0) - aF)n \cdot \delta \dot{r}]_0^L \\ & + [k_b - F(0)] \delta\Delta_b + k_0 \delta\psi(0), \end{aligned} \quad (6.8)$$

where the boundary terms are the external forces and torque, respectively, applied at the end points, and where we have introduced the total tension $\tau = \kappa C^2 - aCF + \Lambda$.

To obtain dynamics in a viscous fluid we use resistive force theory (Camalet and Jülicher, 2000; Lauga and Powers, 2008),

$$\partial_t r = - \left(\frac{1}{\xi_n} nn + \frac{1}{\xi_t} tt \right) \cdot \frac{\delta G}{\delta r}, \quad (6.9)$$

where $\xi_n \approx 2\xi_t$ are the approximate drag coefficients of slender objects. Using $\dot{n} = -Ct$ and $\dot{i} = Cn$ we rewrite

$$\frac{\delta G}{\delta r} = (\kappa\ddot{C} - a\dot{f})n - (\kappa\dot{C} - af)Ct - \dot{\tau}t - \tau Cn, \quad (6.10)$$

such that

$$\begin{aligned} \partial_t r &= -\frac{1}{\xi_n} (\kappa\ddot{C} - a\dot{f} - \tau C)n + \frac{1}{\xi_t} (\kappa C\dot{C} - aCf + \dot{\tau})t \\ &= -\frac{1}{\xi_n} (\kappa\ddot{\psi} - a\dot{f} - \tau\psi)n + \frac{1}{\xi_t} (\kappa\dot{\psi}\ddot{\psi} - a\dot{\psi}f + \dot{\tau})t. \end{aligned} \quad (6.11)$$

By definition, ψ follows $\partial_t t = n\partial_t \psi$. Then, since $\dot{r} = t$, we have $\partial_t \psi = n \cdot \partial_t \dot{r}$ leading to

$$\partial_t \psi = \frac{1}{\xi_n} (-\kappa\ddot{\psi} + a\dot{f} + \dot{\tau}\psi + \tau\dot{\psi}) + \frac{1}{\xi_t} (\kappa\dot{\psi}\ddot{\psi} - a\dot{\psi}f + \dot{\tau})\psi. \quad (6.12)$$

By requiring $\partial_t \dot{r}^2 = 2t \cdot \partial_t \dot{r} = 0$, we find the equation for the tension τ ,

$$\dot{\tau} - \frac{\xi_t}{\xi_n} \dot{\psi}^2 \tau = \partial_s (a\dot{\psi}f - \kappa\dot{\psi}\ddot{\psi}) + \frac{\xi_t}{\xi_n} \dot{\psi} (a\dot{f} - \kappa\ddot{\psi}). \quad (6.13)$$

Lastly, for basal sliding, we find

$$\partial_t \Delta_b = -\frac{1}{\xi_b} \frac{\delta G}{\delta \Delta_b} = \frac{1}{\xi_b} [-k_b \Delta_b + F(0)], \quad (6.14)$$

where ξ_b is the basal drag. These are the equations of motion for the flagellum.

The boundary conditions depend on the system. Taking a flagellum that is held at $r(0) = r_0$ we use Eq. (6.11) with $\partial_t r(0) = 0$ to obtain the boundary conditions

$$\kappa\ddot{\psi}(0) - a\dot{f}(0) - \tau(0)\dot{\psi}(0) = 0, \quad (6.15)$$

$$\kappa\dot{\psi}(0)\ddot{\psi}(0) - a\dot{\psi}(0)f(0) + \dot{\tau}(0) = 0. \quad (6.16)$$

It is often customary to furthermore take the clamped boundary condition $\psi(0) = 0$, but we will allow some rotation at the base. This rotation is resisted by a drag ξ_0 , and noting that $\delta\psi(0) = n(0) \cdot \delta\dot{r}(0)$, we have the torque balance

$$\partial_t \psi(0) = \frac{1}{\xi_0} (-k_0 \psi(0) - aF(0) + \kappa[C(0) - C_0]). \quad (6.17)$$

The other end is free and thus we require no external torque act on the flagellum end, so that

$$\kappa(\dot{\psi}(L) - C_0) = aF(L) \Rightarrow \dot{\psi}(L) = C_0, \quad (6.18)$$

and, similarly, no external forces

$$\kappa\ddot{\psi}(L) - af(L) = 0, \quad (6.19)$$

$$\tau(L) = 0, \quad (6.20)$$

using Eq. (6.8).

The above equations are non-linear. Following [Sartori et al. \(2016\)](#) we expand ψ in a static ψ_0 and time-varying mode $\psi_1(t)$

$$\psi = \psi_0 + \psi_1(t), \quad (6.21)$$

and likewise with τ and f . Assuming $f_0 = 0$ (no extra static forces), we have

$$\psi_0 = C_0 s, \quad (6.22)$$

$$\tau_0 = 0, \quad (6.23)$$

satisfying all boundary conditions.

We now assume ψ_1 small to obtain the governing equations

$$\partial_t \psi_1 = \frac{1}{\xi_n} (-\kappa\ddot{\psi}_1 + a\dot{f} + C_0\dot{\tau}) + \frac{1}{\xi_t} C_0 (\kappa C_0 \dot{\psi}_1 - C_0 a f + \dot{\tau}), \quad (6.24)$$

$$\ddot{\tau} - \frac{\xi_t}{\xi_n} C_0^2 \tau = \left(1 + \frac{\xi_t}{\xi_n}\right) C_0 (a\dot{f} - \kappa\ddot{\psi}_1). \quad (6.25)$$

Likewise, the boundary conditions on $\psi_1, \tau = \tau_1$ become

$$\xi_0 \partial_t \psi_1(0) = -k_0 \psi_1(0) - aF(0) + \kappa\dot{\psi}_1(0), \quad (6.26)$$

$$\kappa\ddot{\psi}_1(0) - a\dot{f}(0) - C_0\tau(0) = 0, \quad (6.27)$$

$$\kappa C_0 \dot{\psi}_1(0) - a C_0 f(0) + \dot{\tau}(0) = 0, \quad (6.28)$$

$$\dot{\psi}_1(L) = 0, \quad (6.29)$$

$$\kappa\ddot{\psi}_1(L) - af(L) = 0, \quad (6.30)$$

$$\tau(L) = 0. \quad (6.31)$$

6.2.1 Feedback Control

The flagellar beat is not (at least solely) regulated by the cell body. This is evident from the fact that flagella can beat even when detached from the cell body (Geyer et al., 2016). Instead it has been hypothesised that the flagellar beatings are spontaneous oscillations (Jülicher and Prost, 1997) resulting from a dynamic instability in a feedback mechanism (Camalet et al., 1999). Concretely, the forcing f is itself a function of local parameters. For instance, in *sliding control* (Camalet and Jülicher, 2000; Riedel-Kruse et al., 2007), the forcing is a function of Δ and in *curvature control* (Hines and Blum, 1978) the forcing is function of ψ .

In *Chlamydomonas*, sliding control has been ruled out as a possibility and there is some evidence suggesting that curvature control is in operation (Sartori et al., 2016). We will consider curvature control and take

$$f_{\text{active}} = \beta_1 h_1 + \beta_2 h_2, \quad (6.32)$$

where h_1 and h_2 are hidden variables that follow

$$\partial_t h_1(s) = \frac{1}{\tau_0} (\dot{\psi} - h_1), \quad (6.33)$$

$$\partial_t h_2(s) = \frac{1}{\tau_0} (h_1 - h_2). \quad (6.34)$$

A simplified choice of this system with $\beta_2 = 0$ has previously been considered (Hines and Blum, 1978), but this only allows self-sustained beating for long flagella such as those in spermatozoa (Bayly and Wilson, 2015). For the shorter flagella of *Chlamydomonas*, we have found that the extra β_2 term allows beating.

Beyond the active forces, we also add some drag due to sliding

$$f_{\text{passive}} = k_\Delta \Delta + \xi_\Delta \partial_t \Delta, \quad (6.35)$$

where we require $k_\Delta, \xi_\Delta \geq 0$ to ensure the passiveness of these forces. In total,

$$f = f_{\text{active}} + f_{\text{passive}}. \quad (6.36)$$

6.3 Data Processing

From the experimental flagella tracks we wish to extract the first Fourier modes to compare to the theoretical model. Fig. 6.3a shows the angle $\psi(s, t)$ extracted directly from the raw data [Fig. 6.1a]. The data is not perfect, and there are a lot of missing values, especially at

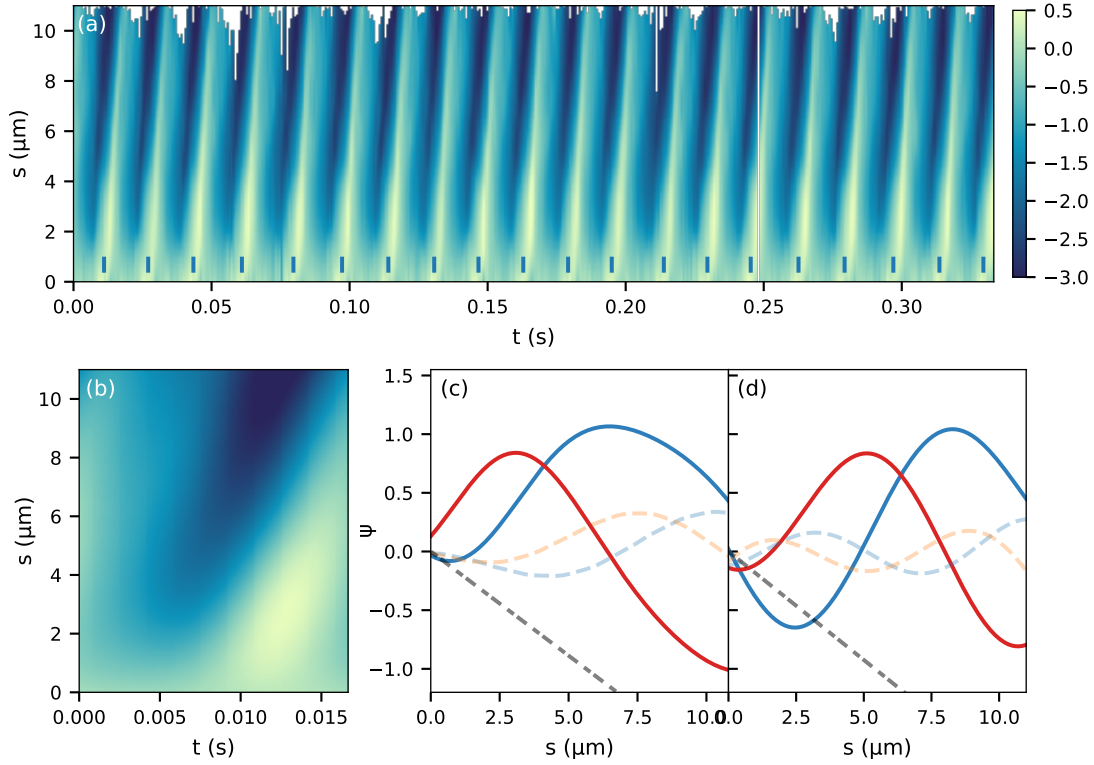


Figure 6.3 Data processing. (a) Raw $\psi(s, t)$ extracted from the IP data. (b) Average $\psi(s, t)$ for one beat period on IP data. (c) Extracted IP data. $\text{Re}[\tilde{\psi}]$ and $\text{Im}[\tilde{\psi}]$ in blue, red, respectively. Next Fourier modes as dashed blue and red. ψ_0 in grey dashed. (d) Extracted AP data.

large s . Furthermore, different beats take different times, as can be seen by the ticks on Fig. 6.3a. This noisy behaviour will influence the Fourier modes massively, and is not what we intend to study. Instead, we need to time-warp the data such that each beat takes the same amount of time. To do this, we start by defining some average angle $\bar{\psi}(t)$. We smooth this signal such that it does not have any large kinks, whereafter we can use a Hilbert transform to define an instantaneous phase. From this phase we can immediately define a smooth time warping such that each beat takes equal time.

On this rescaled data, we then fit to the data a function of the form

$$\psi(t, s) = C_0 s + \text{Re} \left[\sum_{n,m} A_{nm} \exp(k_n s) \exp(\omega_m t) \right]. \quad (6.37)$$

By using a fit function, we naturally extrapolate the missing values of Fig. 6.3a. The time-averaged data $\langle \psi(s, t) \rangle_t$ follows almost perfectly a linear function, which permits the simple form $C_0 s$ for the static part in the function. The fit is shown in Fig. 6.3b.

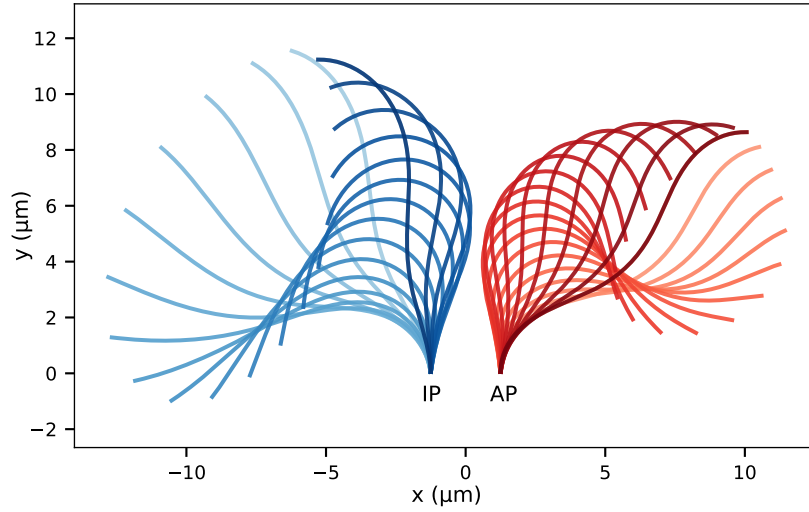


Figure 6.4 First Fourier mode beat waveforms. Left (blue) showing in-phase and right (red) showing anti-phase.

Finally, we extract the first Fourier mode from the fit, and then we can describe the data by

$$\psi(s, t) = \psi_0(s) + \psi_1(t, s) = C_0 s + \text{Re} [\tilde{\psi}(s) e^{i\omega t}], \quad (6.38)$$

which lends itself to immediate comparison with the theory. Fig. 6.3(c–d) shows $\text{Re}[\tilde{\psi}]$ and $\text{Im}[\tilde{\psi}]$ of the in-phase and anti-phase data, respectively. Fig. 6.3(c–d) also shows $\psi_0 = C_0 s$ and the second Fourier mode, the latter of which we will not take into account in our modelling. The data does not fully satisfy the boundary conditions we are expecting: we clearly do not have $\tilde{\psi}_1(L) = 0$. The reasons for this are not fully clear, but it is partly due to noisy data extraction. We could have “fixed” this by enforcing the condition in Eq. (6.37). But it seems a more justifiable approach is to fit our models as well as possible with this data directly instead of performing such data manipulation manoeuvres. The final waveforms of the extracted Fourier modes are shown in Fig. 6.4.

6.4 Eigenvalue Problem

Writing $\psi_1 = \tilde{\psi} e^{\sigma t}$, $\tau = \tilde{\tau} e^{\sigma t}$, $\Delta_b = \tilde{\Delta}_b e^{\sigma t}$, etc., we look for solutions to the governing equations. Since we have linearised the equations, we can look for solutions $\tilde{\psi} = A e^{k_n s}$, $\tilde{\tau} = B e^{k_n s}$ for the governing equations (6.24) and (6.25). We do the same for the forces, and immediately have

$$\tilde{f}_{\text{active}} = \left(\frac{\beta_1}{1 + \tau\sigma} + \frac{\beta_2}{(1 + \tau\sigma)^2} \right) \dot{\tilde{\psi}} \equiv \beta(\sigma) \dot{\tilde{\psi}} \quad (6.39)$$

and

$$\begin{aligned} \sigma A = & \frac{1}{\xi_n} \left(-\kappa k_n^4 A + a k_\Delta k_n^2 A + a \xi_\Delta \sigma k_n^2 A - \beta k_n^3 A + C_0 k_n B \right) \\ & + \frac{1}{\xi_t} \left(\kappa C_0 k_n^2 A - C_0 (a k_\Delta + a \xi_\Delta \sigma - \beta k_n) A + k_n B \right) C_0, \end{aligned} \quad (6.40)$$

where we have ignored the Δ_b term in the tangential drag term. This approximation can be validated by numerical simulations (it changes significantly only τ , not ψ).

Likewise

$$k_n^2 B - \frac{\xi_t}{\xi_n} C_0^2 B = \left(1 + \frac{\xi_t}{\xi_n} \right) C_0 (a k_\Delta k_n A + a \xi_\Delta \sigma k_n A - \beta k_n^2 A - \kappa k_n^3 A) \quad (6.41)$$

leading to

$$B = \frac{C_0 (\xi_n + \xi_t)}{\xi_n k_n^2 - \xi_t C_0^2} (a (k_\Delta + \xi_\Delta \sigma) k_n - \beta k_n^2 - \kappa k_n^3) A = \Gamma_n A, \quad (6.42)$$

implicitly defining Γ_n .

The characteristic equation of these equations defines six $\{k_n\}$ values

$$\begin{aligned} -\kappa k_n^6 - \beta k_n^5 + [a (k_\Delta + \xi_\Delta \sigma) - 2C_0^2 \kappa] k_n^4 - 2\beta C_0^2 k_n^3 + [2a C_0^2 (k_\Delta + \xi_\Delta \sigma) - C_0^4 \kappa - \sigma \xi_n] k_n^2 \\ - \beta C_0^4 k_n + a C_0^4 (k_\Delta + \xi_\Delta \sigma) + C_0^2 \sigma \xi_t = 0. \end{aligned} \quad (6.43)$$

We can thus write $\tilde{\psi}_1 = \sum_{n=1}^6 A_n e^{k_n s}$ and $\tau = \sum_{n=1}^6 \Gamma_n A_n e^{k_n s}$, and the boundary conditions become

$$\begin{aligned} & \left[\begin{array}{ccc} \dots & (k_0 + \xi_0 \sigma) + a(k_b + \xi_b \sigma)(\tilde{\Delta}_b)_n - \kappa k_n & \dots \\ \dots & \kappa k_n^3 - a(k_\Delta + \xi_\Delta \sigma) k_n + \beta k_n^2 & \dots \\ \dots & \kappa C_0 k_n^2 - C_0 (k_\Delta + \xi_\Delta \sigma)(\tilde{\Delta}_b)_n - a C_0 (k_\Delta + \xi_\Delta \sigma) + C_0 \beta k_n & \dots \\ \dots & k_n e^{k_n L} & \dots \\ \dots & [\kappa k_n^2 - a(k_\Delta + \xi_\Delta \sigma) + \beta k_n] e^{\beta_n L} - (k_\Delta + \xi_\Delta \sigma)(\tilde{\Delta}_b)_n & \dots \\ \dots & 0 & \dots \end{array} \right] \\ & + \left[\begin{array}{ccc} \dots & 0 & \dots \\ \dots & -C_0 & \dots \\ \dots & k_n & \dots \\ \dots & 0 & \dots \\ \dots & 0 & \dots \\ \dots & e^{k_n L} & \dots \end{array} \right] \Gamma \begin{pmatrix} A_1 \\ A_2 \\ A_3 \\ A_4 \\ A_5 \\ A_6 \end{pmatrix} = \begin{pmatrix} 0 \\ 0 \\ 0 \\ 0 \\ 0 \\ 0 \end{pmatrix}, \end{aligned} \quad (6.44)$$

where $\Gamma = \text{diag}\Gamma_n$,

$$(\tilde{\Delta}_b)_n = \frac{\beta - \frac{a}{k_n}(k_\Delta + \xi_\Delta \sigma)}{L(k_\Delta + \xi_\Delta \sigma) + a(k_b + \xi_b \sigma)} \left(e^{k_n L} - 1 \right), \quad (6.45)$$

and the subscript n varies across columns.

The solvability condition requires the determinant of the above equation be zero. This complex equation defines the modes $\sigma \in \mathbb{C}$ given the other parameters. Conversely, given a mode σ , two other parameters can be determined by the condition (since σ is complex). With the solvability condition satisfied, ψ can be found by singular value decomposition of the matrix. The solutions are validated by comparing to direct finite difference simulations. Since our equations are of fourth order, these require high-order schemes, which we describe in Appendix 6.A.

In studying our system, we will consider critical points $\sigma = i\omega = 2\pi if$, i. e. modes with no real part. This approach only works if there are no other modes which are unstable, i. e. have $\text{Re}[\sigma] > 0$ (Bayly and Wilson, 2015). Our results have been checked for this. Active forces such as

$$f_{\text{active}} = \beta_1 \psi + \beta_2 \partial_t \psi \quad (6.46)$$

with $\beta_1, \beta_2 < 0$ have previously been studied and shown to work for *Chlamydomonas* (Sartori et al., 2016). This form leads to $\beta = \beta_1 + i\beta_2\omega$ at the critical point [compare to Eq. 6.39], and thus describes a general choice of complex number. In that sense it is more general than the forcing we are considering [Eqs. (6.32)]. However, we find that this form is only valid precisely at the critical point, since it also admits unstable modes. Thus, this cannot be used for simultaneous modelling of flagella of different frequencies, which we intend to study in this chapter. It also cannot be used to understand the underlying dynamic model, since it truly is only valid at the critical point. Our choice, Eq. (6.32), does not have this problem.

6.5 Flagella Waveforms

We start by asking whether our model can describe the waveforms observed. To do so, we must fit the model to the data. We have a lot of parameters, and it is well-known that with a lot a parameters one can fit an elephant wiggling its trunk (Mayer et al., 2010). It turns out that the effective size of our parameters space is actually quite small. In fact, the conclusion of this study will end up involving the opposite of the elephant saying, namely that if you cannot fit the data with a lot of parameters, then the model is probably wrong.

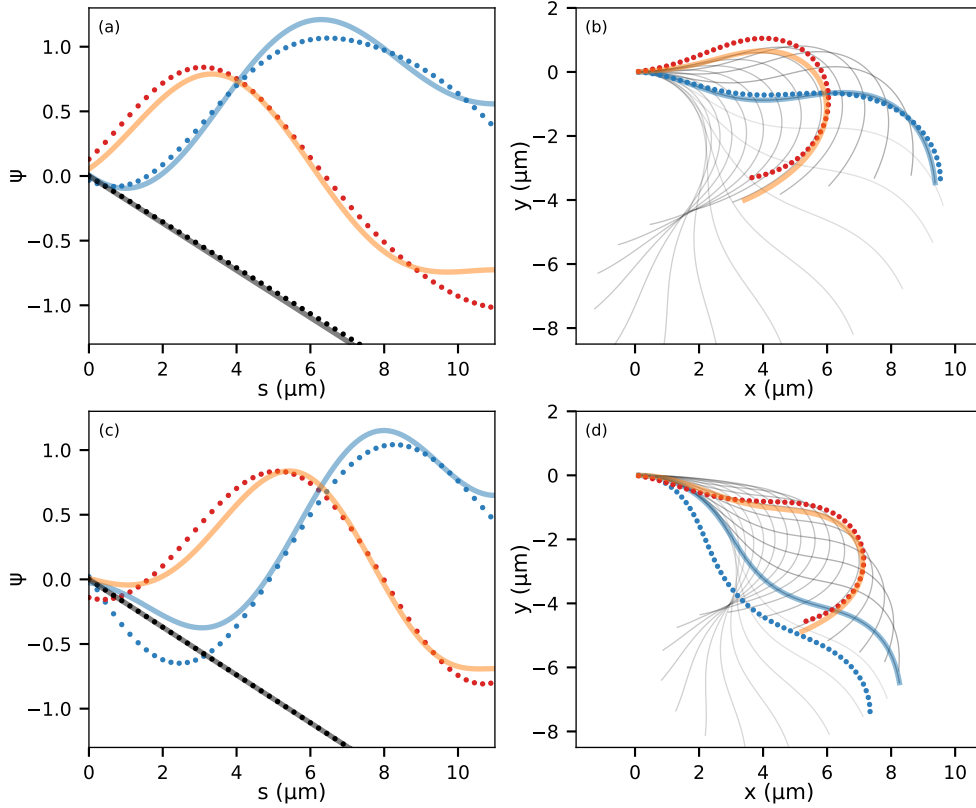


Figure 6.5 Individual fits with passive base. Dots show experimental data, and curves fit. Blue is real part and red imaginary. ψ_0 shown as black in (a,c). Black in (b-d) shows full waveform of the fitted model. (a-b) In-phase. (c-d) Anti-phase. Parameter for IP (AP): $f = 60$ (85) Hz, $C_0 = -0.18 \mu\text{m}^{-1}$, $\xi_D = 0.66$ (2.48) pN s/ μm , $k_D = 1.23$ (2.21) nN/ μm , $\beta_1 = 0.30$ (1.18) nN, $\beta_2 = -1.07$ (-1.15) nN, $\tau_0 = 1.94$ (0.46) ms, $\xi_0 = 1.54$ (3.30) pN s μm , $k_0 = 2.14$ (0.41) pN μm , $\xi_b = 241$ (0.00013) pN s/ μm , $k_b = 2.61 \cdot 10^{-8}$ (0.07) pN/ μm . Fixed physical parameters: $\kappa = 580$ pN μm^2 , $a = 66$ nm, $L = 11 \mu\text{m}$, $\xi_n = 0.0034$ pN s/ μm^2 , $\xi_t = 0.0017$ pN s/ μm^2 .

The magnitude of the beats will be set by non-linear drag responses. In numerical simulations we added $f_{\text{non-lin}} = k_3 \Delta^3$ to Eq. (6.36), but we will not explicitly model these responses here. Instead, we simply assume that the non-linearities set the correct magnitude of the beats such that our fitting procedure is to minimise

$$\mathcal{E} = \min_{A \in \mathbb{C}} \int_0^L [A \tilde{\psi}_{\text{fit}}(s) - \tilde{\psi}_{\text{data}}(s)]^2 ds, \quad (6.47)$$

which also matches the phase of the fit to the data.

We do not expect the base of the flagella to have any extra, active forces. Thus we must require $k_b, \xi_b, k_0, \xi_0 \geq 0$. In other words, we allow extra dissipation at the base because

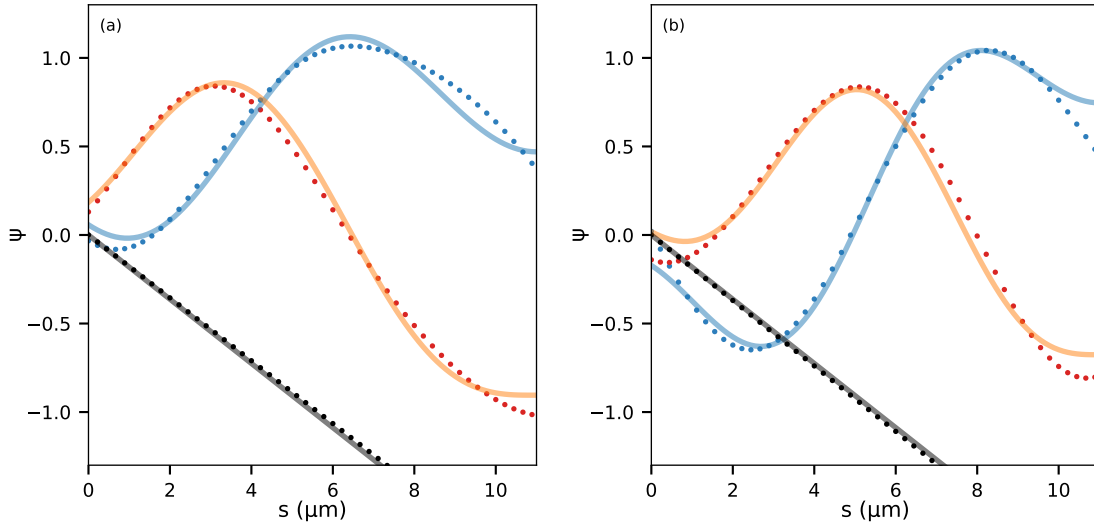


Figure 6.6 Simultaneous fits with active base. Dots show experimental data, and curves fit. Blue is real part and red imaginary. Parameter for IP (AP): $f = 60(85)$ Hz, $C_0 = -0.18 \mu\text{m}^{-1}$, $\xi_D = 2.70 \text{ pN s}/\mu\text{m}$, $k_D = 1.25 \text{ nN}/\mu\text{m}$, $\beta_1 = -2.98 \text{ nN}$, $\beta_2 = 0.43 \text{ nN}$, $\tau_0 = 0.0157(0.0093) \text{ s}$, $\xi_0 = 6.16 \text{ pN s}/\mu\text{m}$, $k_0 = 3.35 \text{ pN}/\mu\text{m}$, $\xi_b = -0.36(-0.53) \text{ nN s}/\mu\text{m}$, $k_b = -219(-207) \text{ nN}/\mu\text{m}$.

of drag, but we do not allow extra energy to be used by the cell (requiring active motors and hydrolysis of ATP). It has previously been shown that single detached *Chlamydomonas* flagella can be fitted using a passive base (Sartori et al., 2016). Fig. 6.5 shows the best fits of the IP and AP mode obeying these requirements. The fits were performed using multiple basinhopping chains started throughout parameter space, ensuring that these are the best fits (Wales and Doye, 1997). The IP mode [Fig. 6.5(a–b)] can be fitted well, but the AP mode fit [Fig. 6.5(c–d)] is not outstanding, despite the large number of parameters.

Even more unsettling are the variations in parameters between the two modes. For instance, the IP mode seems to have a base dominated by sliding drag (ξ_b), whereas for the AP mode, the basal spring response (k_b) is strongest. Previous studies have fitted flagella only in a single mode (but compared mutants). Here, we have the same flagellum beating in two different modes. If the mode-selection is a spontaneous process, the parameters should be the same in the two phases, but simply correspond to different values of σ . We have not been able to find parameters making this possible, not even when including basal coupling (next section).

Instead we find that the parameter τ_0 has a particularly large influence on the frequency selection, and that for the present model, this parameter has to vary between the two models in order to ensure the different beat frequencies. This leads to the other possibility, namely that the mode selection is an active process, i. e. that the cell changes some active parameters

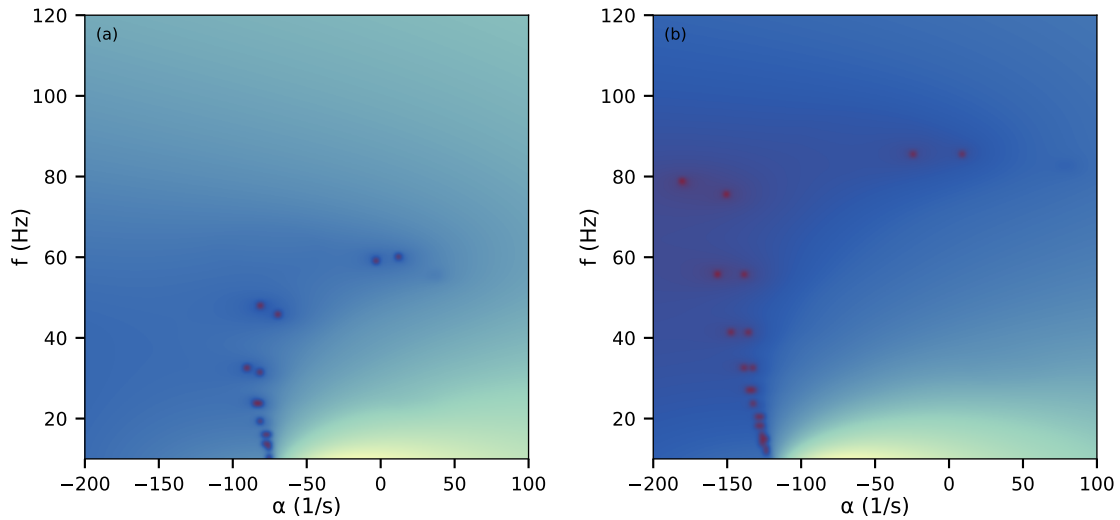


Figure 6.7 Basal coupling modes. Heatmap shows $\log D$ (determinant) of the coupled system, partly specified by Eq. (6.51), as a function of $\sigma = \alpha + 2\pi if$. As shown, including coupling, the single flagellum modes split into an IP and an AP mode. Which is the more unstable depends on the sign of c . (a) Using parameters of IP mode in Fig. 6.6. (b) Using parameters of AP mode in Fig. 6.6. Coupling strength $c = 2.0 \text{ nN}\mu\text{m}$.

in order to change beating gait. This could for instance be used for navigation (Polin et al., 2009), and has been suggested by experiments (Wan and Goldstein, 2017). In this case we should allow only the active parameters (β_1 , β_2 , τ_0) to vary; but passive parameters should still remain the same in the two beating modes. However, we cannot obtain any good fits obeying these requirements and the requirement of a passive base. Thus we rule out the present passive base model.

If we relax the requirement that the base be passive (k_b , ξ_b , k_0 , $\xi_0 \geq 0$), we can obtain great simultaneous fits of the modes as shown in Fig. 6.6. These active base fits share all passive parameters and vary only the active parameters ξ_b , k_b and τ_0 .

6.6 Synchronisation

Hydrodynamic synchronisation has previously been considered for simple actuation models (Goldstein et al., 2016; Lauga and Powers, 2008). Here we take into account recent observations showing that basal coupling is the dominate feature leading to synchronisation of flagella beating in many green algae (Wan and Goldstein, 2016), and in particular in *Chlamydomonas* (Quaranta et al., 2015).

Since we have only been able to match an active base model to the data, we take this model and try here to couple two such flagella exclusively by the base. There are many

choices for such a coupling within the present framework. We could, for instance, couple Δ_b of the two flagella. Alternatively (and leading to very similar results), we could couple the basal rotation, for instance with a torsional spring as

$$\partial_t \psi_1^A(0) = \frac{1}{\xi_0} \left(-k_0 \psi_1^A(0) - aF^A(0) + c[\psi_1^B(0) - \psi_1^A(0)] \right), \quad (6.48)$$

where the superscripts A, B indicate the two flagella. In this case, the characteristic equation [Eq. (6.43)] remains unchanged. We now write $\tilde{\psi}_1^A = \sum_{n=1}^6 A_n e^{k_n s}$ and $\tilde{\psi}_1^B = \sum_{n=1}^6 B_n e^{k_n s}$ and define

$$k^A = (k_1, k_2, k_3, k_4, k_5, k_6, 0, 0, 0, 0, 0, 0), \quad k^B = (0, 0, 0, 0, 0, 0, k_1, k_2, k_3, k_4, k_5, k_6), \quad (6.49)$$

$$\delta^A = (1, 1, 1, 1, 1, 1, 0, 0, 0, 0, 0, 0), \quad \delta^B = (0, 0, 0, 0, 0, 0, 1, 1, 1, 1, 1, 1). \quad (6.50)$$

Likewise we define separate $\Gamma_n, \tilde{\Delta}_b$, etc.

Using these definitions we can write down the eigenvalue problem corresponding to Eq. (6.44) for the two coupled flagella. This is quite a lengthy expression, the ψ matrix part, for instance, reading

$$\begin{pmatrix} \dots & \delta_n^A(k_0 + \xi_0 \sigma) + a(k_b + \xi_b \sigma)(\tilde{\Delta}_b^A)_n - \kappa k_n^A + c(\delta_n^A - \delta_n^B) & \dots \\ \dots & \kappa(k_n^A)^3 - a(k_\Delta + \xi_\Delta \sigma)k_n^A + \beta(k_n^A)^2 & \dots \\ \dots & \kappa C_0(k_n^A)^2 - C_0(k_\Delta + \xi_\Delta \sigma)(\tilde{\Delta}_b^A)_n - aC_0(k_\Delta + \xi_\Delta \sigma) + C_0\beta k_n^A & \dots \\ \dots & k_n^A e^{k_n^A L} & \dots \\ \dots & [\kappa(k_n^A)^2 - a(k_\Delta + \xi_\Delta \sigma) + \beta k_n^A] \delta_n^A e^{\beta n L} - (k_\Delta + \xi_\Delta \sigma)(\tilde{\Delta}_b^A)_n & \dots \\ \dots & 0 & \dots \\ \dots & \delta_n^B(k_0 + \xi_0 \sigma) + a(k_b + \xi_b \sigma)(\tilde{\Delta}_b^B)_n - \kappa k_n^B + c(\delta_n^B - \delta_n^A) & \dots \\ \dots & \kappa(k_n^B)^3 - a(k_\Delta + \xi_\Delta \sigma)k_n^B + \beta(k_n^B)^2 & \dots \\ \dots & \kappa C_0(k_n^B)^2 - C_0(k_\Delta + \xi_\Delta \sigma)(\tilde{\Delta}_b^B)_n - aC_0(k_\Delta + \xi_\Delta \sigma) + C_0\beta k_n^B & \dots \\ \dots & k_n^B e^{k_n^B L} & \dots \\ \dots & [\kappa(k_n^B)^2 - a(k_\Delta + \xi_\Delta \sigma) + \beta k_n^B] \delta_n^B e^{\beta n L} - (k_\Delta + \xi_\Delta \sigma)(\tilde{\Delta}_b^B)_n & \dots \\ \dots & 0 & \dots \end{pmatrix}. \quad (6.51)$$

Calculating the determinant of the entire system matrix for various values of $\sigma = \alpha + 2\pi i f$, the zeros define the possible modes. Fig. 6.7 shows this on the parameters found for active base IP and AP beating in the previous section [as given in Fig. 6.6].

We find that the coupling breaks each single flagellum mode into two modes, one for IP synchrony and one for AP. These modes have different values of α , and depending on the sign of c , either IP or AP is more unstable (i. e. grows the fastest). Differences in stability, however,

increase faster than differences in frequency. This is most clearly evident in the example of Fig. 6.7b, where the difference in α for IP versus AP is much larger than difference in f , but this seems to hold true in general, also for different mechanisms of basal coupling. This means that such a coupling alone cannot explain the co-existence of the IP and AP modes that in reality have very different frequencies. Furthermore, the shape changes induced by this coupling are minor, again arguing against this model being able to describe the system without an active change of some parameters.

6.7 Discussion

The conclusion of this preliminary study is that the IP and AP mode of beating in *Chlamydomonas* can be described as an active switching in a model of beating with active base. There is no experimental evidence, however, indicating that the base of *Chlamydomonas* flagella are more active than the rest of the flagellum. As it has been said, “*the first time someone calls you a horse you punch him on the nose, the second time someone calls you a horse you call him a jerk, but the third time someone calls you a horse, well then perhaps it’s time to go shopping for a saddle*”. In the present scenario, our model is the horse, and it seems the most reasonable conclusion, then, is that the present model does not represent the system well.

The clear candidate to explain what the model is lacking is hydrodynamics. The flagella beat quite close to each other and experiments have shown that in close proximity, flagella on separate organisms have their shape modulated and even synchronise at very close proximity (Brumley et al., 2014) [hydrodynamics is in itself *sufficient* for synchronisation, but not *necessary*, and in *Chlamydomonas* probably not the dominant mechanism]. In particular, the hydrodynamic interactions between the two flagella will be very different in the IP and AP modes. So while the synchrony itself might (primarily) be obtained by basal coupling, the shapes could be strongly influenced by hydrodynamic interactions. This conclusion is reached solely on the basis that our very general model, but which is lacking hydrodynamics, is insufficient to fit the observations.

To include hydrodynamics in the model, one can consider resistive force theory in an external flow,

$$\partial_t r - u = - \left(\frac{1}{\xi_n} n n + \frac{1}{\xi_t} t t \right) \cdot \frac{\delta G}{\delta r}. \quad (6.52)$$

This leads to the equations

$$\partial_t \psi = \dot{u} \cdot n + \frac{1}{\xi_n} (-\kappa \ddot{\psi} + a \dot{f} + \dot{\tau} \psi + \tau \dot{\psi}) + \frac{1}{\xi_t} (\kappa \dot{\psi} \dot{\psi} - a \dot{\psi} f + \dot{\tau}) \psi, \quad (6.53)$$

where $\dot{u} = \partial_s u(x(s), y(s))$. Equally,

$$\ddot{\tau} - \frac{\xi_t}{\xi_n} \dot{\psi}^2 \tau = -\xi_t \dot{u} \cdot t + \partial_s (a \dot{\psi} f - \kappa \dot{\psi} \ddot{\psi}) + \frac{\xi_t}{\xi_n} \dot{\psi} (a \dot{f} - \kappa \ddot{\psi}). \quad (6.54)$$

The boundary condition $\partial_t r(0) = 0$ changes to

$$\kappa \ddot{\psi}(0) - a \dot{f}(0) - \tau \dot{\psi}(0) = \xi_n u \cdot n, \quad (6.55)$$

$$\kappa \dot{\psi}(0) \ddot{\psi}(0) - a \dot{\psi}(0) f(0) + \dot{\tau}(0) = -\xi_t u \cdot t, \quad (6.56)$$

while the others remain unchanged. Our definition of unit vectors here must match the one used in the derivation of the other equations, i. e.

$$t = \begin{pmatrix} \cos \psi \\ \sin \psi \end{pmatrix}, \quad n = \begin{pmatrix} -\sin \psi \\ \cos \psi \end{pmatrix}. \quad (6.57)$$

The two flagella can then be coupled by basal springs and through hydrodynamics by taking the external flow field on one flagellum to be the result of the flow generated by the other flagella. This flow could, in turn, be modelled as a line of (regularised) Stokeslets or through a similar approach.

Hydrodynamic interactions render the system very non-linear and we can no longer use the eigenvalue approach employed above. Hydrodynamic interactions can be linearised, but has so far only been done in the context of flagella without static curvature (Goldstein et al., 2016). The most direct approach is to do numerical simulations using high-order schemes, as discussed in Appendix 6.A.

The final goal of this study is to understand the stochastic switching between modes. In particular, it would be interesting to understand if the two modes, with their distinct frequencies, emerge spontaneously when hydrodynamic interactions are included, or if an active switching mechanism is still required. An active switching could for instance involve the parameter τ_0 , which could be taken as stochastic processes $\tau_0^A(t)$, $\tau_0^B(t)$ on each flagellum. These could then be stochastically coupled, using e. g. Adler/Kuramoto equations (Adler, 1946; Kuramoto, 1984), implying that the basal coupling itself is active (maybe chemical), or they could be considered entirely independent processes that set an intrinsic driving frequency, and the observed synchrony would be due to purely passive interactions. Whatever the mechanism, it is clear that a full model including hydrodynamics is needed to determine which is the correct model.

Appendix 6.A Finite Difference Coefficients

Our equations are of fourth order, and thus we need high-order finite difference schemes to do simulations. These finite difference coefficients are well-known, but to be able to adapt them on-the-fly to various coordinate systems, we present and derive the general equation used here.

Consider an N -order finite-difference approximation to $f^{(n)}(x)$. We can write this as

$$f^{(n)}(x) \approx \sum_{k=1}^N a_k f(x + s_k). \quad (6.58)$$

Here s_k is the stencil, which we can choose for instance to be a linear spacing $s_k = kh$, although this is not a requirement. In the numerical scheme to solve Eq. (4.16), we used unequal spacing for q . We wish to find the best values of $\{a_k\}$. Taylor expanding the function and keeping N terms we have

$$f(x + s_k) \approx \sum_{\ell=0}^{N-1} \frac{1}{\ell!} s_k^\ell f^{(\ell)}(x). \quad (6.59)$$

Hence,

$$f^{(n)}(x) \approx \sum_{\ell=0}^{N-1} \frac{1}{\ell!} f^{(\ell)}(x) \sum_{k=1}^N a_k s_k^\ell. \quad (6.60)$$

Since this must hold for all x , we find a system of equations for a_k :

$$\frac{1}{\ell!} \sum_{k=1}^N a_k s_k^\ell = \delta_{\ell n}, \quad \ell = 0 \dots n \dots (N-1), \quad (6.61)$$

where $\delta_{\ell n}$ is the Kronecker delta. Thus we can always solve the system as long as $n < N$, i. e. to find the n -th derivative, we need at least $n + 1$ stencil points.

For instance taking $s_k \in \{-4h, -3h, -2h, -h, 0, h, 2h, 3h, 4h\}$, we can solve for the fourth derivative ($n = 4$) to find

$$f^{(4)}(x) \approx \frac{1}{240h^4} [7f(x-4h) - 96f(x-3h) + 676f(x-2h) - 1952f(x-h) + 2730f(x) - 1952f(x+h) + 676f(x+2h) - 96f(x+3h) + 7f(x+4h)]. \quad (6.62)$$

Of course, this equation only works in the middle of the solution domain. At the edge we use

$$\begin{aligned} f^{(4)}(x) \approx & \frac{1}{240h^4} [3207f(x) - 21056f(x+h) + 61156f(x+2h) - 102912f(x+3h) \\ & + 109930f(x+4h) - 76352f(x+5h) + 33636f(x+6h) \\ & - 8576f(x+7h) + 967f(x+8h)]. \end{aligned} \quad (6.63)$$

And likewise we can solve for all coefficients needed. For instance, for the second point we use $s_k \in \{-h, 0, h, 2h, 3h, 4h, 5h, 6h, 7h\}$, and so on.

Chapter 7

Conclusions

This thesis has been a smorgasbord of subjects, all connected by the interest to understand physical and stochastic aspects of cell behaviour.

In the colony-forming species *Salpingoeca rosetta* we showed that the beating of each flagellum is stochastic and uncorrelated with others, and the vectorial sum of the flagellar propulsion manifests as stochastic helical swimming. To describe this system theoretically, we developed a set of stochastic differential equations, whose approximate solution could be used to fit these types of random walk trajectories. We used this model to illuminate the variability that exist between colonies of *S. rosetta*. We employed digital inline holography to visualise the three-dimensional nature of these helical trajectories, and used Hamiltonian Monte Carlo to extract smooth trajectories from the noisy data. We also developed likelihood methods for Hamiltonian Monte Carlo that could be used to fit short trajectories and extract physical parameters from them.

Using microfluidic devices, we imposed oxygen gradients on *S. rosetta* colonies and found them to be aerotactic. We quantified this response by temporally varying the oxygen gradient, thus finding evidence that the cells sense oxygen logarithmically. Studying their reorientation dynamics, we found that *S. rosetta* navigate using a stochastic strategy, but without clear reorientation events as seen in bacterial run-and-tumble. This lead us to formulate a continuous version of run-and-tumble which was used to interpret the data.

We studied this continuous form of run-and-tumble as a special case of a more general model of persistent run-and-tumble and asked the question: “why is such a range of persistence observed in nature?” We focused first on the optimisation of the linearised chemotactic response within the two-dimensional parameter space of tumble frequency and angular persistence. We found that although an optimal persistence does exist for a given tumble frequency, in the full parameter space there is a continuum of optimal solutions. In other words, for each persistence there is a base tumbling frequency that leads to similar

chemotactic efficiency. Introducing finite tumble times that depend on the persistence can change this picture, illuminating one possible method for selecting tumble persistence based on species-specific reorientation dynamics. Moving beyond linear theory we found that optimal chemotactic strengths exist, and that these maximise reaction when swimming in a wrong direction, but have little or no reaction when swimming with even the slightest projection along the chemoattractant gradient.

We also studied the feeding efficiency of the various morphological variations of *S. rosetta*. Using regularised boundary element simulations, we found that feeding is optimised for the swimming unicell. The colonial forms all had smaller feeding efficiencies, suggesting that their formation is not driven by feeding advantages. Sessile thecate cells have a feeding advantage in large external flows, since they are not dragged along with the flow. The effects of diffusion was studied using finite element simulations. This was also found to be to the advantage of swimming unicells, in both the limit of small and large prey diffusion constants.

Finally, we introduced a model to study basal coupling in the flagella beating of *Chlamydomonas*. In this preliminary study, we discussed a curvature control feedback mechanism that lead to self-sustained beating. With this model we were able to fit both in-phase and anti-phase synchrony of *Chlamydomonas* using parameters that correspond to an active base, but found that it was not possible with the requirements of a passive base.

There is a lot of future work to be done on many of the studies conducted for this thesis. The three-dimensional holographic tracking of choanoflagellate could be done on a large scale. This would benefit from a better microscopic setup using e. g. lasers instead of LED light sources. Such studies could lead to detailed models for colony swimming. In particular, if studied under aerotactic conditions, detailed single-colony statistics could yield more insights into the navigational aspects. The aerotaxis study itself could be expanded upon by studying smaller oxygen gradients (by e. g. imposing 1 % oxygen on one side and 0 % oxygen on the other). This would enable studies at the limits of sensing, which could be compared to theoretical models such as those presented in [Berg and Purcell \(1977\)](#). It would also be interesting to study the aerotactic behaviour of colonies treated with chemicals that influence the flagellar beating such as ciliobrevin ([Shih et al., 2013](#)).

While it is a heavily studied area of research, there are some interesting avenues for further studies on chemotaxis. We introduced in Appendix 4.F chemotaxis calculations for a cell measuring gradients spatially. An interesting problem is to have temporally and spatially sensing cells compete against each other. This would yield cell sizes dependent on the noise levels that define when spatial sensing becomes worthwhile. Furthermore, not much work has been done on dynamic environments. What chemotactic strategy optimises behaviour in

a situation where the chemoattractant field changes? Methods such as reinforcement learning could be used to tackle such general situations.

For the problems on feeding, the present model could be expanded upon in several ways. For instance, the effect of collars could be quantified by introducing these as elastic rods. The flagella itself could also be modelled by a kinematic description of a wave-like a beat, or even described by actuation such as done in Chapter 6.

Finally, there is a lot to do on the model of basal coupling in the synchronisation of flagella. First and foremost, hydrodynamic interactions need to be implemented in a numerical simulation of the system. This will allow the testing of various models, and, hopefully, enable the distinction between the possible mechanisms for mode selection and the stochastic switching between in-phase and anti-phase beating.

Bibliography

- Adler, J. (1969). Chemoreceptors in Bacteria. *Science*, 166(3913):1588–1597.
- Adler, M., Erickstad, M., Gutierrez, E., and Groisman, A. (2012). Studies of bacterial aerotaxis in a microfluidic device. *Lab on a chip*, 12(22):4835–47.
- Adler, R. (1946). A Study of Locking Phenomena in Oscillators. *Proceedings of the IRE*, 34(6):351–357.
- Ainley, J., Durkin, S., Embid, R., Boindala, P., and Cortez, R. (2008). The method of images for regularized Stokeslets. *Journal of Computational Physics*, 227(9):4600–4616.
- Alegado, R. A., Brown, L. W., Cao, S., Dermenjian, R. K., Zuzow, R., Fairclough, S. R., Clardy, J., and King, N. (2012). A bacterial sulfonolipid triggers multicellular development in the closest living relatives of animals. *eLife*, 2012(1):e00013.
- Allan, D., Caswell, T., Keim, N., Van Der Wel, C., and trackpy: Trackpy v0.3.2. Zenodo. <http://doi.org/10.5281/zenodo.60550> (2016). trackpy: Trackpy v0.3.2.
- Aranson, I. and Tsimring, L. (2003). Model of coarsening and vortex formation in vibrated granular rods. *Physical Review E*, 67(2):021305.
- Babel, S., ten Hagen, B., and Löwen, H. (2014). Swimming path statistics of an active Brownian particle with time-dependent self-propulsion. *Journal of Statistical Mechanics: Theory and Experiment*, 2014(2):P02011.
- Bayly, P. V. and Wilson, K. S. (2015). Analysis of unstable modes distinguishes mathematical models of flagellar motion. *Journal of The Royal Society Interface*, 12(106):20150124–20150124.
- Berg, H. (1993). *Random walks in biology*.
- Berg, H. and Brown, D. (1972). Chemotaxis in *Escherichia coli* analysed by three-dimensional tracking. *Nature*.
- Berg, H. C. (2003). The Rotary Motor of Bacterial Flagella. *Annual Review of Biochemistry*, 72(1):19–54.
- Berg, H. C. and Anderson, R. A. (1973). Bacteria Swim by Rotating their Flagellar Filaments. *Nature*, 245(5425):380–382.
- Berg, H. C. and Purcell, E. M. (1977). Physics of chemoreception. *Biophysical Journal*, 20(2):193–219.

Bibliography

- Berke, A. P., Turner, L., Berg, H. C., and Lauga, E. (2008). Hydrodynamic attraction of swimming microorganisms by surfaces. *Physical Review Letters*, 101(3):1–4.
- Betancourt, M. (2017). A Conceptual Introduction to Hamiltonian Monte Carlo. *Arxiv preprint*.
- Bialek, W. and Setayeshgar, S. (2005). Physical limits to biochemical signaling. *Proceedings of the National Academy of Sciences*, 102(29):10040–10045.
- Blair, D., Neicu, T., and Kudrolli, a. (2003). Vortices in vibrated granular rods. *Physical Review E*, 67(3):031303.
- Blake, J. R. (1971a). A note on the image system for a stokeslet in a no-slip boundary. *Mathematical Proceedings of the Cambridge Philosophical Society*, 70(02):303.
- Blake, J. R. (1971b). A spherical envelope approach to ciliary propulsion. *Journal of Fluid Mechanics*, 46(01):199.
- Blakemore, R., Frankel, R., and Kalmijn, A. (1980). South-seeking magnetotactic bacteria in the Southern Hemisphere. *Physics*.
- Bonner, J. and Savage, L. (1947). Evidence for the formation of cell aggregates by chemotaxis in the development of the slime mold *Dictyostelium discoideum*. *Journal of Experimental Zoology*, 106(1):1–26.
- Brumley, D., Wan, K., Polin, M., and Goldstein, R. (2014). Flagellar synchronization through direct hydrodynamic interactions. *eLife*.
- Brumley, D. R., Polin, M., Pedley, T. J., and Goldstein, R. E. (2012). Hydrodynamic Synchronization and Metachronal Waves on the Surface of the Colonial Alga *Volvox carteri*. *Physical Review Letters*, 109(26):268102.
- Camalet, S. and Jülicher, F. (2000). Generic aspects of axonemal beating. *New Journal of Physics*, 2.
- Camalet, S., Jülicher, F., and Prost, J. (1999). Self-Organized Beating and Swimming of Internally Driven Filaments. *Physical Review Letters*, 82(7):1590–1593.
- Carpenter, B., Gelman, A., Hoffman, M. D., Lee, D., Goodrich, B., Betancourt, M., Brubaker, M., Guo, J., Li, P., and Riddell, A. (2017). Stan : A Probabilistic Programming Language. *Journal of Statistical Software*, 76(1).
- Cash, T. P., Pan, Y., and Simon, M. C. (2007). Reactive oxygen species and cellular oxygen sensing. *Free Radical Biology and Medicine*, 43(9):1219–1225.
- Celani, A. and Vergassola, M. (2010). Bacterial strategies for chemotaxis response. *Proceedings of the National Academy of Sciences*, 107(4):1391–1396.
- Chaté, H., Ginelli, F., Grégoire, G., Peruani, F., and Raynaud, F. (2008). Modeling collective motion: variations on the Vicsek model. *The European Physical Journal B*, 64(3-4):451–456.

- Cheong, F. C., Krishnatreya, B. J., and Grier, D. G. (2010). Strategies for three-dimensional particle tracking with holographic video microscopy. *Optics Express*, 18(13):13563.
- Cortez, R., Fauci, L., and Medovikov, A. (2005). The method of regularized Stokeslets in three dimensions: Analysis, validation, and application to helical swimming. *Physics of Fluids*, 17(3):031504.
- Couzin, I. D. (2003). Self-Organization and Collective Behavior in Vertebrates. 32:1–75.
- Couzin, I. D., Ioannou, C. C., Demirel, G., Gross, T., Torney, C. J., Hartnett, A., Conradt, L., Levin, S. a., and Leonard, N. E. (2011). Uninformed individuals promote democratic consensus in animal groups. *Science (New York, N.Y.)*, 334(6062):1578–80.
- Cox, M. E. (1986). Oxygen Diffusion in Poly (dimethyl Siloxane) using Fluorescence Quenching . I . Measurement Technique and Analysis. *Journal of Polymer Science Part A: Polymer Chemistry*, 24:621–636.
- Cussler, E. (2009). *Diffusion: mass transfer in fluid systems*. Cambridge University Press.
- Dayel, M. J., Alegado, R. a., Fairclough, S. R., Levin, T. C., Nichols, S. a., McDonald, K., and King, N. (2011). Cell differentiation and morphogenesis in the colony-forming choanoflagellate *Salpingoeca rosetta*. *Developmental biology*, 357(1):73–82.
- Drescher, K., Goldstein, R. E., and Tuval, I. (2010). Fidelity of adaptive phototaxis. *Proceedings of the National Academy of Sciences of the United States of America*, 107(25):11171–11176.
- Dunkel, J., Heidenreich, S., Drescher, K., Wensink, H. H., Bär, M., and Goldstein, R. E. (2013). Fluid Dynamics of Bacterial Turbulence. *Physical Review Letters*, 110(22):228102.
- Dunn, C. W., Hejnal, A., Matus, D. Q., Pang, K., Browne, W. E., Smith, S. A., Seaver, E., Rouse, G. W., Obst, M., Edgecombe, G. D., Sørensen, M. V., Haddock, S. H. D., Schmidt-Rhaesa, A., Okusu, A., Kristensen, R. M., Wheeler, W. C., Martindale, M. Q., and Giribet, G. (2008). Broad phylogenomic sampling improves resolution of the animal tree of life. *Nature*, 452(7188):745–749.
- Edelstein, A., Amodaj, N., Hoover, K., Vale, R., and Stuurman, N. (2010). Computer Control of Microscopes Using μ Manager. *Current Protocols in Molecular Biology*, pages 1–17.
- Ellison, D., Mugler, A., Brennan, M. D., Lee, S. H., Huebner, R. J., Shamir, E. R., Woo, L. A., Kim, J., Amar, P., Nemenman, I., Ewald, A. J., and Levchenko, A. (2016). Cell–cell communication enhances the capacity of cell ensembles to sense shallow gradients during morphogenesis. *Proceedings of the National Academy of Sciences*, 113(6):E679–E688.
- Eloy, C. and Lauga, E. (2012). Kinematics of the most efficient cilium. *Physical Review Letters*, 109(3):1–5.
- Endres, R. G. and Wingreen, N. S. (2008). Accuracy of direct gradient sensing by single cells. *Proceedings of the National Academy of Sciences*, 105(41).
- Endres, R. G. and Wingreen, N. S. (2009a). Accuracy of direct gradient sensing by cell-surface receptors. *Progress in Biophysics and Molecular Biology*, 100(1-3):33–39.

Bibliography

- Endres, R. G. and Wingreen, N. S. (2009b). Maximum likelihood and the single receptor. *Physical Review Letters*, 103(15):1–4.
- Erra, U., Frola, B., Scarano, V., and Couzin, I. (2009). An Efficient GPU Implementation for Large Scale Individual-Based Simulation of Collective Behavior. *2009 International Workshop on High Performance Computational Systems Biology*, pages 51–58.
- Fairclough, S., Dayel, M., and King, N. (2010). Multicellular development in a choanoflagellate. *Current Biology*, pages 875–876.
- Flory, P. J. (1969). *Statistical mechanics of chain molecules*. Wiley.
- Fodor, É., Nardini, C., Cates, M. E., Tailleur, J., Visco, P., and Van Wijland, F. (2016). How Far from Equilibrium Is Active Matter? *Physical Review Letters*, 117(3):1–6.
- Fong, G.-H. and Takeda, K. (2008). Role and regulation of prolyl hydroxylase domain proteins. *Cell Death and Differentiation*, 15(4):635–641.
- Friedrich, B. M. and Jülicher, F. (2007). Chemotaxis of sperm cells. *Proceedings of the National Academy of Sciences of the United States of America*, 104(33):13256–13261.
- Friedrich, B. M. and Jülicher, F. (2009). Steering chiral swimmers along noisy helical paths. *Physical Review Letters*, 103(6):068102.
- Geyer, V. F., Sartori, P., Friedrich, B. M., Jülicher, F., and Howard, J. (2016). Independent Control of the Static and Dynamic Components of the Chlamydomonas Flagellar Beat. *Current Biology*, 26(8):1098–1103.
- Goldstein, R. E. (2015). Green Algae as Model Organisms for Biological Fluid Dynamics. *Annual Review of Fluid Mechanics*, 47(1):343–375.
- Goldstein, R. E., Goriely, A., Huber, G., and Wolgemuth, C. W. (2000). Bistable Helices. *Physical Review Letters*, 84(7):1631–1634.
- Goldstein, R. E., Lauga, E., Pesci, A. I., and Proctor, M. R. E. (2016). Elastohydrodynamic synchronization of adjacent beating flagella. *Physical Review Fluids*, 1(7):073201.
- Greer, S. N., Metcalf, J. L., Wang, Y., and Ohh, M. (2012). The updated biology of hypoxia-inducible factor. *The EMBO Journal*, 31(11):2448–2460.
- Grosberg, R. K. and Strathmann, R. R. (2007). The Evolution of Multicellularity: A Minor Major Transition? *Annual Review of Ecology, Evolution, and Systematics*, 38(1):621–654.
- Haas, P. A., Höhn, S. S. M. H., Honerkamp-Smith, A. R., Kirkegaard, J. B., and Goldstein, R. E. (2017). Mechanics and Variability of Cell Sheet Folding in the Embryonic Inversion of Volvox. *Arxiv preprint*.
- Hastings, W. K. (1970). Monte Carlo sampling methods using Markov chains and their applications. *Biometrika*, 57(1):97–109.
- Hein, A. M., Brumley, D. R., Carrara, F., Stocker, R., and Levin, S. A. (2016). Physical limits on bacterial navigation in dynamic environments. *Journal of the Royal Society, Interface*, 13(114):20150844.

- Helbing, D., Farkas, I., Molnar, P., and Vicsek, T. (2002). Simulation of pedestrian crowds in normal and evacuation situations.
- Helbing, D., Johansson, A., Mathiesen, J., Hensen, M. H., and Hansen, A. (2006). Analytical approach to continuous and intermittent bottleneck flows. *Physical Review Letters*.
- Higdon, J. J. L. (1979). The generation of feeding currents by flagellar motions. *J. Fluid Mech*, 94(2):306–330.
- Higham, D. J. (2001). An Algorithmic Introduction to Numerical Simulation of Stochastic Differential Equations. *SIAM Review*, 43(3):525–546.
- Hines, M. and Blum, J. J. (1978). Bend propagation in flagella. I. Derivation of equations of motion and their simulation. *Biophysical Journal*, 23(1):41–57.
- Howse, J., Jones, R., Ryan, A., Gough, T., Vafabakhsh, R., and Golestanian, R. (2007). Self-Motile Colloidal Particles: From Directed Propulsion to Random Walk. *Physical Review Letters*, 99(4):048102.
- Huth, A. and Wissel, C. (1992). The simulation of the movement of fish schools. *Journal of Theoretical Biology*, 156(3):365–385.
- Huth, A. and Wissel, C. (1994). The simulation of fish schools in comparison with experimental data. 76:135–145.
- Inada, Y. and Kawachi, K. (2002). Order and flexibility in the motion of fish schools. *Journal of theoretical biology*, 214(3):371–87.
- James-Clark, H. (1866). Conclusive proofs of the animality of the ciliate sponges, and of their affinities with the Infusoria flagellata. *American Journal of Science, Series 2* V(126):320–324.
- Jepson, A., Martinez, V. A., Schwarz-Linek, J., Morozov, A., and Poon, W. C. K. (2013). Enhanced diffusion of nonswimmers in a three-dimensional bath of motile bacteria. *Physical Review E - Statistical, Nonlinear, and Soft Matter Physics*, 88(4):3–7.
- Jikeli, J. F., Alvarez, L., Friedrich, B. M., Wilson, L. G., Pascal, R., Colin, R., Pichlo, M., Rennhack, A., Brenker, C., and Kaupp, U. B. (2015). Sperm navigation along helical paths in 3D chemoattractant landscapes. *Nature Communications*, 6:7985.
- Jülicher, F. and Prost, J. (1997). Spontaneous Oscillations of Collective Molecular Motors. *Physical Review Letters*, 78(23):4510–4513.
- Kaelin, W. G. and Ratcliffe, P. J. (2008). Oxygen Sensing by Metazoans: The Central Role of the HIF Hydroxylase Pathway. *Molecular Cell*, 30(4):393–402.
- KaewTraKulPong, P. and Bowden, R. (2002). An improved adaptive background mixture model for real-time tracking with shadow detection. *Video-based surveillance systems*, pages 1–5.
- Kalinin, Y. V., Jiang, L., Tu, Y., and Wu, M. (2009). Logarithmic sensing in Escherichia coli bacterial chemotaxis. *Biophysical Journal*, 96(6):2439–2448.

Bibliography

- Kass, M., Witkin, A., and Terzopoulos, D. (1988). Snakes: Active contour models. *International journal of computer vision*.
- Katz, J. and Sheng, J. (2010). Applications of Holography in Fluid Mechanics and Particle Dynamics. *Annual Review of Fluid Mechanics*, 42(1):531–555.
- Keller, E. F. and Segel, L. A. (1971). Model for chemotaxis. *Journal of Theoretical Biology*, 30(2):225–234.
- Kessler, J. O. (1985). Hydrodynamic focusing of motile algal cells. *Nature*, 313(5999):218–220.
- Kim, J. H., Serra-Picamal, X., Tambe, D. T., Zhou, E. H., Park, C. Y., Sadati, M., Park, J.-A., Krishnan, R., Gweon, B., Millet, E., Butler, J. P., Trepate, X., and Fredberg, J. J. (2013). Propulsion and navigation within the advancing monolayer sheet. *Nature materials*, 12(7):1–8.
- Kim, S. and Karrila, S. J. (2005). *Microhydrodynamics*. Dover Publications.
- King, N., Westbrook, M. J., Young, S. L., Kuo, A., Abedin, M., Chapman, J., Fairclough, S., Hellsten, U., Isogai, Y., Letunic, I., Marr, M., Pincus, D., Putnam, N., Rokas, A., Wright, K. J., Zuzow, R., Dirks, W., Good, M., Goodstein, D., Lemons, D., Li, W., Lyons, J. B., Morris, A., Nichols, S., Richter, D. J., Salamov, A., Sequencing, J., Bork, P., Lim, W. A., Manning, G., Miller, W. T., McGinnis, W., Shapiro, H., Tjian, R., Grigoriev, I. V., and Rokhsar, D. (2008). The genome of the choanoflagellate *Monosiga brevicollis* and the origin of metazoans. *Nature*, 451(7180):783–788.
- Kirkegaard, J. B. (2015). Active contour model: <https://github.com/scikit-image/scikit-image/pull/1691>. *scikit-image GitHub Repository*.
- Kirkegaard, J. B., Bouillant, A., Marron, A. O., Leptos, K. C., and Goldstein, R. E. (2016a). Aerotaxis in the closest relatives of animals. *eLife*, 5(e18109).
- Kirkegaard, J. B. and Goldstein, R. E. (2016). Filter-feeding, near-field flows, and the morphologies of colonial choanoflagellates. *Physical Review E*, 94(5).
- Kirkegaard, J. B. and Goldstein, R. E. (2017). The role of tumbling frequency and persistence in optimal run-and-tumble chemotaxis. *Arxiv preprint*.
- Kirkegaard, J. B., Marron, A. O., and Goldstein, R. E. (2016b). Motility of Colonial Choanoflagellates and the Statistics of Aggregate Random Walkers. *Physical Review Letters*, 116(3).
- Kirkegaard, J. B. and Peaudecerf, F. J. (2017). pycuda Rayleigh Sommerfeld: github.com/juliusbierk/pycuda_rayleigh_sommerfeld. *GitHub Repository*.
- Koch, D. L. and Subramanian, G. (2011). Collective Hydrodynamics of Swimming Microorganisms: Living Fluids. *Annual Review of Fluid Mechanics*, 43(1):637–659.
- Kotar, J., Leoni, M., Bassetti, B., Lagomarsino, M. C., and Cicuta, P. (2010). Hydrodynamic synchronization of colloidal oscillators. *Proceedings of the National Academy of Sciences*, 107(17):7669–7673.

- Kudrolli, A., Lumay, G., Volfson, D., and Tsimring, L. (2008). Swarming and Swirling in Self-Propelled Polar Granular Rods. *Physical Review Letters*, 100(5):058001.
- Kuramoto, Y. (1984). *Chemical Oscillations, Waves, and Turbulence*. Springer, New York.
- Kurzthaler, C., Leitmann, S., and Franosch, T. (2016). Intermediate scattering function of an anisotropic active Brownian particle. *Scientific Reports*, 6(1):36702.
- Lahiri, S., Roy, A., Baby, S. M., Hoshi, T., Semenza, G. L., and Prabhakar, N. R. (2006). Oxygen sensing in the body. *Progress in Biophysics and Molecular Biology*, 91(3):249–286.
- Lang, B., O’Kelly, C., Nerad, T., Gray, M., and Burger, G. (2002). The closest unicellular relatives of animals. *Current biology*, 12(02):1773–1778.
- Lauga, E. (2011). Enhanced Diffusion by Reciprocal Swimming. *Physical Review Letters*, 106(17):178101.
- Lauga, E. and Powers, T. R. (2008). The hydrodynamics of swimming microorganisms. *Reports on Progress in Physics*.
- Leadbeater, B. (2015). *The Choanoflagellates. Evolution, Biology and Ecology*. Cambridge University Press, Cambridge, UK.
- Leadbeater, B. S. C., Yu, Q., Kent, J., and Stekel, D. J. (2009). Three-dimensional images of choanoflagellate loricae. *Proceedings of The Royal Society B*, 276(1654):3–11.
- Lee, S.-H. and Grier, D. G. (2007). Holographic microscopy of holographically trapped three-dimensional structures. *Optics Express*, 15(4):1505.
- Lenton, T. M., Boyle, R. A., Poulton, S. W., Shields-Zhou, G. A., and Butterfield, N. J. (2014). Co-evolution of eukaryotes and ocean oxygenation in the Neoproterozoic era. *Nature Geoscience*, 7(4):257–265.
- Leptos, K., Guasto, J., Gollub, J., Pesci, A., and Goldstein, R. (2009). Dynamics of Enhanced Tracer Diffusion in Suspensions of Swimming Eukaryotic Microorganisms. *Physical Review Letters*, 103(19):198103.
- Leptos, K. C., Wan, K. Y., Polin, M., Tuval, I., Pesci, A. I., and Goldstein, R. E. (2013). Antiphase synchronization in a flagellar-dominance mutant of *Chlamydomonas*. *Physical Review Letters*, 111(15):1–5.
- Levin, T. C., Greaney, A. J., Wetzell, L., and King, N. (2014). The rosetteless gene controls development in the choanoflagellate *S. rosetta*. *eLife*.
- Lisicki, M. (2013). Four approaches to hydrodynamic Green’s functions – the Oseen tensors. *Arxiv preprint*.
- Locsei, J. T. (2007). Persistence of direction increases the drift velocity of run and tumble chemotaxis. *Journal of Mathematical Biology*, 55(1):41–60.

Bibliography

- Locsei, J. T. and Pedley, T. J. (2009). Run and tumble chemotaxis in a shear flow: The effect of temporal comparisons, persistence, rotational diffusion, and cell shape. *Bulletin of Mathematical Biology*, 71(5):1089–1116.
- Loenarz, C., Coleman, M. L., Boleininger, A., Schierwater, B., Holland, P. W. H., Ratcliffe, P. J., and Schofield, C. J. (2011). The hypoxia-inducible transcription factor pathway regulates oxygen sensing in the simplest animal, *Trichoplax adhaerens*. *EMBO reports*, 12(1):63–70.
- Lovely, P. S. and Dahlquist, F. W. (1974). Statistical Measures of Bacterial Motility. *Journal of Theoretical Biology*, pages 477–496.
- Lushi, E., Wioland, H., and Goldstein, R. E. (2014). Fluid flows created by swimming bacteria drive self-organization in confined suspensions. *Proceedings of the National Academy of Sciences of the United States of America*, 111(27):9733–9738.
- Lyons, T. W., Reinhard, C. T., and Planavsky, N. J. (2014). The rise of oxygen in Earth’s early ocean and atmosphere. *Nature*, 506(7488):307–315.
- Ma, R., Klindt, G. S., Riedel-Kruse, I. H., Jülicher, F., and Friedrich, B. M. (2014). Active Phase and Amplitude Fluctuations of Flagellar Beating. *Physical Review Letters*, 113(4):048101.
- Magar, V. and Pedley, T. J. (2005). Average nutrient uptake by a self-propelled unsteady squirmer. *Journal of Fluid Mechanics*, 539:93–112.
- Marchetti, M. C., Joanny, J. F., Ramaswamy, S., Liverpool, T. B., Prost, J., Rao, M., and Simha, R. A. (2013). Hydrodynamics of soft active matter. *Reviews of Modern Physics*, 85(3):1143–1189.
- Mayer, J., Khairy, K., and Howard, J. (2010). Drawing an elephant with four complex parameters. *American Journal of Physics*, 78(648).
- Meisl, G., Kirkegaard, J. B., Arosio, P., Michaels, T. C. T., Vendruscolo, M., Dobson, C. M., Linse, S., and Knowles, T. P. J. (2016). Molecular mechanisms of protein aggregation from global fitting of kinetic models. *Nature Protocols*, 11(2):252–272.
- Mesibov, R., Ordal, G. W., and Adler, J. (1973). The range of attractant concentrations for bacterial chemotaxis and the threshold and size of response over this range. Weber law and related phenomena. *The Journal of General Physiology*, 62(2):203–223.
- Metropolis, N., Rosenbluth, A. W., Rosenbluth, M. N., Teller, A. H., and Teller, E. (1953). Equation of State Calculations by Fast Computing Machines. *The Journal of Chemical Physics*, 21(6):1087–1092.
- Michaels, T. C., Dear, A. J., Kirkegaard, J. B., Saar, K. L., Weitz, D. A., and Knowles, T. P. (2016). Fluctuations in the Kinetics of Linear Protein Self-Assembly. *Physical Review Letters*, 116(25):1–5.
- Michelin, S. and Lauga, E. (2010). Efficiency optimization and symmetry-breaking in a model of ciliary locomotion. *Physics of Fluids*, 22(11):111901.

- Michelin, S. and Lauga, E. (2011). Optimal feeding is optimal swimming for all Péclet numbers. *Physics of Fluids*, 23(10):1–13.
- Mills, D. B., Ward, L. M., Jones, C., Sweeten, B., Forth, M., Treusch, A. H., and Canfield, D. E. (2014). Oxygen requirements of the earliest animals. *Proceedings of the National Academy of Sciences*, 111(11):4168–4172.
- Mil'shtein, G. N. (1974). Approximate integration of stochastic differential equations. *Teor. Veroyatnost. i Primenen.*, 19(3).
- Mitchell, D. R. (2000). Chlamydomonas flagella. *Journal of Phycology*, 36:261-273.
- Mora, T. and Wingreen, N. S. (2010). Limits of sensing temporal concentration changes by single cells. *Physical Review Letters*, 104(24):1–4.
- Mortimer, D., Dayan, P., Burrage, K., and Goodhill, G. J. (2011). Bayes-Optimal Chemotaxis. *Neural Computation*, 23(2):336–373.
- Neal, R. M. (2012). MCMC using Hamiltonian dynamics. *Arxiv version*.
- Nicolau, D. V., Armitage, J. P., and Maini, P. K. (2009). Directional persistence and the optimality of run-and-tumble chemotaxis. *Computational Biology and Chemistry*, 33(4):269–274.
- Niklas, K. J. (2014). The evolutionary-developmental origins of multicellularity. *American Journal of Botany*, 101(1):6–25.
- Nursall, J. R. (1959). Oxygen as a Prerequisite to the Origin of the Metazoa. *Nature*, 183(4669):1170–1172.
- Osterman, N. and Vilfan, A. (2011). Finding the ciliary beating pattern with optimal efficiency. *Proceedings of the National Academy of Sciences*, 108(38):15727–15732.
- Parrish, J. K., Viscido, S. V., and Grünbaum, D. (2002). Self-organized fish schools: an examination of emergent properties. *The Biological bulletin*, 202(3):296–305.
- Pazour, G. J., Agrin, N., Leszyk, J., and Witman, G. B. (2005). Proteomic analysis of a eukaryotic cilium. *Journal of Cell Biology*, 170(1):103–113.
- Peaudecerf, F. J. and Goldstein, R. E. (2015). Feeding ducks, bacterial chemotaxis, and the Gini index. *Physical Review E - Statistical, Nonlinear, and Soft Matter Physics*, 92(2).
- Pedley, T. and Kessler, J. (1990). A new continuum model for suspensions of gyrotactic micro-organisms. *Journal of Fluid Mechanics*.
- Pepper, R. E., Roper, M., Ryu, S., Matsumoto, N., Nagai, M., and Stone, H. a. (2013). A new angle on microscopic suspension feeders near boundaries. *Biophysical journal*, 105(8):1796–804.

Bibliography

- Perni, M., Galvagnion, C., Maltsev, A., Meisl, G., Müller, M. B. D., Challa, P. K., Kirkegaard, J. B., Cohen, S. I. A., Cascella, R., Chen, S. W., Limboker, R., Sormanni, P., Heller, G. T., Francesco, A., Cremades, N., Cecchi, C., Chiti, F., Ellen, A. A., Knowles, T. P. J., Vendruscolo, M., Bax, A., Zaslhoff, M., Dobson, C. M., Perni, M., Galvagnion, C., Maltsev, A., Meisl, G., Müller, M. B. D., Challa, P. K., Flagmeier, P., Cohen, S. I. A., Chen, S. W., Limboker, R., Sormanni, P., Heller, G. T., Aprile, F. A., Cremades, N., Cecchi, C., Chiti, F., Nollen, E. A. A., Tuomas, P. J., Vendruscolo, M., Bax, A., and Dobson, C. M. (2017). A natural product inhibits the initiation of α -synuclein aggregation and suppresses its toxicity. *Proceedings of the National Academy of Sciences*, 114(12):E2543–E2543.
- Pettitt, M. and Orme, B. (2002). The hydrodynamics of filter feeding in choanoflagellates. *European Journal of Protistology*, 332:313–332.
- Pisani, D., Pett, W., Dohrmann, M., Feuda, R., Rota-Stabelli, O., Philippe, H., Lartillot, N., and Wörheide, G. (2015). Genomic data do not support comb jellies as the sister group to all other animals. *Proceedings of the National Academy of Sciences*, 112(50):15402–15407.
- Polin, M., Tuval, I., Drescher, K., Gollub, J., and Goldstein, R. (2009). Chlamydomonas swims with two "gears" in a eukaryotic version of run-and-tumble locomotion. *Science*, 325(July):487–491.
- Purcell, E. M. (1977). Life at low Reynolds number. *American Journal of Physics*, 45(1):3–11.
- Quaranta, G., Aubin-Tam, M. E., and Tam, D. (2015). Hydrodynamics Versus Intracellular Coupling in the Synchronization of Eukaryotic Flagella. *Physical review letters*, 115(23):238101.
- Reneaux, M. and Gopalakrishnan, M. (2010). Theoretical results for chemotactic response and drift of E. coli in a weak attractant gradient. *Journal of Theoretical Biology*, 266(1):99–106.
- Reynolds, C. W. (1987). Flocks, herds and schools: A distributed behavioral model. *ACM SIGGRAPH Computer Graphics*, 21(4):25–34.
- Riedel-Kruse, I. H., Hilfinger, A., Howard, J., and Julicher, F. (2007). How molecular motors shape the flagellar beat. *HFSP Journal*, 1(3):192–208.
- Ringo, D. L. (1967). Flagellar Motion and Fine Structure of the Flagellar Apparatus in Chlamydomonas. *The Journal of Cell Biology*, 33(3):543–571.
- Rivero, M. A., Tranquillo, R. T., Buettner, H. M., and Lauffenburger, D. A. (1989). Transport models for chemotactic cell populations based on individual cell behavior. *Chemical Engineering Science*, 44(12):2881–2897.
- Rizzo, F. (1994). *Boundary Integral and Singularity Methods for Linearized Viscous Flow* (C. Pozrikidis), volume 36. Cambridge University Press.
- Roper, M., Dayel, M. J., Pepper, R. E., and Koehl, M. a. R. (2013). Cooperatively Generated Stresslet Flows Supply Fresh Fluid to Multicellular Choanoflagellate Colonies. *Physical Review Letters*, 110(22):228104.

- Ruiz-Trillo, I., Roger, A. J., Burger, G., Gray, M. W., and Lang, B. F. (2008). A phylogenomic investigation into the origin of Metazoa. *Molecular Biology and Evolution*, 25(4):664–672.
- Rusconi, R., Guasto, J. S., and Stocker, R. (2014). Bacterial transport suppressed by fluid shear. *Nature Physics*, 10(February):2–7.
- Ryan, J. F., Pang, K., Schnitzler, C. E., Nguyen, A.-D., Moreland, R. T., Simmons, D. K., Koch, B. J., Francis, W. R., Havlak, P., Smith, S. A., Putnam, N. H., Haddock, S. H. D., Dunn, C. W., Wolfsberg, T. G., Mullikin, J. C., Martindale, M. Q., and Baxevanis, A. D. (2013). The Genome of the Ctenophore *Mnemiopsis leidyi* and its Implications for Cell Type Evolution. *Science*, 342(6164):1242592–1242592.
- Rytkönen, K. T., Williams, T. A., Renshaw, G. M., Primmer, C. R., and Nikinmaa, M. (2011). Molecular evolution of the metazoan PHD-HIF oxygen-sensing system. *Molecular Biology and Evolution*, 28(6):1913–1926.
- Saintillan, D. and Shelley, M. J. (2007). Orientational order and instabilities in suspensions of self-locomoting rods. *Physical Review Letters*, 99(5):058102.
- Sandoval, M. (2013). Anisotropic effective diffusion of torqued swimmers. *Physical Review E*, 87(3):032708.
- Sartori, P., Geyer, V. F., Scholich, A., Jülicher, F., and Howard, J. (2016). Dynamic curvature regulation accounts for the symmetric and asymmetric beats of *Chlamydomonas* flagella. *eLife*, 5:1–26.
- Schnitzer, M. J. (1993). Theory of continuum random walks and application to chemotaxis. *Physical Review E*, 48(4):2553–2568.
- Schwarz-Linek, J., Valeriani, C., Cacciuto, A., Cates, M. E., Marenduzzo, D., Morozov, a. N., and Poon, W. C. K. (2012). Phase separation and rotor self-assembly in active particle suspensions. *Proceedings of the National Academy of Sciences of the United States of America*, 109(11):4052–7.
- Scotti, J. S., Leung, I. K. H., Ge, W., Bentley, M. A., Paps, J., Kramer, H. B., Lee, J., Aik, W., Choi, H., Paulsen, S. M., Bowman, L. A. H., Loik, N. D., Horita, S., Ho, C.-h., Kershaw, N. J., Tang, C. M., Claridge, T. D. W., Preston, G. M., McDonough, M. A., and Schofield, C. J. (2014). Human oxygen sensing may have origins in prokaryotic elongation factor Tu prolyl-hydroxylation. *Proceedings of the National Academy of Sciences*, 111(37):13331–13336.
- Sebé-Pedrós, A., Burkhardt, P., Sánchez-Pons, N., Fairclough, S. R., Lang, B. F., King, N., and Ruiz-Trillo, I. (2013). Insights into the origin of metazoan filopodia and microvilli. *Molecular Biology and Evolution*, 30(9):2013–2023.
- Segall, J. E., Block, S. M., and Berg, H. C. (1986). Temporal comparisons in bacterial chemotaxis. *Proceedings of the National Academy of Sciences of the United States of America*, 83(23):8987–8991.
- Shih, S. M., Engel, B. D., Kocabas, F., Bilyard, T., Gennerich, A., Marshall, W. F., and Yildiz, A. (2013). Intraflagellar transport drives flagellar surface motility. *eLife*, 2013(2):1–19.

Bibliography

- Shioi, J., Dang, C. V., and Taylor, B. L. (1987). Oxygen as attractant and repellent in bacterial chemotaxis. *Journal of Bacteriology*, 169(7):3118–3123.
- Short, M. B., Solari, C. a., Ganguly, S., Powers, T. R., Kessler, J. O., and Goldstein, R. E. (2006). Flows driven by flagella of multicellular organisms enhance long-range molecular transport. *Proceedings of the National Academy of Sciences*, 103(22):8315–8319.
- Shum, H. and Gaffney, E. A. (2015). Hydrodynamic analysis of flagellated bacteria swimming near one and between two no-slip plane boundaries. *Physical Review E - Statistical, Nonlinear, and Soft Matter Physics*, 91(3):1–10.
- Silverman, M. and Simon, M. (1974). Flagellar rotation and the mechanism of bacterial motility. *Nature*, 249(452):73–74.
- Singh, R., Ghose, S., and Adhikari, R. (2015). Many-body microhydrodynamics of colloidal particles with active boundary layers. *Journal of Statistical Mechanics: Theory and Experiment*, 2015(6).
- Smith, D. (2009). A boundary element regularized Stokeslet method applied to cilia-and flagella-driven flow. *Proceedings of the Royal Society of London A*, 465(1):1–20.
- Smith, E. F. (2002). Regulation of flagellar dynein by the axonemal central apparatus. *Cell Motility and the Cytoskeleton*, 52(1):33–42.
- Solari, C. a., Kessler, J. O., and Goldstein, R. E. (2013). A general allometric and life-history model for cellular differentiation in the transition to multicellularity. *The American naturalist*, 181(3):369–80.
- Solon, A. P., Fily, Y., Baskaran, A., Cates, M. E., Kafri, Y., Kardar, M., and Tailleur, J. (2015). Pressure is not a state function for generic active fluids. *Nature Physics*, 11(8):673–678.
- Sourjik, V. and Wingreen, N. S. (2012). Responding to chemical gradients: Bacterial chemotaxis. *Current Opinion in Cell Biology*, 24(2):262–268.
- Sperling, E. A., Frieder, C. A., Raman, A. V., Girguis, P. R., Levin, L. A., and Knoll, A. H. (2013). Oxygen, ecology, and the Cambrian radiation of animals. *Proceedings of the National Academy of Sciences*, 110(33):13446–13451.
- Szabó, A., Ünneper, R., and Méhes, E. (2010). Collective cell motion in endothelial monolayers. *Physica Biology*, 7(4).
- Takatori, S. C. and Brady, J. F. (2015). Towards a thermodynamics of active matter. *Physical Review E - Statistical, Nonlinear, and Soft Matter Physics*, 91(3):1–7.
- Tambe, D. T., Hardin, C. C., Angelini, T. E., Rajendran, K., Park, C. Y., Serra-Picamal, X., Zhou, E. H., Zaman, M. H., Butler, J. P., Weitz, D. a., Fredberg, J. J., and Trepap, X. (2011). Collective cell guidance by cooperative intercellular forces. *Nature materials*, 10(6):469–75.
- Taylor, B., Zhulin, I., and Johnson, M. (1999). Aerotaxis and other energy-sensing behavior in bacteria. *Annual Reviews in Microbiology*.

- Tindall, M. J., Gaffney, E. A., Maini, P. K., and Armitage, J. P. (2012). Theoretical insights into bacterial chemotaxis. *Wiley Interdisciplinary Reviews: Systems Biology and Medicine*, 4(3):247–259.
- Tindall, M. J., Maini, P. K., Porter, S. L., and Armitage, J. P. (2008a). Overview of mathematical approaches used to model bacterial chemotaxis II: Bacterial populations. *Bulletin of Mathematical Biology*, 70(6):1570–1607.
- Tindall, M. J., Porter, S. L., Maini, P. K., Gaglia, G., and Armitage, J. P. (2008b). Overview of mathematical approaches used to model bacterial chemotaxis I: The single cell. *Bulletin of Mathematical Biology*, 70(6):1525–1569.
- Tiribocchi, A., Wittkowski, R., Marenduzzo, D., and Cates, M. E. (2015). Active Model H: Scalar Active Matter in a Momentum-Conserving Fluid. *Physical Review Letters*, 115(18):1–5.
- Trepat, X. and Fredberg, J. J. (2011). Plithotaxis and emergent dynamics in collective cellular migration. *Trends in cell biology*, 21(11):638–46.
- Trepat, X., Wasserman, M. R., Angelini, T. E., Millet, E., Weitz, D. a., Butler, J. P., and Fredberg, J. J. (2009). Physical forces during collective cell migration. *Nature Physics*, 5(6):426–430.
- Tso, W. W. and Adler, J. (1974). Negative chemotaxis in *Escherichia coli*. *Journal of Bacteriology*, 118(2):560–576.
- Tunstrøm, K., Katz, Y., Ioannou, C. C., Huepe, C., Lutz, M. J., and Couzin, I. D. (2013). Collective states, multistability and transitional behavior in schooling fish. *PLoS computational biology*, 9(2):e1002915.
- Turgut, A. E., Celikkanat, H., Gokce, F., and Sahin, E. (2008). Self-organized flocking in mobile robot swarms. *Swarm Intelligence*, 2(2-4):97–120.
- van der Walt, S., Schönberger, J. L., Nunez-Iglesias, J., Boulogne, F., Warner, J. D., Yager, N., Gouillart, E., and Yu, T. (2014). scikit-image: image processing in Python. *PeerJ*, 2:e453.
- van Teeffelen, S. and Löwen, H. (2008). Dynamics of a Brownian circle swimmer. *Physical Review E*, 78(2):020101.
- Varenes, J., Fancher, S., Han, B., and Mugler, A. (2017). Emergent versus Individual-based Multicellular Chemotaxis. *Physical Review Letters*, 188101:1–16.
- Varenes, J., Han, B., and Mugler, A. (2016). Collective Chemotaxis through Noisy Multicellular Gradient Sensing. *Biophysical Journal*, 111(3):640–649.
- Varilly, P., Willard, A. P., Kirkegaard, J. B., Knowles, T. P., and Chandler, D. (2017). Intra-chain organisation of hydrophobic residues controls inter-chain aggregation rates of amphiphilic polymers. *Journal of Chemical Physics*, 146(13):1–5.
- Vilfan, A. and Jülicher, F. (2006). Hydrodynamic flow patterns and synchronization of beating cilia. *Physical Review Letters*, 96(5):1–4.

Bibliography

- Vitorino, P., Hammer, M., Kim, J., and Meyer, T. (2011). A steering model of endothelial sheet migration recapitulates monolayer integrity and directed collective migration. *Molecular and cellular biology*, 31(2):342–50.
- Vitorino, P. and Meyer, T. (2008). Modular control of endothelial sheet migration. *Genes & development*, 22(23):3268–81.
- Vogel, H., Czihak, G., Chang, P., and Wolf, W. (1982). Fertilization kinetics of sea urchin eggs. *Mathematical Biosciences*, 58(2):189–216.
- Wales, D. J. and Doye, J. P. K. (1997). Global Optimization by Basin-Hopping and the Lowest Energy Structures of Lennard-Jones Clusters Containing up to 110 Atoms. *The Journal of Physical Chemistry A*, 101(28):5111–5116.
- Walther, A. and Muller, A. (2013). Janus particles: synthesis, self-assembly, physical properties, and applications. *Chemical reviews*.
- Wan, K. Y. and Goldstein, R. E. (2014). Rhythmicity, Recurrence, and Recovery of Flagellar Beating. *Physical Review Letters*, 113(23):238103.
- Wan, K. Y. and Goldstein, R. E. (2016). Coordinated beating of algal flagella is mediated by basal coupling. *Proceedings of the National Academy of Sciences*, 113(20):E2784–E2793.
- Wan, K. Y. and Goldstein, R. E. (2017). Run stop shock, run shock run: Spontaneous and stimulated gait-switching in a unicellular octoflagellate. *Arxiv preprint*.
- Wan, K. Y., Leptos, K. C., and Goldstein, R. E. (2013). Lag, lock, sync, slip: the many "phases" of coupled flagella. *Journal of the Royal Society Interface*, 11.
- Ward, J. P. (2008). Oxygen sensors in context. *Biochimica et Biophysica Acta - Bioenergetics*, 1777(1):1–14.
- Weber, E. (1834). *On the Tactile Senses*.
- Wensink, H. H., Dunkel, J., Heidenreich, S., Drescher, K., Goldstein, R. E., Löwen, H., and Yeomans, J. M. (2012). Meso-scale turbulence in living fluids. *Proceedings of the National Academy of Sciences of the United States of America*, 109(36):14308–13.
- Whelan, N. V., Kocot, K. M., Moroz, L. L., and Halanych, K. M. (2015). Error, signal, and the placement of Ctenophora sister to all other animals. *Proceedings of the National Academy of Sciences*, 112(18):5773–5778.
- Wiggins, C. H. and Goldstein, R. E. (1997). Flexive and Propulsive Dynamics of Elastica at Low Reynolds Numbers. *Physical Review Letters*, 2(3):3879–3882.
- Wilson, L. and Zhang, R. (2012). 3D Localization of weak scatterers in digital holographic microscopy using Rayleigh-Sommerfeld back-propagation. *Optics Express*, 20(15):16735.
- Wilson, L. G., Martinez, V. A., Schwarz-Linek, J., Tailleur, J., Bryant, G., Pusey, P. N., and Poon, W. C. K. (2011). Differential dynamic microscopy of bacterial motility. *Physical Review Letters*, 106(1):7–10.

- Wioland, H., Woodhouse, F. G., Dunkel, J., Kessler, J. O., and Goldstein, R. E. (2013). Confinement Stabilizes a Bacterial Suspension into a Spiral Vortex. *Physical Review Letters*, 110(26):268102.
- Wittkowski, R. and Löwen, H. (2012). Self-propelled Brownian spinning top: Dynamics of a biaxial swimmer at low Reynolds numbers. *Physical Review E*, 85(2):021406.
- Wittkowski, R., Tiribocchi, A., Stenhammar, J., Allen, R. J., Marenduzzo, D., and Cates, M. E. (2014). Scalar ϕ^4 field theory for active-particle phase separation. *Nature communications*, 5:4351.
- Wong, L., Johnson, M., Zhulin, I., and Taylor, B. (1995). Role of methylation in aerotaxis in *Bacillus subtilis*. *Journal of Bacteriology*, 177(14):3985–3991.
- Woodhouse, F. and Goldstein, R. (2013). Cytoplasmic streaming in plant cells emerges naturally by microfilament self-organization. *Proceedings of the National Academy of Sciences of the United States of America*, 2013.
- Woodhouse, F. G. and Goldstein, R. E. (2012). Spontaneous Circulation of Confined Active Suspensions. *Physical Review Letters*, 109(16):168105.
- Woznica, A., Cantley, A. M., Beemelmans, C., Freinkman, E., Clardy, J., and King, N. (2016). Bacterial lipids activate, synergize, and inhibit a developmental switch in choanoflagellates. *Proceedings of the National Academy of Sciences*, 113(28):7894–7899.
- Yoshimura, K. and Kamiya, R. (2001). The sensitivity of chlamydomonas photoreceptor is optimized for the frequency of cell body rotation. *Plant & cell physiology*, 42(6):665–672.
- Zhulin, I. B., Bespalov, V. A., Johnson, M. S., Taylor, B. L., Zhulin, I. B., Bespalov, V. A., and Johnson, M. S. (1996). Oxygen taxis and proton motive force in *Azospirillum brasilense*. Oxygen Taxis and Proton Motive Force in *Azospirillum brasilense*. *Journal of bacteriology*, 178(17):5199–5204.

Appendix

Materials and Methods

A.1 Culturing Cells

S. rosetta were cultured polyxenically in artificial seawater (36.5 g/L Marin Salts (Tropic Marin, Germany)) with organic enrichment (4 g/L Proteose Peptone (Sigma-Aldrich, USA), 0.8 g/L Yeast Extract (Fluka Biochemika)) at 15 $\mu\text{L}/\text{mL}$, and grown at 23°C, split weekly. Cultures were centrifuged to reach high concentrations. In the aerotaxis experiments, we used $\sim 5 \times 10^6 \text{ ml}^{-1}$.

Experimental designs were tested on the bacterium *B. subtilis*, which were streaked from frozen (-80°) onto terrific broth (Sigma-Aldrich, USA) agar plates from which a single colony could be chosen and subsequently grown in shaken flasks in terrific broth medium at 37°.

A.2 Microfluidic Devices

Microfluidic devices were manufactured using soft-lithography techniques. A protocol to reach a thickness $\sim 115 \mu\text{m}$ is the following.

SU8-2075 (MicroChem, USA) was spincoated onto a silicon wafer at $\sim 500 \text{ rpm}$ for ~ 15 seconds, then $\sim 1200 \text{ rpm}$ for ~ 30 seconds, ending with a 3 s ramp to slow down. The wafer is then heated on a hot plate at 70° for 1 minute and then baked for 5 minutes at 95° under a glass cover. The mask is then placed over the wafer and good contact between the wafer and mask is ensured by the appearance of Newton rings. The wafer is then exposed to UV light for $3 \times 15 \text{ s}$ and subsequently baked for 20 minutes at 95°. Finally, the master is developed in PGMEA.

To cast the actual chambers, PDMS base silicone elastomer (Dow Corning, USA) is mixed with a curing agent (ratio 10:1) and degassed in a vacuum desiccator for 30 minutes.

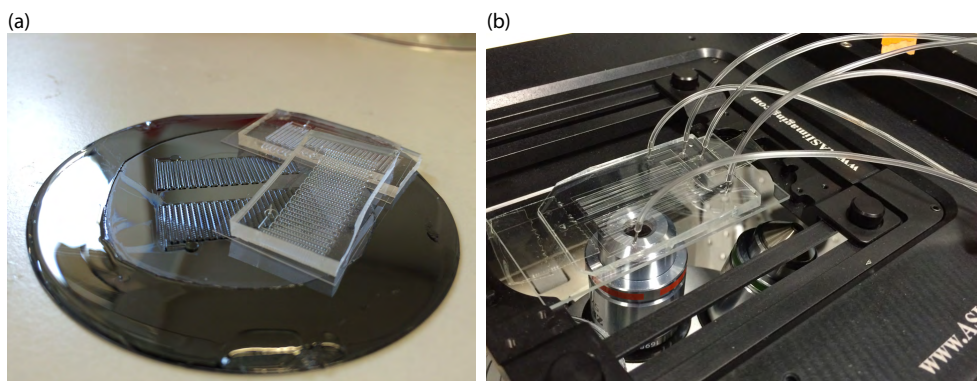


Figure A.1 Microfluidic devices. (a) The master wafer with chambers cast in PDMS on top. (b) A microfluidic device with gas channels in operation.

The mixture is poured over the master and degassed an extra 10 minutes. The chamber is then baked on the wafer for at least 2 hours at 65° . After curing, holes are punctured in the chamber to create inlets and outlets. The PDMS and a glass slide are then plasma etched for 3×10 s., with a wait time of 1 minute between. The PDMS chamber is then adhered to the glass slide creating, finally, the device.

Fig. A.1 shows an example the master and PDMS cast (a) and a device in function on the microscope (b).

A.3 Tracking

To track cells, we start by estimating the background of the video, i. e. a video without the cells present. For static videos, where the microscope is not moving, we first generated a running-median video, where each pixel in each frame of the experimental video is the median of that pixel taken over the neighbouring ~ 2.5 seconds of video. For non-static videos, we used a Gaussian-mixture model (KaewTraKulPong and Bowden, 2002) to estimate the background. Subtracting this from the original video, the resulting video contains only the colonies and noise. Band-pass filters were used to remove the noise, and finally the colony positions were found by locating local maxima in the Gaussian filtered video.

The above procedure produces for each frame in the videos a list of candidate cell positions $\{(x_i, y_i)\}$. These candidates need to be linked from frame to frame to form trajectories $x(t)$. In the naive implementation, one simply links greedily such that the two closest points are linked, then these points removed, and then the next nearest neighbours are linked and so on. However, this can lead to sub-optimal solutions if many particles are close. Instead, we use an algorithm where we choose a maximum distance L that a cell can move in a frame and

then consider all candidates within that radius. This defines a discrete optimisation problem for the minimisation of the sum of distances. To solve this problem, we use the efficient implementation of [Allan et al. \(2016\)](#).

The long tracks of single colonies in Sec. 2.3 required following of the cells during video capture. The movies were filmed at 20x magnification, for which the field of view is $\sim 350\mu\text{m}$. Colonies swim at around $\sim 15\mu\text{m/s}$, giving a time in field-of-view straight swimming on the order of 0.5 min, showing why we must follow the cells if we want long tracks (e. g. > 10 min.). If only short tracks were used, taken at a fixed location, this would create a bias towards swimmers that stay in the field of view long. By inspecting the source code of $\mu\text{Manager}$ ([Edelstein et al., 2010](#)) we found the COM port commands for the our microscope xy -stage (MS-2000, ASI, USA). This enables logging of x, y positions. As a first approach, we developed code to automatically track (by image template matching) the colonies. We were not able to fast enough calculate and adjust the focus to follow colonies in 3D on our present equipment, however, so manual tracking was used with continuous logging.

